IMPERIAL COLLEGE LONDON

Torsional guided wave EMAT for pipeline monitoring

by

Balint Herdovics

A thesis submitted to Imperial College London for the degree of

Doctor of Philosophy

Department of Mechanical Engineering

Imperial College London

London SW7 2AZ

October 2018

This page intentionally left blank

Declaration of Originality

The content of this thesis is my own research work, which was completed with the supervision of Dr. Frederic Cegla and Professor Peter Cawley. Wherever other work was used I clearly acknowledged, and provided references.

Balint Herdovics

31/09/18

This page intentionally left blank

Copyright

The copyright of this thesis rests with the author and is made available under a Creative Commons Attribution Non-Commercial No Derivatives licence. Researchers are free to copy, distribute or transmit the thesis on the condition that they attribute it, that they do not use it for commercial purposes and that they do not alter, transform or build upon it. For any reuse or redistribution, researchers must make clear to others the licence terms of this work.

This page intentionally left blank

Abstract

Non-destructive tests are performed regularly to asses a component's fitness for service. Guided wave ultrasound inspection is a well-established method for non-destructive testing of structures. As the propagation of guided waves can cover larger areas, fewer measurements are required to inspect large structures. While the sensitivity is lower, this enables rapid screening of structures for large defects. Piezoelectric guided wave transducers are widely available, but they require surface preparation and bonding. There is a concern, that adhesive property changes, especially when exposed to repeated temperature changes, can result in output signal variability. The highest possible stability is required for improved sensitivity, therefore the aim of this project is to investigate EMATs, which are non-contact and might be more stable.

The EMAT's excitation mechanism is contactless, therefore it can potentially offer a good alternative for the bonded piezoelectric transducers. The thesis presents the design, simulation and testing of a torsional guided wave EMAT, which excites the fundamental torsional guided wave mode. A high temperature version of the transducer was designed, and signals were recorded at temperatures above 200°C.

The benefit of the permanently installed transducers is that they can deliver more repeatable measurement data, as uncertainties associated with the installation process are more likely to remain constant. However, temperature variations affect the recorded signal, and they need to be compensated for. Previous work has focused on the compensation of propagation speed in ultrasonic signals. This thesis investigates the benefit of additionally compensating the transducer induced waveform changes. By adding the extra compensation term, significant improvement is reached at the location of pipe features.

Structural Health Monitoring (SHM) systems rely on stable transducers to guarantee

the required sensitivity for damage detection. The stability of the EMAT prototype was evaluated during a 1.5-year long test where the transducer and the pipe was exposed to repeated temperature variations. The results show good performance (the changes at the coherent noise level are less, than 0.8% of the signal amplitude), further improvements to transducer design that potentially increase the stability near reflectors are suggested. These can form the basis for future work.

Acknowledgements

I would like to express my heartfelt gratitude towards the people who helped with the Thesis.

First of all, I am grateful to my supervisor Dr. Frederic Cegla for the opportunity to perform the research at the NDE group, assisting me with the research, and his motivation during the years. I would also like to thank Professor Peter Cawley, Professor Peter Nagy and Professor Mike Lowe for their help and insight during the research. I am thankful for the EPSRC community for funding this project under the Grant EP/K033565/1.

I would also like to thank the current and former colleagues at the NDE lab for being a pleasant company during work and at other events. I am especially thankful to Gabor Gubicza and Nina Hancock for their technical help and expertise.

Finally, I would like to thank my friends and family for their continuous support, motivation and help during the last few years. This thesis couldn't have been written without their support. I am most grateful for the support received from my girlfriend Dorottya.

This page intentionally left blank

Contents

1 Introduction **33**

1.1 Non-Destructive Testing 33

1.2 Guided wave ultrasound 34

1.2.1 Mode choice 34

1.2.2 Guided wave propagation in pipes 35

1.3 Structural Health Monitoring 37

1.4 Ultrasonic transducers 39

1.5 Transducer stability 40

1.6 Motivation 41

1.7 Thesis Structure 43

2 Background **45**

2.1 Introduction 45

2.2 Guided waves 46

2.3 Dispersion curves for different pipe dimensions 49

2.4 Electromagnetic principles 56

2.4.1 Maxwell's equations 56

2.4.2 Eddy current and skin depth 58

2.4.3 EMAT transformer model 59

2.5 Signal processing 63

2.5.1 Ultrasonic wave-packets in the frequency-domain 63

2.5.2 Envelope detection using Hilbert transform 67
2.5.3 Signal-to-Noise Ratio of an ultrasonic measurement 67
2.5.4 Complementary sequences for signal averaging 69
2.5.5 Wave propagation directional control on a 1D structure 72
2.6 Summary 76

3 Guided wave EMAT 77

3.1 Introduction 77
3.2 Excitation mechanisms of Electromagnetic Acoustic Transducers (EMATs) 78
3.3 Force generation 79
3.3.1 Static magnetic field 81
3.3.2 Eddy current 84
3.3.3 Generated force distribution 86
3.4 Finite Element simulation of the EMAT generated wave-field 89
3.5 Reception of the fundamental torsional wave 98
3.6 Experimental validation 100
3.6.1 Manufactured transducer 100
3.6.2 Signal Acquisition System 103
3.6.3 Hardware design for cross-talk reduction 105
3.6.4 Experimentally acquired signals 110
3.7 Summary 112

4 Mode purity of the torsional wave that is excited by the EMAT 113

4.1 Introduction 113
4.2 Identification of possible error sources affecting the mode purity of the torsional wave 114
4.2.1 Localized permeability and conductivity changes 115
4.2.2 Transducer lift-off 116
4.3 Simulation of error caused by the change in excitation force 119

4.3.1 FE Simulation details . . . 119
4.3.2 Simulation of propagating waves when the force magnitude on one coil is increased by 10 % . . . 120
4.3.3 Simulation of propagating waves when the force magnitude is randomly varied within ± 10% . . . 121
4.3.4 Simulation of propagating waves when the phase of the excitation is different on one coil . . . 123
4.3.5 Simulation of propagating waves when the phase of the excitation signal is randomly varied within 0°-40°. . . . 125
4.4 Investigation of imperfect excitation due to imperfect installation of the transducer . . . 126
4.4.1 Transducer is misaligned on the pipe . . . 126
4.4.2 Transducer and pipe diameter mismatch . . . 129
4.5 Experimental validation . . . 131
4.6 Discussion . . . 133
4.7 Summary . . . 135

5 High temperature operation 137

5.1 Introduction . . . 137
5.2 Motivation . . . 137
5.3 Design modifications . . . 139
5.4 Experimental validation . . . 140
5.4.1 Heating test . . . 140
5.4.2 Experimental results . . . 141
5.5 Summary . . . 147

6 Compensation of temperature induced waveform changes during monitoring 149

6.1 Introduction . . . 149

6.2 Existing compensation strategies 149
6.3 Variations in transducer performance 151
6.4 Problems with currently used compensation methods 154
6.4.1 Effect of temperature on ultrasonic time trace 154
6.4.2 Mathematical representation of the effect of temperature changes on the signal 154
6.4.3 Imperfect single-stretch based compensation 159
6.5 Proposed, iterative compensation technique 164
6.5.1 Compensation method 164
6.5.2 Frequency dependent phase compensation of the ultrasound signal 166
6.6 Experimental results 169
6.6.1 Compensation of ultrasonic signals acquired with EMATs 169
6.6.2 Residual signals 170
6.6.3 Improved stretch factor estimation 173
6.6.4 Results when defect reflection is present in the acquired reading signal 173
6.7 Discussion 175
6.7.1 Uneven pipe temperature 175
6.7.2 Transducer ageing 176
6.7.3 Phase compensation for signal processing methods other, than baseline subtraction 176
6.7.4 Masking the defect signal 177
6.8 Summary 177

7 Long-term stability of the Guided Wave EMAT system 179

7.1 Introduction 179
7.2 Motivation 179
7.3 Possible effects of instabilities in a transducer array on the ultrasonic signal 180
7.3.1 Uniform changes on all excitation patches 181

7.3.2 Non-uniform changes on the excitation patches 182
7.4 Stability evaluation of the Guided wave EMAT array 182
7.4.1 Temperature cycling of the EMAT Guided wave transducer 182
7.4.2 Long-term stability of the guided wave EMAT array 185
7.5 Investigation of instability sources 188
7.5.1 Signal acquisition electronics system 188
7.5.2 Transducer input current 188
7.5.3 Transducer impedance 189
7.5.4 Mechanical position of the transducer 190
7.5.5 Influence of interlayer material 191
7.6 Investigation of contact material influence 191
7.6.1 Different contact types 191
7.6.2 Amplitude vs lift-off 193
7.6.3 Different number of Kapton layers 193
7.6.4 Transfer function 194
7.6.5 Different number of magnets 195
7.6.6 Mechanism of the wave excitation (reasoning) 197
7.7 Discussion - Compensation and transducer improvement 199
7.7.1 Compensation 199
7.7.2 Transducer improvement 200
7.8 Summary 202

8 Conclusions **203**
8.1 Thesis review 203
8.2 Key findings 204
8.3 Further work 206

References **208**

List of Publications **229**

This page intentionally left blank

List of Figures

2.1 Different types of wave modes can propagate in pipe-like structures. Longitudinal modes (a) have axial and radial displacement, torsional modes (b) have displacement in the tangential direction, whereas flexural modes have complex displacement varying along the circumference (c). 46

2.2 Displacement variation throughout the thickness for the fundamental (a) and second order (b) torsional mode. 47

2.3 Dispersion curves for a 3-inch NPS Schedule 40 pipe showing the phase velocity of each modes 48

2.4 Dispersion curves for a few modes existing on an NPS 4 (Schedule 40) inch pipe. Other guided wave modes are not shown for clarity. 50

2.5 Dispersion curves for a few modes existing on an NPS 8 (Schedule 40) inch pipe. Other guided wave modes are not shown for clarity. 51

2.6 Phase velocity of the F(12,1) mode in function of the frequency for different pipe Schedules on an NPS 3-inch pipe. The fundamental torsional mode is shown for reference. 53

2.7 Dispersion curves of the first higher order torsional mode for different diameter Schedule 40 pipes. The fundamental torsional mode T(0,1) is shown as a reference in red. 54

2.8 Dispersion curves of the first higher order torsional mode for an NPS 24 pipe with different schedules (wall thickness). The fundamental torsional mode T(0,1) is shown as a reference in red. 55

2.9 Dispersion curves of the first higher order torsional mode for different pipe diameters when the wall thickness is 20 mm for all simulations. 55

2.10 Eddy current generation and steps for deducing the EMAT transformer model circuit diagram: (a) physical model of coil, magnetic fluxes, and eddy current loop; (b) same as (a) but showing idealized resistance and inductance of the coil and eddy current loops; (c) electrical circuit diagram corresponding to (b); and (d) circuit diagram of (c) representing the coupling of coil and eddy current loop via the mutual inductance L_m. . . . 60

2.11 Eddy current magnitude at different lift-off values relative to the 0 μm lift-off current calculated from measured electric impedance plots. 62

2.12 A 27 kHz 5 cycle Hanning windowed tone-burst signal. The tone-burst is commonly used as the excitation signal for ultrasonic application. 64

2.13 Method to analytically calculate the frequency content of a tone-burst time signal (bottom left). The tone-burst can be expressed as the product of three time domain signals (left side graphs). The frequency domain of the tone-burst signal (bottom right) is then calculated by convolving the frequency domain of each component (right graphs). 66

2.14 Guided wave ultrasonic signal (27 kHz) and its envelope detected using the Hilbert transform. 68

2.15 Signals recovered when using 2^{10} long Golay pulse compression technique, and the system response is affected by random $\pm$ 1% amplitude changes. Figure (b) shows the response when an additional 100 times larger system response (crosstalk) is present in the signal. 71

2.16 Representation of the directional control algorithm. An individual transducer excites a wave which travels in both direction (+ and $-$ x). With a second transducer placed at distance p constructive and destructive interference can be caused. 75

3.1 Schematics of the excitation of the zero order torsional wave (T(0,1)) with Electromagnetic Acoustic Transducers (EMATs). Several EMAT elements are distributed along the circumference on the circumference of the 3-inch NPS pipe. 80

3.2 Assembly of an EMAT element consisting of a planar elongated current carrying coil and a permanent magnet shown in three-dimensional view (a) and shown from above the planar coil (b). The eddy current flow and the force generated in a conductive substrate is indicated in (b). 81

3.3 Refraction of magnetic field lines when entering a material with higher permeability (μ_2) from a material with smaller permeability (μ_1). The phenomenon is called Snell's law. 82

3.4 Simulated static magnetic field generated by 12 mm cubic magnets with opposite polarity. The magnitude of the static magnetic field is shown in (a), the vertical and horizontal components at the top surface of the steel plate is shown in (b) and (c) for different lift-off values. The remnant magnetization of the magnets is 1.4 Tesla and the magnetization direction is vertical with opposite polarity. 83

3.5 Simulated eddy current density at the symmetry plane of the EMAT for different coil dimensions. The coil width (parameter D) is set to 20, 25, 30 mm (a); the width of the coil turns (parameter c) is set to 7, 10, 13 mm (b). The results are acquired on a 30 kHz frequency domain simulation. . 85

3.6 Simulated force distribution generated by the EMAT. The horizontal y component is shown in (a); the vertical z component is shown in (b). . . . 87

3.7 The horizontal Y and vertical Z component of the EMAT generated force at the symmetry plane of the EMAT. The symmetry plane is shown with dashed line in Figure 3.2a. 88

3.8 Simulated horizontal (Y component) distribution of the force generated by the EMAT on parallel planes at evenly spaced distances from the symmetry plane. 89

3.9 Simulated tangential force (blue) and the 4th order Fourier approximation (dashed black) of an EMAT at the symmetry line. 92

3.10 Simulated radial force (blue) and the 4th order Fourier approximation (dashed black) of an EMAT at the symmetry line. 92

3.11 Simulated force distribution (tangential and radial components) of a 6 coil 12 magnet EMAT array on a 3-inch pipe. 93

3.12 Schematics of the Abacus FE simulation: the displacement of the excited ultrasonic wave propagating on a 1-meter long NPS 3-inch pipe is simulated. The force excitation varies as a function of circumferential location and is is generated at the pipe end, and the displacement is monitored at 122 nodes 250 mm away from the excitation. 94

3.13 Simulated displacement of the outer surface of a 3-inch NPS pipe measured 250 mm from the excitation location (for 15, 30 and 45 kHz frequencies). The displacement is shown in linear (left) and logarithmic (right) scale. The generated force of an 6 coil EMAT array was used as an excitation. . 95

3.14 Simulated displacement of the outer surface of a 3-inch NPS pipe measured 250 mm from the excitation location (for 60, 75 and 90 kHz frequencies). The displacement is shown in linear (left) and logarithmic (right) scale. The generated force of an 6 coil EMAT array was used as an excitation. . 96

3.15 Evaluated coherent noise level of the tangential displacement for different frequencies and different excitations (5 cycle tone-burst, 8, 12 and 16 magnets around the circumference). The frequency range for each excitation method is shown by double arrows. 97

3.16 Result of the finite element simulation for the receiver EMAT on a planar surface. The eddy current flow direction is shown by black arrows, while the eddy current magnitude is indicated by colour plot. The shape of the magnets and one of the coils are shown in faint black lines for reference purposes. 99

3.17 Drawing of the transducer design. The assembly contains the PCB and the magnets which are required for the EMAT operation, the other components (metal rib, positioners, etc.) are used to fix the parts together. 102

3.18 Picture of a manufactured receiver transducer. 102

3.19 Picture of the custom-made signal acquisition system used for measuring the guided wave ultrasonic signal. The signal acquisition system contains the Handyscope HS3 (waveform generator and PC based oscilloscope), 40W power amplifier, relay board for the two-transmitter measurement, the current transformer for current waveform measurement, and the 75 dB analogue receiver amplifier. 105

3.20 Example signal where the ripple of the cross-talk decay is excessively long. This results in the first echoes to be superposed on the cross-talk signal. Signal was collected on a custom-made EMAT transducer using RITEC RPR-4000 Pulser and receiver by Jerome Combaniere. 106

3.21 Capacitive coupling mechanism: the transmitter transducers (Tx1 and Tx2 on (a)) are coupled to the receiver transducer (Rx1). The voltage on the transmitter transducer is first coupled to the pipe, then to the receiver transducer (b). 107

3.22 Inductive coupling mechanism: The magnetic flux generated by the current in the transmit transducer passes through the receiver coils. An EMF voltage is then generated due to the changing magnetic flux. 107

3.23 Solution for eliminating the capacitive coupling between the coils: the transmit transducer is driven in differential mode (the signals with opposite polarity are connected to the coil terminals), therefore the net charge is zero in the pipe. 108

3.24 Solution for eliminating the inductive coupling between the coils: one of the coils are connected with different polarity, therefore the net flux passing through the receiver coils is zero. The reception of the torsional wave on a pipe is guaranteed by respectively flipping the magnets on those coils (shown in Figure 3.25) 109

3.25 Elimination of inductive coupling of the excitation signal to the receiver: Arrangement of the magnets and coils around the pipe circumference is different for the receiver transducer. Every second coil is wired differently, and the magnets on those coils are flipped as well. 109

3.26 Measurement setup for acquiring signals on a 5-meter long 3-inch NPS pipe using two transmitting and one receiving transducer. 110

3.27 Example acquire signals (right (a) and left (b) direction) with reduced cross-talk signal. The signal was acquired when the excitation voltage was set to 3V (~900mA current). The signal was averaged 50 times to reduce the random noise. The cross-talk signal is much smaller than the ultrasonic signal, therefore the ultrasonic signals can be received with minimal travelled distance. 111

4.1 First arrival wave packets of acquired ultrasonic signals when the transmitting transducer is repeatedly installed onto the pipe (same axial location) with different uniform lift-off values. 117

4.2 Measured ultrasonic signal amplitude of the incident (direct) wave for different lift-off values. 117

4.3 First arrival of the acquired ultrasonic signals with different uniform lift-off values. The signals are normalized by their envelope so that the differences in the signal's phase are easier to identify. 118

4.4 Extrapolated phase changes compared to the signals with 0 μm lift-off. The measurement was repeated three times to reduce measurement errors. 119

4.5 Schematics of the ABAQUS FE simulation: the displacement of the excited ultrasonic wave propagating on a 1-meter long NPS pipe is simulated. The force excitation (12 patches of 5mm by 10mm surface area) is generated at the pipe end, and the displacement is monitored on 122 nodes 250 mm away from the excitation. 120

4.6 Simulated ultrasonic signal displacement in linear scale (a) and logarithmic scale (b) when the excitation amplitude was increased by 10% on two excitation patches (equivalent of one coil). 121

4.7 Coherent noise level for each FE simulation when the excitation amplitude on each coil is varied by a random percentage between +10% and -10%. The coherent noise level is calculated as the largest displacement of all the nodes after 0.25 millisecond but before 0.55 millisecond. 122

4.8 Simulated ultrasonic torsional wave displacements when one of the EMAT coils generate the excitation signal with 0 (a), 20° (b) and 40° (c) phase difference. The displacement is monitored 250 mm from the excitation location. 124

4.9 Simulated ultrasonic torsional wave in logarithmic scale (normalized to the signal amplitude) when one of the EMAT coils generate the excitation signal with 0 (a), 20 (b) and 40 (c) phase difference. 124

4.10 Coherent noise level for each FE simulation when the phase of the excitation on all coils are varied by a random phase between 0° and 40°. The coherent noise level is calculated as the largest displacement of all the nodes after 2.5 milliseconds. 126

4.11 Schematics of the investigated imperfect excitation named as “Tilted” (a) and “Spiral” (b) is shown in grey colour. The original (ideal) excitation surfaces are shown with dashed lines. 127

4.12 Simulated ultrasonic wave displacement resulted by exciting the wave on the imperfect excitation called “Tilted”. The tilt angle for the simulation was 4°. 128

4.13 Simulated ultrasonic wave displacement resulted by exciting the wave on the imperfect excitation called “Spiral”. The angle of the spiral excitation compared to the original was 4°. 128

4.14 Evaluated coherent noise levels when the excitation patches are altered by different angles. The coherent noise level is calculated as the largest displacement of all the nodes after 0.25 milliseconds. 129

4.15 Schematics of the investigated imperfect excitation when the wave is not excited on a small circumferential location. 130

4.16 Evaluated coherent noise in the measurements for different circumferential gaps. The coherent noise level is calculated as the largest simulated displacement of all the nodes after 2.5 milliseconds. 130

4.17 Acquired ultrasonic signals when the lift-off was changed on one of the 6 coils on the transmitting transducer. 132

4.18 Acquired ultrasonic signals when the transducer is incorrectly installed onto the pipe in a "Spiral" shape. The Spiral misplacement is shown in Figure 4.11b. 132

4.19 Recorded tangential displacement waveform on 122 receiving nodes in dB scale for the 4° "Spiral" simulation (a), and a signal calculated as the mean of 12 receiving nodes (b). 134

5.1 Computer drawing of the high-temperature EMAT prototype. 140

5.2 Measurement setup for acquiring signals with arbitrary pipe temperature. Finned heater element (red) is used for heating, while the pipe outer surface is well-insulated (grey) from the environment. 141

5.3 Laboratory setup for heating tests: a) schematic of the arrangement of pipe, insulation and heater that was used in experiments and b) photograph of a transducer on the pipe in between insulation. 142

5.4 Recorded thermocouple readings during a typical pipe heating cycle. One thermocouple (TC1-blue) was placed inside of the pipe to monitor the air temperature, the rest was placed on the external surface of the pipe. . . . 143

5.5 Ultrasonic signals acquired on the 3-inch pipe at different temperatures from 30°C to 210°C. The plotted signals contain several reverberations of the echoes. For some signal arrival times of echoes from the same feature are marked by dashed lines. It is clearly visible that at higher temperature waves propagate at reduced velocity (as seen by the later arrival time of the same wave packet). 144

5.6 Ultrasonic signals acquired on the 3-inch pipe at different temperatures. . . 144

5.7 Incident wave of the guided wave signals acquired on the pipe at different temperatures. 145

5.8 Amplitude and phase of the incident wave-packet at different temperatures. 146

5.9 Coherent noise levels for signals acquired at different temperatures 147

6.1 Experimentally acquired impedance of a 6 coil transmitting EMAT at 23 °C (solid line) and 90 °C (dashed). The magnitude of the impedance is plotted at the top figure (a), whilst the phase of the impedance is plotted at the bottom figure (b). 153

6.2 Simulated ultrasonic signals after 3 meters of propagation when the excitation was a 27 kHz 5 cycle Hanning windowed tone-burst. Signals with different propagation speed (3250 and 3234 m/s) are shown in (a). The effect of transducer phase response change is shown in (b), where the excitation phase was0° and 35° (propagation speed was 3250 m/s for both). 155

6.3 Simulated ultrasonic signals with the propagation speeds of 3250 and 3234 m/s (a), and their difference or residuals (b). An increasing trend in the residual error can be observed. 157

6.4 Signals with different excitation phase (0° and 35°) (a), and their difference (b). The error observed on each wave-packet is independent of distance from the source. 158

6.5 Combined effect of propagation speed change and transducer response change on the phase difference of two signals as a function of propagation distance. The phase difference due to the transducer phase response change is independent of the travelled distance, whereas the phase difference due to the propagation speed change is increasing with the travelled distance. 159

6.6 Example of ultrasound time signals with imperfect compensation on simulated signals: The correlation based stretch estimation methods will result in imperfect stretch estimation. The propagation speed is estimated with an error of 12 and 23 m/s when the excitation phase was changed by 57° and 114°. Also, the signals do not overlap, therefore the residual signals will be large. 160

6.7 Problem with single-stretch compensation methods: The phase of the ultrasonic signal is altered according to the dashed line, whereas the signal stretch compensates for the phase error according the dotted line. The remaining phase estimation error is represented by the black line. 161

6.8 Different cases for compensation. Signal stretched using the envelope as the reference (a); stretch estimated using the acquired ultrasonic signal (b); both signal stretch and phase compensation is applied.(c). 162

6.9 Residual error after baseline subtraction associated with different methods (shown in Figure 6.8) on a logarithmic scale. The error was calculated for a 10% reflector. 163

6.10 Measurement setup for acquiring signals on a 5 meter long 3-inch NPS pipe using two transmitting and one receiving transducer 164

6.11 Acquired right travelling torsional guided wave travelling on the 3-inch test pipe. The incident wave-packet of the signal is used for phase change estimation and is highlighted in black on a grey background. 165

6.12 Flowchart of the iterative temperature compensation method: The signal stretch is estimated on a signal which is phase compensated only (in the first iteration the signal is simply the original reading signal). Then the stretch factor is applied on the original reading signal. Then the phase difference is estimated between the baseline and the reading signal, and is applied to the stretched signal. This iteration is repeated 5 times, as after this number of iterations the stretch and phase estimates only change negligibly. 167

6.13 The Fourier magnitude spectrum of the baseline's and the stretched reading signal's incident wave-packet is slightly different due to the performed stretch (a). The frequency dependent correction corrects for its unwanted effect (frequency noise) by applying a magnitude (a) and phase (b) correction on the ultrasonic signal. The compensated frequency range is selected as the main bandwidth of the excitation signal spectra (19 kHz-37.5 kHz in this example). The estimated uniform phase is shown for reference. . . . 168

6.14 The incident wave of the ultrasonic signals: baseline signal (black), reading signal compensated for propagation speed (dashed), phase and propagation speed change compensated (grey). The temperature difference between the baseline and the reading was 41.5 °C. 170

6.15 Calculated residual signals when the temperature difference between the baseline and the reading signals was 41.5 °C. The residual is calculated when the reading signals were compensated for the propagation speed only (dashed), and when it was also phase compensated (solid). For demonstration purposes for each compensation strategy four set of residual signals are shown with different darkness. The signals corresponding for each residual were acquired at a different time during the thermal cycling. 171

6.16 Residual signals plotted for conventional signal stretch (dashed), and when the hereby-presented temperature compensation algorithm was applied (solid). The residual signals and the improvement of the proposed compensation method is shown when the temperature between the baseline and the reading signals was 15°C (a) and 30°C (b). The residual signals are shown for four signals with a different darkness. The compensated signals were selected from different temperature cycles to demonstrate robustness of the technique on different signals. 172

6.17 Estimated wavespeed as a function of the pipe temperature for each steps in the iterative compensation method. The estimated wavespeed quickly converges to the final value. 174

6.18 Residual signals using synthetic reading signal (a 3% defect reflection is simulated 200 mm away from the pipe end reflection and is added to the acquired measurement data). Adding a defect to the reading signal has only a small effect in the residual levels for convention stretch-based temperature compensation (a), however the presence of the defect significantly increase the residual levels when the proposed iterative compensation method is used (b). The temperature difference between the baseline and the reading signal was 41.5 °C. 175

7.1 Different cases of transducer array degradation: all excitation patches generate tangential forces to excite torsional wave in the pipe. The excitation force might change in a uniform way (a), or some of the excitation patches are altered by a different amount (b). The original (reference) excitation is shown by dashed line, and the changed force signals are shown in blue and red. 181

7.2 Measurement setup for evaluating the log-term stability of EMATs: Transmitter and receiver transducers are placed onto a 5-meter long 3-inch NPS 3 SCH 40 carbon steel pipe. The temperature of the pipe is monitored at 7 locations (a). An electric heater placed at the core of the pipe is used for heating (b). The outside of the pipe is insulated for more uniform temperature distribution (during the tests insulation was placed over the transducer as well) (c). 183

7.3 Temperature reading of thermocouple 5 (installed at the receiving transducer) for each measurement during the long-term temperature cycling of the EMAT transducer. 184

7.4 Experimentally acquired right traveling torsional guided wave signals. 57 randomly selected signals are shown which were acquired on a room temperature pipe (22.6-23°C) over the 14 months monitoring period. Signal stretch was applied onto the signals to reduce the effect of propagation speed changes. 185

7.5 Maximum difference between each room temperature signal and the baseline at the coherent noise part of the signal. 186

7.6 Evaluated amplitude (a) and phase (b) values of the incident wave-packet of the acquired ultrasonic signal. The values were evaluated for every measurement during the long-term temperature cycling of the EMAT measurement system. A temperature dependent behaviour can be seen for both the amplitude and the phase, but the long-term trend is obvious only for the phase values. 187

7.7 Measured excitation current waveforms of the EMAT at room temperatures. Legend shows the highest temperature the transducer and the structure have been exposed to. 189

7.8 Measured impedance of the transmitting transducer for the frequency range of 0-50 kHz. All measurements performed at room temperature, the legend shows the highest temperature the transducer and the structure have been exposed to. 190

7.9 Amplitude of the acquired signals for each transducer prototype when different interlayer material was placed between the transducers and the pipe surface. 192

7.10 Measured signal amplitude when different number of plastic sheets were placed between the transducer and the pipe surface to generate artificial lift-off. 193

7.11 Acquired ultrasonic signals when different number of Kapton layers were placed between the EMAT transducer and the pipe surface. 194

7.12 Normalized amplitude of the measured torsional guided wave signal at different frequencies for different contact materials. For all measurements, the excitation voltage was set to the same value. 195

7.13 Transducer setup, which highlights the influence of the contact material on the ultrasound excitation. Measurements are performed when one cubic magnet is placed to all excitation patches, and when an extra set of magnets are placed onto the original ones. 196

7.14 Recorded and normalized time signals when one (blue) and two (yellow) set of magnets have been used in the EMAT. The signals are shown for three cases when different materials (Printed-circuit-board only (a), Kapton sheet (b), Silicon layer(c)) have been placed between the EMAT and the structure. 197

7.15 Recorded and normalized time signals when 1 (blue) and 2 (yellow) set of magnets have been used in the EMAT. The signals are shown for three cases when different materials (Printed-circuit-board only (a), Kapton sheet (b), Silicon layer(c)) have been placed between the EMAT and the structure. . 198

7.16 Excitation mechanism of the EMAT transducer: the Lorentz force acts on both the eddy current and the coil current, but with a different direction (a). The material that is in contact between the coil wiring and structure influences the excitation (b). A simplified model of the excitation is shown on the right (c). 199

7.17 Residual levels of the ultrasonic signals at the pipe right end reflection for each measurement during the long-term stability test of the EMAT. The residual level is shown in blue when the propagation speed and the amplitude of the signal was corrected, and is shown in black when the excitation phase differences are also corrected. 200

7.18 Evaluated phase change of the ultrasonic signals acquired when (a) previous EMAT design was used and (b) when silicon sheet was separating the EMAT coils from the pipe surface. The transducers were exposed to 30, 50, 80, 80 °C heating cycles. 201

List of Tables

2.1 Dimensions of a few Nominal Pipe Size (NPS) pipes 49

2.2 Cut-off frequencies of different flexural modes on various Schedule 40 pipes. Some values are not calculated, as they are well above the frequency range of interest. 51

2.3 NPS pipe dimensions for different pipe schedules. 52

2.4 Cut-off frequencies of the flexural F(12,1) mode for 3-inch pipes with different schedules. 53

3.1 Fourier coefficients a_n and b_n for estimating the tangential and radial force components along the pipe circumference. 91

4.1 Randomly generated excitation amplitudes (%) used as an input for 9 ABAQUS Finite Element simulations. 122

4.2 Randomly assigned excitation phases in degrees used as an input for 5 Finite Element simulations. 125

4.3 Comparison of simulated and experimentally measured coherent noise level. 133

This page intentionally left blank

Chapter 1

Introduction

1.1 Non-Destructive Testing

Non-Destructive Evaluation (NDE), also termed Non-Destructive Testing (NDT) includes many analysis techniques for material or structure evaluation. The most important characteristic of NDE and NDT techniques is that they are "non-destructive" which means that they can be carried out on components before and during service without degrading the functional performance of the component. Preliminary examination methods have started several centuries ago as rudimental measurement techniques [1,2]. Since then, the testing of structural components has become a required part of critical industrial operations. These non-destructive tests are performed regularly to estimate the health of the structure and to asses a component fitness for service. Several inspection methods have been standardized, and the tests are performed routinely [3–5]. Numerous NDE methods exists, from which the radiographic X-ray [6–8], eddy current [9–11], magnetic [12–15] and ultrasonic testing are the ones most referred to. Other NDE methods are also available such as magnetic particle testing, penetrant testing, leak testing and visual testing [16]. Often these methods are used in combination to evaluate the condition of the investigated component, or a second choice method might be used as a follow-up test.

1.2 Guided wave ultrasound

Guided wave ultrasound inspection is a well-established method for non-destructive testing of structures. The guided waves can interrogate much larger areas compared to conventional bulk ultrasonic waves, which suffer from beam spread related energy loss [17,18]. For guided wave ultrasound lower frequencies are used so that the wavelength (λ) becomes comparable with the structure's thickness. The guided waves are then "guided" by the boundaries to travel along the structure. Furthermore, materials (for example metals and polymers) tend to attenuate the ultrasonic waves less at low frequencies, therefore also increasing the insonified area [19,20]. As the propagation of guided waves can cover larger areas, fewer measurements are required to inspect large structures [17]. While the sensitivity is lower, this enables rapid screening of structures for large defects. Measurement systems have become commercially available over the last 20 years, with national and international standards established [3,21]. Theoretically, guided wave inspections can be performed on any type of structures, but tests have been mainly established for simpler structures (e.g. plates, pipes) due to practical reasons.

1.2.1 Mode choice

The main scope of this thesis is the long-range guided wave inspection and monitoring of pipelines. The modes which can propagate in pipe-like structures are the longitudinal L(0,y), the torsional T(0,y), and the flexural F(x,y) mode families, where x stands for the circumferential order and y denotes the mode number [22]. Ideally, one would choose a single mode for a guided wave measurements, so that the echo location can be determined as the wave-speed is usually known [17,18].

In the 1990's the longitudinal L(0,2) mode was used for guided wave inspection by Alleyne et al. [23]. The mode choice had the advantage of being the fastest wave mode at the frequency region, and the phase velocity of this mode is relatively constant in medium and high frequencies [24,25]. Later, test methods were established for the zero order fundamental torsional mode T(0,1) as well. The propagation of this mode is frequency independent in the whole frequency range, therefore the wave packets travel along the pipe and their shape is undistorted. Although researchers investigated the possibility of higher

frequency excitation (around MHz range) [26], the frequency range of standard torsional guided wave testing is usually lower than 100 kHz. For standard pipes higher order torsional modes are not present in this frequency range; for example the cut-off frequency of the higher order torsional modes is above 300 kHz for an NPS 3-inch Schedule 40 pipe [27,28]. The displacement of the fundamental torsional mode-shape is uniform across the pipe wall and the circumference; therefore it is equally sensitive to defects and cracks at the inner or outer surface of the pipe at any location [29]. The torsional mode also has the advantage that, in contrast to the L(0,2) mode, its propagation characteristic is not affected by the presence of liquid in the pipe. Companies have developed commercially available guided wave transducers, and guided wave testing is now well established as a test method in industry [30–32].

1.2.2 Guided wave propagation in pipes

For the investigated measurement type the torsional wave T(0,1) mode is excited which travels along the structure, and the reflected ultrasound is analyzed. The features and potential defects along the pipe length are identified from the reflections. The interaction of the torsional wave with defects and pipe features has been widely studied. If axisymmetric modes (T(0,1) or L(0,2)) interact with axisymmetric features (e.g. welds and uniform wall thickness changes along the axis) only axisymmetric modes are reflected. When the operating frequency is below the cut-off frequency of the higher order torsional modes part of the wave is reflected and no mode conversion occurs from the axisymmetric features. In this case, the interaction is described by the reflection coefficient, which is the ratio of the reflected wave amplitude compared to the amplitude of the incident wave. The geometry of the feature influences the reflection coefficient, as the change of acoustic impedance reflects Γ part of the wave:

$$\Gamma = \frac{Z_0 - Z_1}{Z_0 + Z_1} \tag{1.1}$$

where Z_0 and Z_1 is the acoustic impedance of the medium at two different sections. It is harder to calculate the reflection coefficient for more complex axisymmetric changes, such

as gradual wall thickness changes and notches. In these cases the reflection coefficient is often calculated by Finite Element (FE) methods [33].

However, defects are usually non-axisymmetric and their ultrasound response is more complex. The reflection of the torsional mode caused by cracks and notches have been studied by Demma et al. [22]. It is generally said that the largest factor influencing the reflection coefficient is the cross-sectional area loss. However, other factors such as axial extent, defect shape and frequency also influence the torsional mode reflection [22, 29]. Therefore, the amplitude of the reflected wave can only be used as a rough estimate of the cross-sectional loss. In addition, a localized deep corrosion and a larger but shallower defect might have the same cross-sectional loss. This means unfortunately, the amplitude of the reflected wave does not clearly describe the defect severity.

Non-axisymmetric defects do not only reflect part of the incoming wave, but part of the energy is converted, and other modes (e.g. flexural) are additionally reflected. These flexural modes can provide information about the circumferential extent of the defect, as defects with smaller circumferential extent will generate larger amplitude flexural modes. Alternatively, focusing methods can be used to determine more information about the defect [34]. Non axisymmetric structural components also have complex behaviour. Galvagni et al. investigated the effect of pipe supports at different loading conditions and discussed the reflection and mode conversion properties of the supports [35, 36]. In his study the influence of pipe support was investigated over large frequency range and different loading conditions.

The propagation of guided wave modes in pipes can be influenced by several other factors. Depending on the mode shape, the guided wave mode can be influenced by the transported material. Gases, due to the different acoustic impedance have no effect on the guided wave propagation. However, incompressible fluids attenuate the modes that have radial displacement component (e.g. L(0,1) mode) [37]. The tangential displacement of the torsional modes is not impeded by the liquid, unless very viscous material (thick oil, etc.) is transported.

The guided waves can usually propagate far, but the range can be decreased if for example coating is applied onto the pipes. Depending on the coating type the range of the measurement can be drastically reduced, Bitumen for example can decrease test range

from ~50 meters to ~5 meters [38]. Leinov et al. have investigated the propagation of guided waves when the pipe is buried in sand [39, 40]. It was found that the energy can leak to the surrounding soil and attenuation can vary between 1-5 dB/m depending on the sand type, moisture, mode, etc..

1.3 Structural Health Monitoring

Traditionally non-destructive evaluation (NDE) has always been carried out in discrete inspections, where the sensors and instrumentation are brought to the structure and scanned along it for detecting defects [41]. Other means of follow-up inspections might be performed afterwards, but for traditional guided wave inspections the acquired data is not compared to previous measurements. Each time access is gained to the inspected structure and a single shot measurement is carried out. For each test access to the plant component needs to be gained, insulation must be removed and manual labour is needed for each inspection. For example to gain access to some plant locations scaffolding needs to be built, roads or the ground need to be dug up or insulation removed and these costs far exceed the cost of the measurement. Also, personal safety costs can be larger than the cost of the measurement itself [42, 43]. Costs can further increase, if the plant is located in a hazardous or remote location.

It is therefore beneficial to reduce the access and manual costs by leaving the NDE equipment in place. The structure then needs to be accessed only for the permanent installation of transducers, and the manual inspections can be substituted by performing automated measurements. Remotely initiated measurements are performed, and the recorded data is sent back to the operators. Permanently attached sensor systems have recently become available because of rapid development of electronics, wireless communications and advanced battery technology making it possible and cost effective to permanently install devices.

Improved defect detection characteristics can be achieved when employing the transducers in monitoring mode [44, 45]. The permanently installed transducers allow more frequent measurements to be taken, increasing the chance to detect a newly developing defect. Plant shutdown and maintenance can be better optimized if the damage is detected in an

early stage, and damage growth is monitored. Another benefit of permanently installed transducers is that they can deliver more repeatable measurement data, as uncertainties associated with the installation process are more likely to remain constant. The environmental effects influencing the acquired signal can often be reduced, as better knowledge of background variability is available [46, 47]. Furthermore, during the monitoring process, the difference between ultrasonic signals can result in gaining detailed knowledge about changes in the structure that are not available from a single ultrasound measurement itself. The methodology which uses the permanently installed transducers to frequently collect data from the structure is called Structural Health Monitoring (SHM) [44, 45, 48].

The SHM methods does not directly measure the structure's status, but they estimate the change of condition from the acquired signals. The ultimate goal of the monitoring method is to detect and monitor the severity of defects in the structure from the changes in the acquired signals. However, signal processing techniques are required to evaluate the large datasets, and estimate the change in structure from the monitored ultrasonic signals. The most common signal processing technique is the baseline subtraction method. The baseline ultrasound signal is collected in an early measurement, when the structure's health condition is known (ideally defect-free). This baseline signal is then compared with the later measurements (often termed readings).

Ideally, any change in ultrasonic signal refers to a change in the structure only. However, in real life, the change of Environmental and Operational Conditions (EOCs) will also affect the recorded ultrasound signal. Baseline subtraction method without EOC compensation is ineffective in industrial applications [49]. The acquired signals need to be compensated first, and the compensated signal can be compared to the baseline (reference) signal. Various compensation methods and signal processing techniques [44, 50, 51] have been developed to overcome the effect of EOC and make SHM possible.

Once the signals are compensated for EOCs (to a certain extent), the baseline subtraction method can be applied. The residual signal is calculated as the difference of the baseline and the reading signal. Depending on how well the environmental and operational conditions were compensated, the residual signal will show the changes in the signal, which are the result of structural changes. Once the residual signal increases above a certain threshold, it is marked as a potential defect.

Lately, more sophisticated signal processing algorithms were proposed. Singular Vector Decomposition (SVD) [52] and Independent Component Analysis (ICA) [53, 54] can further improve the damage detection capability. The Independent Component Analysis decomposes the input set of signals (which are usually temperature compensated) into statistically independent components. A slowly growing defect will result in a monotonically increasing amplitude signal component in the ultrasonic time signal, whereas the environmental conditions alter the ultrasonic signal randomly. The ICA algorithm separates the defect time signal and the effect of the changing Environmental and Operational Conditions from the measured ultrasonic signal. A potential defect can be identified when a monotonic trend is seen in these separated components' amplitude.

First guided wave transducer products, which were developed for pipeline inspection, claimed to identify defects with ~5% cross-sectional loss [37]. Since then, significant improvement was made by deploying the transducers in monitoring mode. With baseline subtraction methods, smaller defects could be identified [42, 51]. Newly developed sophisticated signal processing methods, which search for trends in large datasets further improved sensitivity. It was reported that Singular Value Decomposition (SVD) and Independent Component Analysis (ICA) methods allow sensitivity of 1-2%. Since then, field trials have shown, that it is possible to detect damage reflections smaller, than 1% [55].

1.4 Ultrasonic transducers

Several different types of transducers are available for the generation of ultrasonic waves. Piezoelectric transducers are one of the most common transducer types. They are not only used for guided wave measurements, but also for ultrasonic array probes and other general ultrasonic transducers. The main advantage of piezoelectric transducers is that they excite strong signals. Several piezoelectric-based transducers were developed for pipeline inspection [23, 56]. Several manufacturers also offer such transducers [30–32].

Electromagnetic based transducers (EMATs) usually excite much weaker signals, therefore the development of the electronics is usually much more challenging. Different types of excitation mechanisms can contribute to the EMAT wave excitation, however, in non-magnetic structures (such as aluminium) only Lorentz force exists. [57]. In ferromagnetic

materials Lorentz, Magnetostriction, Magnetization forces are present.

Magnetostrictive GW transducers were presented, which excite torsional or longitudinal waves, [58–61]. The otherwise weak signal generated by the magnetostrictive transducers is usually enhanced by magnetostrictive patches (such as Nickel), which is bonded to the structure's surface [62]. In contrast, Lorentz force EMATs operate contactless, therefore offers a good alternative, with a significant benefit of easy installation and high expected stability.

1.5 Transducer stability

When the NDE equipment is used for long term monitoring the biggest concern is the measurement repeatability over long time periods. Any instability in the transducer or its bonding will result in a change of the excited and measured signal. The change in the ultrasonic time trace caused by the changing transfer function of the transducer can be misinterpreted as the effect caused by a defect or mask the small changes introduced by growing defects. Transducer stability is therefore a key requirement for SHM applications. Only a few reports investigate the long-term stability of the available sensors.

Piezoelectric transducers are widely used for ultrasound generation as they excite strong signals. Most commonly adhesive bonding is used to attach the piezoelectric crystal to the test specimen. The stability of these bonded transducers was investigated by Mulligan et al. [63]. Others have shown that measurements with piezoelectric transducers have great performance in the short-term, but their performance can decrease for long-term applications [64]. Different research has reported that temperature swings alter the performance of bonded piezoelectric transducers [65,66]. As high temperature variations are expected in industrial applications (for example pipes carrying varying temperature fluids), the use of adhesively bonded transducers can result in instability and drifts.

In case the signals are processed with the baseline subtraction method the instability of the signals will increase the residual signal, resulting in lower probability of damage detection, or increased false alarm rates. It is anticipated, that the damage sensitivity is also reduced if the sophisticated (SVD, ICA) signal processing methods are applied. The ICA method still searches for changes in signals (which is plotted in the weights functions),

with the difference, that the changes are plotted individually, for different parts of the signal (components). Then, the drifts in the signal will increase the weight of different signal components. Then, it will be harder to distinguish between growing components which are the result of transducer drifts and damage growth.

1.6 Motivation

The main aim of this project is to investigate the possibility of using Electromagnetic Acoustic Transducers (EMATs) for pipeline health monitoring. The fundamental torsional mode at 27 kHz was selected for the inspection mode, which allows quick screening of large pipe sections from a single location.

A key requirement for monitoring is the use of transducers, which can generate and receive highly stable ultrasound signals for long time periods. The EMATs excitation mechanism is contactless, therefore it can potentially offer a good alternative for the bonded piezoelectric transducers. Researchers suggested that the contactless operation of the EMAT inherently makes it a stable transducer, [67]. However, just because EMATs are not bonded it cannot be directly inferred that they are stable. Therefore, the long-term stability of the EMATs is evaluated in this research work.

As Electromagnetic Acoustic Transducers operate contactless, they excite weak signals. Therefore it is challenging to implement a Lorentz force based EMAT with sufficient Signal-to-Noise ratio (SNR). EMATs can often be deployed to hazardous locations, where the power (both current and voltage) used by the transducer is limited [68]. In the past it was often quoted that very high powers are required to drive EMATs, which might make them unsuitable for use in restricted areas where intrinsic safety is required. Nonetheless, the work presented in this thesis investigates how the SNR of the EMAT can be increased so that it can be excited with low power inputs.

The operational temperature of pipes located at industrial plants can often be high, therefore it is desired to use transducers which can operate at (or withstand) high temperatures. The conventional piezoelectric materials lose the piezoelectric effect at their respective Curie temperature, but this is usually not a large issue, as high-temperature compounds are available [69]. Nevertheless, it must be noted, that the maximum operat-

ing temperature of the piezoelectric materials is lower so that the aging mechanisms can be avoided [70]. Unfortunately, high-temperature piezoelectric materials are sometimes less efficient [71]

Temperature range of bonded transducers is sometimes limited to 110-120 °C if for example epoxy is used as a couplant [72]. High-temperature bonding can be selected to increase operational temperature range of the transducers [71, 73]. Another option for high temperature operation is to use dry coupled transducers, where the ultrasonic energy is transmitted through a waveguide which is pressed to the structure [74]. Often, for dry coupled transducers more throughout surface preparation is required. With dry coupled transducers the piezoelectric element can be placed further from the high temperature structure, therefore gaining advantage of the natural cooling of the transducers. It was for example reported, that high temperature guided wave inspection can be performed at high temperatures (180 °C-400 °C), but the time duration of the measurement is limited to prevent overheating of the transducers. [43].

The motivation for using Lorentz force based EMATs is that the transducer operates contactless, therefore does not require bonding, and minimal or no surface preparation is needed. The essential components of the EMAT are the permanent magnet and the conductor coil, the operational temperature range can be extended when high-temperature magnets are used. High temperature Neodymium Boron magnets are available for elevated temperatures [75], but Samarium Cobalt magnets can offer even higher operational temperature limits (above 300 °C, or 350 °C in some cases) [76]. Of course, the rest of the EMAT design (structural components, cabling, etc.) must be optimized, but the fundamental parts of the EMAT allows the high-temperature applications. Test results are shown in this document, as signals acquired on a high-temperature transducer are shown.

The presented transducer is designed so that it can operate at a large temperature range. However, Environmental and Operational Conditions (EOCs) influence the signals, which potentially limit the damage detection capabilities. Signal compensation techniques are currently available which correct for the differences in ultrasound propagation speed. However, it is useful to further investigate the possible compensation techniques, which can potentially improve the sensitivity. As increased complexity of the transduction mechan-

ism is a natural property of the EMAT, the temperature fluctuations can have reversible influence on the transducer performance. Then, signal processing techniques that compensate the transducer can potentially improve the sensitivity of the monitoring system. Other design considerations should be taken into account as well to provide further advantages for monitoring with EMATs. For example, the ease of deployment and installation of the EMAT can increase attractiveness. In contrast to the dry coupled transducers, no clamping force is required to operate an EMAT. Additionally, the permanent magnets within the EMATs structurally hold the transducers in place.

1.7 Thesis Structure

This thesis is structured into 8 chapters as outlined below. The first two chapters present the findings of previous research and literature, and the new contribution of the thesis is presented in chapters 3 to 8.

Firstly, chapter 2 gives a general overview of the previous research and serves as a theoretical introduction for the thesis. A few topics investigated in this chapter includes the propagation of ultrasound waves in solids, electromagnetic theory, and basic signal processing principles. A few novel items are also presented in this chapter, for example the investigation of noise generated by the instabilities of transmit sequences and an improved directional control technique.

Chapter 3 presents the concept and design of a Lorentz force Electromagnetic Acoustic Transducer (EMAT) for fundamental torsional mode excitation on 3-inch NPS pipes. Separate simulations are performed to estimate the magnetic field and the eddy current generated by permanent magnets and the transducer coils respectively. Then, the displacement generated by the resulted Lorentz force is simulated for a range of frequencies to find the operational frequency range of the designed EMAT. The manufactured transducer prototype is experimentally tested with a purpose-built signal acquisition hardware, and a special cross-talk reduction system.

Chapter 4 investigates how the mode purity of the generated torsional mode is influenced when the transducer is used in non-ideal conditions. Trial measurements were performed in laboratory conditions, and it is thought that in field applications the measurements

might be affected by imperfections. It is investigated how the localized material properties and uneven transducer lift-off changes the excitation forces of the transducer. Then, the result of imperfect transducer positioning is simulated. The FE simulations were performed in ABAQUS CAE program.

In chapter 5 it is described how the transducer prototype can be modified for high temperature applications. The chapter presents the hardware modifications, with the test setup and measurement procedure, which was used to acquire ultrasonic signals on high temperature environment.

Chapter 6 presents a novel temperature compensation technique which builds on the currently available temperature compensation methods but additionally compensates for the transducer performance changes. The proposed compensation method has the advantage that it enables better propagation speed change estimates, and higher sensitivity near large reflectors, as it automatically compensates for the frequency distortion caused by the propagation speed compensation methods.

Chapter 7 describes the long-term evaluation of the EMAT measurement system. The EMAT is designed for SHM applications with the hope that it can deliver repeatable signals for long time periods. The performance of the constructed EMAT over a ~18 months period is presented when the transducer was exposed to more than 100 repeated temperature cycles with the maximum temperature of 80°C.

Finally, the results, conclusions and key findings are then summarized in chapter 8 at the end of the document.

Chapter 2

Background

2.1 Introduction

This chapter introduces literature, calculations and simulations describing the theoretical framework for the thesis. Part of the presented material is well known and has previously been presented by other authors, but it is worth summarizing them so that the later discussion is understood by all readers. Also, novel calculations and simulations are included to further support the understanding of the topics. The main reason for presenting this chapter is to summarize the relevant theoretical background and to allow easier understanding of the following chapters. Throughout the document, these presented theories are repeatedly referred to.

The chapter starts with the introduction of bulk waves, and the derivation of the bulk wave velocities. Then, the guided wave behaviour is discussed, investigating the effect of geometry changes on the guided wave mode propagation. The electromagnetic principles are explored via Maxwell's equations, focusing on the parts, which are related to Electromagnetic Acoustic Transducers. The chapter ends with the discussion of signal processing techniques, which allows the efficient signal processing of acquired signals, and enhancement of the Signal-to-Noise ratio.

2.2 Guided waves

Two major types of ultrasound signal can propagate in isotropic solids: bulk waves and guided waves [17,18,77]. Bulk waves travel in infinite media, and are not governed by the boundaries. It has been discovered, that in homogeneous and isotropic materials only two types of bulk wave exist: dilatational (longitudinal) and distortional (shear) waves. These waves have different propagation speed, and these velocities can be calculated analytically from the material properties. For a typical mild steel material the longitudinal and shear wave velocity is around 5960 and 3260 m/s respectively.

Guided waves propagate throughout the whole thickness of the structure, and can cover large distances. The wavelength of the guided wave modes is large, usually comparable to the structure's dimensions. Contrary to the bulk wave ultrasound, an infinite number of guided wave modes can propagate in a structure.

The dominant particle motion of the longitudinal mode is axial and/or radial, whereas the torsional mode generates tangential displacement in the cross-section of the pipe (see Figure 2.1). The displacement of the longitudinal and torsional modes do not vary with the circumference, only variations along the wall thickness is possible. Flexural modes have varying displacement along the pipe circumference, and this variation is described as the circumferential order.

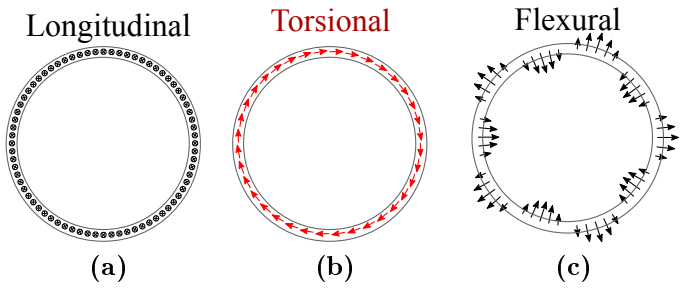

Figure 2.1: Different types of wave modes can propagate in pipe-like structures. Longitudinal modes (a) have axial and radial displacement, torsional modes (b) have displacement in the tangential direction, whereas flexural modes have complex displacement varying along the circumference (c).

The fundamental modes (e.g.) zero order torsional T(0,1) mode has a uniform rotational displacement along the pipe wall thickness. On the other hand, higher order modes have non-uniform displacement distribution along the thickness. Figure 2.2 compares the

displacement of the fundamental T(0,1) and the higher order T(0,2) mode.

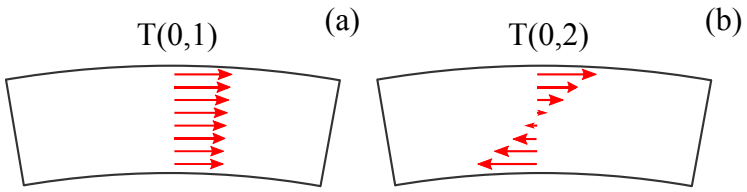

Figure 2.2: Displacement variation throughout the thickness for the fundamental (a) and second order (b) torsional mode.

The propagation of most guided wave modes are frequency dependent, as the wave-number (spatial frequency k) of the wavemodes is not a linear function of the temporal frequency (ω). The propagation properties of the wavemodes are often described by the phase and group velocities (c_p and c_g respectively):

$$c_p = \frac{\omega}{k} \tag{2.1}$$

$$c_g = \frac{\partial \omega}{\partial k} = c_p + \frac{\partial c_p}{\partial c_k} \cdot k \tag{2.2}$$

Where ω_1 and ω_2 are the angular frequencies, k_1 and k_2 are the respective wavenumber.

The group velocity is the speed at which the wave-packet travels, whereas the phase velocity is the propagation speed of the phase inside the wave-packet. If the two velocities are equal the wave-packet will travel dispersion-free, and the shape of the wave-packet is maintained for the propagation. However, in case the group and the phase velocities are different then dispersion occurs. This means that the shape of the wave-packet spreads out, and its amplitude decreases.

The frequency dependence of each mode is often visualized via the dispersion curves. The dispersion curves show the phase or group velocity of each mode for a given frequency range. The propagation speed of the guided wave modes depend on the material properties and the geometry of the structure. These dispersion curves are well known for simple

structures such as plates and pipes. Software programmes (e.g. Disperse®) have been developed to calculate these dispersion curves [78, 79]. Figure 2.3 shows the dispersion curves for a 3-inch NPS Schedule 40 carbon steel pipe (dimensions shown in Table 2.1) generated using the Disperse® software. Torsional, longitudinal, and flexural modes exists in the pipe for the frequencies of 0-100 kHz. For this 3-inch Schedule 40 pipe the higher order torsional mode (e.g. T(0,2)) is not present at this frequency region. The dispersion curves will be shown later for different pipe diameters and different wall thicknesses as well.

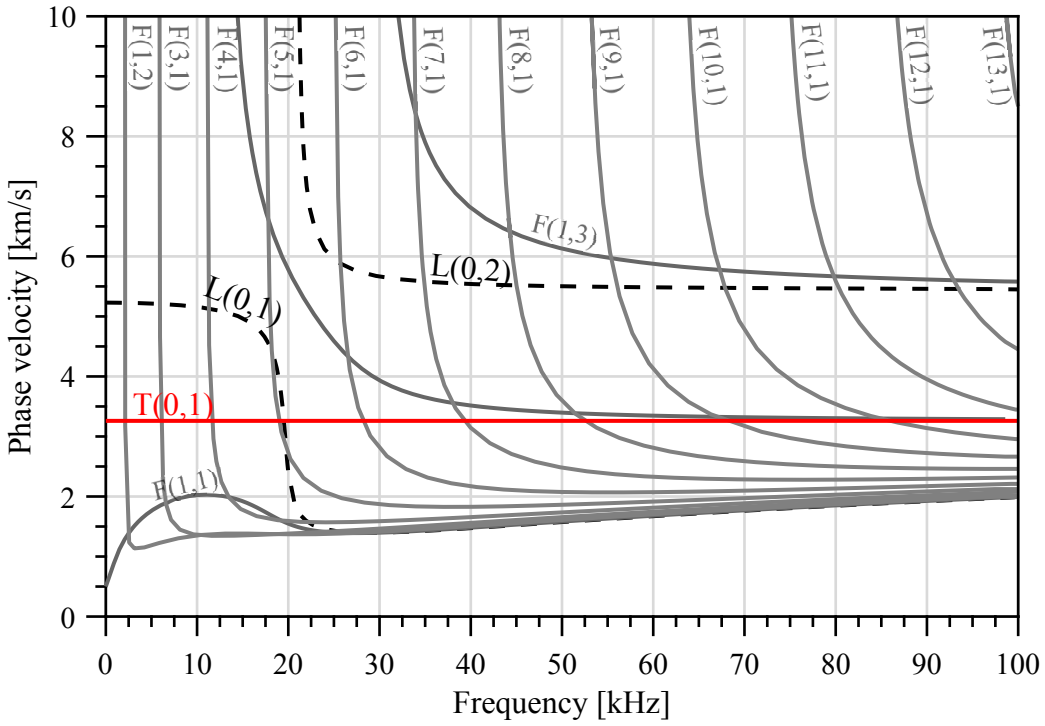

Figure 2.3: Dispersion curves for a 3-inch NPS Schedule 40 pipe showing the phase velocity of each modes

The dispersion properties of the wave modes are usually calculated so that the generation of an appropriate mode is guaranteed. Often, the generation of the dispersive modes is avoided, as the shape of the pulse distorts, meaning that the wave-packet spreads out and decreases in amplitude. Then the extraction of arrival time is more challenging. Nevertheless, there are a few inspection techniques that employ the dispersion properties, as for example wall thinning can be estimated from dispersion characteristics [80–83].

2.3 Dispersion curves for different pipe dimensions

The dispersion curves show the behaviour of each guided wave mode, which can propagate in the structure. The excitation of unwanted higher order modes can be avoided by selecting an appropriate transducer design and excitation frequency range. However, the wave propagation of the different modes are influenced by the structure's geometry. It would take excessively long time to perform FE simulations for all the pipe sizes. Instead, it is investigated how the dispersion curve characteristics of each guided wave mode vary for different pipe dimensions. This section presents numerous simulations performed in Disperse, and investigates how guided wave modes change with the pipe dimensions. If the phase and group velocity and the frequency where each mode exists is known, the guided wave transducers can more conveniently be designed for a specific pipe size. In the first instance the effect of pipe diameter change is investigated. The NPS standard [84] defines the common pipe dimensions from $\frac{1}{8}$ inch to 72+ inches. Dimensions of the standard 3,4,6 and 8 inch (Schedule 40) pipes are shown in Table 2.1.

Table 2.1: Dimensions of a few Nominal Pipe Size (NPS) pipes

Investigated pipe size	Outer diameter [mm]	Wall thickness [mm]	Inner radius [mm]
NPS 3 Sch 40	88.90	5.486	38.96
NPS 4 Sch 40	114.30	6.02	51.13
NPS 6 Sch 40	168.28	7.11	77.03
NPS 8 Sch 40	219.08	8.20	101.30

For plates it is well known, that frequency of the wave modes scale linearly with the thickness. Therefore, usually a more general solution is presented where dispersion curves are described in function of the frequency-thickness product [85]. For pipes, the dispersion curves also change as a function of geometry, and the dispersion curves can be described as a function of frequency-diameter product [86], assuming the pipe wall thickness scales with the diameter as well. However, pipes are available with different schedules, and even for the Schedule 40 NPS pipes the ratio of pipe diameter and wall thickness is not constant. Thus, the dispersion curves are presented for pipes with different sizes. The dispersion curves have been calculated for the NPS 3, 4, 6 and 8 inch (Schedule 40) carbon steel pipes. The zero order torsional T(0,1), longitudinal L(0,2) and a few flexural modes are shown in Figures 2.4 and 2.5 for NPS 3, 4 and 8 inch pipes respectively. The

figures show that most guided wave modes for larger pipe sizes will shift to the lower frequency region (except the non-dispersive torsional mode), and the cut-off frequency for each mode decreases. This then means, that for increased pipe diameters more flexural modes will exist at a given frequency bandwidth. This implies that as more unwanted modes can exist for the same frequency region on a larger pipe, a transducer with the same number of excitation locations might not perform as desired, and the transducer needs to be modified. The cut-off frequency of a few flexural modes are evaluated for each investigated pipe sizes and is shown in Table 2.2. The cut-off frequency of each mode was conveniently estimated as the frequency of the mode where the phase velocity is 10 $\frac{km}{s}$ or larger.

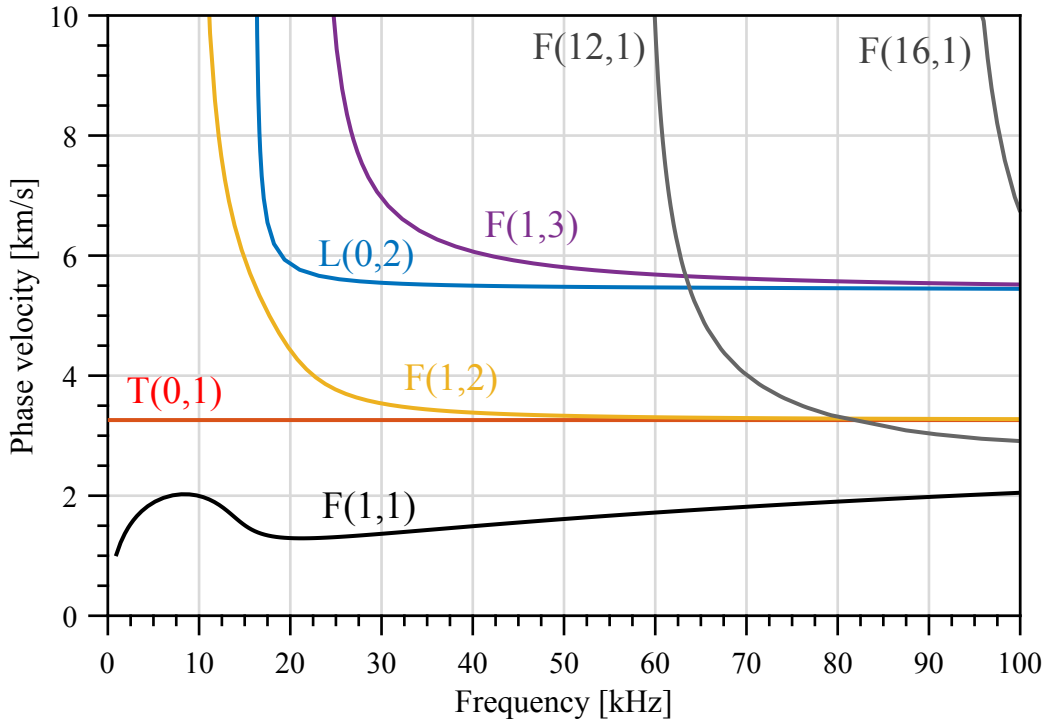

Figure 2.4: Dispersion curves for a few modes existing on an NPS 4 (Schedule 40) inch pipe. Other guided wave modes are not shown for clarity.

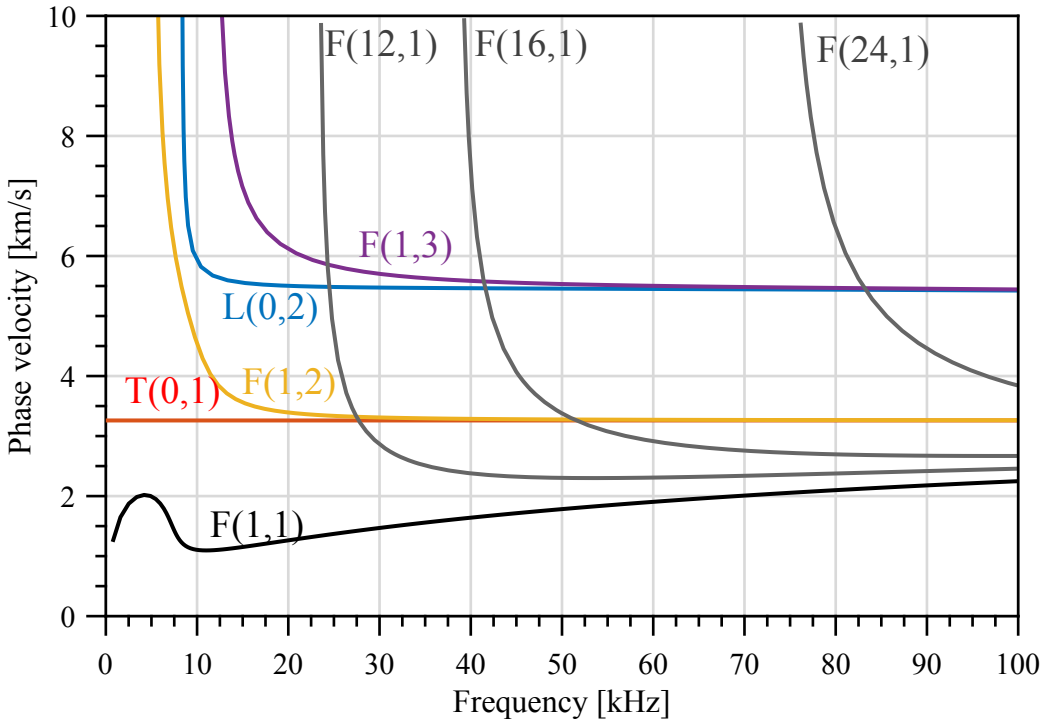

Figure 2.5: Dispersion curves for a few modes existing on an NPS 8 (Schedule 40) inch pipe. Other guided wave modes are not shown for clarity.

Table 2.2: Cut-off frequencies of different flexural modes on various Schedule 40 pipes. Some values are not calculated, as they are well above the frequency range of interest.

	F(1,3)	F(12,1)	F(16,1)	F(24,1)	F(32,1)
NPS 3 Sch 40	29.4 kHz	86.8 kHz	-	-	-
NPS 4 Sch 40	22.8 kHz	56.0 kHz	95.8 kHz	-	-
NPS 6 Sch 40	15.3 kHz	34.1 kHz	56.0 kHz	106.2 kHz	-
NPS 8 Sch 40	11.7 kHz	23.6 kHz	39.3 kHz	76.2 kHz	116.5 kHz

For pipe inspection and monitoring it is desired to excite a single mode only, so that the source of the echo can be identified easily and so that there is no location ambiguity due to the different propagation velocity of the different modes. For the inspection wave-mode the fundamental torsional mode T(0,1) was chosen. It is then desired to eliminate the generation of other modes such as higher order flexural modes. It will be detailed in the next chapter that the generation of F(N,1) mode (present at the excitation frequency region) can be avoided when the transducer has more than N number of excitation patches around the circumference. Therefore, if the dimension of the pipe is changed the trans-

ducer design must be accommodated as well to offset the changes in the cut-off frequency of the unwanted modes.

This means, that for pure torsional wave excitation the number of excitation patches needs to be increased for larger pipe diameters. A convenient solution is to keep the density of the excitation locations constant for all measurements. As a transducer with 12 excitation locations can operate on a 3-inch Sch 40 pipe below 86.78 kHz, a transducer with 16 excitation locations can operate on a 4-inch Sch 40 pipe up-to 95.94 kHz. Consecutively, a 6 and 8 inch pipe requires 24 and 32 excitation patches to operate below the frequencies of 106 and 116 kHz.

Other than the pipe diameter change, the wall thickness of pipelines has an effect on the dispersion curves as well. NPS 3-inch pipes with different wall thickness (as shown in Table 2.3) are investigated, and the dispersion curves has been calculated for each pipe. The flexural F(12,1) mode is shown for each pipe schedule in Figure 2.6. It can be seen, that pipes with low schedule (thin wall thickness) have the lowest cut-off frequencies for flexural modes.

The same mode purity is then harder to maintain for pipes with thin walls. As a solution, either the excitation frequency should be reduced, or a transducer with more excitation locations should be used. On the other hand, the flexural modes are less likely to be generated on pipes, which have larger wall thickness. The cut-off frequencies for the pipes with different wall thicknesses has been summarized in Table 2.4.

Table 2.3: NPS pipe dimensions for different pipe schedules.

Investigated pipe schedule	Outer diameter [mm]	Wall thickness [mm]	Inner radius [mm]
NPS 3 SCH 20	88.90	3.05	41.40
NPS 3 SCH 30	88.90	4.78	39.68
NPS 3 SCH 40	88.90	5.49	38.97
NPS 3 SCH 80	88.90	7.62	36.83
NPS 3 SCH 120	88.90	8.89	35.56

Therefore, it has been shown that both the pipe size, and the pipe wall thickness affect the dispersion curves. As the pipe diameter increases, more flexural modes are present in the frequency region. This practically results in transducers which have more excitation locations distributed along the circumference. It has been also shown that pipes with

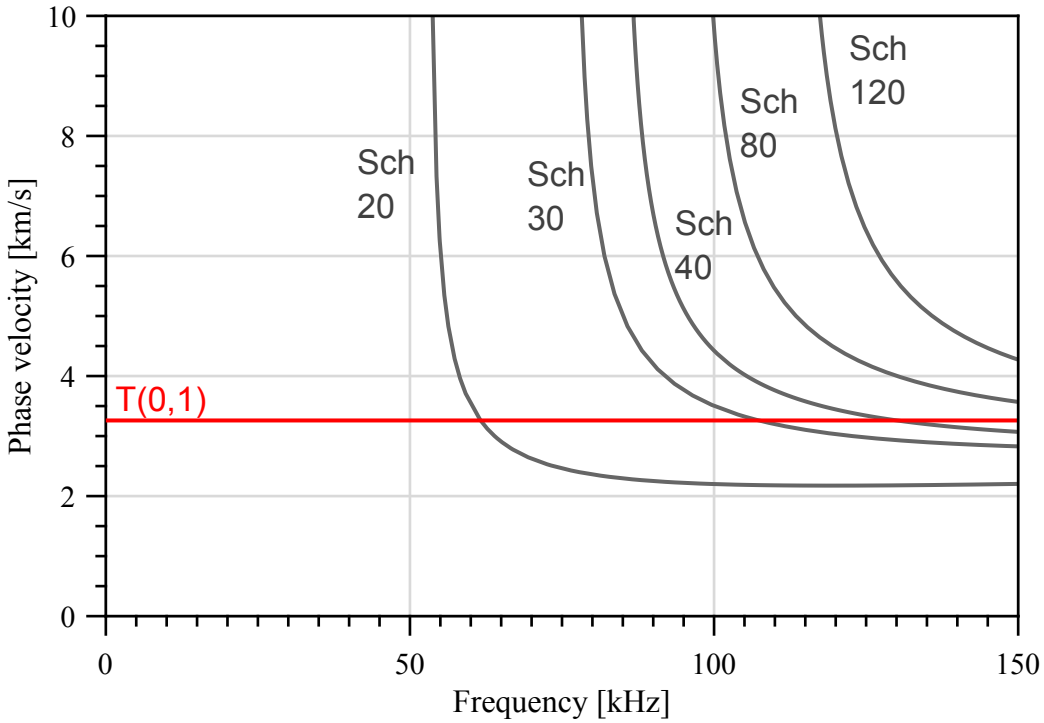

Figure 2.6: Phase velocity of the F(12,1) mode in function of the frequency for different pipe Schedules on an NPS 3-inch pipe. The fundamental torsional mode is shown for reference.

Table 2.4: Cut-off frequencies of the flexural F(12,1) mode for 3-inch pipes with different schedules.

	Sch 20	Sch 30	Sch 40	Sch 80	Sch 120
Wall thickness [mm]	3.05	4.78	5.49	7.62	8.89
Cut-off frequency [kHz]	53.7	78.2	86.6	99.8	117.4

thinner walls the cut-off frequency of the flexural modes can shift to the lower frequency region, limiting the excitation frequency range.

Apart from the generation of flexural modes, the generation of higher order torsional modes should be avoided as well. The cut-off frequency of the higher order torsional mode is high for standard pipes [87], but for pipes with thick walls the first higher order torsional mode T(0,2) can exist at lower frequencies, therefore can limit the excitation frequency of the transducer. Further simulations have been performed to investigate the behaviour of the higher order torsional mode. Figure 2.7 shows the first higher order torsional mode T(0,2) for different diameter Schedule 40 pipe sizes. The figure suggests that the cut-off frequency of this higher order torsional mode decreases as the pipe gets

larger, however the effect is mainly due to the increase in wall thickness. The simulations have been repeated for the case, when the pipe outer diameter was fixed, and the wall thickness is varied (see Figure 2.8). The results show, that the cut-off frequency of the higher order torsional mode is decreased for pipes with large wall thickness, even if the pipe diameter is the same. Further simulations have been performed to investigate the effect of changing pipe diameter when the wall thickness is constant. Figure 2.9 shows the dispersion curves of the higher order torsional mode for different pipe diameters with fixed 20 mm wall thickness.

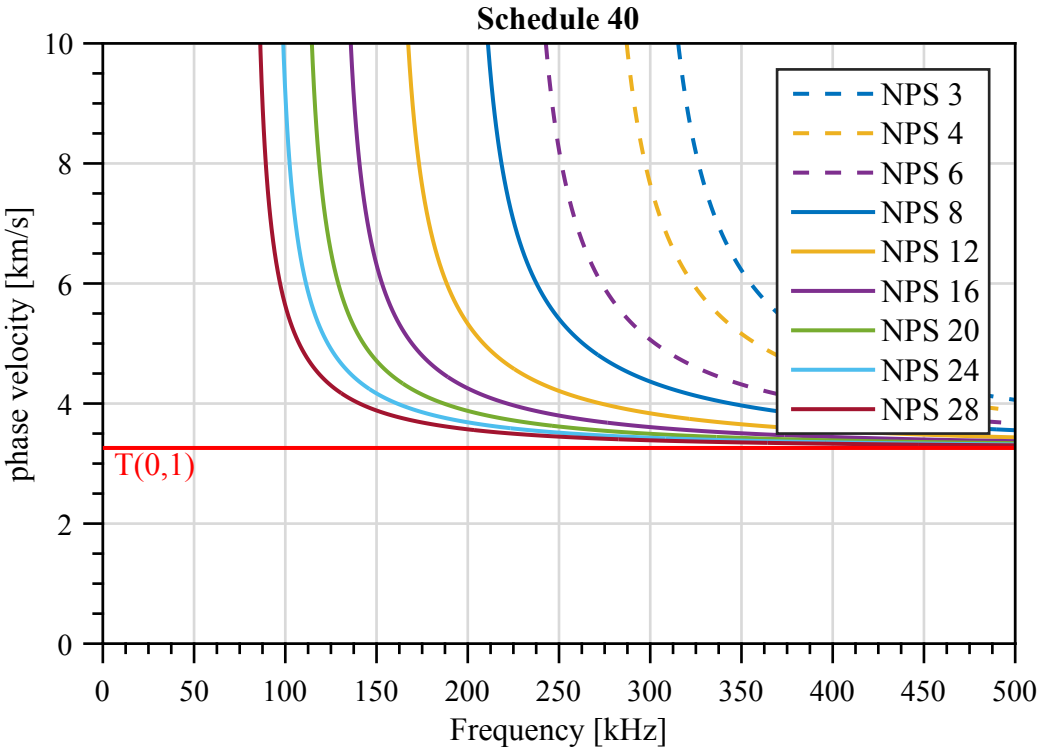

Figure 2.7: Dispersion curves of the first higher order torsional mode for different diameter Schedule 40 pipes. The fundamental torsional mode T(0,1) is shown as a reference in red.

The results in Figure 2.9 show that the pipe diameter has little effect on the behaviour of the higher order torsional mode when the pipe wall thickness is the same. If the pipe diameter is large compared to the wall thickness, the wall thickness is the only influencing factor in the T(0,2) behaviour. For the results shown in Figure 2.9, it must be noted, that the ratio of 20mm wall thickness for the NPS 6 inch pipe diameter is uncommon. It can also be noted, that the torsional modes in pipes are often referred to as the equivalent of shear horizontal modes in plates [56,88,89]. It is usually said, that if the pipe diameter is

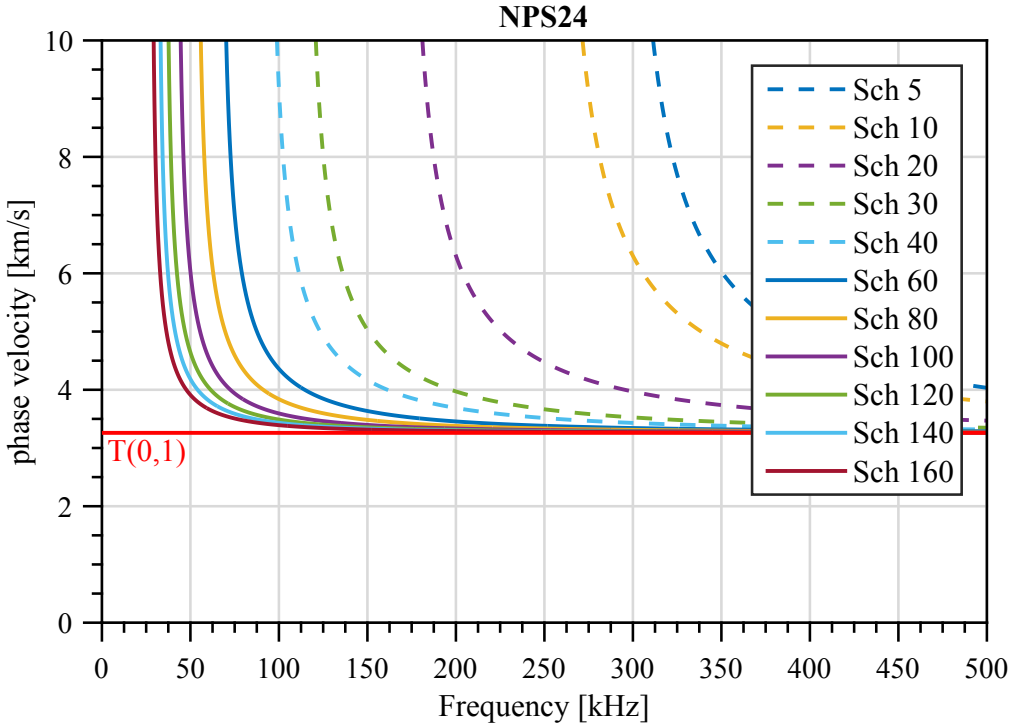

Figure 2.8: Dispersion curves of the first higher order torsional mode for an NPS 24 pipe with different schedules (wall thickness). The fundamental torsional mode T(0,1) is shown as a reference in red.

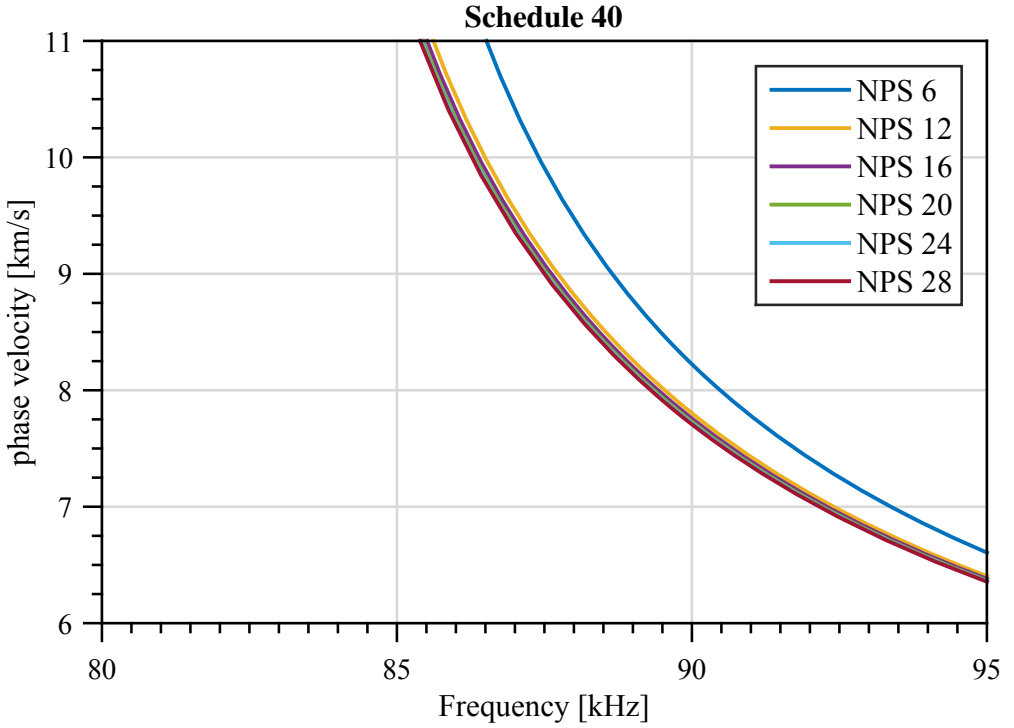

Figure 2.9: Dispersion curves of the first higher order torsional mode for different pipe diameters when the wall thickness is 20 mm for all simulations.

large compared to the wall thickness the structure is approximated as a plate by unrolling the pipe. The cut-off frequency of the SH1 (1st order shear horizontal -equivalent of the T(0,2) in pipes) mode in plates is given [17]:

$$f_n = \frac{n \cdot c_T}{2 \cdot d} \tag{2.3}$$

where n is the order of the mode, c_T is the shear wave velocity, d is the thickness of the material. Then, as the higher order torsional mode is the equivalent of the SH1 mode for pipes, the cut-off frequency of the higher order torsional modes can be conveniently estimated with the formula. The cut-off frequency of higher order torsional modes is important when investigating large pipes with thick walls. Then, to ensure single-mode excitation the operational bandwidth stays below the cut-off frequency of the higher order torsional modes.

2.4 Electromagnetic principles

2.4.1 Maxwell's equations

Throughout the thesis, the electromagnetic principles are repeatedly discussed, mainly due to the Electromagnetic Acoustic Transducer's (EMAT) operation mechanism. In the following chapters, mainly Finite Element (FE) simulations are presented for the electromagnetic problems. As the FE software solves the problems numerically it is not necessary to solve these problems analytically, but it is useful to understand the governing equations and their meaning. Traditionally, Maxwell's four equations are used to describe the basic electromagnetic principles for materials with linear properties [90].

Maxwell's equations can be written in integral and differential forms as well. Here both forms of the equations are noted, but their meaning is explained via the integral form. Maxwell's first equation is the so-called Gauss's Law. This law states, that the electric flux (integral of the electric field E on a closed surface) is proportional to the charge ρ

enclosed within the surface.

$$\oint_s \epsilon E \cdot dA = \int_V \rho \cdot dV \tag{2.4}$$

$$\nabla \cdot \epsilon E = \rho \tag{2.5}$$

The second Maxwell equation is Gauss's Magnetism Law. It describes, that the magnetic flux (integral of the magnetic flux density B) over a closed surface is zero. In other words, no magnetic monopoles exists; and magnetic field lines must be a closed loop. This equation is used for the simulation of the magnetic field lines generated by permanent magnets.

$$\oint_s B \cdot dA = 0 \tag{2.6}$$

$$\nabla \cdot B = 0 \tag{2.7}$$

Faraday's Law of induction states, that the line integral of the electric field E around a closed loop is equal to the negative of the change of magnetic flux (surface integral of the magnetic field B) through the area enclosed by the loop. This equation is necessary to understand how the changing magnetic field generates the electrostatic field (and then the eddy current in a conductive material).

$$\oint_C E \cdot dl = -\frac{d}{dt} \int_s B \cdot dA \tag{2.8}$$

$$\nabla \times E = -\frac{\partial B}{\partial t} \tag{2.9}$$

Maxwell's last equation is called Ampere's Law. It states, that the magnetic field strength over a closed loop equals to the electric current density J enclosed on the closed surface plus the change in the electric flux density D. This equation is also used in the Finite Element simulations, and has an important role in the impedance calculation of the Electromagnetic Acoustic Transducer.

$$\oint H \cdot dl = \int_S J \cdot dA + \int \frac{\partial D}{\partial t} \cdot dA \tag{2.10}$$

$$\nabla \times H = J + \frac{\partial D}{\partial t} \tag{2.11}$$

2.4.2 Eddy current and skin depth

Any changing magnetic field creates an electrostatic field as described in Equation 3.9 and 2.9. In case this induced electric field is generated in a conductive material a so-called eddy current is induced. This eddy current flows in closed loops, with the direction so that its magnetic field opposes the original magnetic field. This means the eddy current generated magnetic field then opposes the original magnetic field. It decreases exponentially with the penetrated depth. Therefore, the eddy current is concentrated near the surface of the conductor. Equation 2.12 shows the eddy current I for a given depth (x) [11,91]. As the eddy current decreases exponentially with the distance, its phase changes as well due to the $e^{-i \cdot x/\delta}$ term.

$$I(x) = I_0 \cdot e^{-x/\delta} \cdot e^{-i \cdot x/\delta} \tag{2.12}$$

This exponential decay is conventionally described by the skin-depth δ which is the penetration depth, where the eddy current magnitude has decreased by 63% (factor of 1/e). The skin-depth is dependent on the excitation frequency f, the resistivity ρ and the permeability μ of the conductor in which the eddy current is induced in. The equation for the skin-depth calculation is shown in Equation 2.13.

$$\delta = \sqrt{\frac{\rho}{\pi \cdot f \cdot \mu}} \tag{2.13}$$

The typical skin-depth for a mild steel substrate (resistivity of $\rho = 15 \cdot 10^{-8} [\Omega \cdot m]$, $\mu_r = 80$) is 125 μm at the frequency of 30 kHz.

2.4.3 EMAT transformer model

The eddy current is generated by the Electromagnetic Acoustic Transducer via electromagnetic induction. Researchers have investigated the induction mechanism, and created electrical circuit-equivalent models [92,93]. In this document, a similar EMAT transformer model is presented, but it differs from the previous reports at several points.

The principle of the eddy current generation is shown in Figure 2.10a. the changing current in the coil generates changing magnetic flux. A small part of the magnetic flux does not reach the metal conductor, this flux is termed as the leakage flux Φ_{S1}. The rest of the flux Φ_m penetrates into the conductor. The change of this flux generates the eddy current, which again generates a magnetic flux which opposes the original one. As the eddy current–generated magnetic flux opposes the main flux generated by the coil current, the main magnetic flux Φ_m is reduced. A small part of the eddy current–generated flux is a secondary leakage flux (Φ_{S2}) which does not interact with the coil.

Electric power transformers generate the output current in a similar way, as the changing magnetic field in the transformer core induces the output current. As the mechanism of the transformer is well understood, it is useful to compare them. The equivalent transformer model is introduced so that the eddy current magnitude and the factors which influences it can be estimated. The EMAT coil behaves as a primary coil and the eddy current flow

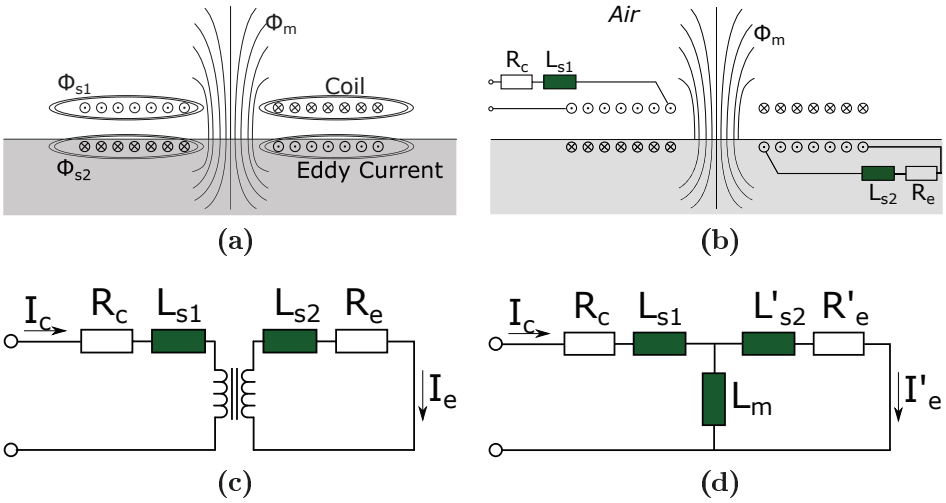

Figure 2.10: Eddy current generation and steps for deducing the EMAT transformer model circuit diagram: (a) physical model of coil, magnetic fluxes, and eddy current loop; (b) same as (a) but showing idealized resistance and inductance of the coil and eddy current loops; (c) electrical circuit diagram corresponding to (b); and (d) circuit diagram of (c) representing the coupling of coil and eddy current loop via the mutual inductance L_m.

as a secondary coil. This transformer-like arrangement can be converted into an electrical circuit diagram. First, the resistance of the coil and the eddy current can be expressed as concentrated resistances R_c and R_e. Furthermore, the leakage fluxes can be concentrated into inductances L_{s1} and L_{s2}. This step is shown in Figure 2.10b. Now, as the resistances and the leakage inductances are modelled as concentrated parameters, the coil and the eddy current flow can be modelled as an ideal transformer with a core inductance of L_M (Figure 2.10c). The eddy current flow is a single-turn secondary coil, whereas the EMAT coil has N turns. This leads to the third stage of the simplification: the secondary equivalent resistance and inductance is calculated, leading to the transformer model circuit representation as shown in Figure 2.10d. The reduced variables are as follows:

$$R_e^{'} = R_e \cdot N^2 \tag{2.14}$$

$$L_{S2}^{'} = L_{S2} \cdot N^2 \tag{2.15}$$

$$I_e^{'} = I_e/N \tag{2.16}$$

The losses in the electric power occur in three different parts of the assembly: (a) power is dissipated in the coil resistance; (b) the eddy current flows in resistive material, hence, power is dissipated in it as well; and (c) the hysteresis in the magnetization curve results in a loss during the magnetization. The magnetization losses are usually neglected in the calculations, as they are small (especially for low-powered EMATs).

The power loss inside the EMAT then equals the power dissipated in the coil resistance and eddy current flow path.

$$I_c^2 \cdot Re\{Z_{in}\} = I_c^2 \cdot R_c + I_e^2 \cdot R_e \tag{2.17}$$

The resistance of the eddy current flow can be calculated from the resistivity of the mild steel and the eddy current flow path dimensions. Then, if the input current and the impedance is known the eddy current magnitude can be estimated as:

$$\frac{\mid I_e \mid}{\mid I_c \cdot N \mid} = \frac{1}{N} \cdot \sqrt{\frac{Real\{Z_{in}\} - R_c}{R_e}} \tag{2.18}$$

The reason for presenting the equation in this form is that the right hand side is a dimensionless number. The coupling between the coil and the eddy current is ideal, if this number is close to 1. Once the value of the formula is close to 1, the eddy current can mainly be maximized by maximizing the input current. This formula can be used for example to compare the eddy current magnitude at different lift-off values using electric impedance measurements. After performing calculations, from Equation 2.18 the relative current magnitude for different lift-off values can be estimated. The estimated relative current magnitude for lift-off values from 0 to 2500 μm is shown in Figure 2.11.

The presented EMAT transformer model focuses on the transmission, but the transformer

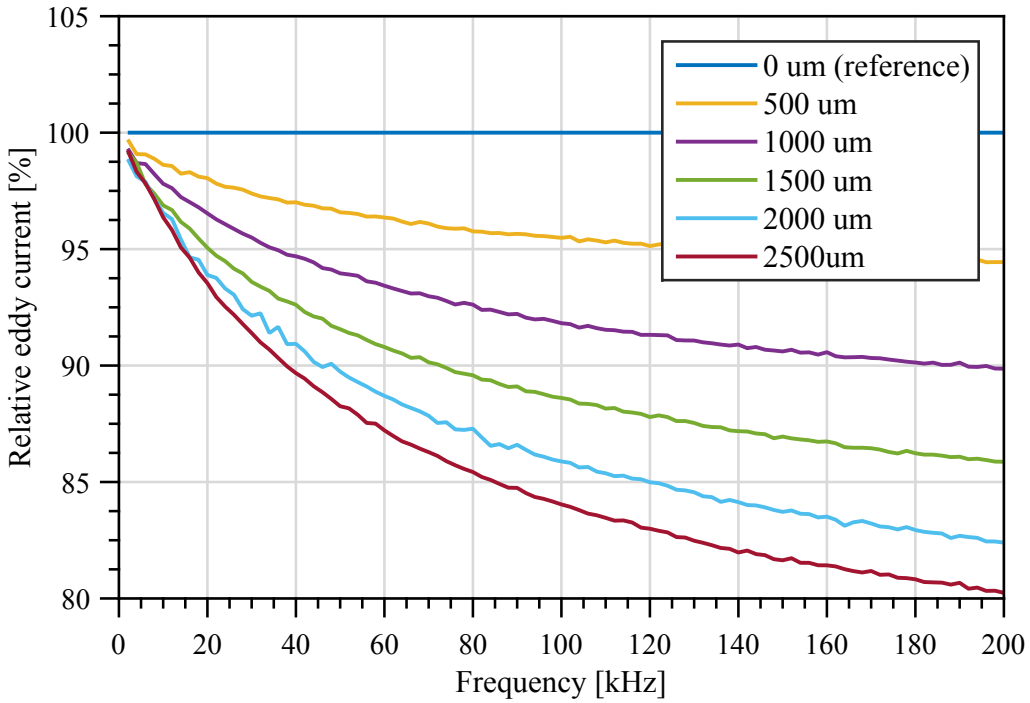

Figure 2.11: Eddy current magnitude at different lift-off values relative to the 0 μm lift-off current calculated from measured electric impedance plots.

model can be extended to the operation of the receiver EMAT. For the receiver case the reverse mechanism applies. The relative motion of the pipe and the transducer generates the electromotive force (EMF) which results in an eddy current flow in the conductor. This eddy current is then transformed to the coil, and voltage is generated on the coil terminals.

2.5 Signal processing

Often, ultrasonic measurements produce low signal amplitudes, and the measurements are usually influenced by electrical noise sources. This is especially true for Electromagnetic Acoustic transducers which produce extremely low signal amplitudes, as the coils can easily pick-up large electrical noise.

Therefore large effort is spent on signal conditioning, which can for example be a tool for improving Signal-to-Noise ratio, or compensation of environmental effects. Furthermore, signal processing methods are commonly used for feature extraction like envelope detection, wave packet arrival time extraction. This section introduces the basic signal processing methods, which are used throughout the document.

2.5.1 Ultrasonic wave-packets in the frequency-domain

Ideally, ultrasonic wave-packets are short, so that the highest possible resolution can be achieved. However, short pulses have large bandwidth in the frequency domain, which is problematic to excite with bandwidth limited transducer. In addition, the electronics design and the instrumentation recommends narrowband signals. Usually a compromise is set, and wave-packets are used which consists of a few cycles. Commonly, a window function is applied onto the high-frequency carrier harmonic function to generate the excited wave-packet (often called as tone-burst signal). In ultrasonic applications the Hanning window is a common window function, as it has a great suppression in the side lobe frequencies [94, 95]. An example 5 cycle 27 kHz Hanning windowed tone-burst is shown in Figure 2.12. Other window functions like Gaussian, Rieker, Tukey are available [96].

In order to reliably design the transducer and simulate the wave propagation it is recommended to exactly know the frequency content of the excited signal. The tone-burst signal has the peak frequency component at the carrier frequency, but has a distinct frequency bandwidth. This section presents the analytical calculation of the frequency bandwidth of a Hanning windowed tone-burst with N cycles. Instead of calculating the frequency content of a signal with a particular example, it is more useful to determine a general formula. The Hanning window $w(t)$ is also called as a raised cosine, and it is defined

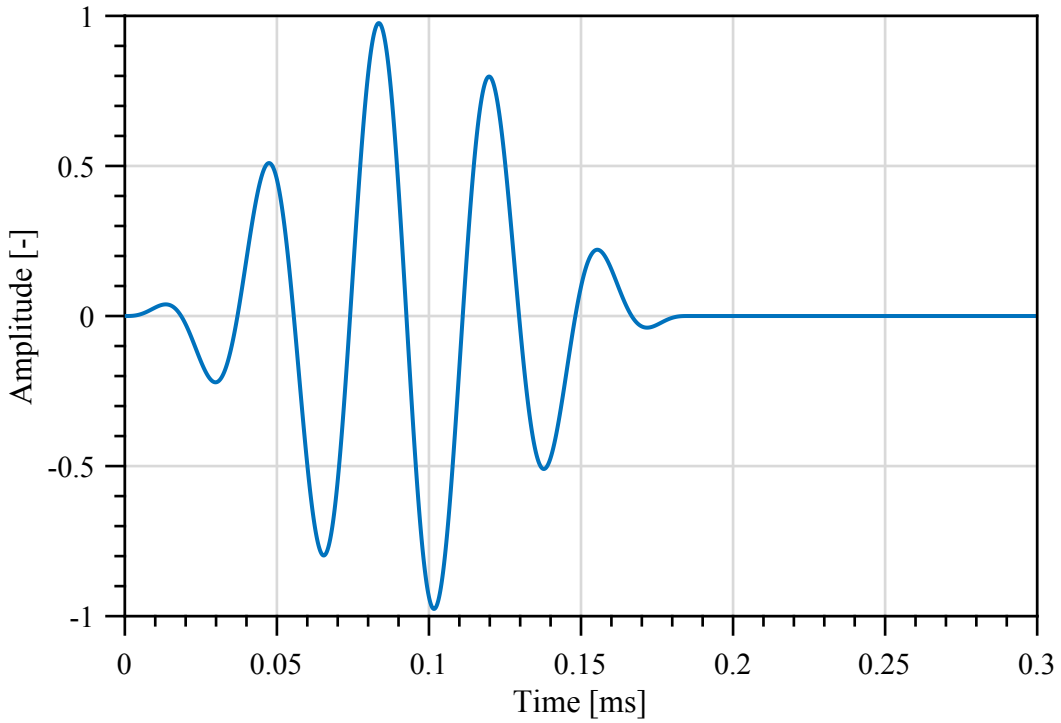

Figure 2.12: A 27 kHz 5 cycle Hanning windowed tone-burst signal. The tone-burst is commonly used as the excitation signal for ultrasonic application.

as [94]:

$$w(t) = \frac{1}{2}\left(1 - cos\left(\frac{2\pi f_c}{N}\right)\right); \tag{2.19}$$

where f_c is the frequency of the carrier sine wave and N is the number of cycles of the Hanning windowed signal.

As the window function is applied onto the carrier harmonic signal the frequency content is a broadband signal. The frequency domain $F(\omega)$ of the Hanning windowed signal $f(t)$ is by definition:

$$F(\omega) = \int_{-\infty}^{\infty} f(t) \cdot e^{-i\omega t} dt \tag{2.20}$$

The Hanning windowed tone-burst signal can be constructed as the product of three

functions (carrier harmonic signal, raised cosine and rectangular window function) as shown in Figure 2.13 (left graphs). The frequency content of each function can be specified analytically. The carrier sine wave is transformed to a Dirac-delta function as shown in the top right graph in Figure 2.13. The raised cosine function is again a harmonic signal, but with a mean value of 0.5.

The Fourier transform of the rectangular window function can be expressed as:

$$F\left\{rect\left(\frac{t}{N\cdot T}\right)\right\} = \int_{-\infty}^{\infty} rect\left(\frac{t}{N\cdot T}\right)\cdot e^{-i\omega ft}dt = \int_{\frac{NT}{2}}^{\frac{NT}{2}} 1\cdot e^{-i\omega ft}dt \tag{2.21}$$

$$F\left\{rect\left(\frac{t}{N\cdot T}\right)\right\} = \frac{sin(\pi\cdot f\cdot N\cdot T)}{\pi\cdot f} \tag{2.22}$$

The multiplication of functions in time domain corresponds to a convolution in the frequency domain:

$$F\left\{g(t)\cdot h(t)\right\} = F\left\{g(t)\right\} * F\left\{h(t)\right\} \tag{2.23}$$

Therefore the general formula for the frequency content of a Hanning windowed tone-burst signal (Figure 2.13 bottom right graph) can be calculated as the convolution of the three separately calculated Fourier domains. The main frequency content of the tone-burst signal is centred around the carrier frequency f_c, and the bandwidth of the main lobe has the extent of $\pm\frac{2f_c}{N}$ [95].

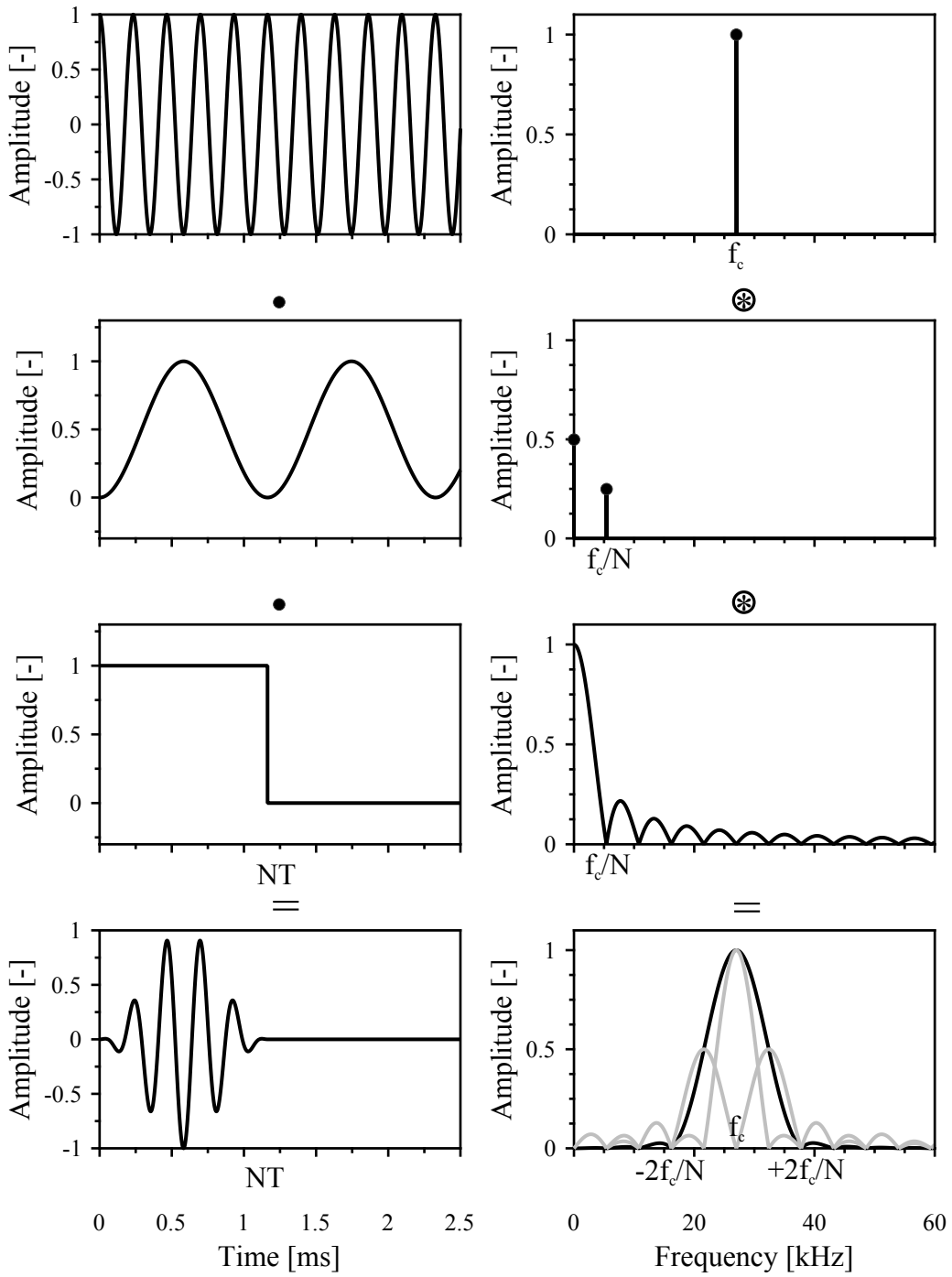

Figure 2.13: Method to analytically calculate the frequency content of a tone-burst time signal (bottom left). The tone-burst can be expressed as the product of three time domain signals (left side graphs). The frequency domain of the tone-burst signal (bottom right) is then calculated by convolving the frequency domain of each component (right graphs).

2.5.2 Envelope detection using Hilbert transform

Often it can be desired to recover the envelope of a measured ultrasonic signal. A few of the numerous reasons are: calculation of signal amplitude, estimation of signal arrival time, etc. A commonly used method for envelope detection is the use of Hilbert transform [97, 98]. The Hilbert transform $f_1(t)$ of a real signal $f(t)$ is given by convolution:

$$f_1(t) = -\frac{1}{\pi} \int_{-\infty}^{\infty} \frac{f(x)}{t-x} dx \tag{2.24}$$

The Fourier transform of $f(t)$ and $f_1(t)$ is $F(\omega)$ and $F_1(\omega)$ respectively, the functions then satisfy the following expression in the frequency domain:

$$F_1(\omega) = j \cdot F(\omega) \cdot sgn(\omega) \tag{2.25}$$

where $sgn(\omega)$ is the signum function. Therefore, the Hilbert transform recovers the imaginary part of the signal. Then, both the phase and the envelope can be calculated as the Hilbert transform of the signal is known. An example signal and its detected envelope is shown in Figure 2.14.

2.5.3 Signal-to-Noise Ratio of an ultrasonic measurement

Signal-to-Noise Ratio (SNR) is defined as the power of the useful signal to the power of unwanted interference [98]. Generally, the SNR is often evaluated as the ratio of the root-mean-square (RMS) values. This definition might seem quite explicit, however, ultrasonic signals usually contain discontinuous wave packets, therefore calculating the RMS does not recover the true signal power. In addition, comparing the signal amplitude to the noise amplitude is problematic, as evaluating the noise from its amplitude is not reliable. It is possible to get around the problem by calculating the SNR from the ratio of the signal amplitude to the noise RMS value. This definition then overestimates the SNR by ~3dB (as the amplitude is always larger for a signal than the RMS value), but has the

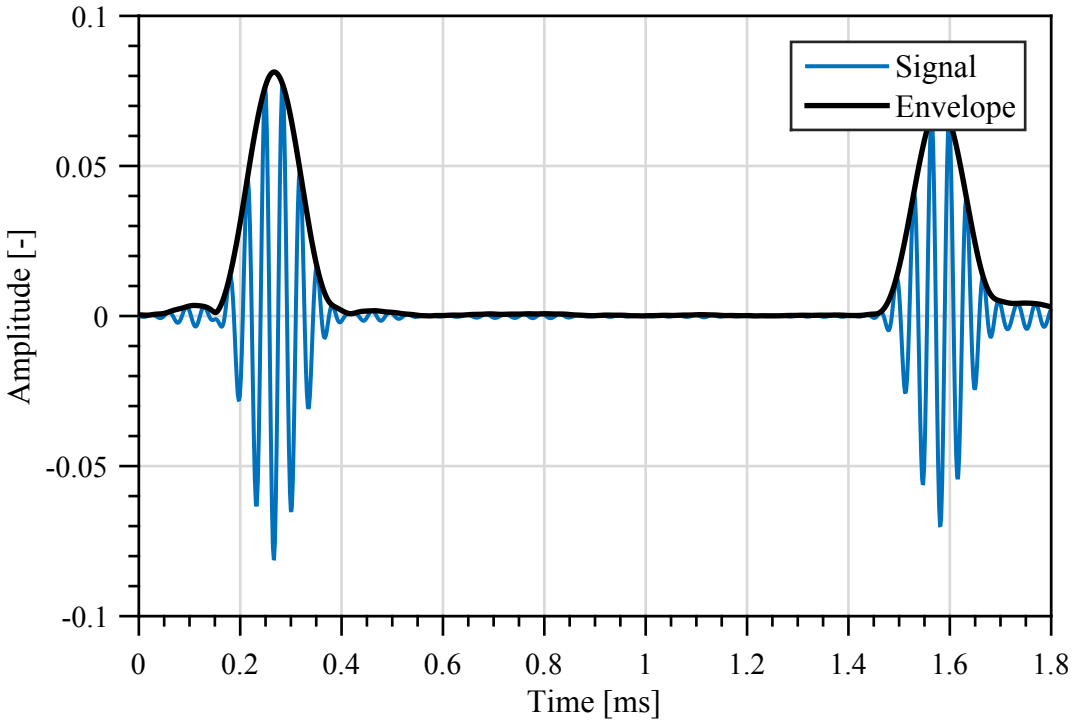

Figure 2.14: Guided wave ultrasonic signal (27 kHz) and its envelope detected using the Hilbert transform.

advantage of being more robust estimation method.

The SNR required for the acquired signal depend on the specific application. For example, the image formation processes (tomography and imaging) are themselves filtering processes, hence the SNR required for an individual signal is lower. On the other hand, for example high accuracy thickness measurements require large SNR [99]. Guided wave signals however, often require large SNR, for example torsional wave pipe screening requires SNR in excess of 40 dB [100].

Ultrasonic measurements (especially using EMATs) do not always produce high-enough SNR, therefore signal processing is used to improve the Signal-to-Noise Ratio. As the ultrasonic signal is usually a narrow-band pulse, electrical filtering is used to remove noise outside the signal bandwidth. This filtering can either be performed on the signal acquisition instrument (electrical analogue filtering), or can be performed during post-processing (digital filter). The SNR of a measurement can be improved when the excitation level is increased, hence larger signal amplitude is recorded. Unfortunately, the excitation levels are often limited due to instrumentation and safety constraints [68]. Alternatively, the

Signal-to-Noise ratio of the measurement can be increased by performing averages on the signal. The measured noise is incoherent, it is gradually decreasing during the averaging process, while the signal amplitude remains unchanged (assuming environmental effects did not change the signal during averaging). The SNR of the signal after performing N number of averages is increased by the square root of N:

$$SNR_{out} = \sqrt{N} \cdot SNR_{in} \tag{2.26}$$

This way the SNR can conveniently be improved by averaging the signal.

2.5.4 Complementary sequences for signal averaging

For measurements with poor Signal-to-Noise ratio large number of averages needs to be performed to decrease the noise level, which would practically take too long to perform. In case the number of averages becomes excessively large the use of pulse compression methods is preferred. With these pulse compression techniques the time required for the measurement is substantially reduced [101]. One of the popular method is the use of Golay coded complementary sequences [102]. In each sequence the system is excited by multiple signals with coded polarity. An example of a complementary sequence a_k and b_k is:

$$a_k = (+1, +1, +1, -1) \tag{2.27}$$

$$b_k = (+1, +1, -1, +1) \tag{2.28}$$

The auto-correlation function ($R_a(k)$ and $R_b(k)$) of the sequences will be large for $k = 0$, but will also contain self-noise at $k \neq 0$.

$$R_x(k) = \sum_{j=0}^{N-k-1} x_j x_{j+k} \tag{2.29}$$

However, when the two complementary sequences are excited the sum of the auto correlation functions will add up so that the self-noise will cancel out, and the sum will be large at $k = 0$:

$$R_a(k) + R_b(k) = (4, 1, 0, -1) + (4, -1, 0, 1) = (8, 0, 0, 0) \tag{2.30}$$

To use the pulse compression methods in ultrasonic measurements the transmitted signal contains repeated tone-burst pulses, and the sequence is coded in the polarity (phase) of each pulse. The practice when recovering the original system response is to correlate the received response with the transmitted signal for each sequence, and then sum the two correlation functions.

In theory, the coded sequences perfectly eliminate the self-noise. However, in case there is a small variability in the excitation of each pulse (or the system) the self-noise of the sequences will not cancel out. A simulation has been carried out where a system with an arbitrary response was excited by a 1024 pulse long Golay sequence, and the amplitude of each system response was randomly changed within +-1%. The random amplitude changes in the excitation will generate noise in the reconstructed signal. Figure 2.15. shows two signals reconstructed from a 2^{10} long transmitted sequence.

The simulated self-noise of the signal due to the random amplitude variations is small (-76.5 dB) when only the signal echoes are recorded in the measurement (Figure 2.15 a). However, if an extra system response (like cross-talk in the signal) is added to the system at $t = 0$ with an amplitude 100 times larger than the rest of the signal the self-noise is much larger (-37.5 dB compared to the signal amplitude) as shown in (Figure 2.15 b). The -37.5 dB self-noise level can be unacceptable for several ultrasonic applications, like

torsional guided wave measurements.

The reason of this simulation was to highlight that the pulse compression techniques should not be used if the expected ultrasonic signal have non-ultrasonic related pulses (like cross-talk) which is magnitudes larger than the useful ultrasonic signal. Additionally, the implementation of pulse compression techniques can be even more problematic, if the transmitted signals saturate the receiver amplifier.

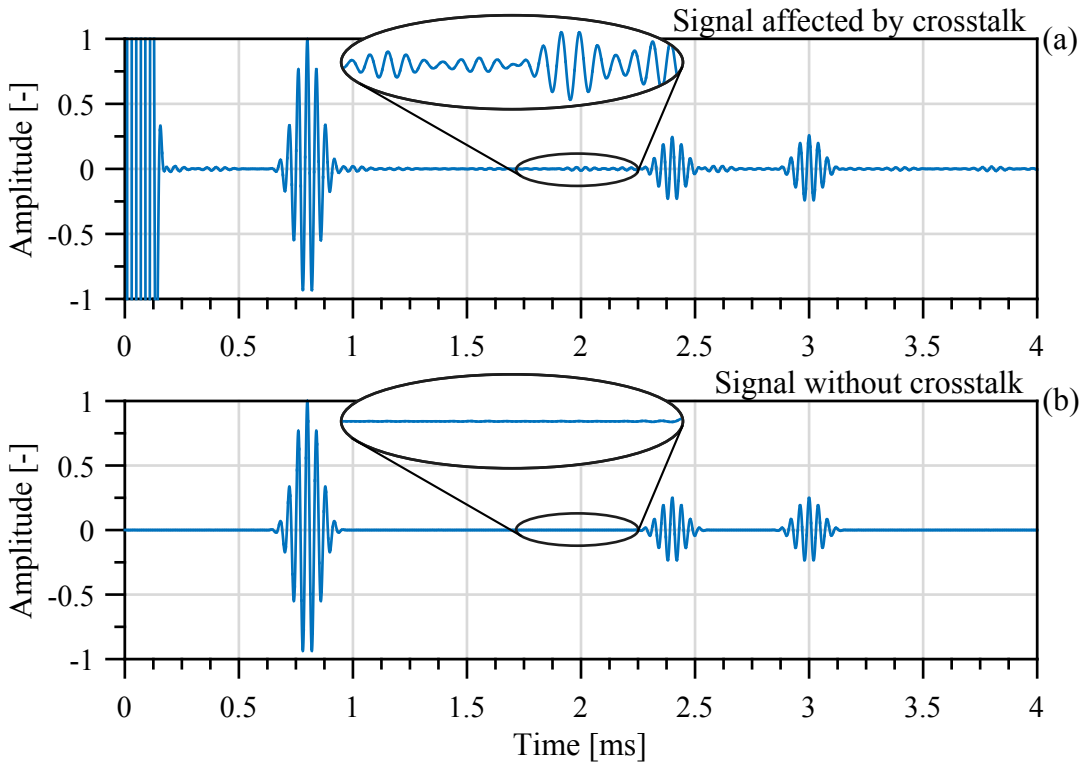

Figure 2.15: Signals recovered when using 2^{10} long Golay pulse compression technique, and the system response is affected by random ± 1% amplitude changes. Figure (b) shows the response when an additional 100 times larger system response (crosstalk) is present in the signal.

Recent work has been presented which overcomes the problem of the large initial pulses (e.g. in pulse-echo systems) [101]. The proposed sequence consists of receive intervals with random length between excitation pulses so that the signal can be received in those intervals.

2.5.5 Wave propagation directional control on a 1D structure

When the torsional wave is excited at a given section of the pipe the torsional wave travels in both directions. Both right and left travelling waves are propagating with the same amplitude. During monitoring, the echoes from a slowly growing defect of corrosion may be detected. When the ultrasonic wave travels in both directions, the location of the received echoes cannot be determined, only the distance from the sender location can be calculated. Therefore it is beneficial to excite ultrasound waves which travel only in one direction and diagnose the echoes exact location. Directional guided wave sending can be achieved using two rings of EMATs (linear arrays of transmitter EMATs) separated by a specified distance. Both rings of transmitter transducers generate the left and right travelling wave, but these waves will cancel out (destructively interfere) in one direction, while they will add up (constructively interfere) in the other direction. Guided wave transducers have already been developed with directional control by deploying double rings with the axial separation of quarter wavelength to generate the constructive and destructive interference [38]. Yet, the exact signal processing methods used by companies are not shared with the public.

It is possible to implement the directional control of dispersive modes, however, most commonly directional control is implemented for non-dispersive modes. These non-dispersive wave-modes (like the fundamental torsional wave T(0,1) mode) have a constant phase velocity independent of the frequency, and their propagation can be described with d'Alembert's Solution.

$$f(x,t) = y(x - ct) + y(x + ct) \tag{2.31}$$

The excitation signal used for testing is a windowed tone-burst signal. The signal f(t) is the product of the window function w(t) and the carrier sinewave sin(t). The window function allows sending of finite-length signals for inspection. The window function is

usually 3-10 times of the carrier sinewave period.

$$f(t) = w(t) \cdot sin(t) \tag{2.32}$$

Consider two rings of transducers placed at a certain distance (p) apart. The position of the first transducer (Node1) is chosen to $x = 0$ while the second transducer is then at position p. The transducer at Node2 will be excited $\frac{p}{c}$ later than the first transducer with negative polarity. The excited waves at the two locations will then be:

$$F(ct - x) + F(ct + x) \tag{2.33}$$

at Node 1, and

$$-F\left(c\left[t - \frac{p}{c}\right] - [x - p]\right) - F\left(c\left[t - \frac{p}{c}\right] + [x - p]\right) \tag{2.34}$$

at Node 2. The right travelling wave when $t > \frac{p}{c}$ is then:

$$F(c \cdot t - x) - F\left(c\left[t - \frac{p}{c}\right] - [x - p]\right) = 0 \tag{2.35}$$

Meaning that the right travelling wave will cancel out after time $\frac{p}{c}$. The same calculation with the left travelling wave results in:

$$F(ct+x)+F\left(c\left[t - \frac{p}{c}\right] + [x - p]\right) = w(ct+x)\cdot sin(ct+x) - w(ct+x-2p)\cdot sin(ct+x-2p) \tag{2.36}$$

Consider p being the multiple of quarter wavelength and odd number as given by:

$$\frac{p}{c} = \frac{2n+1}{4}\frac{\lambda}{c} = \frac{2n+1}{4}T \tag{2.37}$$

using the information from Equation 2.37 and the fact that $sin(x) = -sin(x+\pi)$ the left travelling wave can be rewritten as:

$$[w(ct+x) + w(ct+x-2p)] \cdot sin(ct+x) \tag{2.38}$$

From this form it can be seen, that the two window functions with a time difference of $\frac{2p}{c}$ will be added together. So when the two rings of transmitter transducers are close, the window functions will overlap and the signal amplitude of the left travelling wave will add up. The travelling waves can be represented in a 2D diagram, where the horizontal axis is proportional to the time, and the vertical axis is the propagated distance. The travelling wave-packets then move linearly to the negative or positive direction. The waves excited at the two locations is plotted in Figure 2.16, where the constructive and destructive interference can be seen as well.

Exciting the two rings of transmitter transducer does not necessarily have to be done in one measurement. The signals can be collected and added together during post-processing. Furthermore, the time delay and the negative polarity on one of the sensor can also be implemented after the measurement by suitable post processing. In other embodiments, the raw signals could be captured with a receiver transducer at any location. When the left travelling wave is calculated the signal acquired from Node 2 is delayed and subtracted from the signal acquired from Node 1. Similarly, when the right travelling wave is calculated the signal from Node 1 is delayed and subtracted from the signal acquired from Node 2. This method for calculating the directionally controlled signal allows perfect cancellation of waves in the other direction (see positive direction in Figure 2.16), but the duration of the excitation signal unavoidably becomes longer in the directionally controlled signal.

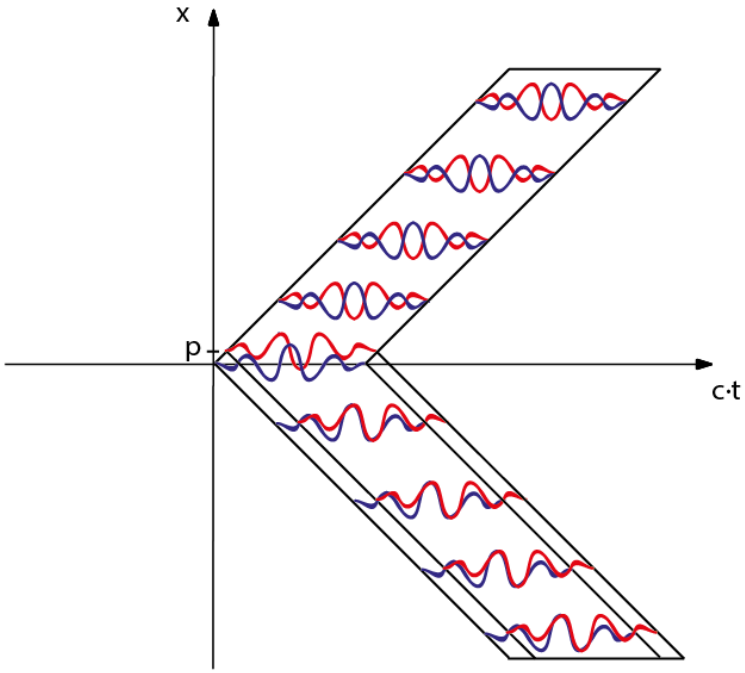

Figure 2.16: Representation of the directional control algorithm. An individual transducer excites a wave which travels in both direction (+ and − x). With a second transducer placed at distance p constructive and destructive interference can be caused.

2.6 Summary

This chapter summarizes the most relevant theoretical knowledge, which is used or referred to in the rest of the thesis. The chapter starts with the introduction of bulk wave ultrasound, where the formula for the longitudinal and shear wave speeds are analytically derived. Then, the guided wave modes which can propagate in pipe-like structures are introduced, and it is detailed how the dispersion curves are used to describe their propagation. Furthermore, knowledge about the propagation of guided wave modes on different pipe sizes is recalled.

The introduction of the electromagnetic principles helps to have a general understanding of the EMAT operation mechanism (eddy current generation and magnetic fields). The chapter then finishes with the fundamentals of signal processing, where the frequency content of the broadband ultrasonic signals is discussed. It is detailed how the signal averaging and complementary sequences improve Signal-to-Noise Ratio (SNR), and how directional control of guided waves can be implemented.

Chapter 3

Guided wave EMAT

3.1 Introduction

This chapter presents the design and simulation of a torsional guided wave EMAT system for pipeline Structural Health Monitoring. The aim is to design an array of EMAT coils that can excite and sense the zero order torsional mode using the Lorentz force. The generation of pure torsional waves is desired, where the amplitude of the unwanted modes in the time signal (often referred to as coherent noise) is minimal. The target mode purity is 40 dB (factor of 100), as it is sufficient for most practical applications [100]. Finite element simulations were employed to quantitatively understand the excitation mechanism of the Lorentz force. In order to reduce computation time and simplify the calculations, the simulations are split into several subproblems. The force generated by an EMAT element is calculated first. The ultrasound waves that are generated when several EMAT elements are evenly distributed around a pipe will be investigated in a separate simulation afterwards.

Parts of this chapter have been extracted from publication [P1], with the permission of SAGE Publications Ltd.

3.2 Excitation mechanisms of Electromagnetic Acoustic Transducers (EMATs)

Electro Magnetic Acoustic Transducers (EMATs) can generate acoustic waves by different transduction mechanisms. Transducers generate ultrasonic waves via magnetostrictive [26, 27, 59, 61, 103–109], magnetization [110–112] and Lorentz force [57, 87, 92, 113–117] mechanisms. The Lorentz force can be generated in any conductive materials, but magnetostriction and magnetization only occurs in ferromagnetic media [57]. It has been found, that the dominant force generated by a transducer is dependent on the EMAT configuration and the material properties [109]. Several researchers have investigated the transduction mechanisms of EMATs, but the complexity of the problem still makes it the topic of ongoing research and it regularly features in scientific publications.

While Electromagnetic Acoustic Transducers are usually referred to as contactless transducers, this is not true for the magnetostrictive types of EMATs, which usually employ a bonded highly magnetostrictive strip (like nickel) [59, 104]. The use of the magnetostrictive strip enhances the otherwise poor strength but sacrifices the contactless feature of the transducer [61, 109, 113].

In most cases, the main transduction mechanism for EMATs using strong bias magnetization (e.g. permanent magnets) is the Lorentz-force [108, 118]. This chapter introduces the design of a Lorentz force based transducer, which uses permanent magnets for the generation of the static magnetic field. The eddy current is generated by the alternating magnetic field of a current carrying coil. The alternating magnetic field generated by the coil is usually smaller than the bias magnetic field. This is particularly true for the presented prototype, as it employs low excitation power, therefore the alternating magnetic field is magnitudes smaller than the DC magnetic field of the permanent magnet. The calculations consider the Lorentz force mechanism only, and the magnetostrictive and magnetisation forces are excluded from the calculations.

3.3 Force generation

The purpose of the EMAT is to excite and receive the fundamental torsional guided wave mode T(0,1) in pipes. An ideal transducer would generate the force distributed uniformly over the pipe cross-section, matching the tangential displacement of the torsional mode.

The Lorentz force is generated as the vector (cross) product of the static magnetic field and the eddy current [57]. The highest efficiency is then reached when the eddy current, static magnetic field and the generated force is mutually perpendicular to each other. Furthermore, the eddy current flow is always concentrated to the surface of the conductor due to the skin effect, it will never have radial component on the pipe. Then, the only efficient way to generate the tangential force is to design the EMAT so that the eddy current flows in the axial direction. The desired component of the magnetic field is then in the radial direction of the pipe.

The ideal uniform tangential displacement of the torsional wave can only be achieved when the magnetic field magnitude penetrating into the pipe is also uniform. Commercial magnets are available, which have a shape to conform to the pipe curvature, and have magnetic field in the radial direction. Such magnets for example ring or arc magnets are often used for electric motors. Nevertheless, the use of these magnets were not considered for the following reasons: It is practically impossible to place a circular ring magnet onto existing pipe structures; it is hard to place arc segments next to each other with the same polarity, as they repel each other; and the magnet assembly which covers the whole pipe circumference is most likely to be heavy. In addition, it would be needed to manufacture custom-made arc magnets specially to the pipe dimensions. It is also challenging to generate circumferentially uniform axial eddy current flow (as designing the return path of the coil is problematic).

Therefore, instead of trying to generate a uniform force distribution, a compromise is made, resulting to a design, where several EMAT elements are distributed along the circumference with each exciting a tangential force. Figure 3.1 shows the schematics of the proposed configuration of the EMAT array and the direction of wave propagation. The array of EMATs containing identical elements will operate together to generate the zero order torsional wave.

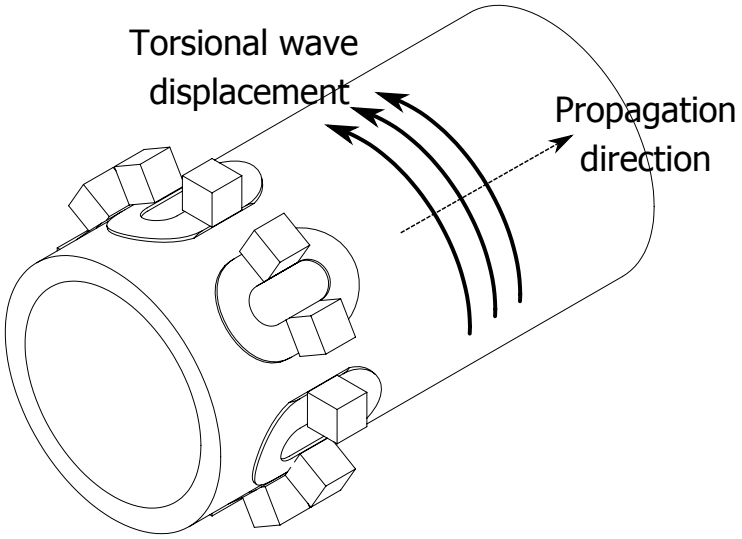

Figure 3.1: Schematics of the excitation of the zero order torsional wave (T(0,1)) with Electromagnetic Acoustic Transducers (EMATs). Several EMAT elements are distributed along the circumference on the circumference of the 3-inch NPS pipe.

The force generated by an element of the EMAT array is simulated on a planar surface (Making the simulation on a planar conductor is a reasonable assumption as the pipe radius is large compared to the thickness). Consider a planar coil elongated in the x direction and two permanent magnets (vertically magnetized) placed onto the straightened section of the coil as shown in Figure 3.2a. This assembly is placed onto a conductive, highly permeable material (e.g. mild steel). The alternating current in the coil generates eddy current in the metal substrate, and this eddy current interacts with the static magnetic field.

The Lorentz force is then excited as the interaction of the eddy current and the static magnetic field. Figure 3.2b shows the eddy current flow, and the generated Lorentz force in y direction, which would be a tangential force when the EMAT element is placed onto the pipe surface.

In order to calculate the force generated by the EMAT, first the static magnetic field is simulated; then the eddy current flow is analysed. The force is then estimated by combining the result of these independent simulations.

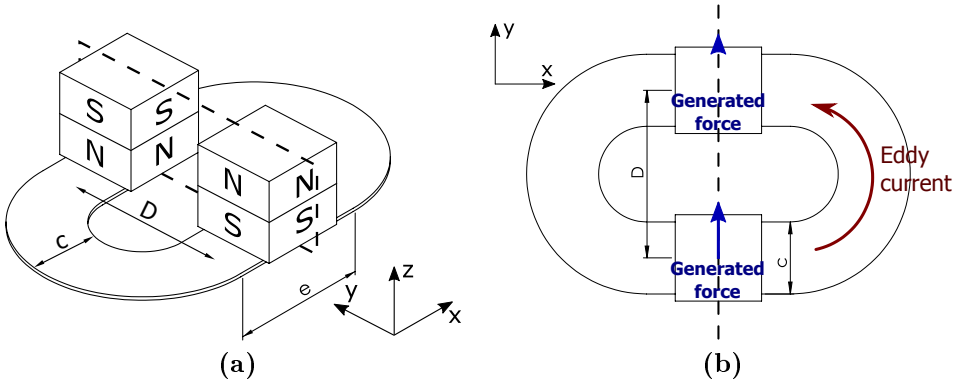

Figure 3.2: Assembly of an EMAT element consisting of a planar elongated current carrying coil and a permanent magnet shown in three-dimensional view (a) and shown from above the planar coil (b). The eddy current flow and the force generated in a conductive substrate is indicated in (b).

3.3.1 Static magnetic field

The permanent magnets placed onto the elongated section of the EMAT are magnetized vertically. However, this does not result in a pure vertical (z direction) magnetic field in the mild steel substrate for several reasons.

First, as the second Maxwell equation describes that no magnetic charges exist, the magnetic field lines must be closed loops. As the magnetic field lines of the permanent magnets need to form a closed loop the magnetic field will divert from the permanent magnet's magnetization direction. This results in magnetic field components in x and y direction.

Due to another phenomena, Snell's law, the magnetic field component in the unwanted x and y direction will be even higher. Snell's law describes that at the boundary of two media with different magnetic permeability (μ_1 , μ_2) the angle of incidence (θ_1 , θ_2) satisfies Equation 3.1 [90, 119]. These results in the magnetic field lines being diverted even more from the interface normal plane as shown in Figure 3.3.

$$\frac{sin(\theta_1)}{sin(\theta_2)} = \frac{\mu_1}{\mu_2} \tag{3.1}$$

A three-dimensional Finite Element simulation was carried out in COMSOL Multiphysics ® Finite Element modelling software [120] to evaluate the static magnetic field generated

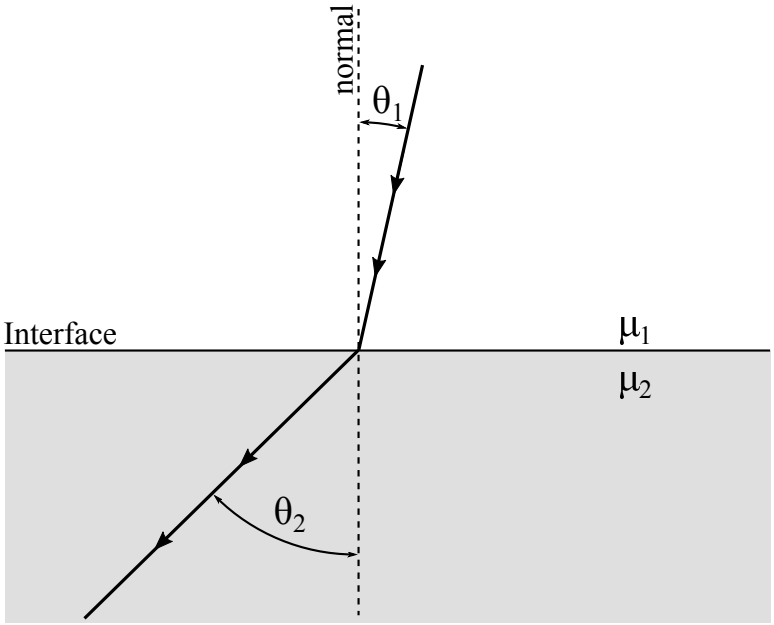

Figure 3.3: Refraction of magnetic field lines when entering a material with higher permeability (μ_2) from a material with smaller permeability (μ_1). The phenomenon is called Snell's law.

by multiple permanent magnets of the EMAT. 12 mm cubic magnets were modelled 1 mm above the 5 mm thick mild steel plate. The distance between the magnets was 23.3 millimetres, which equals the same distance when 12 magnets are placed around a 3-inch pipe. The remnant magnetization of the magnets was set to 1.4 Teslas with alternating polarity. The value of 1.4 Teslas was specifically chosen for remnant magnetization, as it is approximately the field strength of the N42 grade Neodymium (NdFeB) magnets [75]. In the FE simulation 12 magnets were placed side by side to mimic the periodic placement of the magnets, but the result is only shown for two magnets in the middle section. The relative permeability of 80 was set for the mild steel (the relative permeability of air is 1). The model was simulated in a stationary study, magnetic insulation was set to the model boundaries and Ampere's law was set for the region of interest. Free tetrahedral mesh was chosen, with computer controlled mesh size.

The magnetic field strength with the streamlines are shown in Figure 3.4a for the symmetry plane (symmetry plane is shown by dashed line in Figure 3.2). The streamlines are not evenly distributed due to the random starting seeds used by the FE software.

Despite the permanent magnet's vertical magnetization, the magnetic field lines are tilted relative to the vertical remnant magnetization. This is due to the discussed properties

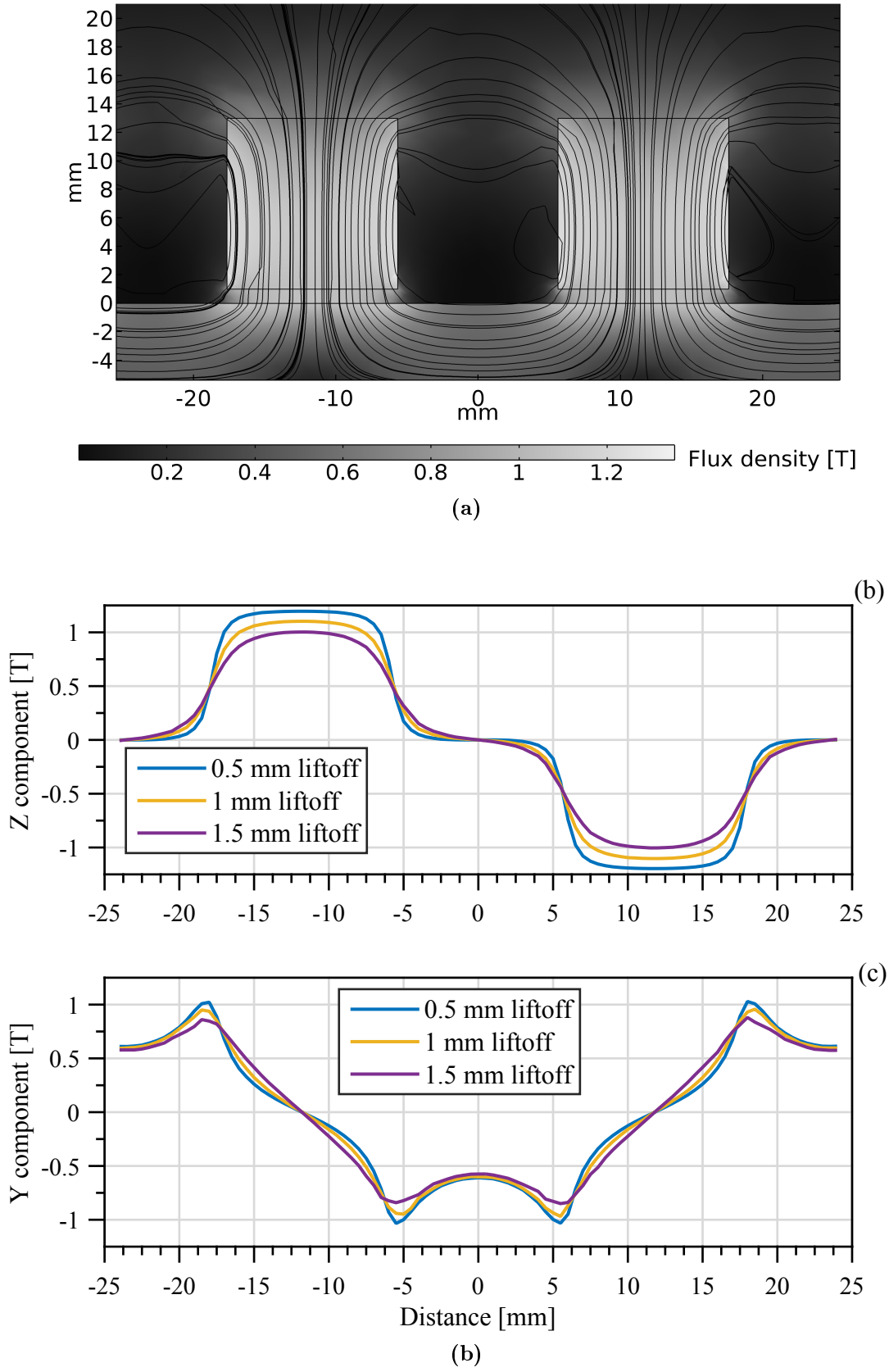

Figure 3.4: Simulated static magnetic field generated by 12 mm cubic magnets with opposite polarity. The magnitude of the static magnetic field is shown in (a), the vertical and horizontal components at the top surface of the steel plate is shown in (b) and (c) for different lift-off values. The remnant magnetization of the magnets is 1.4 Tesla and the magnetization direction is vertical with opposite polarity.

of the closed loop magnetic fields, and Snell's law as the magnetic field lines enter the highly permeable mild steel ($\mu_r \sim 80$). This results in a large horizontal component of the magnetic field in the mild steel. The vertical (z) and horizontal (y) component of the static magnetic field 10 µm under the mild steel surface is shown in Figure 3.4b.

From the experience of repeated simulations with different dimensions, it was found that the y component of the static magnetic field in the central region (under the coil wiring) can only be reduced by using larger magnets, but it cannot be totally eliminated.

3.3.2 Eddy current

The eddy current flow induced by a 34-turn coil on a mild steel material was simulated using COMSOL Multiphysics® Finite Element modelling software [120]. A 1 mm thick racetrack coil was constructed with the elongation (denoted by e in Figure 3.2a) of 25 mm and the mean radius of 23.3 mm. The width of the coil-wiring path was set to 10 mm. The lift-off between the coil and the mild steel specimen was set to $100\mu m$ in the simulations.

A frequency domain study was performed on the model, when the coil was set to a multi-turn coil domain with 34 turns and 1 Ampere 30 kHz input current. Other necessary parameters have been set like magnetic insulation on the model boundary, and Ampere's Law on the region of interest. A multi-turn coil with 34 turns and 1 Amp of input current was selected for the coil domains. Free tetrahedral mesh was chosen, with computer controlled mesh size.

The simulation revealed that the shape of the eddy current flow is similar to the coil's shape. The eddy current flow also has a straight section underneath the coil's straightened section. The coil elongation parameter, therefore, was kept 25 mm so that the static magnetic field of the permanent magnet can only interact with a straight flow of eddy current.

The effect of changing the coil width (parameter D) and width of the wire tracks (parameter c) was investigated in further simulations. It was concluded that the eddy current flow is easy to manipulate by changing the coil dimensions. The magnitude of the eddy current density flowing through the symmetry plane (indicated by a dashed line in Figure

3.2b) is plotted in Figure 3.5 when the coil mean diameter is set to 20, 25, 30 mm (a) and the coil track width is set to 7, 10, 13 mm (b). The coil track width of 10 mm was used for the simulation in plot (a), whereas the coil diameter of 25 mm was used while simulating plot (b). Note that the total eddy current flowing through the symmetry plane did not change whilst varying the coil dimensions and the coil had the same number of turns for all simulations. It can also be seen that the highest current density flows under the central turns of the coil.

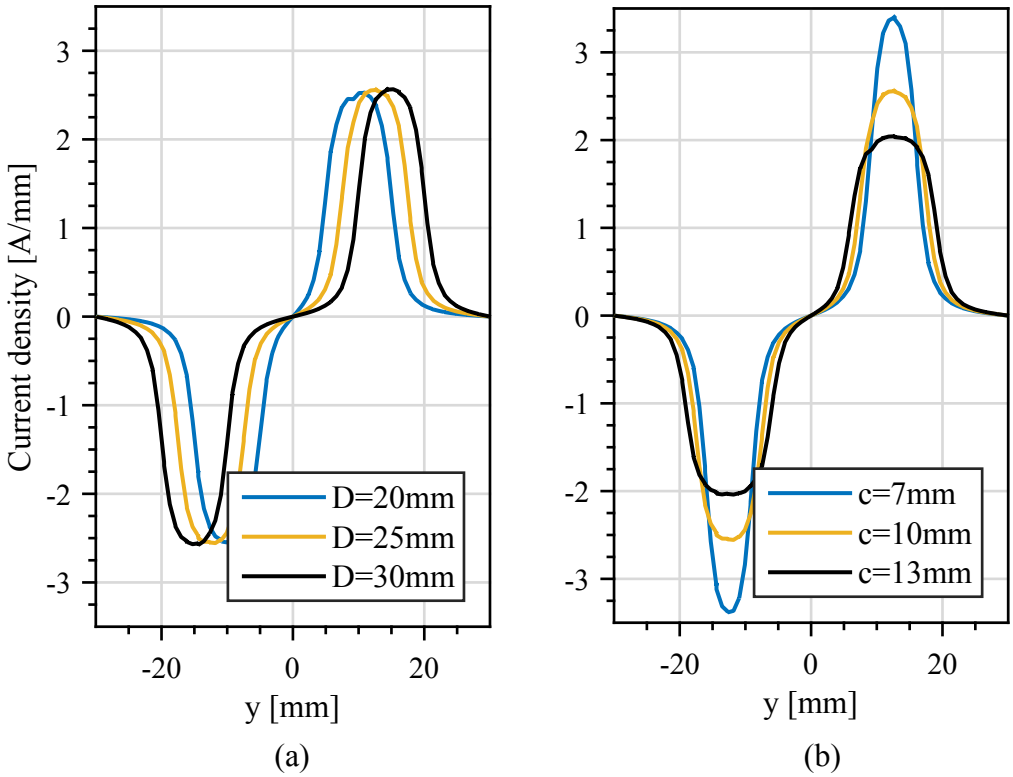

Figure 3.5: Simulated eddy current density at the symmetry plane of the EMAT for different coil dimensions. The coil width (parameter D) is set to 20, 25, 30 mm (a); the width of the coil turns (parameter c) is set to 7, 10, 13 mm (b). The results are acquired on a 30 kHz frequency domain simulation.

The frequency of the excitation current has indiscernible effect on the shape of the eddy current, but it changes the eddy current penetration depth. The eddy current magnitude in the conductor is decreasing exponentially as a function of depth from the surface, and this decay is the function of frequency.

3.3.3 Generated force distribution

The Lorentz force generated by the EMAT is calculated as the cross product of the eddy current and the magnetic vector field. Equation 3.2 describes the Lorentz force, where $\boldsymbol{f}$ is the generated force, $\boldsymbol{J}$ is the eddy current, $\boldsymbol{B}$ is the magnetic field.

$$\boldsymbol{f} = \boldsymbol{J} \times \boldsymbol{B} \tag{3.2}$$

This equation for the vector field can be expanded noting the three dimensional components separately:

$$\begin{bmatrix} fx \\ fy \\ fz \end{bmatrix} = \begin{bmatrix} Jx \\ Jy \\ Jz \end{bmatrix} \times \begin{bmatrix} Bx \\ By \\ Bz \end{bmatrix} = \begin{bmatrix} J_y B_z - J_z B_y \\ J_z B_x - J_x B_z \\ J_x B_y - J_y B_x \end{bmatrix} \tag{3.3}$$

The physical constraints of the eddy current flow imposed by the elongated coil design (straight flow in x direction at the area where the magnets are placed) will lead to a simplified expression for the body force:

$$\begin{bmatrix} fx \\ fy \\ fz \end{bmatrix} = \begin{bmatrix} Ix \\ 0 \\ 0 \end{bmatrix} \times \begin{bmatrix} Bx \\ By \\ Bz \end{bmatrix} = \begin{bmatrix} 0 \\ -J_x B_z \\ J_x B_y \end{bmatrix} \tag{3.4}$$

In other words, as the coil is elongated and the eddy current flows in a straight x direction, the generated force will not have any component in the x (axial) direction. However, as the static magnetic field simulation revealed, the unwanted component of the magnetic field will result in a force component in the z direction (normal to the conductor surface). The result of the separate eddy current and magnetic field simulation was interpolated by FE software built-in function on a pre-specified grid (same for both simulations). The

interpolation from the FE mesh results to the specified grid size introduced little errors, which can be observed from the results (e.g. Figure 3.7). The force distribution can then be calculated for the region of the whole mild steel numerically.

As the force acts on a thin volume ($\sim 120\mu m$) near the surface of the conductor due to the skin effect, the generated force is simplified to an equivalent surface force. By using the surface force equivalent of the force distribution the results are also much easier to present. The generated force distribution on the surface of the mild steel is shown in Figure 3.6. The desired y component is shown in Figure 3.6a, whereas the unwanted z component is shown in Figure 3.6b.

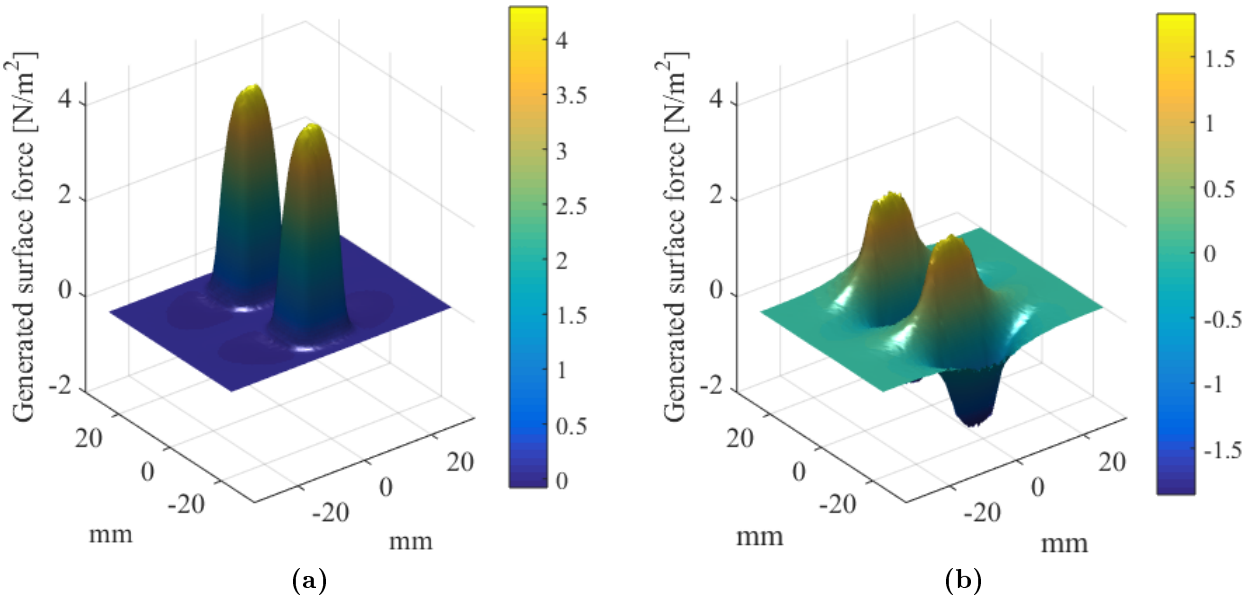

Figure 3.6: Simulated force distribution generated by the EMAT. The horizontal y component is shown in (a); the vertical z component is shown in (b).

The y and z component of the force distribution at the symmetry line is shown in 3.7. It can be seen that the main force is generated in the y direction, however, (due to the imperfect static magnetic field) the z component of the force is significant. The existence of the vertical component of the force is well known for EMATs, see for example [57].

Obviously, this unwanted force component can be suppressed, by changing the transducer design. In case larger magnets are placed on the top of the coils the unwanted magnetic field component at the coil wirings will be smaller. Also, if the width of the coil turns

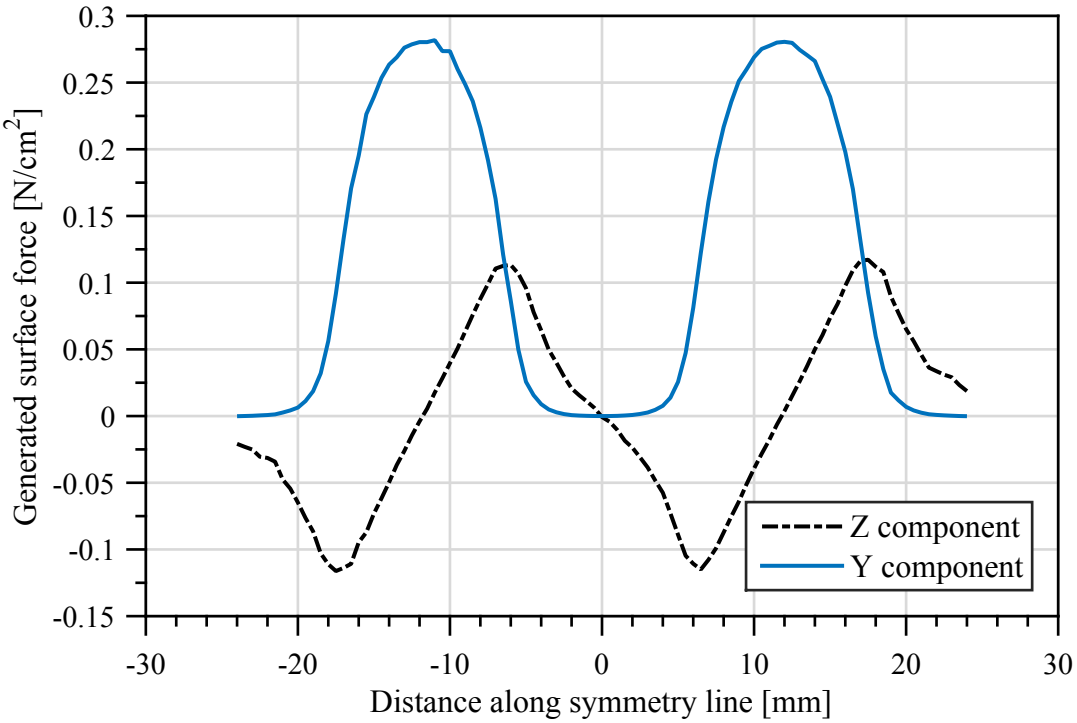

Figure 3.7: The horizontal Y and vertical Z component of the EMAT generated force at the symmetry plane of the EMAT. The symmetry plane is shown with dashed line in Figure 3.2a.

(parameter c) is decreased (as shown in Figure 3.5) the eddy current interacts with lower unwanted magnetic field component and on a smaller area. Unfortunately, increasing the magnet size drastically is not possible, as it is hard to handle/ assemble magnetic assemblies, which are really close to each other. On the other hand, decreasing the width of the coil turns is not advised, as that would decrease the maximum number of turns, and therefore decrease efficiency. The parameter D (coil mean diameter) was chosen to be ~23.6 mm so that 6 coils will be evenly distributed along the pipe circumference. Parameter c (width of the coil wiring) was selected to be 10 mm which allows generating torsional wave with high power efficiency.

The y (horizontal) component of the surface force at different distances (0 to 6 mm) from the symmetry plane is shown in Figure 3.8. The plot indicates that the relevant area where the EMAT generates a force is approximately 10 mm deep (in axial dimension) as the surface force decreases rapidly at the distance of 5 mm from the symmetry plane.

Note that the force amplitude is very small, meaning that this excitation magnitude is expected to result in ultrasound waves with extremely low displacements.

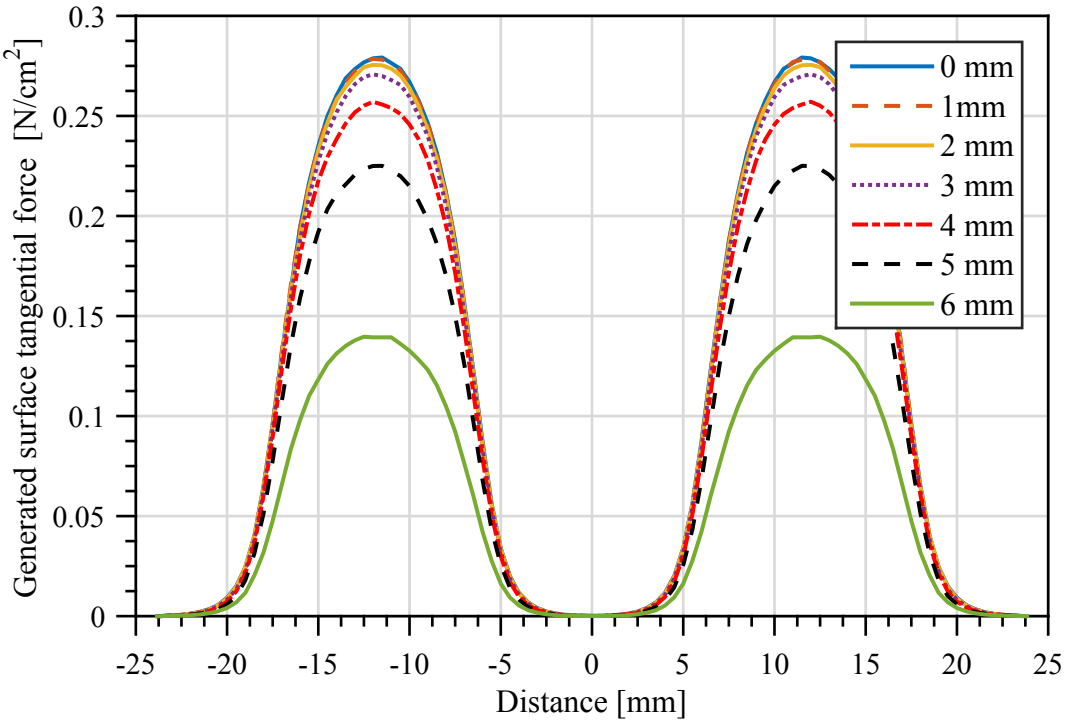

Figure 3.8: Simulated horizontal (Y component) distribution of the force generated by the EMAT on parallel planes at evenly spaced distances from the symmetry plane.

3.4 Finite Element simulation of the EMAT generated wave-field

As mentioned in the above sections, the ideal excitation of the torsional wave would be a uniform tangential force distributed uniformly over the whole cross section of the pipe. However, for numerous reasons it cannot be achieved with EMATs:

1. The Lorentz force EMATs generate the excitation force only on the surface of the pipe, as the skin-depth (~120 μm at 30 kHz) is small. As the skin depth is small compared to both the acoustic wavelength and the pipe wall thickness, the force is modelled as surface traction.

2. As discussed, the EMAT proposed in this work generates the tangential force (previously referred to as y component in Figure 3.2) at discrete patches along the circumference. Wave modes from the flexural mode family might be generated when too few excitation patches are used.

3. Radial forces (z component in Figure 3.2) act on the pipe surface, which might excite some further flexural modes. It is expected that an increased number of coils reduces the flexural modes that are excited by the radial forces.

Despite the non-uniform force distribution, the proposed EMAT arrangement can still generate pure wave modes. Practically, the suppression of unwanted modes below -40 dB (1%) of the T(0,1) signal amplitude is considered as pure wave excitation.

1. The surface excitation is adequate as the higher order torsional modes are not present at the frequency, as the excitation frequency range is well below 100 kHz (tone-burst signal centre frequency) [121] . The cut-off frequency of the second order torsional mode T(0,2) is around 300 kHz for the particular thickness of the NPS 3-inch Schedule 40 pipe [27, 28]. Therefore the surface excitation can only excite the zero order torsional wave (T(0,1)) mode.

2. It has been reported that in order to reduce the flexural modes (generated by the discrete tangential forces) more surface tractions should be used than the highest order flexural mode within the operational bandwidth [24, 122]. The cut-off frequency of the F(12,1) mode is around 85 kHz, therefore 12 surface tractions (6 coils and 12 magnets) is expected to be suitable for pure torsional wave excitation below this cut-off frequency (transducer with fewer coils might be operational for lower frequency excitation). Other researchers reported that in order to excite a pure mode the distance between the surface tractions should be smaller than half the wavelength [34, 35]. On a 3-inch pipe, the 12 surface tractions satisfy this criterion as well, as the wavelength at 30 kHz is ~109 mm, and the distance between the surface tractions is around 23 mm.

3. The presence of radial forces is unique to the EMATs (is not necessarily present in the piezoelectric transducers), therefore the displacement of the generated wave modes should be simulated in the Finite Element program. In this document, the main focus is on the excitation of the torsional wave on a 3-inch Schedule 40 NPS pipe. The actual outer diameter of the pipe is 3.5 inch (88.90 mm) and the wall thickness is 0.216 inch (5.486 mm) [84]. Despite the fact that all the simulations are performed for the NPS 3-inch pipe size, at the end of the chapter it is detailed how the mode purity is influenced by scaling the transducer and the pipe diameter.

ABAQUS CAE Finite Element simulation program [123] was selected in order to simulate the coherent noise which is present in the time signal due to excitation of other unwanted modes. A Dynamic, Explicit full analysis simulation was created in Abaqus. The pipe was modelled as a 3D deformable part with the standard dimensions (3-inch, schedule 40). In the first instance, it was modelled that an EMAT array consisting of 6 coils and 12 magnets are placed along the circumference of the pipe. The torsional and radial force distribution simulated with COMSOL in the previous section (1.3.3) is used as an input for the ABAQUS simulation. As the 6 coils are evenly distributed along the circumference, the generated force will be periodic around the circumference. Therefore, the numerical results (shown in Figure 3.7) can be approximated by the first five components of its spatial Fourier series. This means, that the simulated force distribution (both tangential and radial forces) is approximated as the sum of multiple force distributions with different cycle numbers. The advantage of decomposing the force distributions into a series of components with different cycle numbers is that each of this component corresponds to a different guided wave mode. (The force component with 12 cycles correspond to the F(12,1) mode, whereas the 24th order force component corresponds to the F(24,1) mode).

The Fourier coefficients were calculated by Matlab's curve fitting tool and are shown in Table 3.1. The spatial Fourier series estimates the simulated results with a maximum error of 3.6% and 4.3% for the radial and tangential components respectively. The tangential and radial forces are shown in Figure 3.9 and Figure 3.10. The blue plot shows the numerical data simulated in Comsol, the black dotted line shows the result of the Fourier series fit.

Table 3.1: Fourier coefficients a_n and b_n for estimating the tangential and radial force components along the pipe circumference.

n	$a_n \left[\frac{N}{cm^2}\right]$	$b_n \left[\frac{N}{cm^2}\right]$
0	0.1350	-
1	-0.1811	-0.1091
2	0.0334	0.0164
3	0.0245	0.0147
4	-0.0095	0.0052

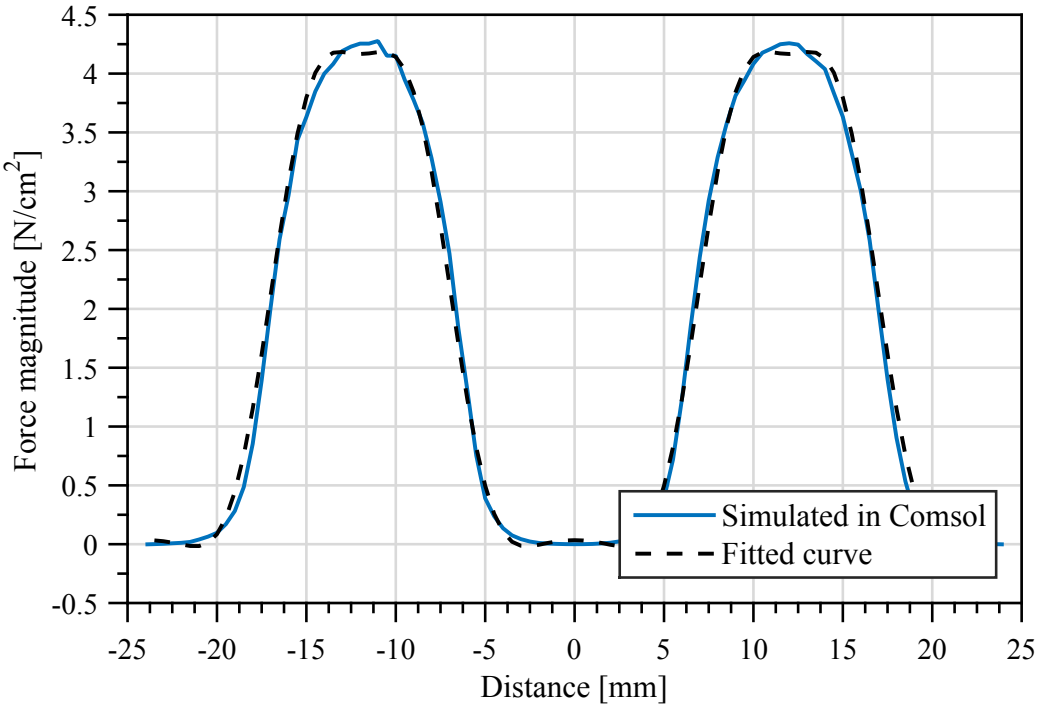

Figure 3.9: Simulated tangential force (blue) and the 4th order Fourier approximation (dashed black) of an EMAT at the symmetry line.

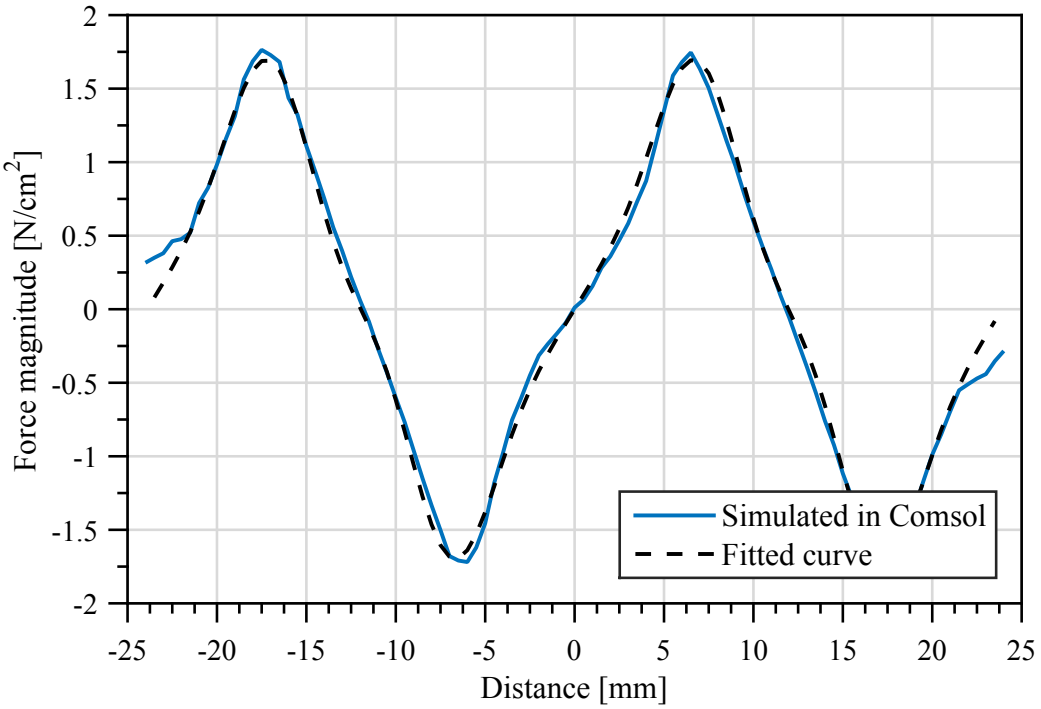

Figure 3.10: Simulated radial force (blue) and the 4th order Fourier approximation (dashed black) of an EMAT at the symmetry line.

Then, as multiple EMAT elements are placed around the circumference of the pipe the force distribution is shown in Figure 3.11 as a function of the circumferential position. The Fourier series of the tangential (f_T) and radial (f_R) forces is expressed (in function of the angular position (θ)) as:

$$f_T(\theta) = \sum_{n=0}^{n=4} a_n \cdot cos(12 \cdot n \cdot \theta) \tag{3.5}$$

$$f_R(\theta) = \sum_{n=1}^{n=4} b_n \cdot sin(12 \cdot n \cdot \theta) \tag{3.6}$$

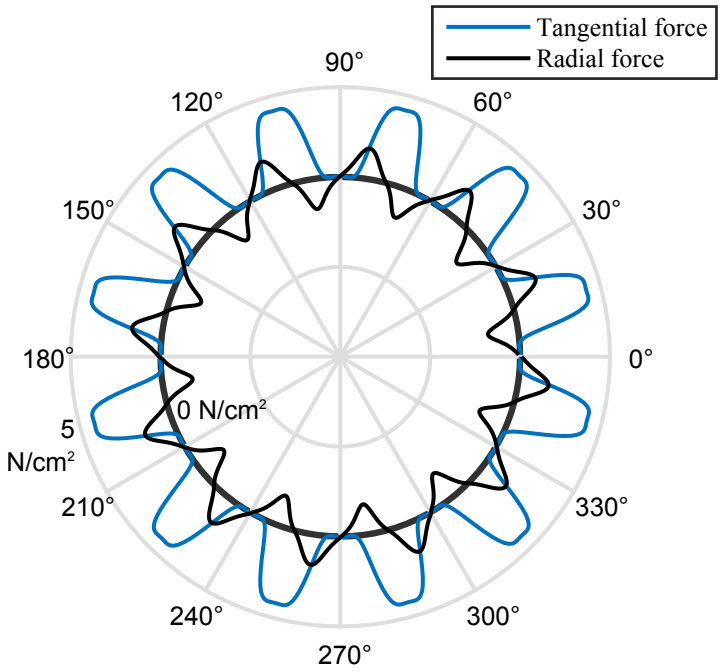

Figure 3.11: Simulated force distribution (tangential and radial components) of a 6 coil 12 magnet EMAT array on a 3-inch pipe.

In the ABAQUS simulations the forces acting on the pipe were simulated as surface tractions, as the eddy current skin depth is magnitudes smaller than the thickness of the pipe and the ultrasonic wavelength. A 5 cycle Hanning-windowed tone-burst signal was used for the excitation. The displacement caused by the tangential and radial forces of a 6 coil evenly distributed EMAT array (using 12 magnets) was monitored 250 mm

away from the excitation location (see Figure 3.12). It can be assumed that the torsional wave purity will further increase for longer propagation distances as the amplitude of the unwanted dispersive modes are decreasing during the propagation. Previous studies revealed that for efficient finite element modelling the mesh size in the simulation should be 10-20 times smaller than the wavelength of the propagating wave [124]. This criterion was fulfilled throughout the simulations. The displacement time signal was recorded for the input frequencies of 15, 30, 45, 60, 75 and 90 kHz.

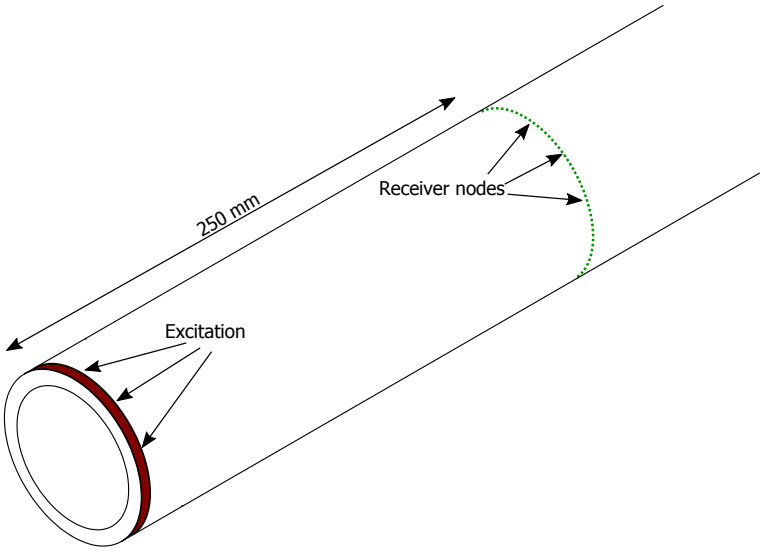

Figure 3.12: Schematics of the Abacus FE simulation: the displacement of the excited ultrasonic wave propagating on a 1-meter long NPS 3-inch pipe is simulated. The force excitation varies as a function of circumferential location and is is generated at the pipe end, and the displacement is monitored at 122 nodes 250 mm away from the excitation.

The simulated force (result of COMSOL simulation shown in Figure 3.7) was originally presented for a 30 kHz signal. As the Abaqus simulations are performed for different frequencies, the input force distribution is re-simulated in Comsol for each frequency. Nevertheless, it has been found, that the eddy current flow has the same distribution independent to the excitation frequency (apart from the skin-depth, but it is much smaller than the ultrasonic wavelength for all frequencies).

This means that the force distribution will be identical for all frequencies, only the amplitude and phase can vary between different frequency simulations. However, the amplitude and the phase of the excitation signal does not influence the coherent noise of the signal.

A 1-meter long NPS 3-inch Schedule 40 pipe was modelled, with the pipe outer diameter of 88.9 mm and the wall thickness of 5.486 mm. The density of the pipe material was set to 7800 $\frac{kg}{m^3}$, the Young modulus was 200 GPa, and the Poisson's ratio was 0.3. The mesh was selected to be made of quadratic elements with the element size less, than 3 mm, which satisfies the criteria for the mesh size [124], as each element is more than 10 times smaller than the torsional wave's wavelength.

Figure 3.13 and Figure 3.14 show the tangential displacements recorded on 122 nodes (evenly distributed along the pipe circumference) at the receiver location for different frequencies. The plots on the left show the recorded displacement in linear scale, whereas the right hand-side plots show the same displacement in logarithmic scale (normalized to the displacement amplitude). The coherent noise is then calculated as the highest tangential displacement after the incident torsional wave has passed the receiver location.

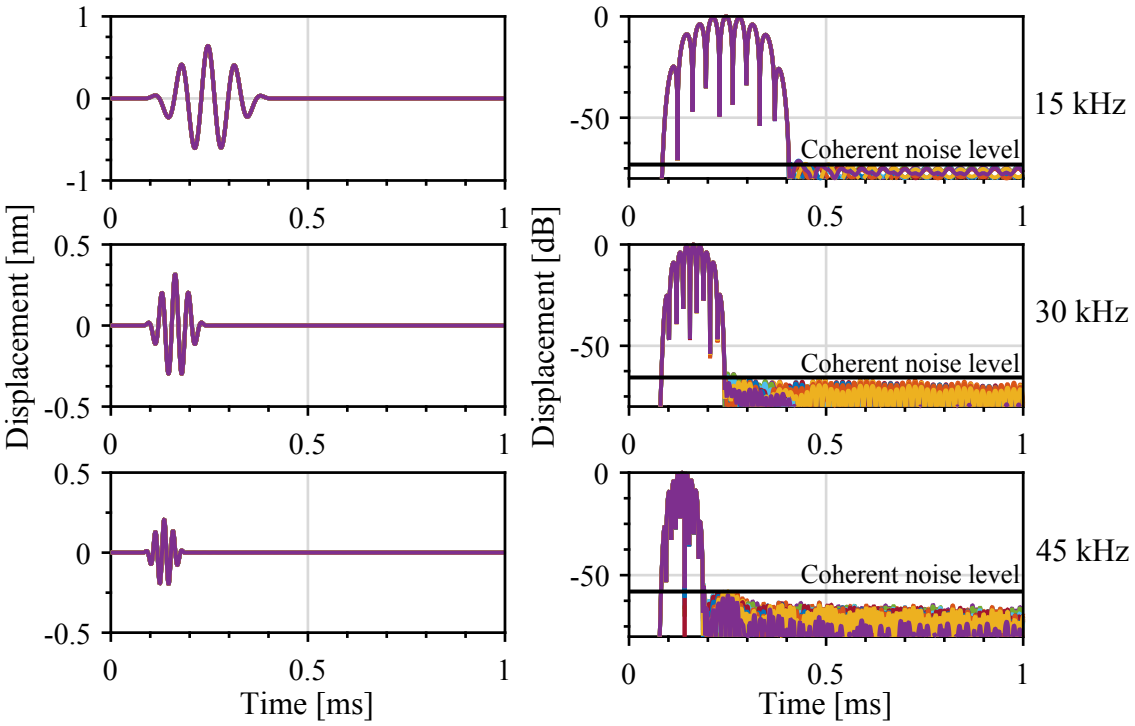

Figure 3.13: Simulated displacement of the outer surface of a 3-inch NPS pipe measured 250 mm from the excitation location (for 15, 30 and 45 kHz frequencies). The displacement is shown in linear (left) and logarithmic (right) scale. The generated force of an 6 coil EMAT array was used as an excitation.

The simulations revealed that in case the 12 magnet (6 coil) arrangement was simulated the requested mode purity of 40 dB was achieved when the centre frequency of the excit-

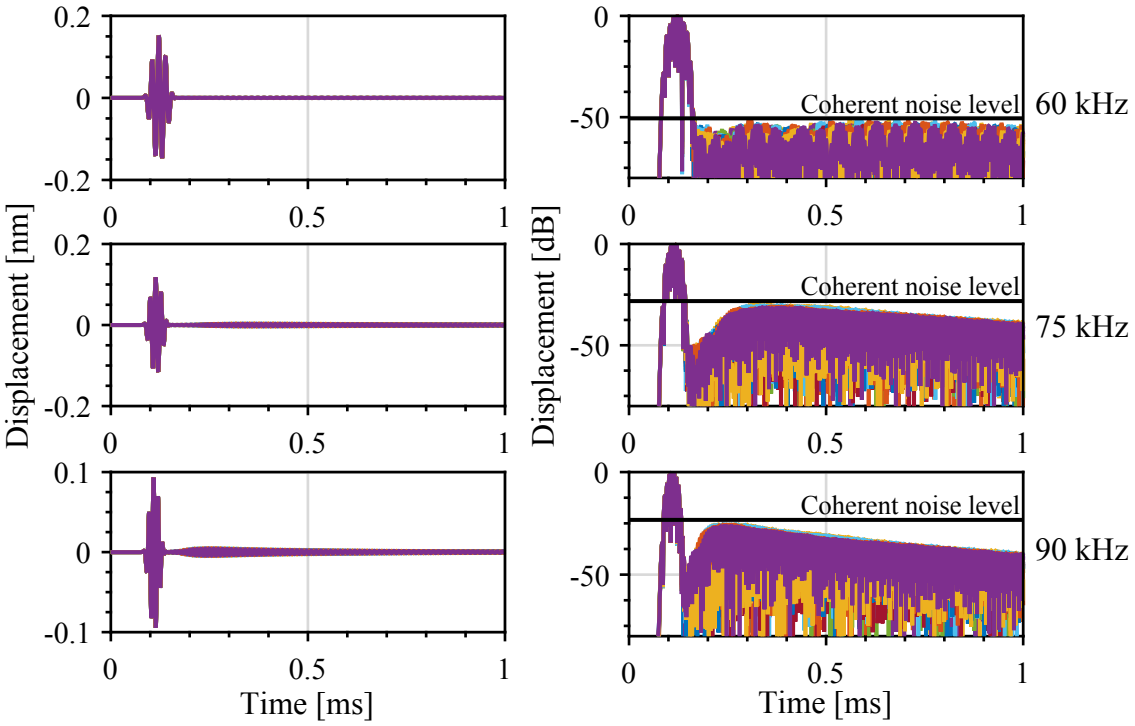

Figure 3.14: Simulated displacement of the outer surface of a 3-inch NPS pipe measured 250 mm from the excitation location (for 60, 75 and 90 kHz frequencies). The displacement is shown in linear (left) and logarithmic (right) scale. The generated force of an 6 coil EMAT array was used as an excitation.

ation signals was below 60 kHz. Previously, it was discussed, that the higher limit of the excitation bandwidth is 85 kHz (the cut-off frequency of the F(12,1) mode) [24,34,35,122]. It must be noted, that the 60 kHz 5 cycle tone-burst signal has frequency components (main lobe) of 36-84 kHz [95]. Therefore, the limitation in the excitation frequency estimated from the literature/dispersion curves limits all frequency components of the excitation waveform.

The ABAQUS simulations were repeated for the cases when only an 8 magnet arrangement, and also when 16 magnet arrangement is used for excitation. The coherent noise levels were calculated again, and are plotted in Figure 3.15 for the 8, 12, 16 magnet arrangement. The coherent noise level suddenly increases at ~35, ~65, ~95 kHz for the 8, 12, 16 magnet arrangement respectively. The sudden increase in coherent noise is due to the appearance of the corresponding unwanted flexural mode (8^{th}, 12^{th}, 16^{th} order). The plot indicates that the 8 magnet arrangement has the smallest operational frequency range (up to ~35 kHz tone-burst centre frequency), and the 16 magnet arrangement has even

higher operational frequency range (the 105 kHz excitation still produced pure torsional wave propagation). This result is also in line to the expectations as the F(8,1) cut-off frequency is around 43 kHz for the investigated pipe dimensions.

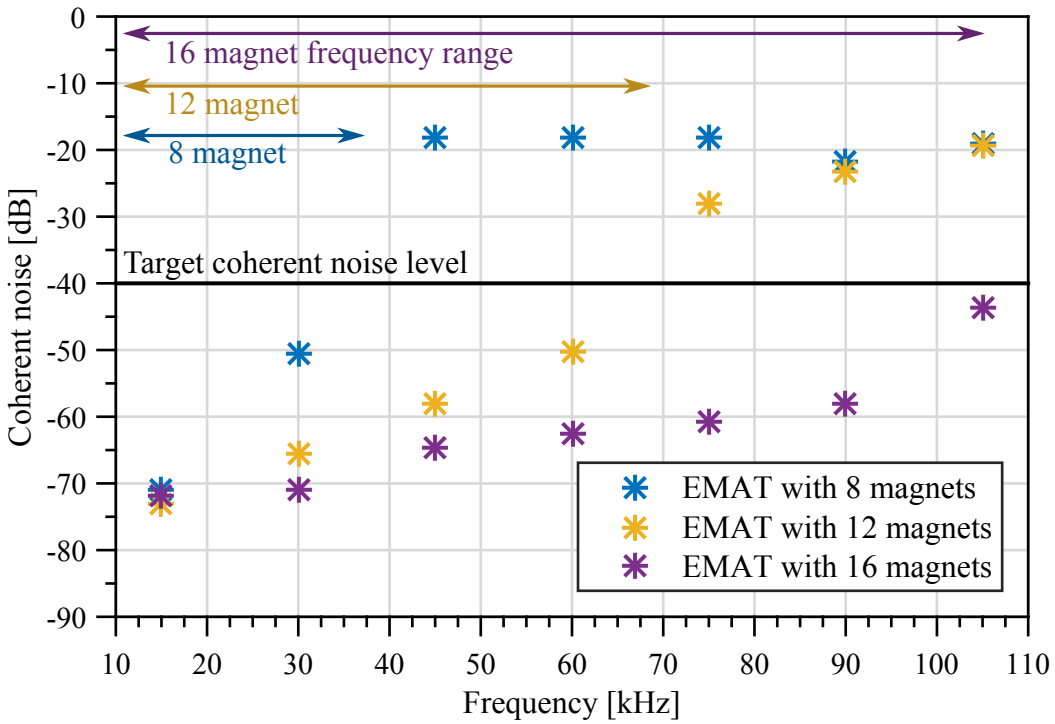

Figure 3.15: Evaluated coherent noise level of the tangential displacement for different frequencies and different excitations (5 cycle tone-burst, 8, 12 and 16 magnets around the circumference). The frequency range for each excitation method is shown by double arrows.

So despite the presence of radial forces generated by the EMAT, the general conclusion can be drawn for the operational frequency range, which agree with the available literature: If the excitation patches (transducer elements) are evenly distributed along the pipe circumference and they are the same, the generation of pure torsional wave is possible. The frequency range must be kept below the frequency, where flexural mode corresponding to the number of magnets present in the EMAT array exists. In other words, the number of excitation patches (N magnets) must be high enough so that the flexural F(N,1) mode is not present in the excitation frequency region.

This generalized conclusion means that designing an EMAT array for different pipe sizes and pipes with different wall thicknesses can conveniently be designed, as the frequency range of each unwanted mode can be determined using the dispersion curves. The dis-

persion curves should be calculated for each pipe and the number of magnets (excitation patches) around the circumference must be chosen accordingly to avoid flexural mode generation.

3.5 Reception of the fundamental torsional wave

Generally, publications mainly focus on the wave excitation mechanism of the electromagnetic transducers. Several reports investigate only the excitation mechanism of the EMATs but not the reception [114, 125–127]. However, some researchers investigated the reception mechanism along with the excitation mechanism [128–130].

The zero order torsional wave has a uniform tangential displacement on the pipe surface, and it can be detected using an EMAT receiver similar to (or the same as) the transmitter transducer. The torsional wave can be received by the transducer as the static magnetic field generates a current loop inside the moving specimen, and this current loop is transformed back to the receiver coils. The modelled reception mechanism is as follows: the static magnetic field of the magnets (B_0) interacts with the moving particles of the passing wave and creates an electric field inside it. The generated electric field is described by the inverse Lorentz force and is proportional to the displacement velocity and the static magnetic field. The electromagnetic field generates closed-loop eddy currents (J) inside the test specimen:

$$J = \frac{1}{\rho}\left[E + \frac{\partial u}{\partial t} \times B_0\right] \tag{3.7}$$

where $\frac{\partial u}{\partial t}$ is the velocity of the specimen, and ρ is the resistivity of the conductor. This eddy current then generates a magnetic field (Maxwell 4^{th} equation):

$$\nabla \times B = \mu J \tag{3.8}$$

The changing magnetic field B generated by the current flow will generate an electric field

E in the coil according to Maxwell's 3^{rd} equation:

$$\oint_C E \cdot dl = -\frac{d}{dt} \int_s B \cdot dA \tag{3.9}$$

In the coils of the receiver transducer this electric field creates the sensed voltage.

FE simulations were carried out simulating linear harmonic displacements of the mild steel conductor underneath the EMAT coils. Since the pipe radius is large compared to the tangential displacements, the linear movement of the conductor under a planar coil (instead of rotation of the curved conductor) is again a reasonable assumption to simplify the analysis.

The COMSOL Multiphysics Modelling Software was used to simulate the induced eddy current inside the specimen. EMAT elements with dimensions identical to the excitation EMATs were modelled in the FE program. The magnets were modelled with the same 1.4 Tesla remnant magnetization and alternating polarity. Figure 3.16 shows the generated eddy current direction and magnitude at the surface of the mild steel conductor when the linear particle movement was set to 1 m/s.

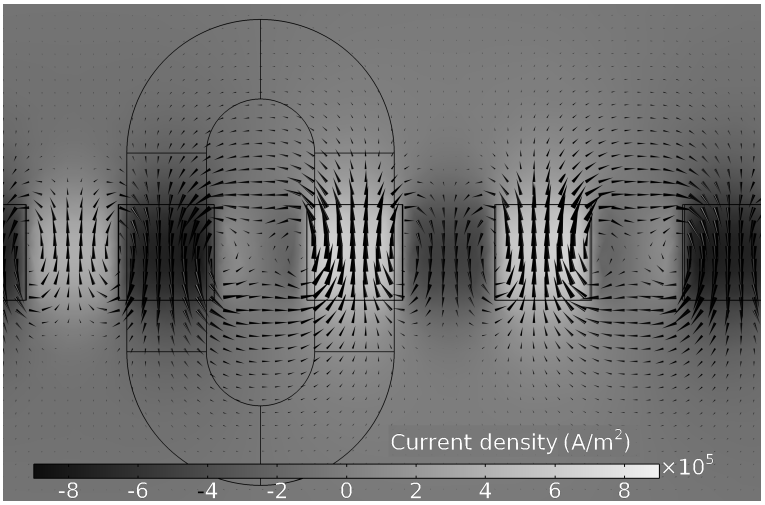

Figure 3.16: Result of the finite element simulation for the receiver EMAT on a planar surface. The eddy current flow direction is shown by black arrows, while the eddy current magnitude is indicated by colour plot. The shape of the magnets and one of the coils are shown in faint black lines for reference purposes.

The generated eddy current flow forms a closed-loop circuit, with a shape similar to

the transmitting coils, and with the highest magnitude current flowing underneath the magnets. Therefore, it is a deliberate idea to use a receiving coil, which also has an elongated race-track shape and has a similar size. The coil elongation parameter can be optimized by finding the best coupling factor between the eddy current and the receiver coils. This optimization requires running complex simulations and was not studied in details. The elongation of the coil was chosen to be the same as for the transmitter side of the transducer. This results in a relatively good coupling factor between the eddy current flow and the coil and makes the design and manufacturing process easier.

The receiver EMAT transducer receives really low amplitude signals. Therefore, it is useful to note the possible ways of improving signal strength and sensitivity. For example, the coil terminals can be connected in series, enhancing the otherwise weak reception of each individual coil. Also, if a separate receiver transducer is used in the measurements the number of turns in the coil can be independently optimized.

A few test measurements were performed, where the effect of the number of turns was investigated. For the performed tests it was found that the received voltages increased linearly with the number of turns. This increase in received signal amplitude has been tested only for a limited number of turns, and it is possible that the gain is decreased for coils with extremely large number of turns, as the increase of the output impedance might cause an impedance mismatch between the receiver transducer and the amplifier. Nevertheless, it is shown in the next sections that the current EMAT design can lead to sufficient Signal-to-Noise Ratio (SNR), and further optimization was not required.

3.6 Experimental validation

3.6.1 Manufactured transducer

The previous sections showed that an EMAT array consisting of multi-turn coils and permanent magnets can be designed which can generate pure torsional guided waves. For easier handling, an assembly is required that is rigid in one direction (the direction axially along the pipe) and holds the magnets. At the same time, it also needs to be flexible in the other direction (circumferentially around the pipe) so that the coils which are deposited

on a flexible substrate (flexible PCB) can conform near perfectly to the shape of the pipe with conducting surface below.

The EMAT coils are printed onto a flexible kapton-polyimide Printed Circuit Board (PCB) which is highly resistant to mechanical forces and can operate at elevated temperatures. Each coil consists of 17 turns on both the top and bottom layer, with the copper wire width of ~0.35 μm, and the thickness of each copper layer is 35 μm. The DC resistance of the coil is then around 4 Ω. This coil is attached to a metal rib (made from metal for high temperature durability, will be explained in the later chapters), which has the role of holding the magnets in place and form a structurally rigid body in the longitudinal direction. This assembly of the PCB, magnets and metal ribs is then encapsulated in a flexible compound, so that the components are held together but can also be arranged to conform to the pipe surface.

For practical reasons, a few other design modifications must be made to create a fully functioning EMAT array transducer. For example, the permanent magnets must be attached to the transducer ribs. Otherwise, when the transducer is moved close to the pipe during the installation, the magnets would tear or damage the PCB. Hence, a steel shim is embedded to the metal ribs, which then attracts the magnet to the non-magnetic metal ribs.

At the same time as creating the desired eddy current in the pipe, eddy currents can also be generated in the conductive permanent magnets. This then decreases the efficiency of the EMAT. The magnets should be lifted-off by installing a non-conductive spacer underneath it to reduce generated eddy currents. However, as the magnets are lifted off, the magnetic field is slowly decreasing (not drastically, as the steel attracts the magnetic field lines), the highest excited Lorentz force can be generated at an optimal lift-off value, where the best trade-off is reached between the eddy current efficiency and the magnetic field strength. The optimal magnet lift-off for the constructed coil size and 12 mm cubic magnet was experimentally measured to be 0.5 mm for the transmitting and receiving transducer as well. A Computer-Aided-Drawing of the designed transducer is shown in Figure 3.17, and the picture of the actual manufactured transducer is shown in Figure 3.18.

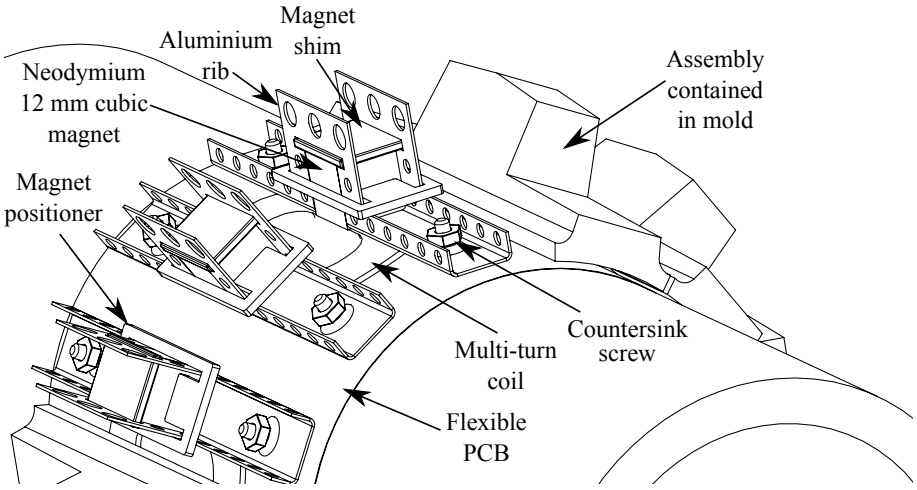

Figure 3.17: Drawing of the transducer design. The assembly contains the PCB and the magnets which are required for the EMAT operation, the other components (metal rib, positioners, etc.) are used to fix the parts together.

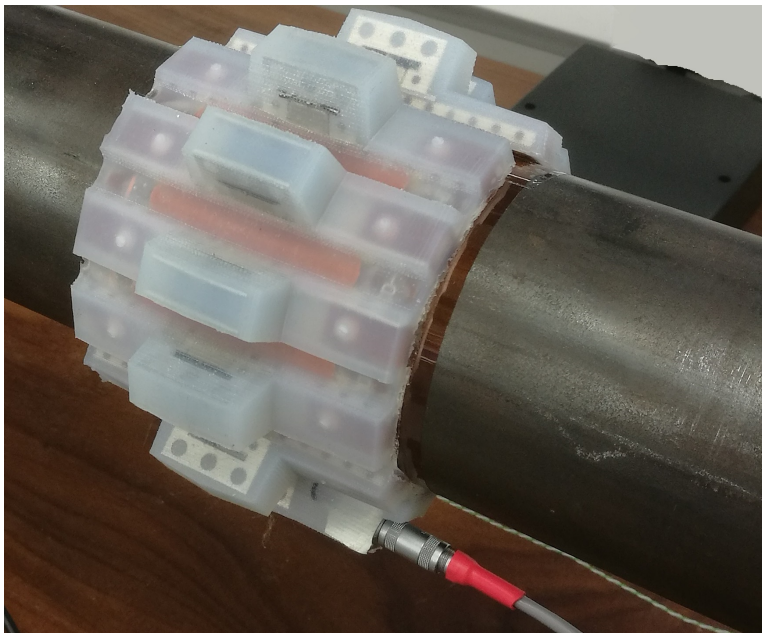

Figure 3.18: Picture of a manufactured receiver transducer.

The directional control is achieved by using two transmitter transducers, and a single receiver transducer (in theory it could be done with one transmitter and two receiver transducers as well). The distance between the two transmitter transducers was selected to be $\frac{3\lambda}{4}$ (~81mm for the 27 kHz measurement), so that the coils do not overlap. It is desired to place the transducer with the separation of $\frac{\lambda}{4}$, to increase spatial resolution of the measurement, but this solution was not investigated.

3.6.2 Signal Acquisition System

For industrial monitoring applications, the design of a robust and reliable signal acquisition system is very important. The aim during the design process was that cost-effective instrumentation should be developed which allows the measurement system (with some degree of modification) to be utilized for monitoring applications. Therefore, an in-house custom-built system was developed focusing on low frequency (20-60 kHz) ultrasonic applications. The transmitting and receiving transducers are separated, which results in simpler electronics, as no switches and timing circuits are required for the instrumentation. The separated transmitter and receiver transducer means that the acquisition system operates in pitch-catch mode, even though the useful information in the torsional guided wave measurement are the reflected echoes.

An acquisition system was designed which contains all necessary instrumentation which is required to acquire the signal data from the EMAT transducer and transmit it to the PC. The excitation signal is generated with a computer based arbitrary function generator and oscilloscope (Handyscope HS3; TiePie Engineering Ltd, Sneek, The Netherlands [131]). This waveform generator is capable of delivering small currents only due to the waveform generator's 50 Ω output impedance. In order to deliver the desired power, a 40 W audio transmit amplifier (40 W Power Amplifier, Kemo Electronic GmbH) is used as a buffer to deliver the desired current to the EMAT coils [132]. This transmit amplifier generates differential voltage output, which is necessary for the cross-talk reduction system described in the next Subsection 3.6.3. Even though the buffer amplifier can deliver larger power, the excited voltage was set to be below 4V Peak-to-peak, which in all measurements resulted in a current below 1 Amp. This delivered power (lower, than 4 Watts) is less than the intrinsic safety limits for most applications near hazardous locations [68]. The drive for intrinsically safe power levels is the increase in the number of potential monitoring locations. Note, that the actual electronics is not yet adapted for intrinsic safety, only the input power was limited to the safety standards.

EMATs generally have low SNR, therefore several EMATs use high power (voltages often exceeding 1 kV) excitation pulses to improve SNR [101, 133, 134]. In order to compensate the low excitation power sent to the transmitter, the SNR is improved by reducing the

noise on the receiver transducer. The first adaptation was to supply the receiver coils with a copper noise-protection sheet functioning as a Faraday's cage. In addition, the cables used for connecting the receiver transducer to the instrumentation was chosen to be a twisted-pair shielded cable as it gives the best noise performance. Furthermore, the AD8331 ultra-low noise amplifier (optimized for ultrasonic applications) was selected for receiver amplification [135, 136]. Furthermore, a custom-built operational amplifier and a ~300 kHz low-pass filter was added for additional signal conditioning (the signal was filtered electronically as well). The added low-pass filter is used for filtering out the remaining high-frequency noise components from the signal. The receiver amplifier stages overall resulted in a 75 dB (factor of 5623) amplification.

The amplified ultrasonic signal is then connected back to the first input channel (CH1) of the Handyscope HS3. The input waveforms were digitalized with 16-bit precision and at 5 MHz sampling frequency (oversampled to reduce anti-aliasing).

For low number of signal averages the excitation signal was slightly unstable due to the jitter in the electronics, which is the result of small timing changes in the excitation trigger. However, when more than 50 averages were performed, the random jitter was suppressed below of the desired level.

A precision current transformer (CT-B1.0-B, AMS Technologies AG [137]) was used to measure the input current waveform and was connected back to the second input of the HS3 (CH2). The input current was measured so that the stability of the excitation current can be evaluated. The aim was to have a variation (difference between any two signals) less, than 1 % of the signal amplitude.

The last instrumentation to be added to the system was an USB controlled relay board (RLY-08 developed by Devantech Limited, Norfolk, UK) so that ultrasonic signals can be collected from both transmit transducers and directional control of the guided wave signal can be implemented [138]. The method for the directional control method is detailed in Chapter 2. The signal acquisition electronics containing all the necessary items is shown in Figure 3.19.

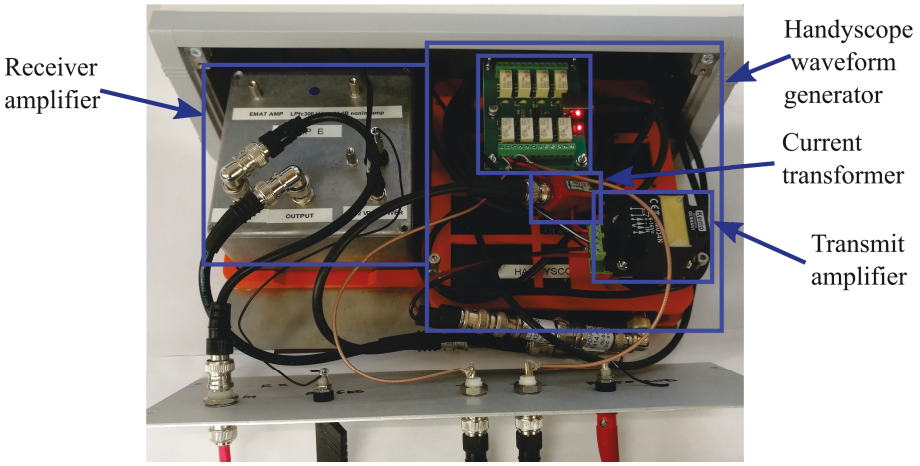

Figure 3.19: Picture of the custom-made signal acquisition system used for measuring the guided wave ultrasonic signal. The signal acquisition system contains the Handyscope HS3 (waveform generator and PC based oscilloscope), 40W power amplifier, relay board for the two-transmitter measurement, the current transformer for current waveform measurement, and the 75 dB analogue receiver amplifier.

3.6.3 Hardware design for cross-talk reduction

The previous sections have shown that the expected ultrasonic signal amplitude is extremely low, and therefore high-gain analogue amplifier is required to increase signal level measurable with standard digital acquisition (DAC) equipment. Apart from receiving the ultrasonic signals, the direct coupling mechanisms between the transmitting and receiving transducer will also contribute to the acquired signal. The so-called cross-talk signal is received, which is the excitation signal electromagnetically coupled to the receiver transducer.

Ideally, the transmit and receive coils should be placed close-by to minimize the dead-zone of the measurement. Unfortunately, the small separation of the transmitting and receiving transducers results in a cross-talk signal, which can easily be larger than the ultrasonic signal itself. Several research papers have presented results with high cross-talk in several types of ultrasonic measurements (torsional, longitudinal, shear-horizontal) [59, 113, 114, 126, 129, 139–141].

The problem arises when the cross-talk signal is so large that it saturates the receive amplifier, and the recovery of the receiver amplifier takes so long that the early echoes are superposed to the coupling. An example signal with large cross-talk was recorded by a colleague Jerome Combaniere is shown in Figure 3.20. The signals were acquired with a

custom-made Lorentz-force EMATs placed onto a plate, using a RITEC RPR-4000 high power pulser and receiver [142]. Note, that even if the echo is visible from the time trace, the information is corrupted due to the instability of the large cross-talk. Alternatively, a crosstalk signal, which is magnitudes larger than the useful signal the use of coded sequences can be problematic as discussed in Chapter 2.

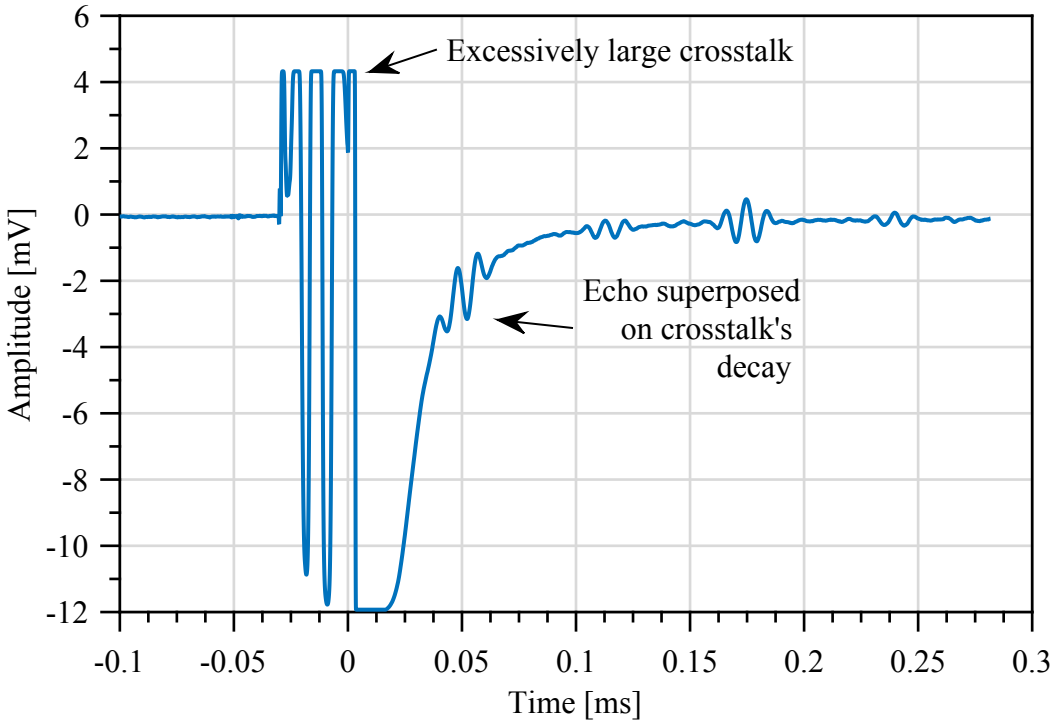

Figure 3.20: Example signal where the ripple of the cross-talk decay is excessively long. This results in the first echoes to be superposed on the cross-talk signal. Signal was collected on a custom-made EMAT transducer using RITEC RPR-4000 Pulser and receiver by Jerome Combaniere.

Measurements were performed, and it has been identified, that the cross-talk signal is generated by capacitive and inductive coupling mechanisms. These coupling mechanisms are well known in electronic circuit design [143].

Parasitic (stray) capacitance exists between the conductive pipe and the transducer coils. This capacitance even if being small, results in the net charge on the excitation coil to be coupled to the receiver coil throughout the pipe. As the net charge on the transmitter coil is coupled to the receiver coil, the magnitude of the capacitive cross-talk is linear with the excitation voltage. The schematics of the capacitive coupling is shown in Figure 3.21.

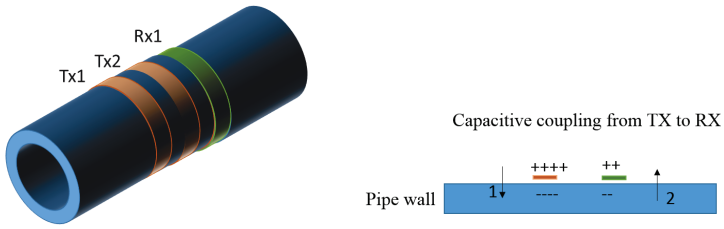

(a) (b)

Figure 3.21: Capacitive coupling mechanism: the transmitter transducers (Tx1 and Tx2 on (a)) are coupled to the receiver transducer (Rx1). The voltage on the transmitter transducer is first coupled to the pipe, then to the receiver transducer (b).

The other mechanism for cross-talk generation is the inductive coupling of the excitation current to the receiver coils. The excitation current creates a magnetic field. The part of the changing magnetic flux which passes through the receiver coils generates an electromotive force (EMF) which is the cross-talk signal itself. The transmitter and receiver coils therefore act as an air-core transformer with a relatively week coupling (still stronger than the ultrasound signal). It is also worth mentioning that the inductively generated cross-talk is linear with the excitation current. The schematics of the inductive coupling is shown in Figure 3.22.

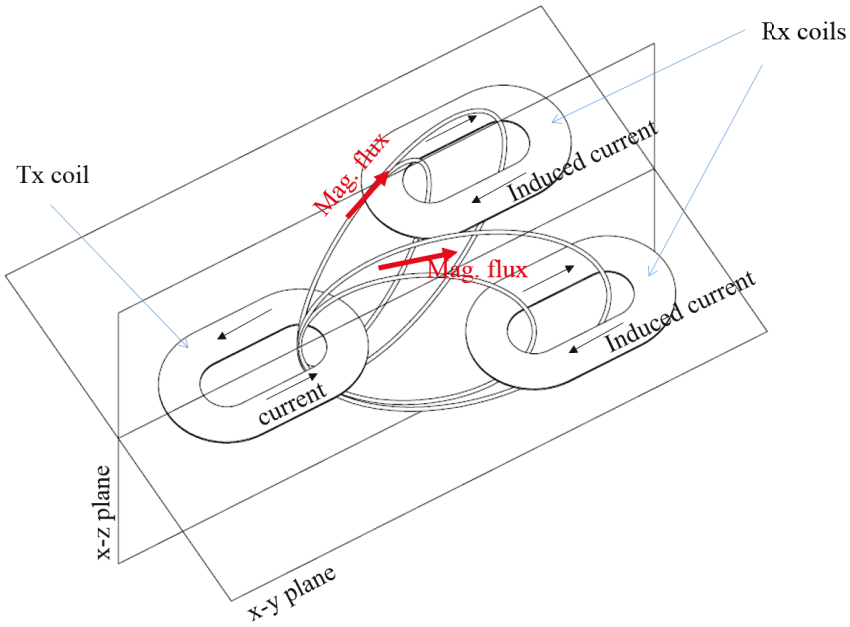

Figure 3.22: Inductive coupling mechanism: The magnetic flux generated by the current in the transmit transducer passes through the receiver coils. An EMF voltage is then generated due to the changing magnetic flux.

It is possible to overcome both the capacitive and inductive coupling mechanism by developing clever arrangement of transmitter and receiver coils and utilizing a well-designed instrumentation. The following paragraphs explain a method to completely eliminate the cross-talk signal. The method has been patented by Imperial Innovations, and has been given the publication number WO2017/158318 [P2] [144] .

In order to cancel out capacitive coupling the transmitter coils need to be driven in differential mode. The differential excitation mode is achieved when the same electrical signals with different polarity are connected to the coil terminals. The mean voltage of the coil is then zero, therefore no net charge accumulates on the pipe. The method for eliminating the capacitive coupling is shown in Figure 3.23.

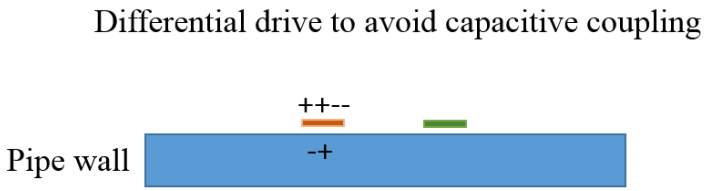

Figure 3.23: Solution for eliminating the capacitive coupling between the coils: the transmit transducer is driven in differential mode (the signals with opposite polarity are connected to the coil terminals), therefore the net charge is zero in the pipe.

To overcome the inductive coupling mechanisms, and to make sending and receiving of guided wave EMAT signals available, a special magnet arrangement and wiring pattern of the receiver coils can be used. To cancel the cross-talk generated by inductive coupling the wiring pattern of the receiver coils is changed so that every second coil is flipped (wired with different polarity) as shown in Figure 3.24. The generated flux in each receiver coil is the same due to symmetry reasons, so by connecting them alternatively reduces the overall flux and hence the generated cross-talk signal.

In order to receive the zero order torsional wave, the orientation of the magnets appropriate to the flipped coils must be flipped as well (shown in Figure 3.25). This results in an overall design, which does not pick up the inductive cross-talk, but receives the ultrasonic signal.

In addition to the differential excitation voltage and special coil wiring, it is needed that the instrumentation is well designed as well. For example, all wiring should be done either

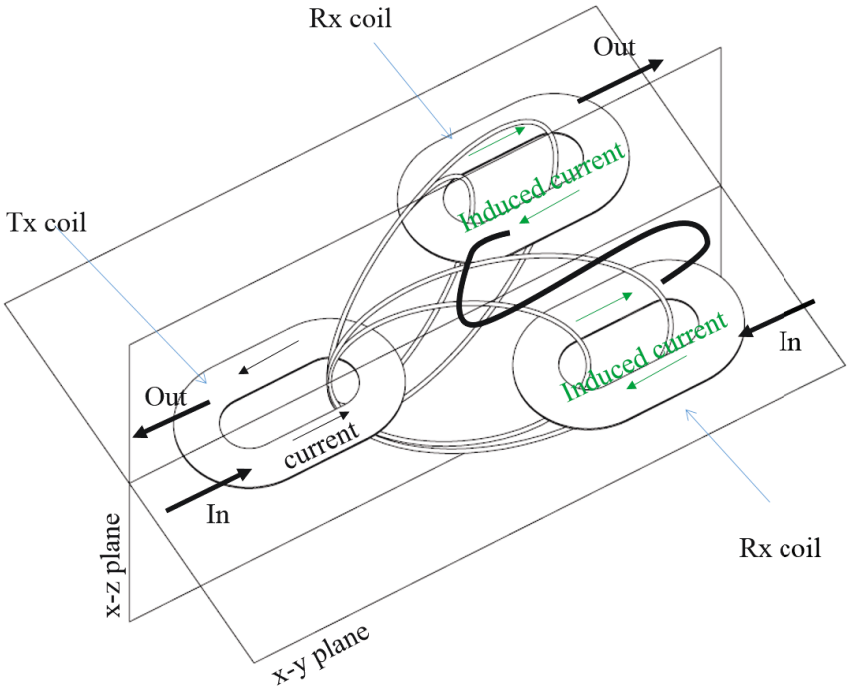

Figure 3.24: Solution for eliminating the inductive coupling between the coils: one of the coils are connected with different polarity, therefore the net flux passing through the receiver coils is zero. The reception of the torsional wave on a pipe is guaranteed by respectively flipping the magnets on those coils (shown in Figure 3.25)

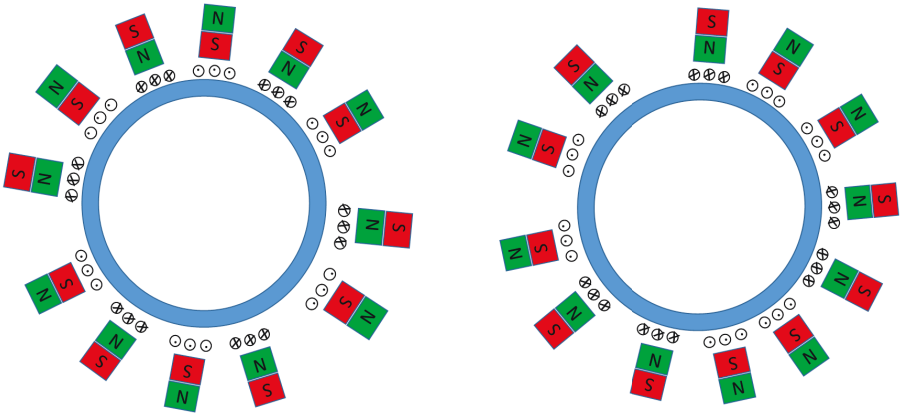

Figure 3.25: Elimination of inductive coupling of the excitation signal to the receiver: Arrangement of the magnets and coils around the pipe circumference is different for the receiver transducer. Every second coil is wired differently, and the magnets on those coils are flipped as well.

in co-axial or twisted pair arrangement so that the least disturbance is caused inside the instrument. Furthermore, the current loops must be removed, as they can pick up the small magnetic flux inside the instrument [145].

After implementing the design changes, and upgrading the instrumentation, signals with minimal amplitude cross-talk were collected. Figure 3.27 shows the acquired ultrasonic signals where the cross-talk is reduced, which allows the reception of ultrasonic signals after minimal time. Subsection 3.6.4 shows example plot where the incident wave is recorded after the propagation of 400 mm, and the cross-talk signal is reduced to a minimal level.

3.6.4 Experimentally acquired signals

The manufactured transducer was placed onto a 5-m-long, 3-inch NPS Schedule 40 pipe as shown in Figure 3.26. The pipe is a seamless pipe with the outer diameter of 88.9 mm, and the wall thickness is 5.486 mm. The pipe material is mild steel (catalogue number ASTM A106 Grade B).

Two transmitting transducers are placed in the middle of the 5 m pipe, within 90 mm separation ($\frac{3}{4}\lambda$) so that directional control can be achieved. For the directional control of guided waves, the separation of the transmitting transducers would ideally be $\frac{\lambda}{4}$ only, but this would result in overlapping coils. The exact influence of overlapping coils was not studied, therefore the $\frac{3}{4}\lambda$separation was implemented. The receiver transducer is placed 0.4 m away from the transmitting transducers.

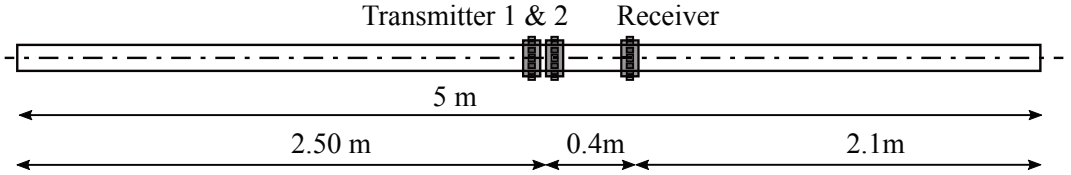

Figure 3.26: Measurement setup for acquiring signals on a 5-meter long 3-inch NPS pipe using two transmitting and one receiving transducer.

The acquired signals are shown in Figure 3.27 when 5 cycle 27 kHz tone-burst excitation was used. The signals were averaged 200 times to increase SNR above 40 dB. The plot shows signals, which were directionally post-processed. Plot (a) shows right travelling,

whereas plot (b) shows left travelling waves. For conventional EMAT measurements the cross-talk is magnitudes larger than the ultrasonic signal [113, 114], however, due to the patented coil design, the cross-talk (see plot (b) at 0.5 milliseconds) is largely attenuated (being much smaller than the signal amplitude). The right travelling wave contains the incident wave (which travels directly from the transmitting transducers to the receiver) which can be identified after ~0.2 ms. The reflection from the pipe right end can be observed at ~1.5 milliseconds. In between the incident wave and the pipe end reflection the coherent noise level can be observed, which has the level of around -40 dB.

Figure 3.27b shows the calculated signal in the left direction. The coherent noise can be seen from 0.2 to 1.4 milliseconds; which is followed by the left end reflection at 1.75 milliseconds.

The signal strength was also evaluated when two sets of signals were compared. The difference between the two signals is lower than 1% of the signal, which means that the SNR is above 40 dB and the short-term repeatability of the measurement is good as well.

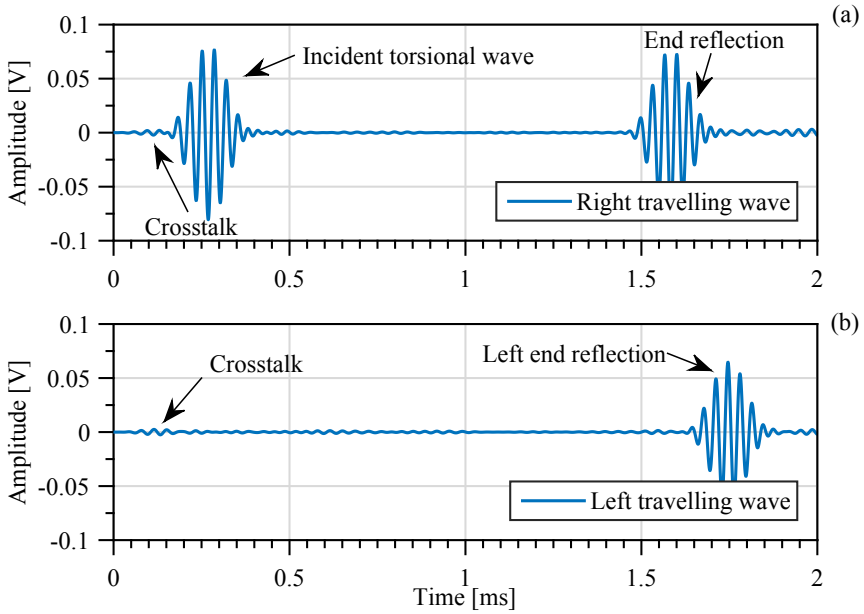

Figure 3.27: Example acquire signals (right (a) and left (b) direction) with reduced cross-talk signal. The signal was acquired when the excitation voltage was set to 3V (~900mA current). The signal was averaged 50 times to reduce the random noise. The cross-talk signal is much smaller than the ultrasonic signal, therefore the ultrasonic signals can be received with minimal travelled distance.

3.7 Summary

The design of a Lorentz force based Electromagnetic Acoustic Transducer is presented in this chapter. The transducer was developed for torsional guided wave measurements on a 3-inch pipe. Finite Element simulations were performed to investigate the excitation and reception mechanism. It was found that apart from the desired tangential force a smaller amplitude radial Lorentz force component is also generated because of the refraction of the magnetic field in steel. Nevertheless, simulations revealed, that the radial force component does not excite unwanted modes, and generally low coherent noise is expected if the excitation frequency bandwidth is below the cut-off frequency of the F(12,1) mode (as the transducer consists of 12 excitation locations/magnets).

The transducer and the required signal acquisition system were then manufactured and tested. Experimental signals were acquired on a 5-meter long NPS 3-inch pipe. The generally poor random noise performance of EMATs was improved by the specially designed signal acquisition system, and relatively few number of averages (~50) are required despite the low excitation power (less, than 4 W peak). The signals show, that the cross-talk signal (which was originally magnitudes larger than the signal) can be suppressed down to a few percent (~3%) of the signal. The SNR respect to random noise is well above 40 dB, and the mode purity of the acquired signal is around 40 dB.

Chapter 4

Mode purity of the torsional wave that is excited by the EMAT

4.1 Introduction

The previous chapter has shown that an efficient Lorentz force Electromagnetic Acoustic Transducer (EMAT) can be designed which can excite and receive zero order torsional waves on a NPS 3-inch Schedule 40 pipe. Trial measurements showed that signals with high mode purity and sufficient Signal-to-Noise ratio could be recorded.

However, these trial measurements were performed in ideal laboratory conditions, and on a clean pipe. It might be expected that for applications in non-ideal conditions the transducer performance is going to be altered. Therefore, this section investigates a few of the possible error sources that can lead to imperfect wave excitation. Finite Element (FE) simulations are performed to estimate the result of imperfect excitation on the acquired ultrasonic signals. At the end of the chapter, the simulation results are compared with measurement results.

4.2 Identification of possible error sources affecting the mode purity of the torsional wave

The torsional guided wave transducer shown in the previous Chapter is designed with a 12-magnet arrangement to generate the ultrasound. The excitation elements (underneath the magnets) are uniformly distributed along the pipe circumference. It was also assumed during the simulations that the material properties are uniform, and each excitation patch excites the same tangential force. In this chapter, it is investigated what happens if these ideal conditions are not met. The investigated error sources can be grouped into two different categories:

For the first investigations, it is assumed that the transducer is placed onto the pipe, the coils and magnets are equally distributed along the pipe circumference. In this case, imperfect excitation could for example be caused by non-uniform coating thickness, uneven coil lift-off or a rough pipe surface (at the excitation locations). Variations in magnet strength can also contribute to imperfect wave generation. Furthermore, localized conductivity or permeability variations in the pipe might affect the wave generation.

The second category of the errors is caused by imperfect positioning/ installation of the transducer. An example of such imperfection is a transducer, which is installed onto the pipe with transducer elements placed slightly at different axial position (see Figure 4.11). Additionally, pipe sizes can be different due to the manufacturing tolerances, or the transducer might have been manufactured with a slight dimensional error. It will then result in the transducer ring not covering the whole circumference of the pipe, and the excitation locations are not evenly distributed along the circumference.

A few other possible error sources were noted, but not investigated, such as variations in pipe wall thickness, or pipe cross-sections with ovoid shape. Both the variation in pipe wall thickness and the ovoid pipe cross-section affects all guided wave transducers, and is not specific to the EMAT transducer.

4.2.1 Localized permeability and conductivity changes

The magnetic permeability of the manufactured steel is highly dependent on the alloys and cold works performed on the metal [146]. Beside the alloy properties, the manufacturing process can influence the manufactured steel pipe. Seamed (or welded) pipe is manufactured by rolling metal and then welding it along the pipe axis, whereas seamless pipe is manufactured by extruding and drawing the pipe from a billet [147]. Studies revealed that localized permeability changes could be measured for both seamed and seamless pipes [15, 148, 149]. No literature was found which reports on the localized conductivity changes inside mild steel pipes; however, it might be expected that micro cracks, surface roughness, or small corrosion influence the effective conductivity at the pipe surface.

Finite Element simulations were performed in COMSOL Multiphysics® Modelling Software to evaluate the influence of permeability and conductivity differences on the excitation. Other than the material property changes in the simulation it was identical to the simulations presented in Chapter 3.

The behaviour of the eddy current was simulated for an individual EMAT coil when the conductivity and permeability values were uniform along each material. Localised variations (smaller than the magnet's length) in material property were not investigated, as this deviation would most likely even out due to the larger wavelength. The frequency domain simulation (with fixed input current) in COMSOL Multiphysics® has shown that a 10 % difference in the steel conductivity (5.8824e6 [S/m] instead of 6.4706e6 [S/m]) resulted in 7.23% decrease in the eddy current magnitude, and a 0.56° phase change. The effect of permeability change ($\mu_r = 120$ instead of $\mu_r = 80$) was simulated as well, and it was concluded that the eddy current magnitude increased by 9.74% and its phase has changed by 1.99°.

The electrical conductivity difference of the material has no effect on the magnetic field strength or distribution. However, the effect of permeability change caused on the magnetic field generated by 12 mm cubic magnets is simulated in an another stationary study. The permeability change ($\mu_r = 120$ instead of $\mu_r = 80$) showed that the magnetic field strength changes only by 0.57%. The reason for this marginally small change is most likely due that the magnetic reluctance of the carbon steel pipe is much smaller than the

air for both cases of μ_r.

4.2.2 Transducer lift-off

The lift-off of an EMAT element changes the force excitation. If the lift-off is uneven on the EMAT coils, the generated force will not be uniform around the circumference, and the purity of the generated mode is going to be affected. A few of the various reasons for expecting uneven lift-off on the pipe are: uneven coating thickness, part of the coating is missing, part of the pipe surface is corroded, or the transducer was not installed correctly to the pipe surface.

It is expected, that once a transducer element has different lift-off from the surface, both the magnetic field and the eddy current will change. The magnetic field change does contribute only to changes in the force amplitude. Whereas the coil lift-off changes both the magnitude and the phase of the generated force (as the input impedance of the EMAT is changed).

From the simulation results, the signal amplitude is expected to decrease when the transducer is lifted off. The simulated magnetic field strength decreases by 20 % for 1 mm lift-off. On the other hand, the eddy current amplitude decreases by 5 % for 1 mm lift-off. Therefore, according to simulations the combined effect of 1 mm lift-off will result in 24 % decrease in signal amplitude. Unexpectedly, the experimentally measured signal amplitude values show a completely different trend with lift-off. The signals are shown in Figure 4.1 when all EMAT coils were lifted off with the same value (transmitting transducer only).

The measurements were repeated for different lift-off values from 0 to 1.5 mm. The transmitting transducer was carefully placed back to the same axial position (with the error of 1 mm or less), so that only marginal errors are created when evaluating the phase of the acquired signal (the axial placement error of one wavelength would create 360° phase error). Then, the amplitude values of the recorded wave packet was evaluated from the Hilbert envelope, and are shown in Figure 4.2 for the lift-off values from 0 to 1.5 mm.

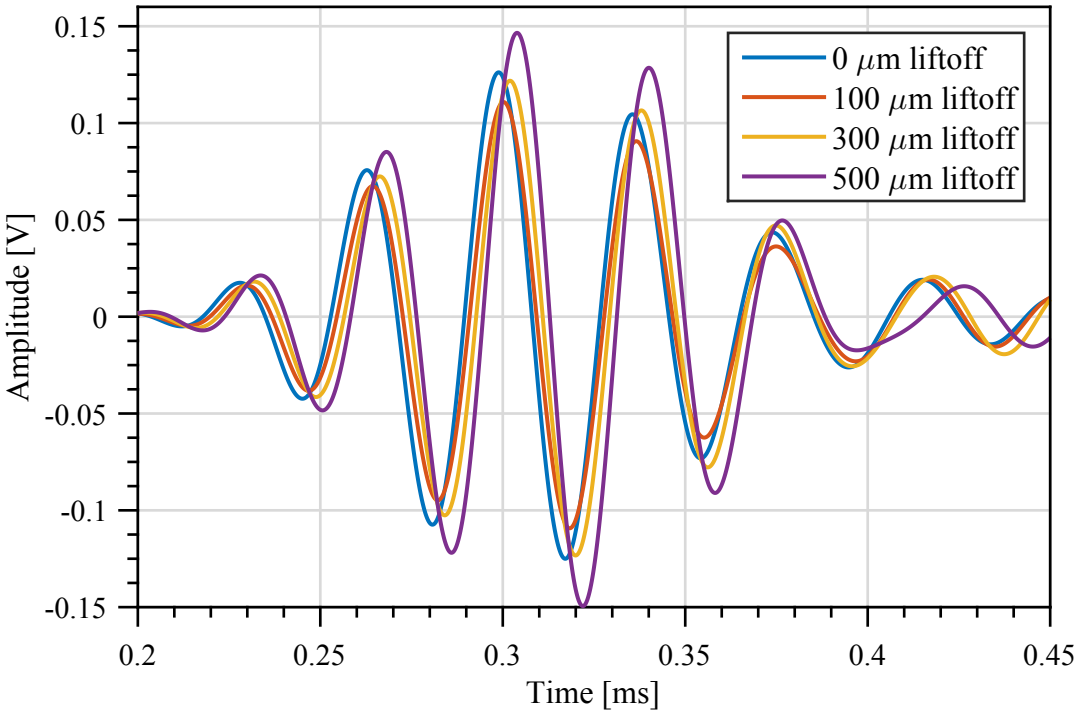

Figure 4.1: First arrival wave packets of acquired ultrasonic signals when the transmitting transducer is repeatedly installed onto the pipe (same axial location) with different uniform lift-off values.

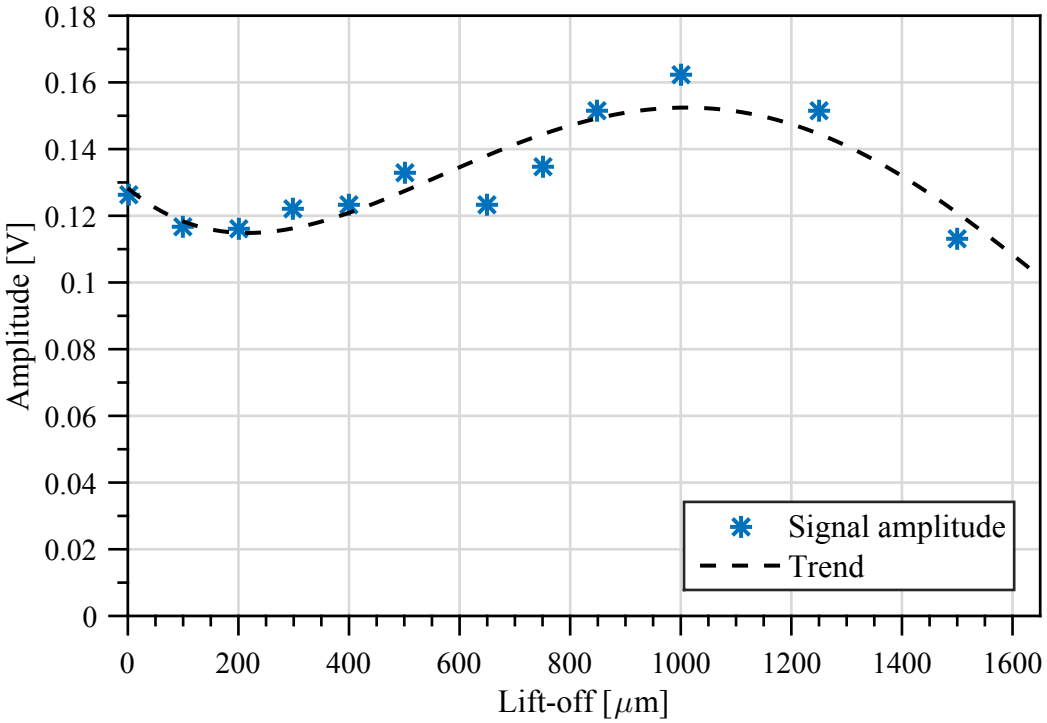

Figure 4.2: Measured ultrasonic signal amplitude of the incident (direct) wave for different lift-off values.

The phase differences between signals can be more easily observed when inspecting the normalized signals (Figure 4.3). The phase of each signal was evaluated, and is shown in Figure 4.4 for each lift-off value. The measurement was repeated several times to reduce variability between measurements.

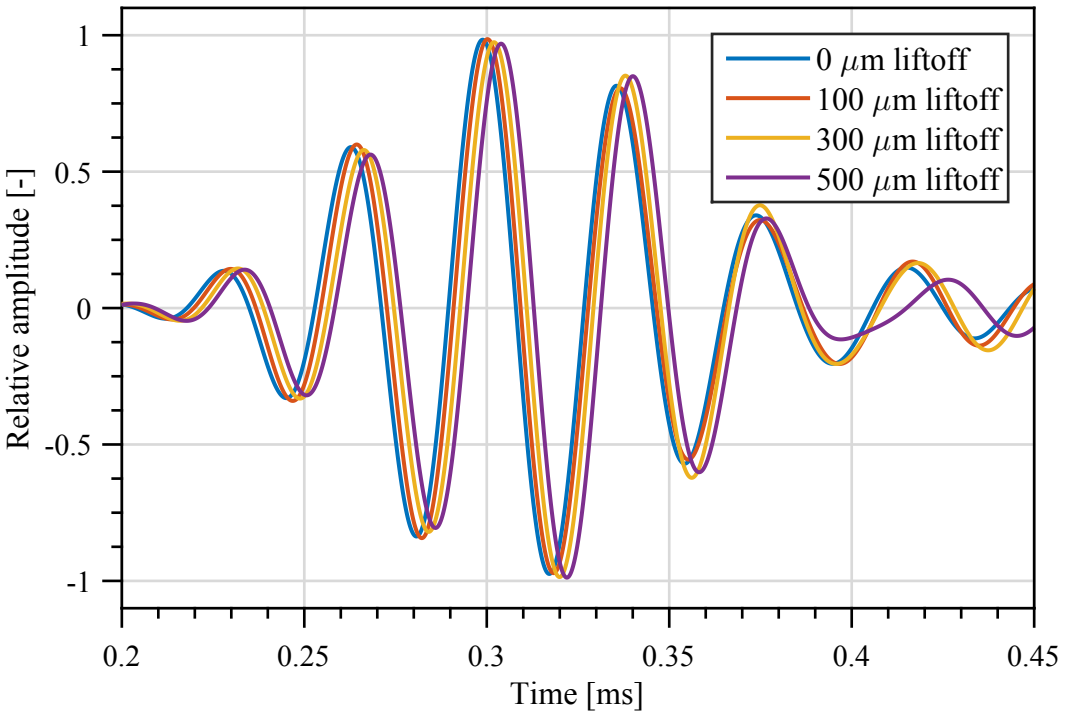

Figure 4.3: First arrival of the acquired ultrasonic signals with different uniform lift-off values. The signals are normalized by their envelope so that the differences in the signal's phase are easier to identify.

The experimental results have shown, that uniform transducer lift-off (0-500μm) can vary the signal amplitude by ~20%, and it's phase by ~50° , therefore an uneven lift-off would generate imperfect excitation on the pipe .

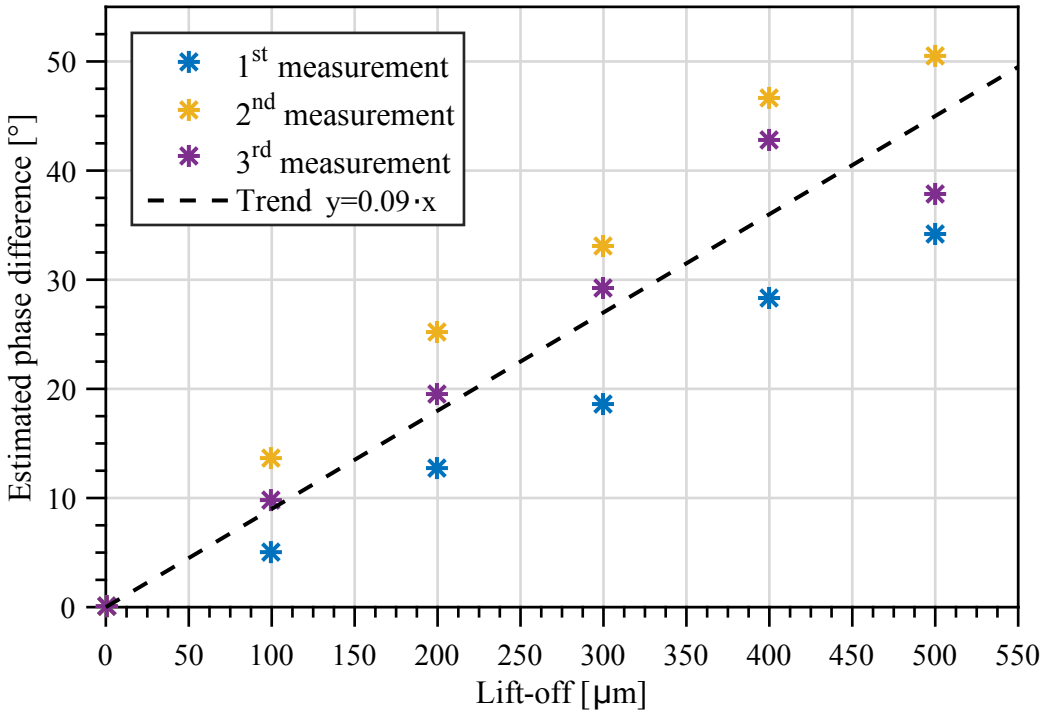

Figure 4.4: Extrapolated phase changes compared to the signals with 0 μm lift-off. The measurement was repeated three times to reduce measurement errors.

4.3 Simulation of error caused by the change in excitation force

The previous section has identified different types of error sources, which can potentially change the excitation force of the EMAT transducer. This section shows FE simulations, which investigate the ultrasonic waves generated by these imperfect excitations. First, the Finite Element simulation details are described, and then the effect of magnitude increase is investigated, which is followed by the excitation phase difference investigations.

4.3.1 FE Simulation details

A Finite Element simulation (similar to the one shown in the previous chapter) was performed in ABAQUS CAE simulating the propagating waves on a 3-inch pipe. 12 excitation patches were placed onto the pipe end. Each excitation patch has 10 mm circumferential, and 5 mm axial extent (the axial extent is half the effective area as only

half the pipe was modelled to save computation time). A 30 kHz tone-burst signal was selected for the excitation, and the default surface traction magnitude of 1000 $\frac{N}{m^2}$.
The displacement was monitored on 122 output points (all nodes of the generated mesh) along the whole circumference 250 mm away from the excitation location as shown in Figure 4.5. Signals long enough to evaluate the coherent noise (slower unwanted modes) were recorded with 5 MHz sampling rate.

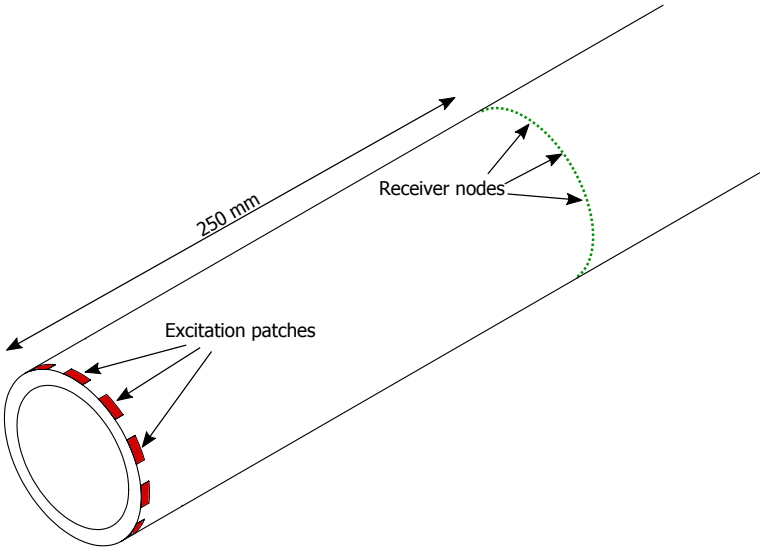

Figure 4.5: Schematics of the ABAQUS FE simulation: the displacement of the excited ultrasonic wave propagating on a 1-meter long NPS pipe is simulated. The force excitation (12 patches of 5mm by 10mm surface area) is generated at the pipe end, and the displacement is monitored on 122 nodes 250 mm away from the excitation.

4.3.2 Simulation of propagating waves when the force magnitude on one coil is increased by 10 %

In the first simulation the displacement signal was simulated when the tangential excitation force was increased by 10 % on two (out of twelve) excitation patches (equivalent of one coil). Figure 4.6a shows the recorded tangential displacement on all 122 monitored output points. Figure 4.6b shows the same displacement in logarithmic scale normalized to the signal amplitude. The direct wave can be observed between 0.09 and 0.24 millisecond, which is followed by the coherent noise until ~0.55 milliseconds. The coherent noise level is evaluated as the maximum tangential displacement of all nodes within this time range. The coherent noise level (shown in Figure 4.6b) was evaluated to be -39.66

dB (1.04%) for this simulation. The pipe end reflection is then seen at the end of the signal from ~0.58 millisecond.

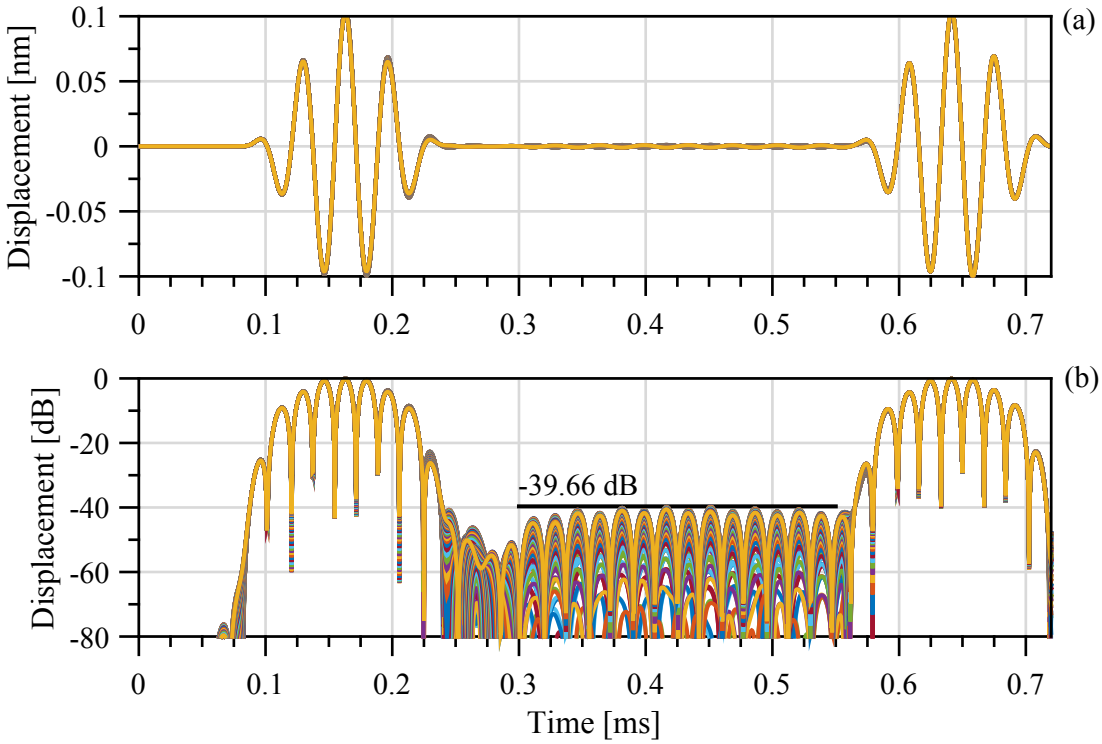

Figure 4.6: Simulated ultrasonic signal displacement in linear scale (a) and logarithmic scale (b) when the excitation amplitude was increased by 10% on two excitation patches (equivalent of one coil).

4.3.3 Simulation of propagating waves when the force magnitude is randomly varied within ± 10%

The effect of randomly changing excitation magnitude was simulated in a repeated ABAQUS simulation. A random force magnitude within ±10% was assigned to each coil (one coil consists of two excitation patches). Table 4.1 shows the randomly assigned excitation magnitudes for each coil and each of the nine simulations. The standard deviation is then calculated and shown in the right-hand column for each simulation.

The simulations were performed, and the coherent noise level was evaluated for each simulation the same way as before (maximum tangential displacement between 0.25 and 0.55 ms). The coherent noise level is shown in Figure 4.7 for each simulation. The mean

Table 4.1: Randomly generated excitation amplitudes (%) used as an input for 9 ABAQUS Finite Element simulations.

Simulation	Coil 1	Coil 2	Coil 3	Coil 4	Coil 5	Coil 6	Standard deviation
1	98	100	110	94	93	106	6.7
2	101	93	99	95	106	97	4.6
3	104	96	95	91	94	101	4.8
4	103	91	99	108	109	98	6.8
5	109	101	107	106	108	98	4.4
6	108	102	99	108	99	106	4.2
7	91	101	107	108	95	98	6.7
8	94	109	106	105	102	107	5.3
9	97	107	93	103	96	108	6.2

coherent noise level was -41.05 dB, with the standard deviation of ±4.99 dB.

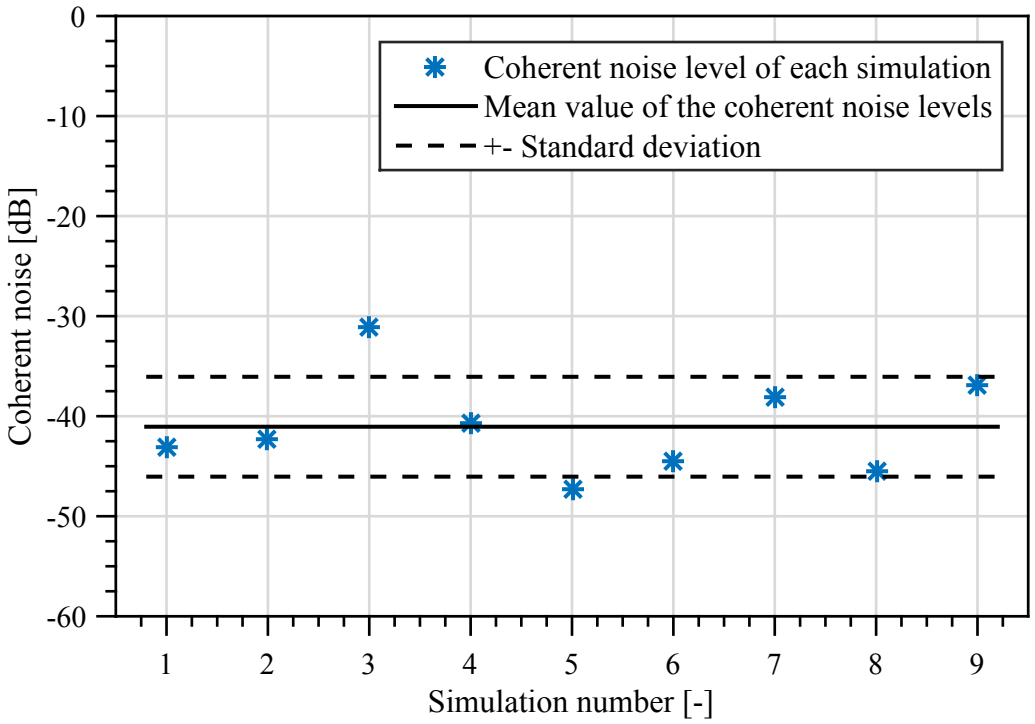

Figure 4.7: Coherent noise level for each FE simulation when the excitation amplitude on each coil is varied by a random percentage between +10% and -10%. The coherent noise level is calculated as the largest displacement of all the nodes after 0.25 millisecond but before 0.55 millisecond.

One might think that the larger deviation from the uniform tangential load the larger the coherent noise is. Surprisingly, the standard deviation of the excitation force (shown in Table 4.1) does not directly relate to the coherent noise level in the simulated time

signal. The amplitude of the generated unwanted mode might be sensitive for different distributions of the force amplitude deviations. For example, a "+ - + - + -" deviation in force amplitude is expected to generate different unwanted mode compared to the "+ + + - - -" deviation, despite having the same standard deviation. This was not further studied in details.

4.3.4 Simulation of propagating waves when the phase of the excitation is different on one coil

Another error found in Subsection 4.2.2 was that the phase of the excitation waveform might be affected by the uneven lift-off or the localized changes in conductivity and permeability. In the first instance, the effect was simulated, when the phase of the excitation waveform is changed on one coil only (two excitation patches). The simulated phase change was set to 0° (reference signal), 20°, and 40°. The recorded tangential displacement is shown in Figure 4.8 in linear scale, whereas Figure 4.9 shows the same displacement in decibel scale. Plot (a) shows the reference simulation when the excitation was the same on all patches; plot (b) show the result for the 20° phase change, and plot (c) shows the result for 40° phase change simulation.

The coherent noise levels were evaluated the same way as before (maximum tangential displacement between 0.25 and 0.55 milliseconds). The 20° phase change resulted in the unwanted coherent noise level of -28.94 dB, whereas the 40° excitation phase change (on one coil) resulted in the unwanted coherent noise amplitude of -22.98 dB. It can be observed, that the phase change has resulted in a quite significant coherent noise level. This is due if the excitation phase changes, the difference between the excited and reference signal will be very large. For example, the difference between a reference tone-burst signal and a second tone-burst with 30° phase change will be ~52% in amplitude (compared to the reference signal).

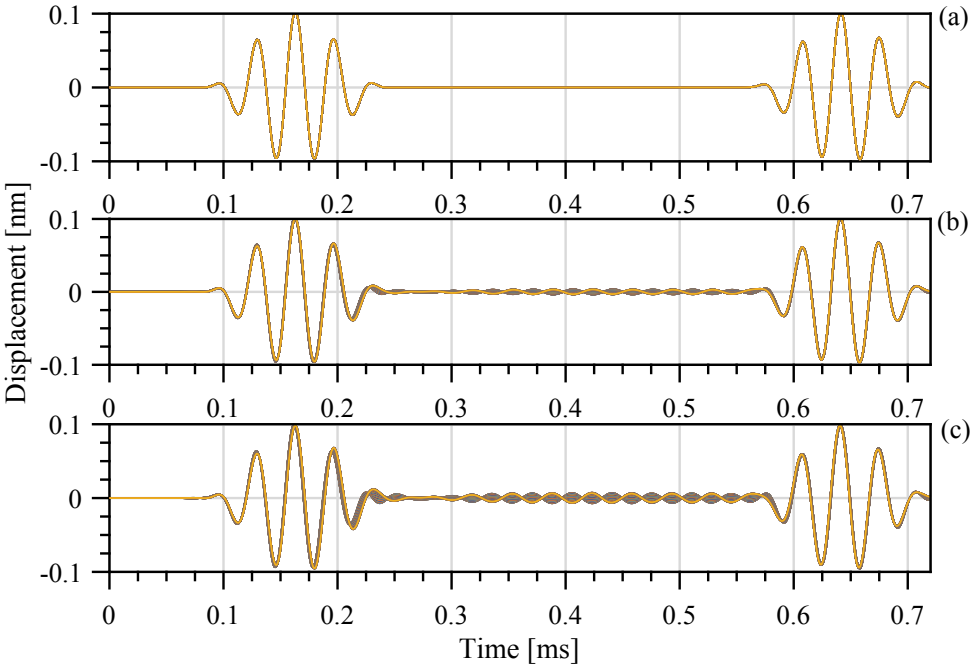

Figure 4.8: Simulated ultrasonic torsional wave displacements when one of the EMAT coils generate the excitation signal with 0 (a), 20° (b) and 40° (c) phase difference. The displacement is monitored 250 mm from the excitation location.

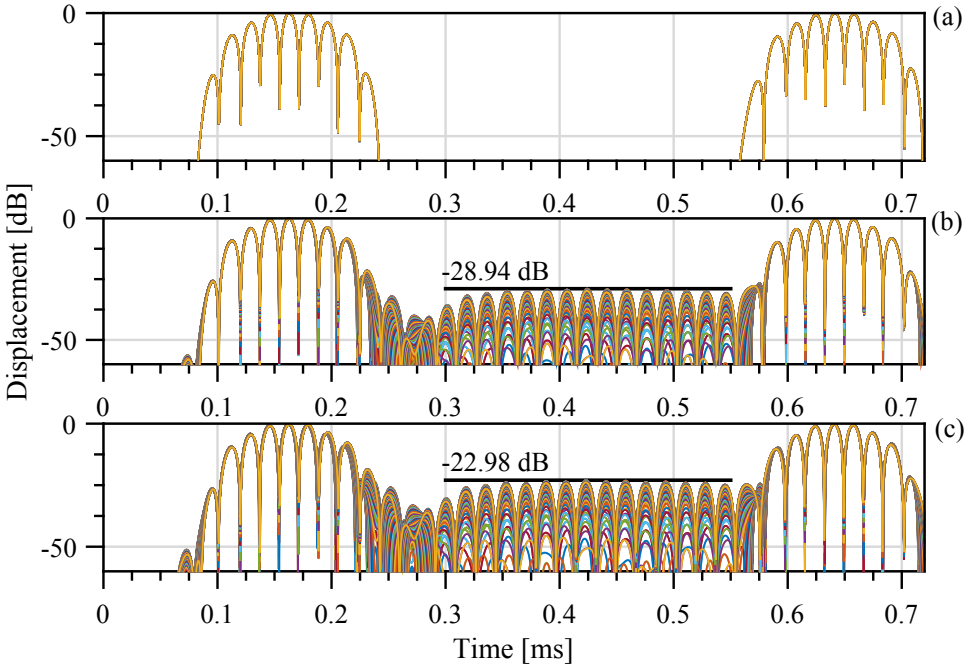

Figure 4.9: Simulated ultrasonic torsional wave in logarithmic scale (normalized to the signal amplitude) when one of the EMAT coils generate the excitation signal with 0 (a), 20 (b) and 40 (c) phase difference.

4.3.5 Simulation of propagating waves when the phase of the excitation signal is randomly varied within 0°-40°.

The effect of randomly varying excitation phase changes was simulated as well. A random phase value (between 0° and 40°) was assigned for the excitation of each coil for each simulation. The assigned phase values are shown in Table 4.2, the standard deviation of the input values are shown in the right-end column.

Table 4.2: Randomly assigned excitation phases in degrees used as an input for 5 Finite Element simulations.

Simulation	Coil 1	Coil 2	Coil 3	Coil 4	Coil 5	Coil 6	Standard deviation
1	0°	16°	8°	32°	16°	40°	14.90°
2	8°	40°	0°	32°	32°	32°	16.00°
3	16°	24°	8°	24°	8°	24°	7.87°
4	8°	8°	16°	0°	40°	40°	17.28°
5	16°	16°	40°	16°	8°	32°	12.04°

The evaluated coherent noise level for each simulation is shown in Figure 4.10. This time, correlation can be observed between the standard deviation of the excitation phase values and the resulted coherent noise values. The lowest coherent noise was simulated for the simulation that had the lowest deviation in the excitation phases. In addition, simulation 4 had the highest standard deviation in the excitation phases, and resulted in the largest coherent noise level.

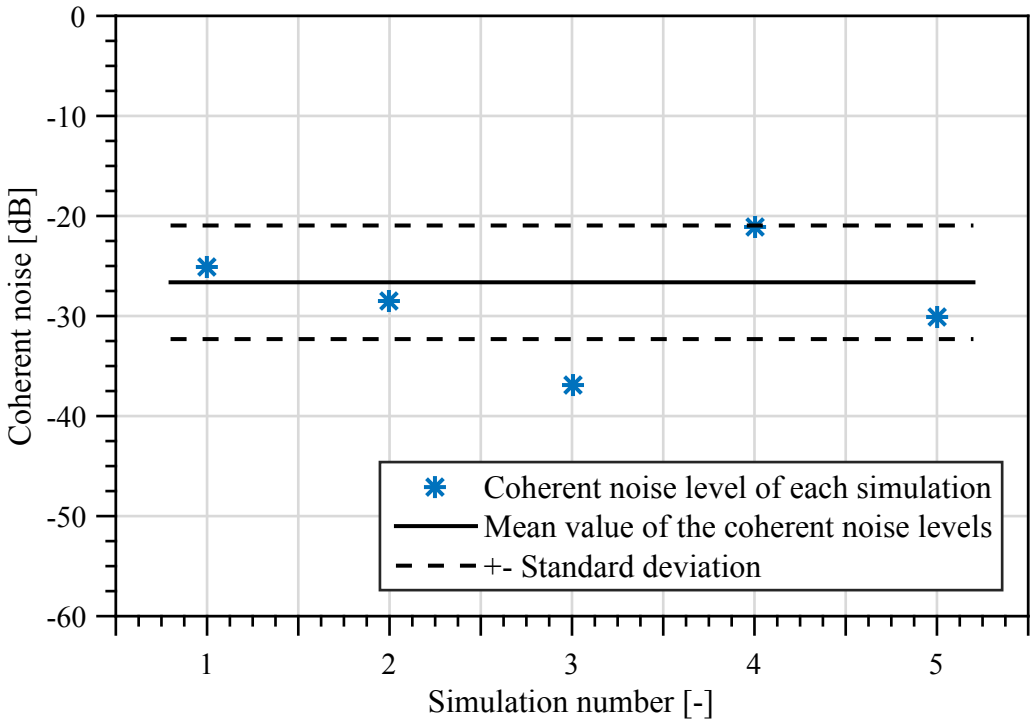

Figure 4.10: Coherent noise level for each FE simulation when the phase of the excitation on all coils are varied by a random phase between 0° and 40°. The coherent noise level is calculated as the largest displacement of all the nodes after 2.5 milliseconds.

4.4 Investigation of imperfect excitation due to imperfect installation of the transducer

4.4.1 Transducer is misaligned on the pipe

Any error in the mechanical installation of the transducer will change the location of each excitation patch. This will most likely influence the generated ultrasonic wave in the pipe. A possible error source is that the transducer is placed onto the pipe in such a manner that the axial position of each element is inconsistent. Two types of axial placement error is investigated, from which the first type of misalignment is named as “Tilted” and is shown in Figure 4.11a. The other type of error source is the “Spiral” misplacement shown in Figure 4.11b. The ideal excitation location is shown with dashed lines.

The force amplitude was set to be uniform surface traction on the selected (shown in grey in Figure 4.11a) surface areas. This way, a general guided wave propagation problem is

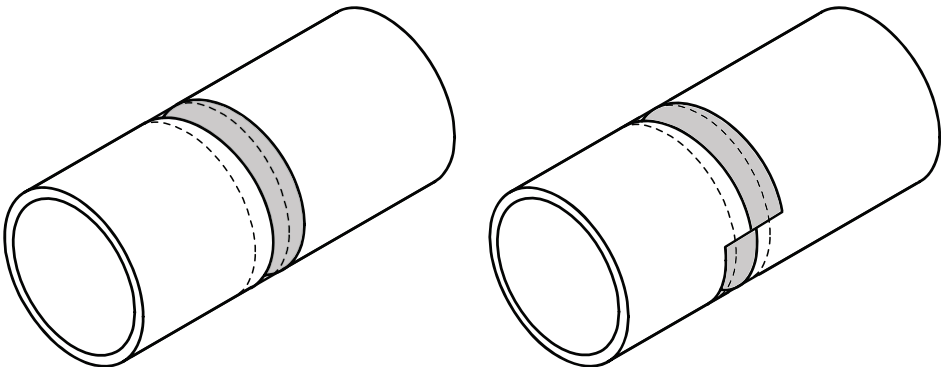

Figure 4.11: Schematics of the investigated imperfect excitation named as "Tilted" (a) and "Spiral" (b) is shown in grey colour. The original (ideal) excitation surfaces are shown with dashed lines.

simulated, rather than a specific problem of the EMAT. The ABAQUS model was adapted and adjusted so that the excitation is performed on the modified area. The model was re-meshed to adapt the mesh to the geometry changes in the excitation area. The pipe length was increased to 3 meters, because modelling half the pipe is not feasible as the symmetry is broken. Then, the axial location of the excitation was set to be in the middle of the pipe. The tangential displacement was again simulated and recorded at 250 mm away from the excitation location. 122 displacement signals (recorded at all nodes) are shown in Figure 4.12 and in Figure 4.13 for the 4° "Tilted" and "Spiral" misplacement respectively.

A few values of axial error between 1° and 10° is simulated for the "Tilted" case. The "Spiral" misplacement is simulated only for 2° and 4° error, as generating the mesh for other values was not successful.

The coherent noise level is evaluated for all simulations, and their level are displayed in the time signals. The coherent noise levels are also displayed in Figure 4.14 in function of the misplacement angle.

As expected, the coherent noise is increasing with increasing misplacement angle. Another important observation is that the 2° "Spiral" misplacement already generates coherent noise in excess of the -40 dB target level. It is therefore suggested that the axial misplacement is checked upon installation and the transducer is reinstalled if the misplacement exceeds 2° (equivalent of 9.75 mm axial error on the simulated pipe). It must

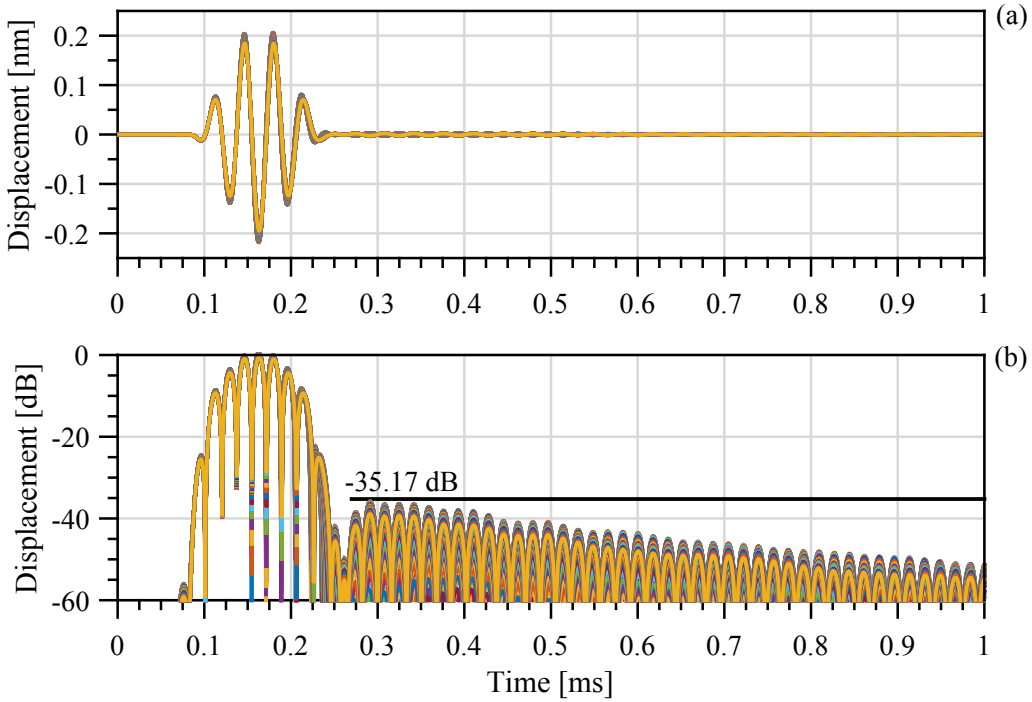

Figure 4.12: Simulated ultrasonic wave displacement resulted by exciting the wave on the imperfect excitation called "Tilted". The tilt angle for the simulation was 4°.

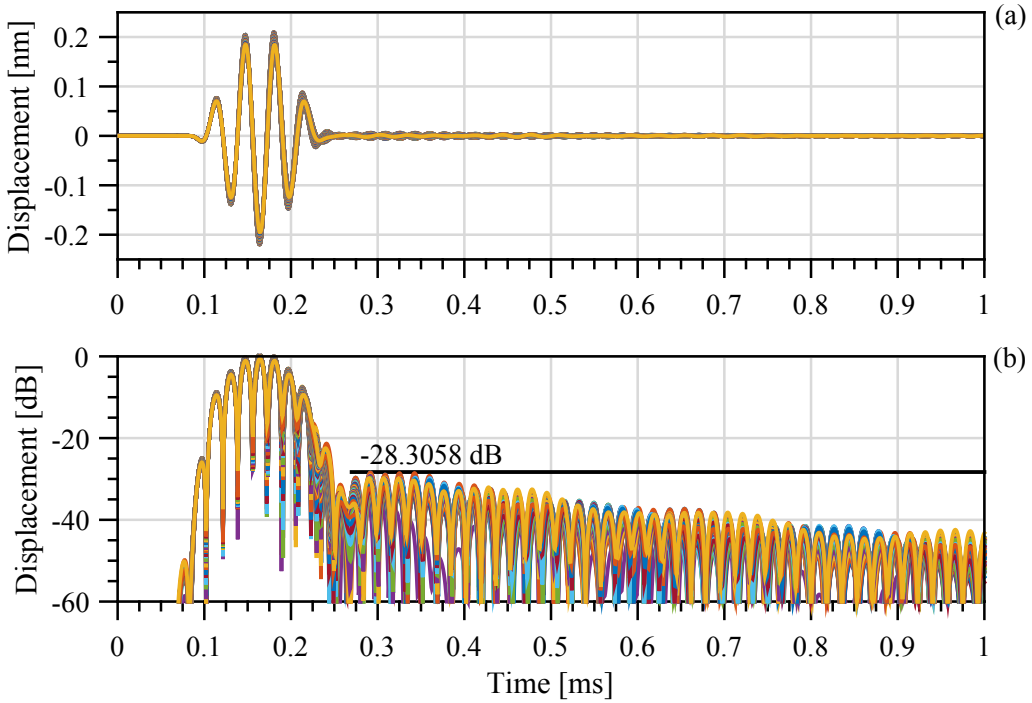

Figure 4.13: Simulated ultrasonic wave displacement resulted by exciting the wave on the imperfect excitation called "Spiral". The angle of the spiral excitation compared to the original was 4°.

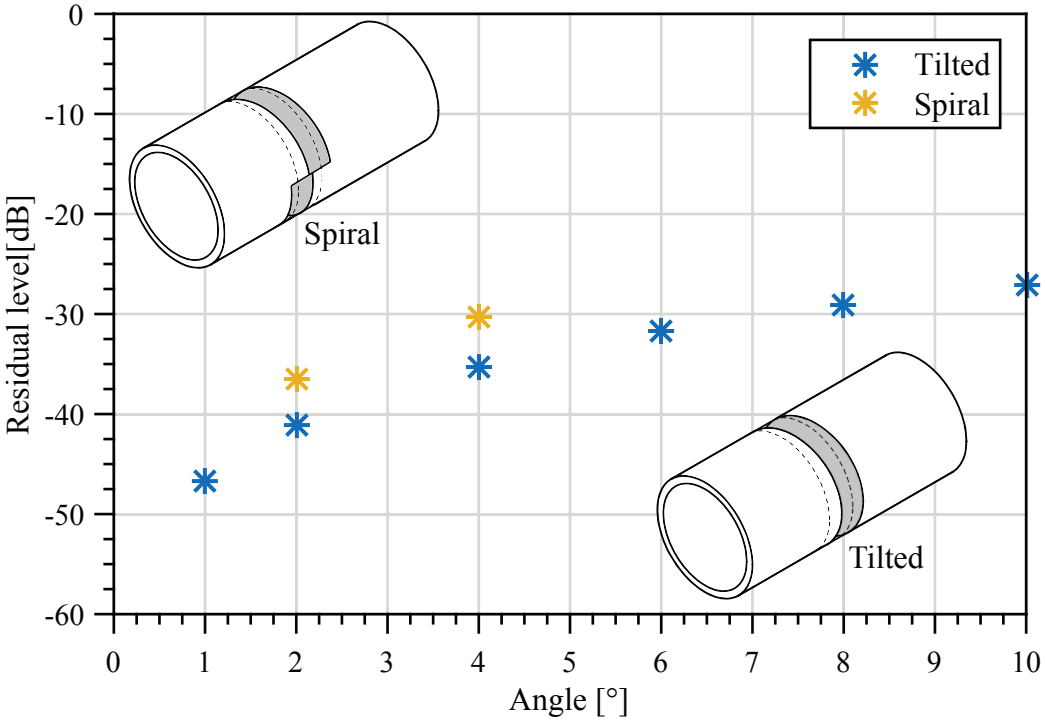

Figure 4.14: Evaluated coherent noise levels when the excitation patches are altered by different angles. The coherent noise level is calculated as the largest displacement of all the nodes after 0.25 milliseconds.

be noted, that the axial difference between the forward-most and backward-most part of the excitation area is double for the "Spiral" misalignment compared to the "Tilted" misalignment. This could be a reason for seeing larger coherent noise levels for the "Spiral misalignment".

4.4.2 Transducer and pipe diameter mismatch

Due to the inconsistency of the manufacturing process and suppliers, it can be expected that the pipe diameter can vary between pipes. According to standards (e.g. ASTM A530/A530M, DIN 2391) deviation in pipe diameter around 0.8 mm is allowed. Coating with various thicknesses might be applied to pipes, resulting in an even larger variations in the pipe circumference. In addition, the transducer array could potentially be manufactured with a slight dimension error. The results is that the transducer does not cover the whole circumference of the pipe, and a small circumferential gap is present where the tangential surface force is not excited. Figure 4.15 shows the schematics of such an

imperfection.

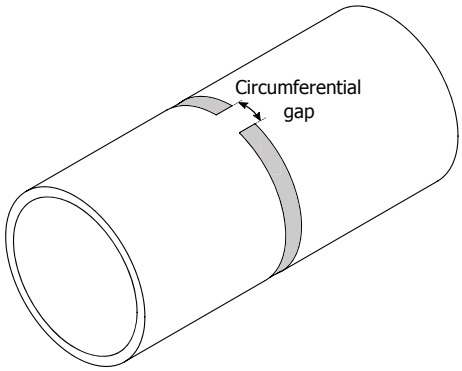

Figure 4.15: Schematics of the investigated imperfect excitation when the wave is not excited on a small circumferential location.

An ABAQUS simulation was performed where the tangential force was excited on the incomplete circumferential area. The generated coherent noise is evaluated the same way as in the previous simulations. The coherent noise level is displayed in Figure 4.16, also showing the trend with dashed line.

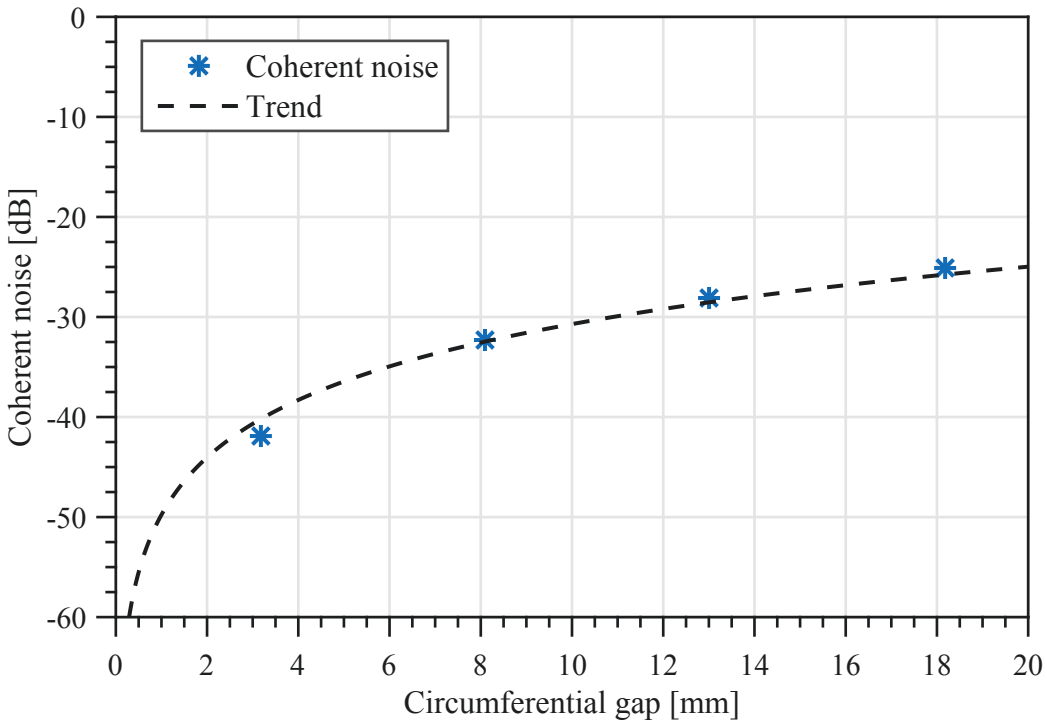

Figure 4.16: Evaluated coherent noise in the measurements for different circumferential gaps. The coherent noise level is calculated as the largest simulated displacement of all the nodes after 2.5 milliseconds.

The target 40 dB coherent noise suppression is sustained when the circumferential gap is kept below ~3 mm. The manufacturing tolerance of the steel pipes is below 1 mm *[150]*, and manufacturing a transducer with this precision is feasible.

4.5 Experimental validation

The simulated coherent noise results were validated with measurements. It was chosen to experimentally measure the result of non-uniform lift-off, and the result of spiral transducer misalignment on the acquired signals.

In the first instance, the non-uniform lift-off was measured. A transmitting transducer was placed onto the a 5 meter long pipe ~1 meter away from the receiving transducer, and these transducers were placed axially in the middle of the pipe so that the pipe end reflections don't mask the coherent noise. A reference signal was recorded, which is acquired when all coils of the transmitting transducer was placed with no lift-off. After acquiring the reference signal, plastic sheets were placed underneath one coil so that a lift-off of 0.5 and 1.5 millimetres were generated on the transmitting transducer. The rest of the transmitting transducer and the whole receiving transducer was not disturbed whilst the plastic sheet was installed. The recorded time signals are shown in Figure 4.17.

The 1 mm lift-off generates a coherent noise level of -28.2 dB, whereas the 0.5 mm generates -35.7 dB. The reference signal acquired with uniform lift-off had -39.1 dB coherent noise relative to the torsional wave amplitude. As the receiver transducer and 5 out of 6 coils were not repositioned, the coherent noise is thought to be entirely due to the change in lift-off on the specific coil.

The coherent noise generated by the "Spiral" misplacement error is also measured. The transmitting transducer is placed onto the pipe with a spiral misplacement, and ultrasonic signal was recorded. The acquired signal is shown in Figure 4.18. The coherent noise was evaluated to be -37.3 dB for the 2°, and -33.9 dB for the 4° misalignment. The simulated and experimentally measured coherent noise levels are compared in Table 4.3.

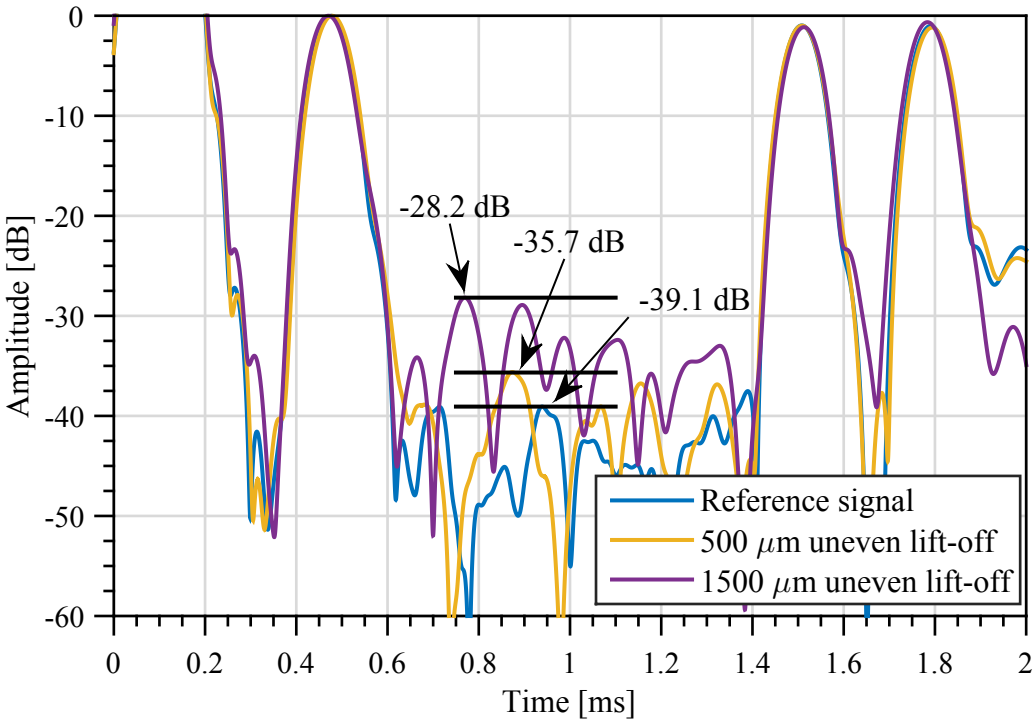

Figure 4.17: Acquired ultrasonic signals when the lift-off was changed on one of the 6 coils on the transmitting transducer.

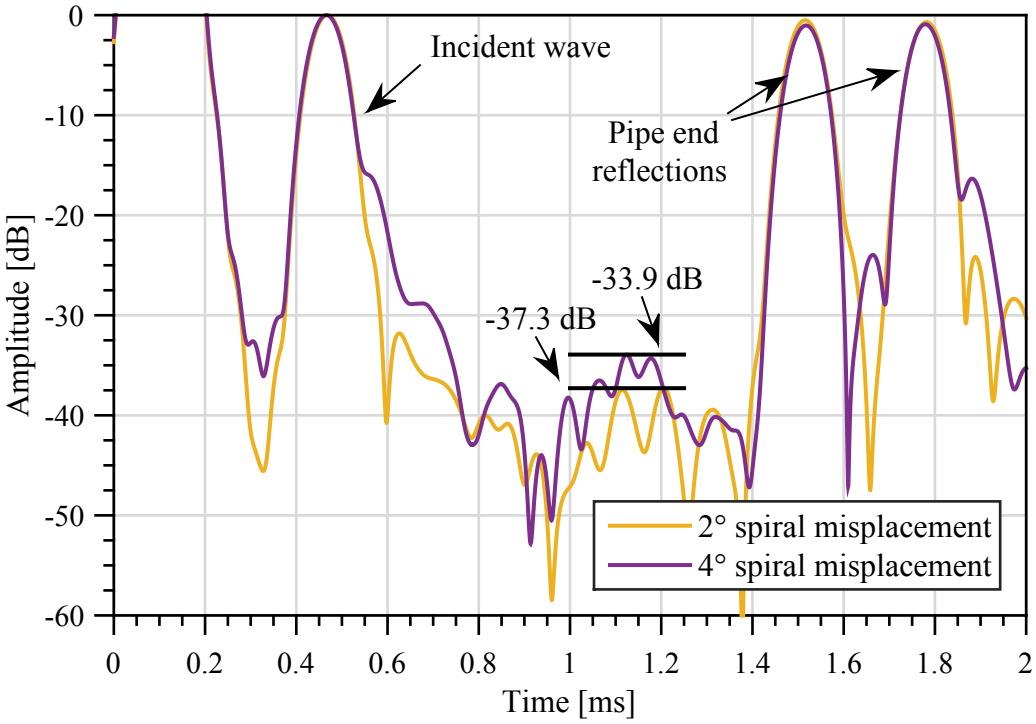

Figure 4.18: Acquired ultrasonic signals when the transducer is incorrectly installed onto the pipe in a "Spiral" shape. The Spiral misplacement is shown in Figure 4.11b.

Table 4.3: Comparison of simulated and experimentally measured coherent noise level.

Error Source		Simulation	Experimental
Uneven Lift-off	$250\mu m$	-28.94 dB	-
Uneven Lift-off	$500\mu m$	-22.98 dB	-35.7 dB
Spiral misplacement	2°	-36.49	-37.3 dB
Spiral misplacement	4°	-30.28	-33.9 dB

4.6 Discussion

When comparing the experimental results with the simulated signals it can be observed that significantly lower coherent noise was measured for the uneven lift-off case. This difference is most likely caused by the different evaluation of the coherent noise. In the simulated data, the maximum tangential displacement on any monitored output node was recorded as the coherent noise level. On the other hand, the receiving transducer receives the guided wave signal on 12 locations around the circumference, and the received ultrasonic waveform is constructed as the average of these displacements. Therefore, the experimentally measured coherent noise level is lower than the coherent noise on the individual node.

The effect of the guided wave reception is simulated. 12 evenly distributed nodes were selected (out of the 122 mesh nodes) to mimic the averaging of the receiver transducer, and the respective simulated displacement signals were averaged (the result of the 4-degree "Spiral" simulation was used). Figure 4.19 shows the displacements on 12 nodes (a) and the averaged output signal (b).

The coherent noise acquired on the receiving transducer however, is only a bit better than the simulated coherent noise.

Imperfect positioning or uneven lift-off on the receiving transducer can also influence the acquired signal. If for example the lift-off is uneven on the receiver transducer as well, the coherent noise level does not necessarily increase significantly. This effect could potentially be simulated if amplitude and phase changes are simulated for the receiver transducer nodes as well. Therefore, further work needs to be done to further increase the understanding of the mode purity of the excited signals. Nevertheless, the above presented simulation results can still be interpreted as a guide for a safety limits in the

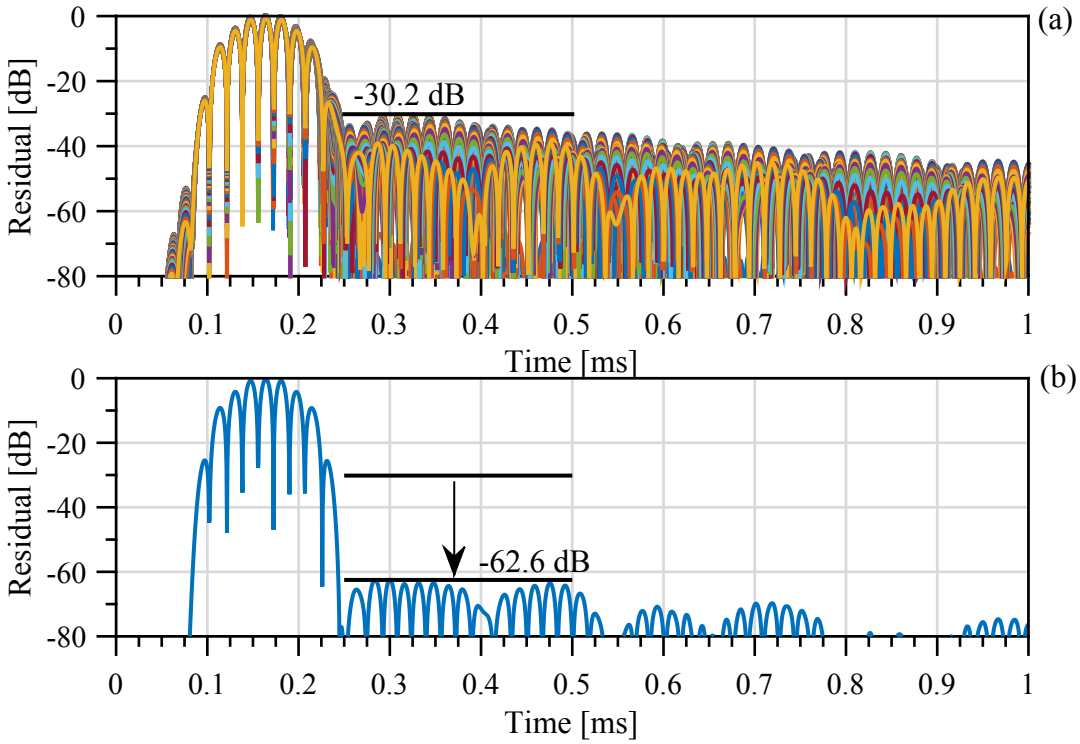

Figure 4.19: Recorded tangential displacement waveform on 122 receiving nodes in dB scale for the 4° "Spiral" simulation (a), and a signal calculated as the mean of 12 receiving nodes (b).

misalignment and material property changes.

One might ask which imperfections poses the biggest risk for the transducer performance. It is easy to check the mechanical installation errors (Spiral misalignment, circumferential gap) after installation. Furthermore, the transducer can be reinstalled if the alignment is not satisfactory. In addition, the transducer might be designed to be slightly stretchable to reduce circumferential gaps. However, the amplitude and phase consistency of the transducers in the array is much harder to check. Measuring (and controlling) the exact coil lift-off, magnet strength, coating thickness is impractical. There is an option to compensate for deviations in excitation strength, if each coil in the EMAT is addressed individually (this is a general practise for other guided wave transducers). This can be an advantageous solution if the transducer is expected to be deployed to pipes where the exact conditions (pipe surface, coating) are not known. Unfortunately, this solution increases complexity of the transducer.

4.7 Summary

This chapter investigated how uneven transducer lift-off, imperfections in mechanical installation, or localized changes in material properties influence the acquired ultrasonic signal. First, the possible error sources were listed which can influence the wave excitation mechanism. Then, Finite Element simulations were performed to simulate the resulting displacement at 122 receiving nodes after the propagation of 250 mm. It was investigated how the force magnitude or excitation signal's phase on individual elements affects the mode purity. First, a 10% increase was simulated on one of the excitation locations, which resulted in a -39.66 dB coherent noise. It was then investigated how a randomly changing (within ±10%) force magnitude generates imperfect wave displacement. The results showed that the average coherent noise of -41.05 dB (with ~5 dB variation) should be expected. Then, further simulations were performed to investigate the mode purity when the excitation phase changes (20° and 40° on one location, then randomly). The resulted coherent noise was -28.94 dB and -22.98 dB for the 20° and 40° change respectively, whereas the simulation for the random phase change resulted in the average coherent noise of -26.63 dB. It was therefore concluded, that the system is sensitive for phase variations in the transducer.

Then, the effect of the transducer's mechanical installation errors was investigated. The scenarios were investigated when the transducer is installed in a spiral path around the circumference (see Figure 4.11) and a transducer installed with a circumferential gap (see Figure 4.15). It was concluded that 2° Tilt (4.87 mm axial deviation) generates -41 dB coherent noise. Alternatively, it was simulated that a 3 mm circumferential gap in the excitation area generates the coherent noise of -42 dB, therefore the circumferential gap should not exceed 3 mm.

The simulated coherent noise level was then compared with experimentally acquired signals, and the results were discussed.

This page intentionally left blank

Chapter 5

High temperature operation

5.1 Introduction

For industrial applications, it is advantageous to increase the operating temperature range of ultrasonic transducers. This chapter investigates the motivation for high-temperature ultrasonic transducers and then explains the design modifications that were made to the transducer prototype so that the operating temperature range is increased above 200°C. Then, it is detailed how the heating of the transducer and the structure is performed, and signals are presented which were acquired in a high temperature environment.

5.2 Motivation

Industrial pipeworks operate at many different temperatures. Often, due to the particular chemical process that is being carried out, such as the processing of crude oils, the pipe is deliberately heated and operated at a particular temperature. In addition, in transmission pipelines the carried liquid is sometimes heated for better transportation [151–153].

Therefore, in order to be able to perform guided wave measurements in these environments, it is desired to develop equipment that can operate at elevated temperatures. Although most conventional inspections are carried out at plant downtime (resulting in usually ambient temperature conditions), some transducers have been designed for high temperature (400°C) applications [43]. Nonetheless, even for most of these instruments,

limited time is allowed to do the measurements before the transducer is overheated.

Since high temperature pipes are usually insulated and require removal and reinstallation of insulation material before and after inspection, it is even more desired to deploy permanently installed transducers for high temperature operation. These transducers must operate (or at least survive) high temperature exposures so that the highest temperature does not destroy or degrade the transducer. With increased operating temperature range, the monitoring system can be deployed to an increased number of locations in a plant.

Piezoelectric crystals are available with various Curie temperatures (temperature where the crystal loses the piezoelectric properties). High-temperature crystals are reported with Curie temperature above 500°C [69, 154]. For most transducers, it is not the piezoelectric crystal, but the bonding that fails first. Although high-temperature bonding adhesives are available, common bonding materials such as epoxy are not suitable for high temperature [154]. Sometimes, this problem is overcome by dry-coupled waveguides, which separate the bonding of the piezo element from the hot specimen [155, 156]. Nevertheless, the piezoelectric crystal needs to be bonded to the waveguide. For guided wave transducers this means that insulation might not be applied over the transducer so that the natural cooling is sufficient. It was reported, that high temperature inspections can be performed with dry-coupled transducers, but the duration is strictly limited to prevent transducer overheating [43].

On the other hand, bulk wave Electromagnetic Acoustic Transducers have previously been designed for temperatures up-to 450°C without active cooling [157]. Other researchers have presented water-cooled transducers, and reported on the temperature range up-to 500°C [158].

Guided wave transducers usually excite the ultrasonic field on a larger surface area close to the heated pipe, therefore the potential to cool them by natural cooling is much lower. Hence, the maximum operating temperature of permanently attached guided wave transducers is usually lower. In addition, in case of bonding is required for the guided wave transducers the maximum operational temperature range can be limited, for example, a few commercial products are limited to temperatures up-to 90°C [30]. Nevertheless, dry coupled guided wave transducers were reported which can survive if the structure is heated to 200°C [74].In this thesis, the motivation is to develop a torsional guided wave EMAT

that can operate at moderate-high temperatures (~200-250°C). Above this temperature range, the manufacturing complexity is expected to drastically increase (soldering, coil manufacturing, etc.), therefore testing above 250°C was not considered.

5.3 Design modifications

For EMATs, the key to enabling high temperature operations is material selection. As the excitation mechanism (electromagnetic induction and Lorentz force) is not limited by the temperature, the main motivation is then to select components, which can operate and withstand high temperatures.

Often, the permanent magnet is the limiting factor of the EMAT operation. Neodymium Iron Boron (NdFeB) magnets are often chosen for EMAT applications as they generate high magnetic fields. Their Curie temperature (above this temperature the magnet loses its strength) and coercivity is highly dependent on the alloy type used during manufacturing [159,160]. High temperature NdFeB are available with maximum rated temperatures of ~200°C [75]. For even higher temperatures other rare earth magnets have better performance. Samarium-Cobalt (SmCo) provides one of the best performances at higher temperatures of ~300-350°C [161,162]. It was reported, that special SmCo magnets could also be manufactured for the maximum temperature range of 550°C [163].

Multi-turn coils generate the time-varying component of the magnetic field, which induces the eddy current in the structure. It is usually not the coil conductor (copper) itself that fails first, but the insulator which separates the coil wiring of each turn or from the rest of the structure. The coils of the constructed EMAT are printed onto a flexible kapton-polymide Printed Circuit Board (PCB) which is highly resistant to mechanical forces, and can operate at elevated temperatures up-to 200°C (according to the manufacturer application instruction).

Other parts of the EMAT prototype function as structural items, which fix and hold the EMAT in place. A few of these items were originally made of polymer parts, which were substituted for alternative components: The transducer was equipped with custom-made aluminium ribs that are responsible for the transducer's longitudinal rigidity. Stainless Steel screws and nuts were selected to fasten the aluminium ribs to the flexible PCB. This

assembly of the PCB, magnets and metal ribs is then encapsulated in a flexible silicone compound (Dragon Skin® 30, Smooth-On, Inc. [164]), so that the components are held together but can also be arranged to conform to the pipe surface. This silicone compound is rated for temperatures up-to 232°C. Other compounds with similar properties can be selected for even higher temperature ranges. Additionally, a high-temperature soldering compound was selected for connecting the coils to the cabling.

Figure 5.1 shows a drawing of a section of the high-temperature transducer ring assembly designed for a 3-inch NPS pipe.

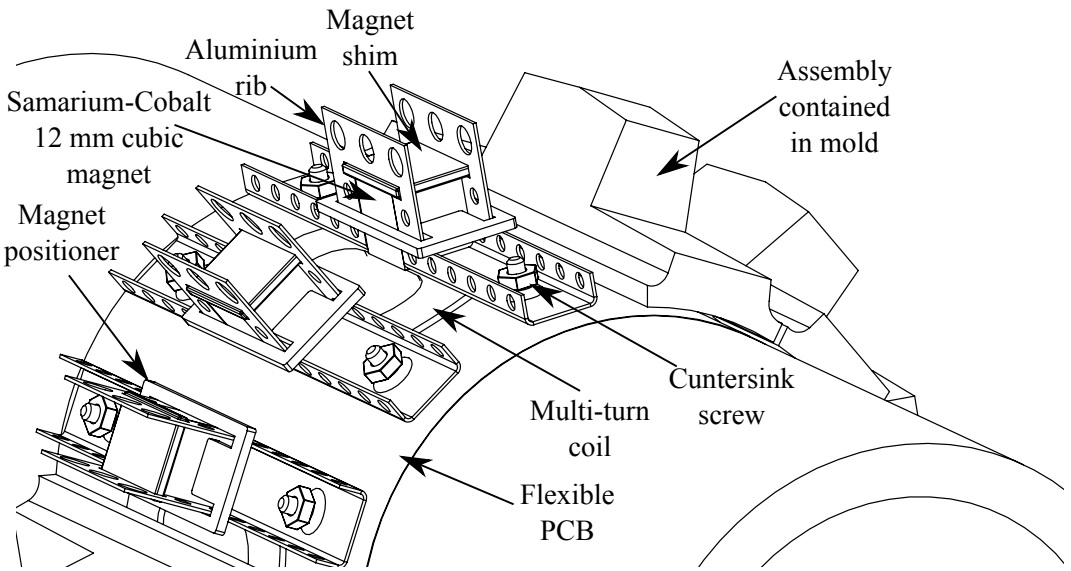

Figure 5.1: Computer drawing of the high-temperature EMAT prototype.

5.4 Experimental validation

5.4.1 Heating test

A 5-meter long 2 kW finned electric heater (custom-made heater, Clarian UK Ltd.) element was placed inside the pipe so that signals can be acquired at an arbitrary pipe temperature. A thermocouple was attached to the heater element to monitor the heating temperature. This thermocouple was also used to provide input for the heating controller. Additional thermocouples were installed onto the outer surface of the pipe. The whole pipe was surrounded with insulation, in order to reach a uniform temperature distribu-

tion within the pipe. The drawing of the pipe fitted with the electrical heating element, insulation and the thermocouples is shown in Figure 5.2. A CAD drawing and a picture of the transducer on the pipe with the insulation are shown in Figure 5.3.

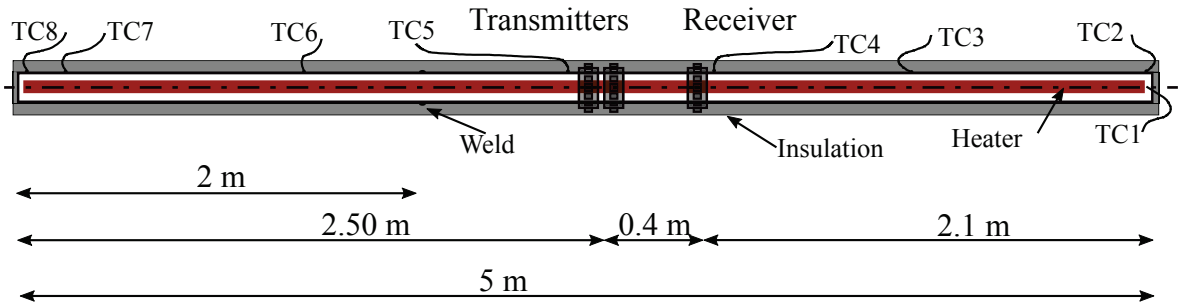

Figure 5.2: Measurement setup for acquiring signals with arbitrary pipe temperature. Finned heater element (red) is used for heating, while the pipe outer surface is well-insulated (grey) from the environment.

The temperature of the pipe was controlled by a custom-built temperature controller setup. An On/Off Temperature controller was used to control the heating power. This controller uses the temperature reading of the thermocouple placed inside of the pipe (near the heating element), and then controls a solid-state relay to switch the high power input connected to the heater element.

In practice, when the pipe heating is started the heating element first heats up to the desired temperature, and then the controller repeatedly switches on and off to maintain the temperature. As the inside of the pipe is heated up, the heat slowly diffuses into the pipe. After reaching a steady temperature, and a uniform temperature distribution, the heating was cut-off, and the pipe was left to cool down naturally.

5.4.2 Experimental results

Figure 5.4 shows temperature recordings of the eight thermocouples for a typical high temperature heating cycle. The maximum temperature of the heating element was reached at ~2.5 hours, from then on the power controller was switching the power on and off repeatedly to prevent overheating. The heating was then turned off at ~4 hours, and the pipe was left to cool down naturally. The cooling process is long, with the time constant of the cooling being around 4 hours. As acquiring signals with 50 averages takes less than 30 seconds, the changes in the pipe temperature while acquiring a signal are small. The signal

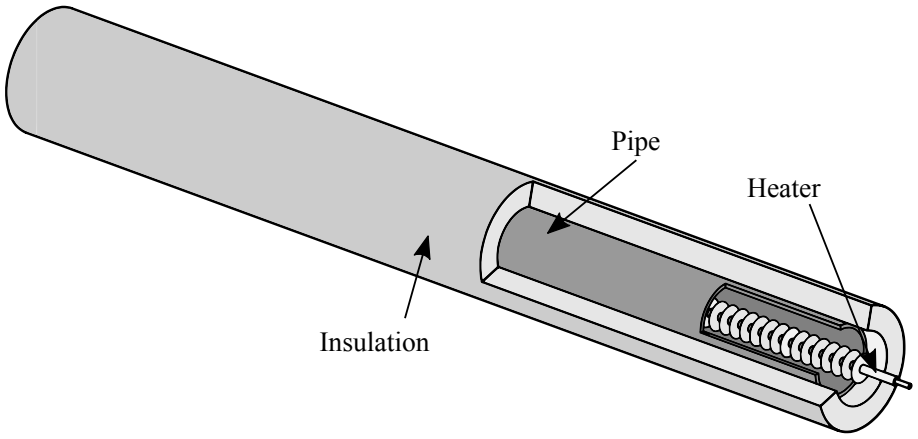

(a)

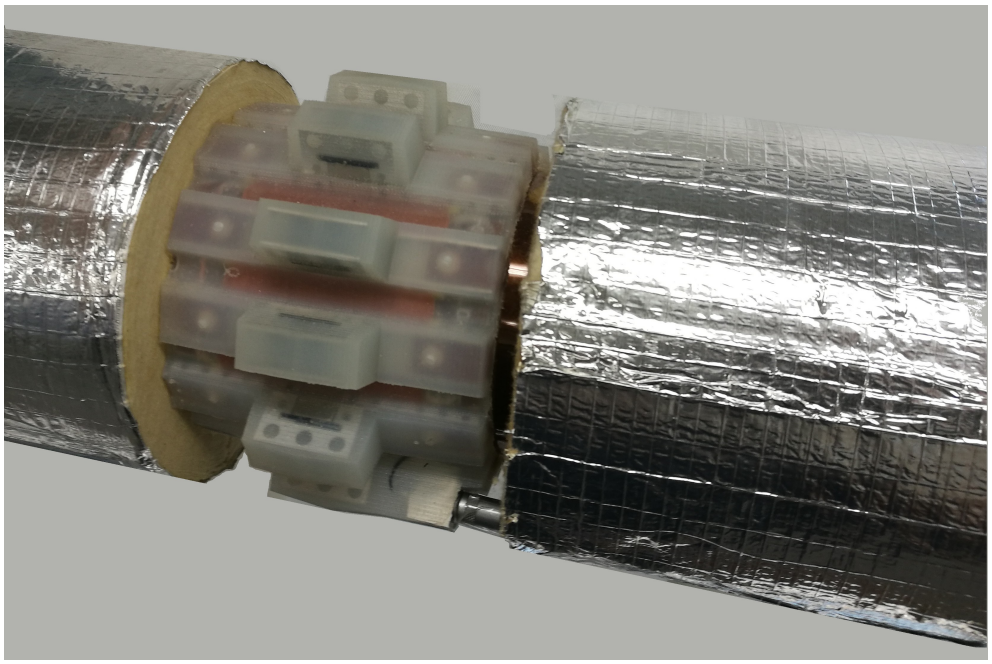

(b)

Figure 5.3: Laboratory setup for heating tests: a) schematic of the arrangement of pipe, insulation and heater that was used in experiments and b) photograph of a transducer on the pipe in between insulation.

acquisition system was set so that a signal is collected at roughly every degree Celsius during cooling off. After reaching a temperature close to room temperature, signals are acquired every 2-3 hours.

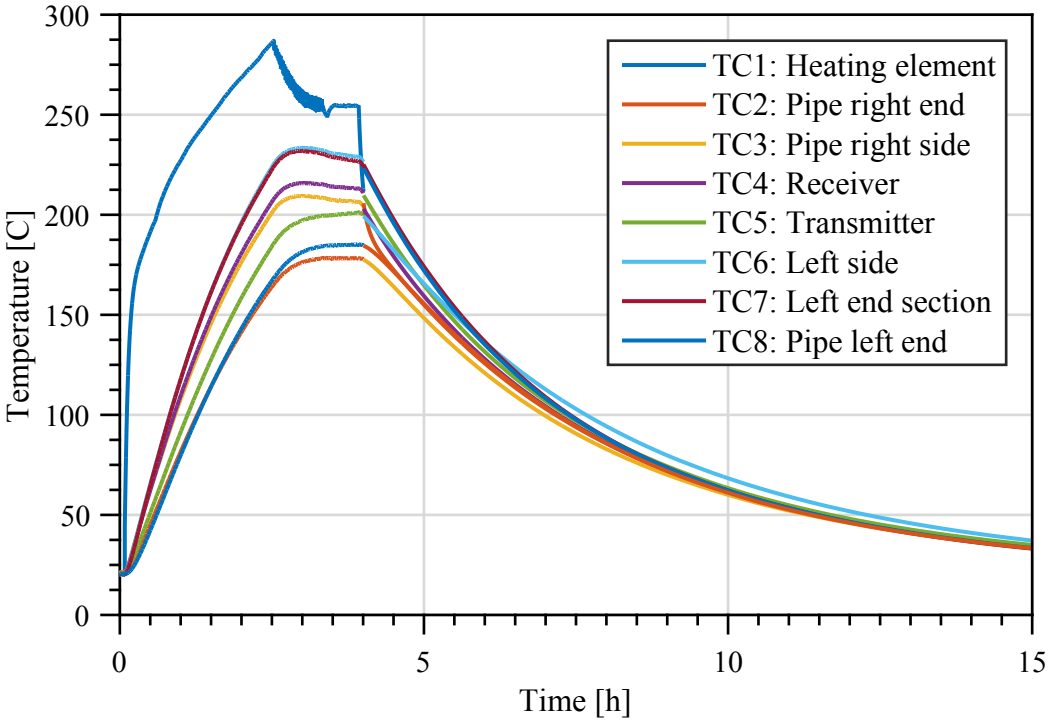

Figure 5.4: Recorded thermocouple readings during a typical pipe heating cycle. One thermocouple (TC1-blue) was placed inside of the pipe to monitor the air temperature, the rest was placed on the external surface of the pipe.

Example signals, which were acquired at temperatures between 30°C and 210°C are shown in Figure 5.5. The signals contain multiple reverberations, which is the result of the torsional wave reflected multiple times from the pipe ends. As the propagation speed of the torsional wave is dependent on the structure's temperature, the arrival time of the echoes changes with the temperature. The effect of propagation speed change is more dominant on the later arrivals (the difference in arrival times are highlighted by dashed lines in Figure 5.5).

A few of the presented signals (25°C, 50°C, 75°C, 100°C, 125°C, 150°C, 206°C) are shown enlarged in Figure 5.6.

The two distinct echoes which can be observed from the time trace are the incident wave (~0.25 millisecond) and the pipe end reflection (~1.4 milliseconds). Furthermore, a weld

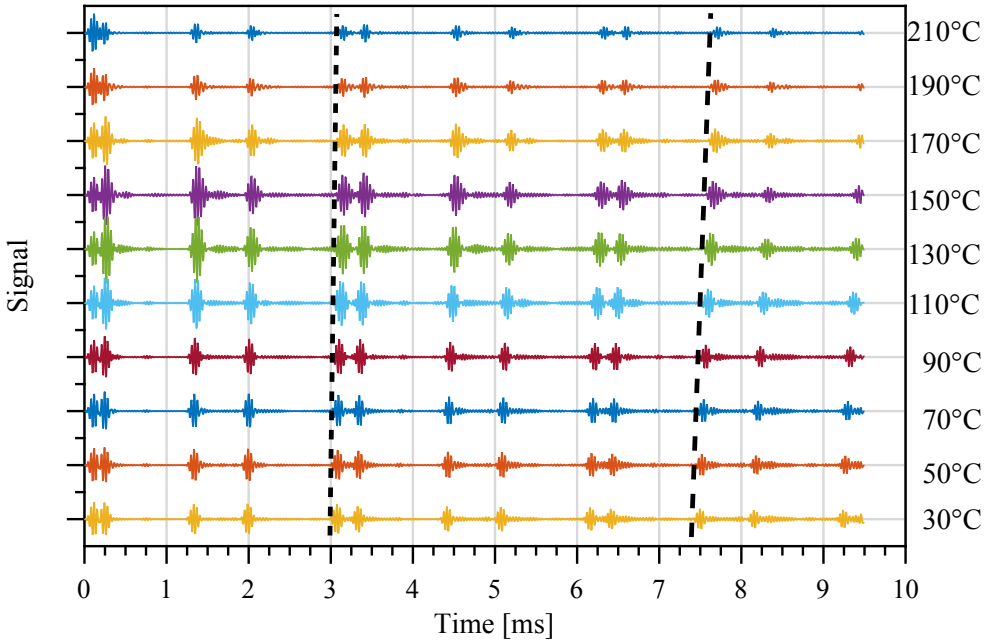

Figure 5.5: Ultrasonic signals acquired on the 3-inch pipe at different temperatures from 30°C to 210°C. The plotted signals contain several reverberations of the echoes. For some signal arrival times of echoes from the same feature are marked by dashed lines. It is clearly visible that at higher temperature waves propagate at reduced velocity (as seen by the later arrival time of the same wave packet).

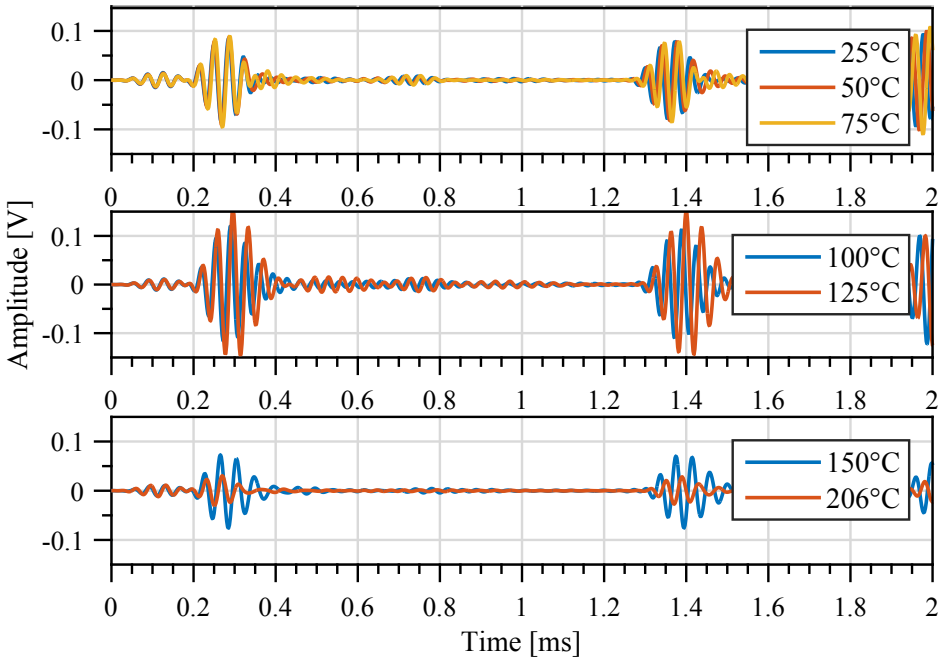

Figure 5.6: Ultrasonic signals acquired on the 3-inch pipe at different temperatures.

reflection (with a ~ 5% amplitude) can be observed at ~0.7 millisecond. The rest of the ultrasonic wave is the coherent noise, which is the result of imperfect excitation. It can be observed, that the wave packets change significantly with the temperature. The incident waves (direct arrival from the transmitting transducer to the receiving transducer) are shown in Figure 5.7 for different temperatures. These signals were compensated for propagation speed differences (method will be detailed in the next chapter).

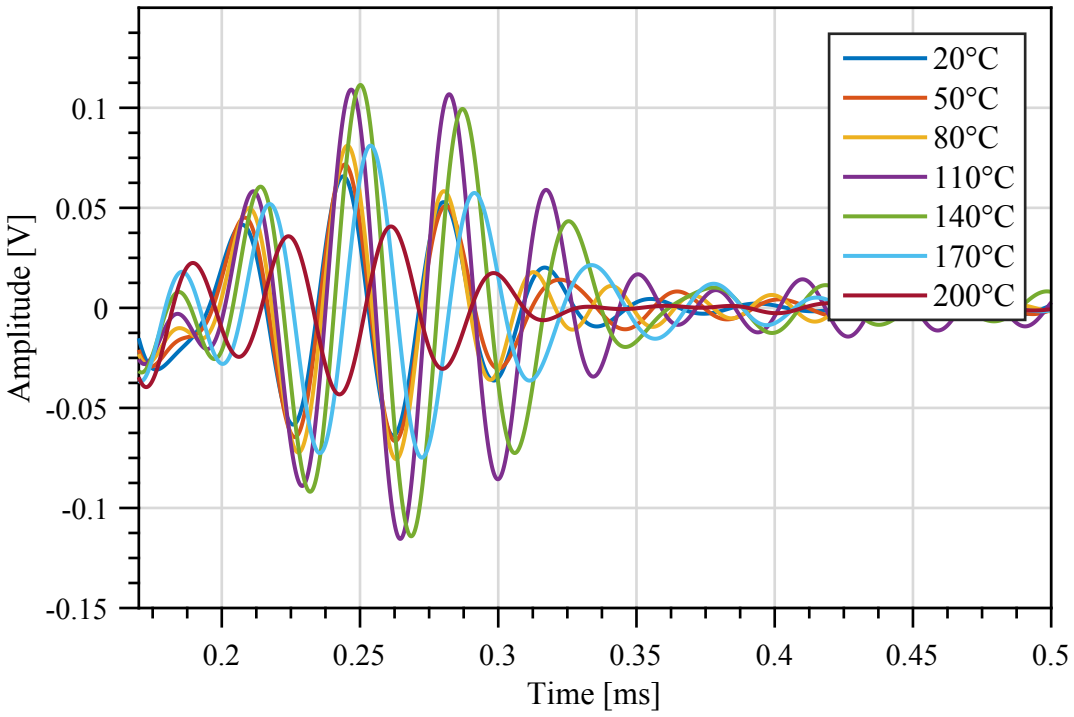

Figure 5.7: Incident wave of the guided wave signals acquired on the pipe at different temperatures.

The amplitude of the incident wave was evaluated for every signals in the heating cycle, and is shown as a function of temperature in Figure 5.8a. It can be observed, that the largest signal amplitude is recorded for temperatures around ~120°C. Signals with the same amplitude as the room temperature ones were recorded at the temperature of ~170 °C. The phase of the incident wave packet for the centre frequency (27 kHz) was evaluated from the FFT of the signal, and is shown in Figure 5.8b. The observed differences in the excitation phase are quite significant. As the differences in arrival times were compensated in the signals, the observed phase changes are the result of differences in the transduction mechanism.

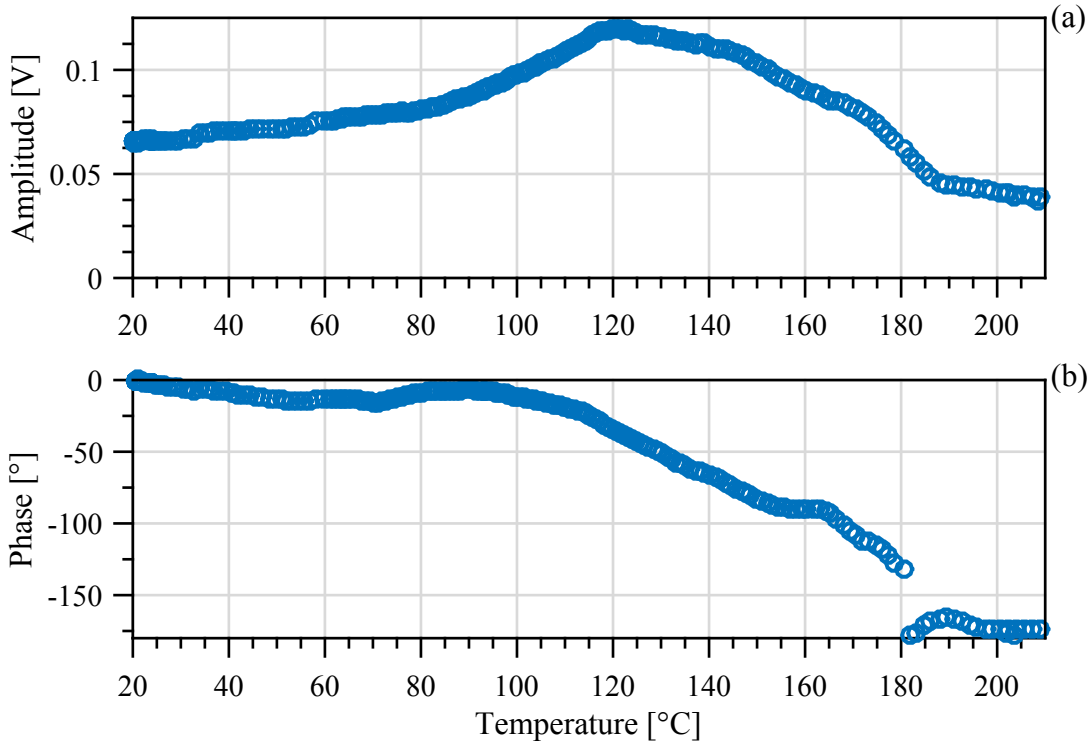

Figure 5.8: Amplitude and phase of the incident wave-packet at different temperatures.

Alternatively, the coherent noise of the signal (undesired wave modes generated by imperfect excitation) was evaluated as well. Figure 5.9 shows the coherent noise levels of the signals relative to the incident wave's amplitude. The differences between ultrasonic signals can be quite significant, therefore it is suggested that compensation methods are investigated which reduce the effect of temperature variations.

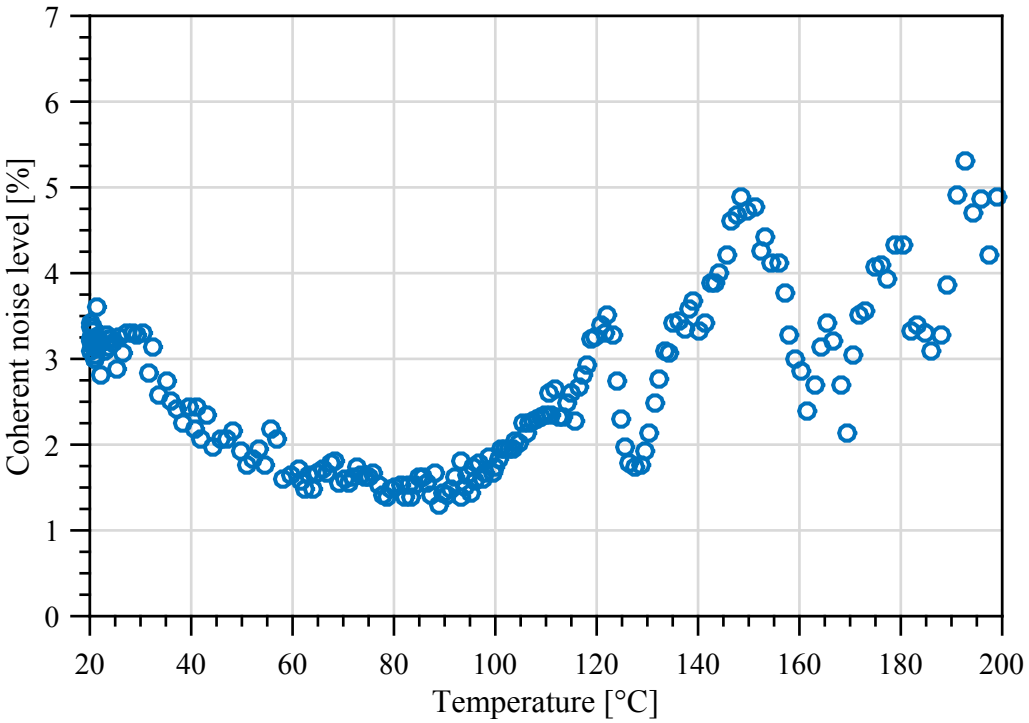

Figure 5.9: Coherent noise levels for signals acquired at different temperatures

5.5 Summary

For permanently installed transducers it is desired to increase the maximum operating temperature range so that the number of potential applications is increased. Although inspections can be performed during the downtime of the plant, the permanently installed transducers must survive the highest temperature of the pipeline. In this chapter, it was detailed how the EMAT prototype was modified to increase its temperature range above 200°C. The prototype was tested for temperatures up-to 210°C on an insulated pipe, which was internally heated by an electric finned air heater. Signals were acquired during the cooling of the pipe.

It was shown that the signal properties change with temperature. The signal amplitude shows nonlinear behaviour as a function of temperature. The strongest signals were recorded at ~120°C environment, above which the signal amplitude decreases. At ~170°C, signals with the same amplitude as room temperature ones can be collected. The overall

phase difference between excited waves at room temperature and 200°C is 180°. The coherent noise performance is again non-linear with the lowest coherent noise is recorded at the temperature of ~80°C. These signal changes are the result of propagation speed change, amplitude and phase change of the excited wave-packets, and changes in the coherent noise of the signal. It is suggested that for efficient monitoring these temperature effects should be compensated for.

Chapter 6

Compensation of temperature induced waveform changes during monitoring

6.1 Introduction

The work reported in this chapter starts with the investigation of the combined effect of the propagation speed change and transducer performance change (induced by temperature variations) on the ultrasound signal. An iterative compensation method is suggested which estimates the phase and propagation speed change solely from the measured ultrasonic time signal. The key point of the method is that separated transmitting and receiving transducers are used, so that the incident wave (direct travel between transmitting and receiving transducers) is recorded, and the phase information of the outgoing wave can be evaluated from it. It is believed that the method could work for different types of guided waves as long as the incident wave is received and the signal is that of a single mode.

Parts of this chapter have been extracted from publication [P3], which has been published under a CC-BY 4.0 license.

6.2 Existing compensation strategies

Detailed investigations have already been conducted on the temperature-induced changes to ultrasonic wave propagation [42, 46, 49]. In solid media, the major effect that is caused

by temperature change is an alteration of the wave-packet arrival times. It was found that the largest factor influencing the wave-packet arrival times is due to the changes in the material's elastic properties. Other factors like thermal expansion, change of material density have much smaller effects on the arrival times [165]. This implies that the dispersion curves for the guided wave modes change as well [166, 167]. Changes in the wave attenuation can also be caused by variations in the Environmental and Operational Conditions (EOCs). For guided waves, the variation in attenuation is also strongly dependent on the coating type, therefore a general solution is hard to be find [168].

The Optimal Baseline Selection (OBS) method was suggested to circumvent the problem of changing EOCs, where several baseline signals are acquired on a clean pipe at different temperatures and each reading is compared to the best baseline signal [50]. For long-range guided wave measurements, where the signals usually travel long distances even small temperature differences (~0.1 °C) will result in large differences for echoes that have travelled far. In case really large numbers of acquired signals are available, OBS has multiple advantages. If signals from the same temperature range are available, then less compensation needs to be applied to the signals, which reduces the change that the defect signal is lost due to the compensation method. Also, if signals can be grouped by operational temperature (enough signals are acquired at high and low temperature) detection algorithms can be applied separately. Results can then be compared, which could potentially reduce false call rate. However, in industrial pipeline health monitoring, where the structure's temperature cannot be controlled, the OBS method might not be feasible as it is practically impossible to acquire the required number of baseline signals so that it matches the exact temperature of interest. Also, seasonal changes can affect EOC conditions, which makes OBS less practical.

It is therefore required that the result of EOCs are compensated in the ultrasonic signal. By applying a well-chosen temperature compensation method, the residual levels (difference between the baseline and the reading signal) can be decreased. Once the residual levels are decreased by EOC compensation, it is more likely that changes due to defects can be identified. The better the EOC compensation is, the smaller defects can be distinguished from the temperature effects. Alternatively, defect-free structures can be diagnosed with higher confidence if the signal compensation decreases the residual

levels. The Baseline Signal Stretch (BSS) method was proposed to compensate for the temperature dependent propagation speed of the ultrasonic waves. The reading signals are stretched in the best possible way before subtracting them from the baseline signal. This approach works relatively well when the temperature differences between the baseline and the reading signals are small. For large temperature differences, the signal stretch alters the wave packet shape and creates a so-called frequency noise effect [44].

Combined strategy of OBS and BSS have also been proposed for improved temperature compensation performance [51]. This combined method uses multiple baseline signals and the reading signal is stretched to the best available baseline signal. Ideally, with this method the effect of only a small temperature difference is compensated, as baselines should have been recorded for several temperature ranges.

Apart from the compensation of propagation speed changes, a Distance Amplitude Correction (DAC) algorithm is often applied to the acquired signals. For general ultrasonic applications (e.g. imaging or tomography) this compensates for the beam spreading [64,129]. For 1D problems like pipeline inspection and monitoring there is no beam-spread. The guided waves can still be attenuated by the features present on the pipeline, or by the material damping [42]. Furthermore, as the guided waves interact with the structure boundaries, the pipe coating strongly influences the attenuation as well [168]. For guided wave inspections the DAC curve is often based on an approximation [169]. The DAC curves are particularly useful in monitoring when the wave attenuation is temperature dependent, so that the amplitude differences in the echoes are corrected.

6.3 Variations in transducer performance

Most ultrasonic signal compensation methods correct for changes in the ultrasonic propagation, and neglect the possible effects of changes in the transducer output. EOC induced changes of the transducer performance have received considerably less attention compared to the effects induced by changes in propagation speed, this is probably due to the fact that the variety of transducers that are employed all have different excitation mechanisms. Nonetheless, some previous works (not all related to NDE) that quantifies transducer performance changes and corrects for them have been carried out. Morrison et al. have

investigated how the lift-off of the Electromagnetic Acoustic Transducers (EMATs) affects the arrival times of Lamb waves that they excite in plates [170]. As a result, they have applied a correction to the extrapolated arrival time values, rather than the ultrasonic signal itself. Kim et al. have applied a calibration procedure for the receiving transducer in order to obtain a conversion transfer function and to compensate for any small variations in the coupling of the receiving transducer [171]. The calibration was performed prior to every measurement where the transducer transfer function was calculated from the transducer input current and voltage signal. Assous et al. have investigated the phase-response of wideband piezoelectric transducers at different frequencies. The magnitude and phase of the transducer transfer function was measured for a wide frequency range. As a compensation the excitation signal was digitally inverse filtered. As the measured ultrasonic signal is compensated for the amplitude and phase response, the bandwidth of the transducer system is enhanced [172]. A real-time advanced electrical filtering hardware was developed by Hurst et al. for similar purposes. An analogue second-order electrical filter is applied on the measured ultrasonic signal, which compensates for the transducer transfer function [173]. The drawback of analogue filtering is that only causal filtering can be applied which results in a minor time delay of the signal. This compensating electrical filter did include a fine-tuning, which could compensate for the temperature effects.

It was observed by Labyed et al. that imaging algorithms can be corrupted due to the transducer phase response. This change in the phase response of the transducer was corrected using a glass scatterer as a reference [174]. The imaging algorithm was modified to account for the phase response of the transducer elements.

It must be noted, that all of the above listed transducer compensation methods improve performance, but they need calibration, or a priori knowledge about the transducer behaviour.

There are several possible reasons for the temperature induced performance changes for bonded (either piezoelectric or magneto-strictive) transducers and EMATs as well: For example, the adhesives used for bonding piezoelectric and magneto-strictive transducers can become softer at higher temperatures. Once the stiffness of the adhesive changes, it alters the resonant frequency of the transducer [165, 175]. Then, as the frequency response is altered, the excited ultrasonic wave will be affected by a phase change. When

the piezoelectric transducer excitation frequency is close to the resonant frequency, the phase response is the most sensitive to EOCs.

EMATs are also affected by temperature. For example, the temperature changes the impedance of the EMAT (the conductivity of the coil and test specimen changes) and the excited signals will exhibit a phase change. As shown in Figure 6.1, the magnitude (Figure 6.1a) and the phase (Figure 6.1b) of an EMAT are affected by temperature variations. The EMAT whose construction is described in Chapter 3 was used for the reported measurements.

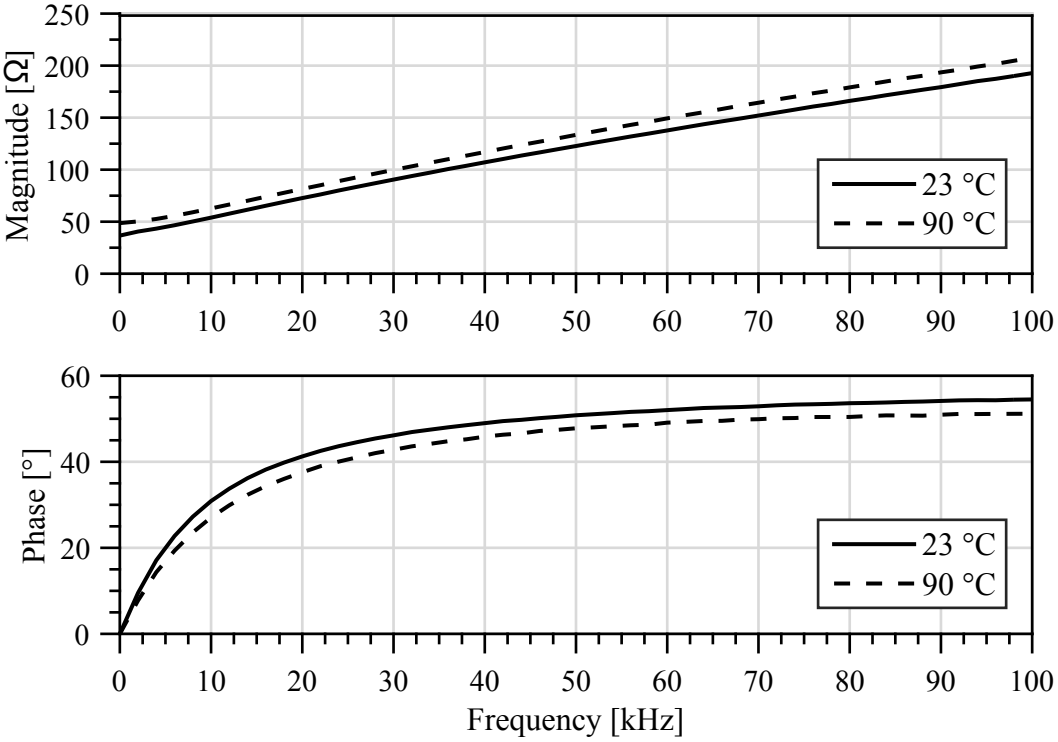

Figure 6.1: Experimentally acquired impedance of a 6 coil transmitting EMAT at 23 °C (solid line) and 90 °C (dashed). The magnitude of the impedance is plotted at the top figure (a), whilst the phase of the impedance is plotted at the bottom figure (b).

For similar reasons, additional phase changes will influence the receiving transducer performance. Furthermore, the performance of the instrumentation, for example the signal amplifiers can be affected by temperature and can introduce further phase changes. The overall phase change that the recorded ultrasonic signal exhibits is then the addition of the phase change experienced by each part of the measurement system.

6.4 Problems with currently used compensation methods

6.4.1 Effect of temperature on ultrasonic time trace

The change in the structure's temperature will affect the phase velocity of the wave-mode. For non-dispersive signals this will simply result in a delayed signal arrival, and each wave-packet will be delayed proportionally to the propagated distance; for longer travelled distances, the arrival time change will be more significant. Figure 6.2a shows the difference between non-dispersive ultrasonic wave-packets (5 cycle 27 kHz tone-burst) after 3 meters of propagation, when the propagation speed was 3250 and 3234 m/s respectively. (Note, that the simulated signals have propagated for 3 meters, and only the part of the signal is shown where the wave packet arrives.)

On the other hand, as discussed it is expected that all types of transducers will change performance when their temperature is changed. The transducer's transfer function change (amplitude and phase response change) will unavoidably result in a different wave packet being excited. In the first approximation, the phase change is modelled so that the phase change is uniform across all frequencies. The uniform phase change on all frequencies will alter the carrier wave's phase, but has no effect on the signal envelope (calculated as the Hilbert envelope), as shown in Figure 6.2b.

6.4.2 Mathematical representation of the effect of temperature changes on the signal

Let's consider a non-dispersive ultrasonic wave packet which has travelled attenuation-free in one dimension. The reference time signal recorded after x meters of travel is:

$$y(t) = \frac{1}{\sqrt{2\pi}} \int_{-\infty}^{\infty} F(\omega) \cdot e^{i\omega(\frac{x}{c}-t)} d\omega \tag{6.1}$$

where ω is the angular frequency and c is the wavespeed; t denotes the time. $F(\omega)$ is the

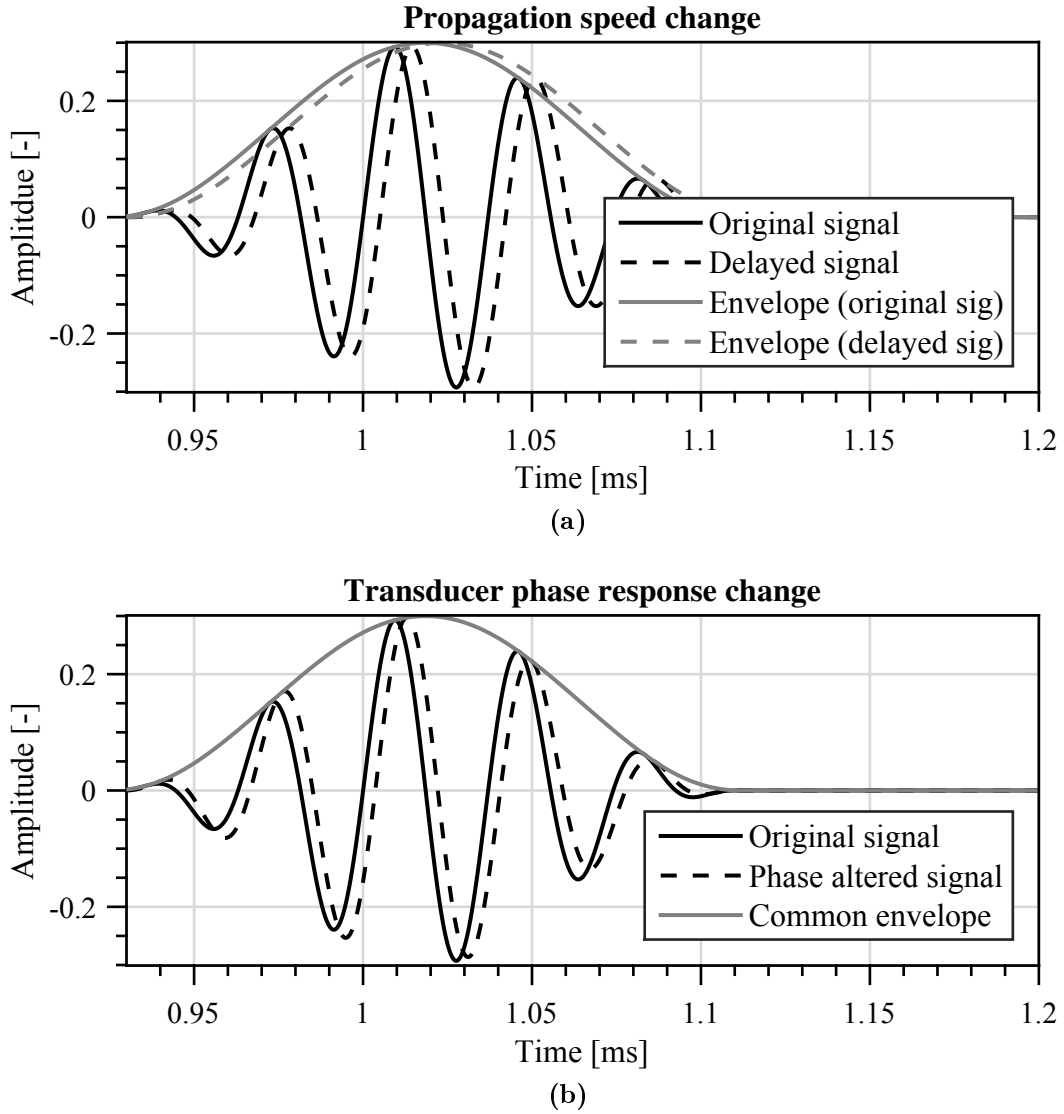

Figure 6.2: Simulated ultrasonic signals after 3 meters of propagation when the excitation was a 27 kHz 5 cycle Hanning windowed tone-burst. Signals with different propagation speed (3250 and 3234 m/s) are shown in (a). The effect of transducer phase response change is shown in (b), where the excitation phase was0° and 35° (propagation speed was 3250 m/s for both).

Fourier transform of the excited signal $f(t)$:

$$F(\omega) = \frac{1}{\sqrt{2\pi}} \int_{-\infty}^{\infty} f(t) \cdot e^{i\omega t} dt \tag{6.2}$$

The temperature changes the propagation speed of the ultrasonic wave. Each wave packet will be delayed, and the delay of each ultrasonic wave packet will be proportional to the travelled distance. The time delay in the Fourier domain corresponds to the function:

$$f\left(t - (\frac{x}{c_1} - \frac{x}{c_2})\right) \xrightarrow{Fourier} F(\omega) \cdot e^{-i\omega t \Delta \frac{x}{c}} \tag{6.3}$$

where c_1 and c_2 are the wave-speeds at different temperatures.

The effect of propagation speed change is demonstrated on simulated signals and is shown in Figure 6.3a. The time signals consist of 4 echoes which corresponds to 5, 17.5, 30, 42.5 wavelengths of travel. In the simulation, the two signals have different propagation speeds (3250 and 3234 $\frac{m}{s}$). The difference between the two signals (shown in Figure 6.3b) is the residual error, which is increasing as a function of distance.

If the transducer transfer function is affected by the temperature, the excited signal will suffer a phase change (referred to as p). Usually the excitation frequency is a narrow-band pulse, so in the first instance the temperature effects will be simulated as a constant amplitude and constant phase change on the whole excitation bandwidth. It is not genuinely true that the phase change is uniform across all frequencies, therefore Subsection 6.5.2 further investigates the compensation when the phase change is frequency dependent (envelope of the wave-packet is altered as well). For uniform phase change, the Fourier transform of the altered excited signal ($F'(\omega)$) can then be written as:

$$F'(\omega) = e^{-i \cdot p} \cdot F(\omega) \tag{6.4}$$

The effect of excitation phase change was investigated in a separate repeated simulation,

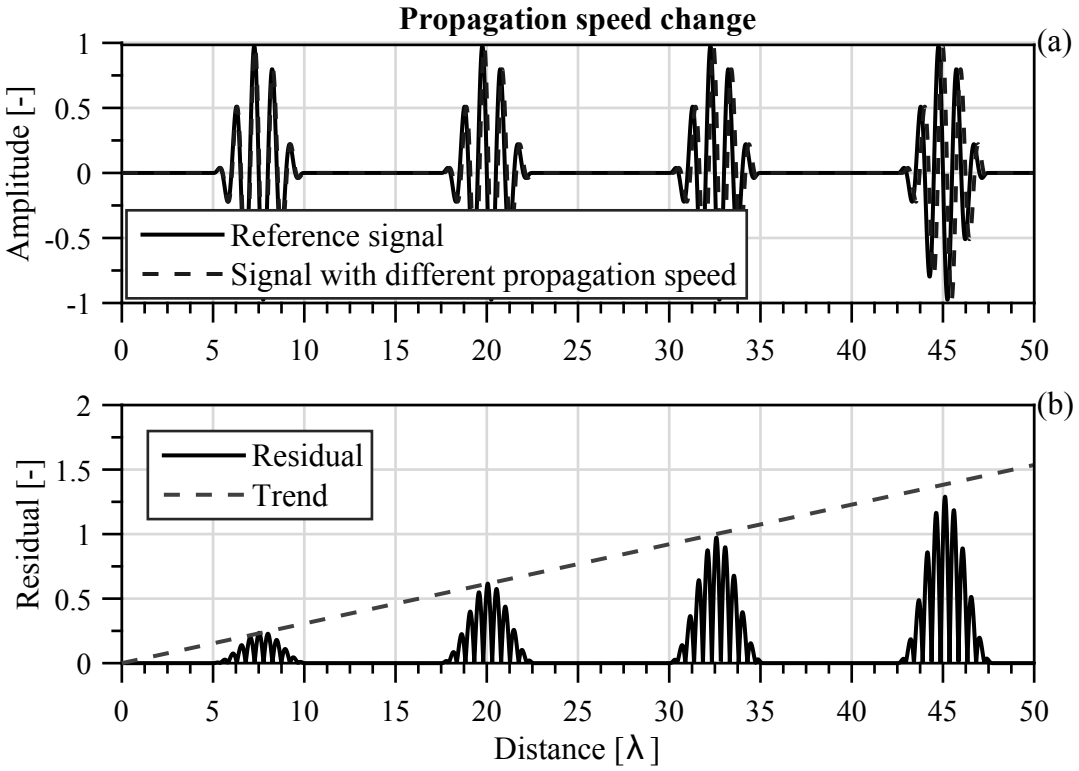

Figure 6.3: Simulated ultrasonic signals with the propagation speeds of 3250 and 3234 m/s (a), and their difference or residuals (b). An increasing trend in the residual error can be observed.

where two signals were constructed, and the excitation phase on one signal is altered by 35° (Figure 6.4a). It was concluded, that the phase change of the excitation signal has an equal effect on all echoes. The difference of the wave-packets is independent of the propagation distance as shown in Figure 6.4b.

The overall effect of the temperature change will be the combination of the propagation speed change, and the transducer transfer function change. The time signal of the temperature altered y(t) signal is then calculated as:

$$y'(t) = \frac{1}{\sqrt{2\pi}} \int_{-\infty}^{\infty} F(\omega) \cdot \mathbf{e^{-i \cdot p}} \cdot e^{i\omega(\frac{x}{c}-t)} \cdot \mathbf{e^{-i\omega t \Delta \frac{x}{c}}} d\omega \tag{6.5}$$

The terms which the temperature altered signal differs from the reference signal (Equation 6.1) are shown with bold text. Therefore, it can be seen that the Fourier transform of the ultrasonic wave packet which is affected by propagation speed change and transducer

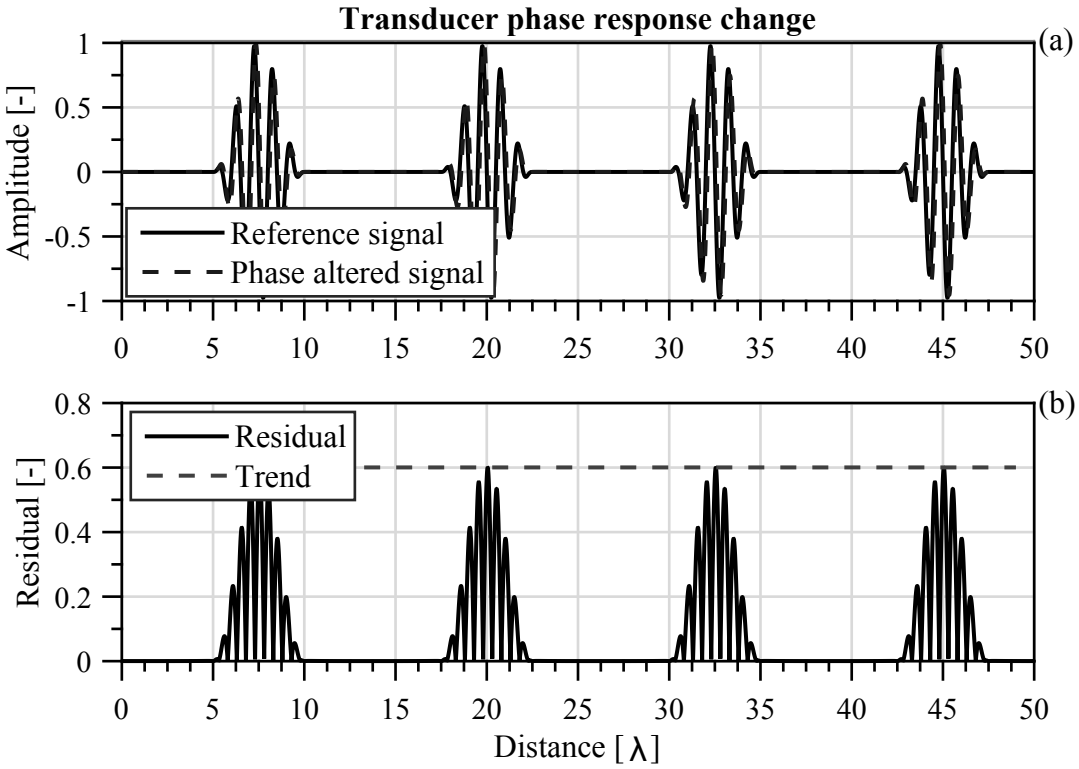

Figure 6.4: Signals with different excitation phase (0° and 35°) (a), and their difference (b). The error observed on each wave-packet is independent of distance from the source.

transfer function change will be altered by the function:

$$e^{-i\cdot p}\cdot e^{-i\omega\Delta\frac{1}{c}t}=e^{-i\left(p+\omega t\Delta\frac{1}{c}\right)} \tag{6.6}$$

The phase change on each wave packet of the signal after x meter travel is:

$$\phi(x)=p+\omega t\Delta\frac{1}{c}\cdot x=p+s\cdot x \tag{6.7}$$

where p is the transducer phase change, and s is a constant which depends on the propagation speed change. The combined phase difference $\phi(x)$ is a linear function of the travelled distance x. An example of the combined phase difference is shown in Figure 6.5.

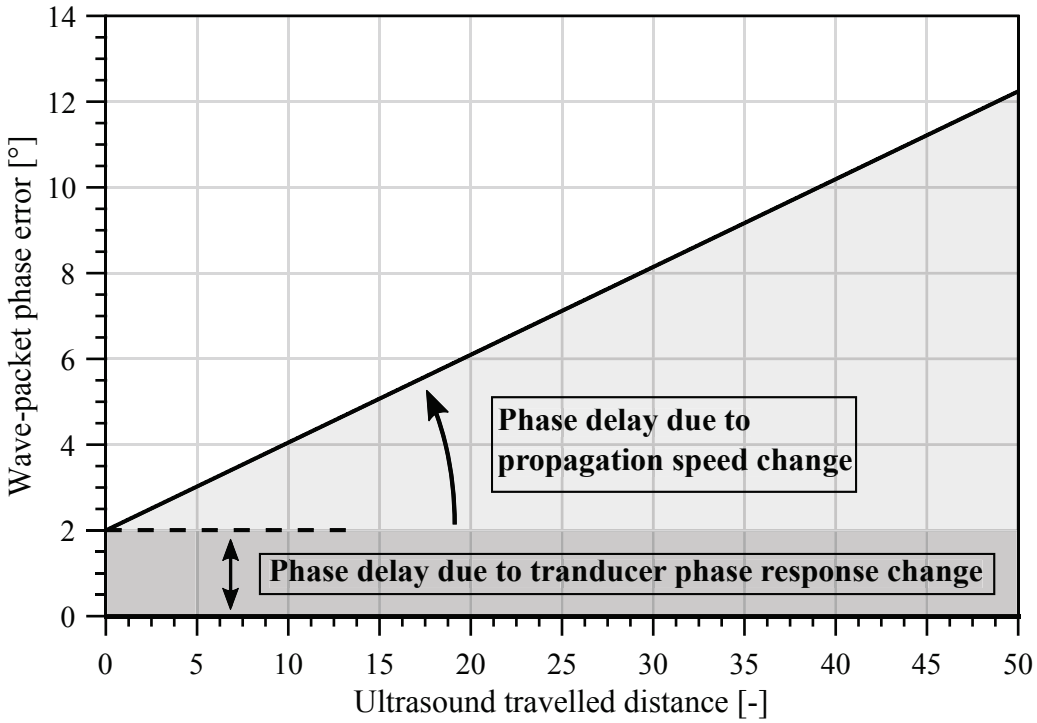

Figure 6.5: Combined effect of propagation speed change and transducer response change on the phase difference of two signals as a function of propagation distance. The phase difference due to the transducer phase response change is independent of the travelled distance, whereas the phase difference due to the propagation speed change is increasing with the travelled distance.

6.4.3 Imperfect single-stretch based compensation

The conventional temperature compensation methods try to compensate the altered signal by a single stretch. The stretch estimation method searches for the optimal stretch factor where the correlation between the baseline and the stretched reading signal is maximized [51]. Advanced algorithms were developed which are optimized with respect to computation time [176]. The work that is reported here uses these improved stretch estimation and signal stretch transformations.

If the excited signal's phase is altered, the single stretch based temperature compensation methods will result in an imperfect stretch estimation. Propagation of ultrasonic wave-packets (5 cycle 27 kHz tone-burst excitation) were simulated, where the propagation was 6 meters for all signals, but each wave was excited with a different phase. The signals are shown in Figure 6.6 after the baseline signal stretch (BSS) was performed on them.

As the phase of the excited signal is changed, the highest correlation between the baseline

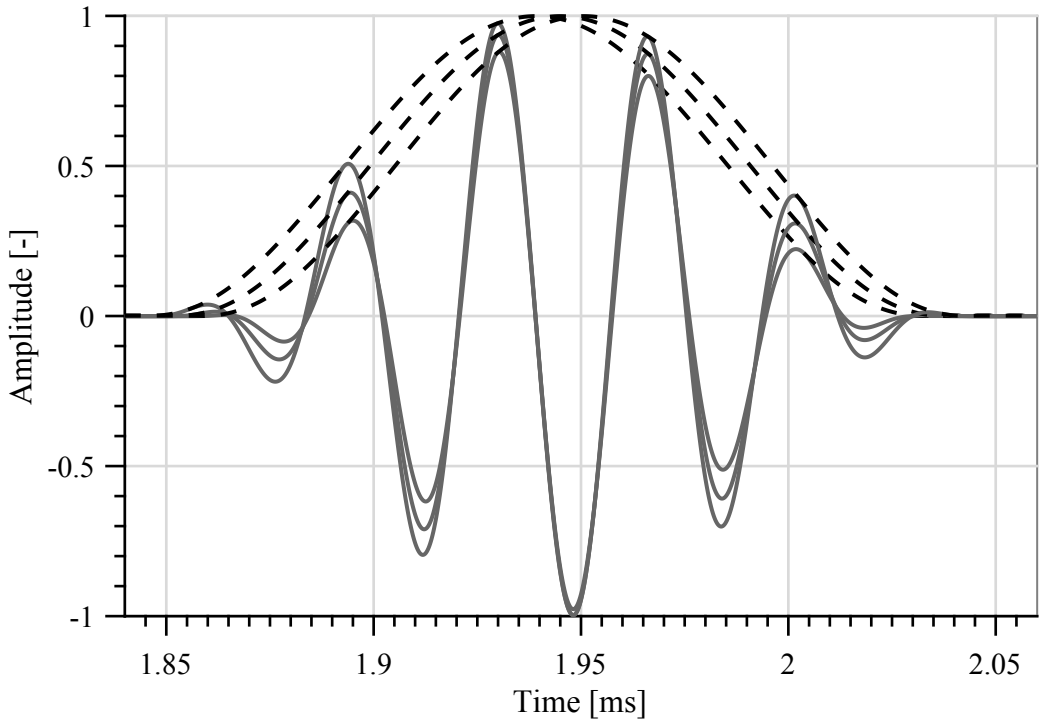

Figure 6.6: Example of ultrasound time signals with imperfect compensation on simulated signals: The correlation based stretch estimation methods will result in imperfect stretch estimation. The propagation speed is estimated with an error of 12 and 23 m/s when the excitation phase was changed by 57° and 114°. Also, the signals do not overlap, therefore the residual signals will be large.

and the reading is reached when the tone-burst itself is mislocated (wrong signal stretch is estimated). The imperfect stretch is most notable when comparing envelopes; the envelopes of the different signals are not aligned time-wise. The error in propagation speed estimation was 12 and 23 m/s when the excitation phase was altered by 57° and 114° respectively.

The origin for the imperfect stretch can be explained using the phase error vs propagated distance plots. The combined phase error (transducer and propagation speed change) caused by the temperature in function of the travelled distance is plotted with a dashed line in Figure 6.7. The signal stretch compensates for a linear error proportional to the travelled distance (dotted line). The remaining phase error (plotted in black) will be present in the residual signals after subtraction. It can then be observed that the estimated signal stretch (which is equal to the gradient of the slope) is different compared to the signal stretch which corresponds to the actual propagation speed change.

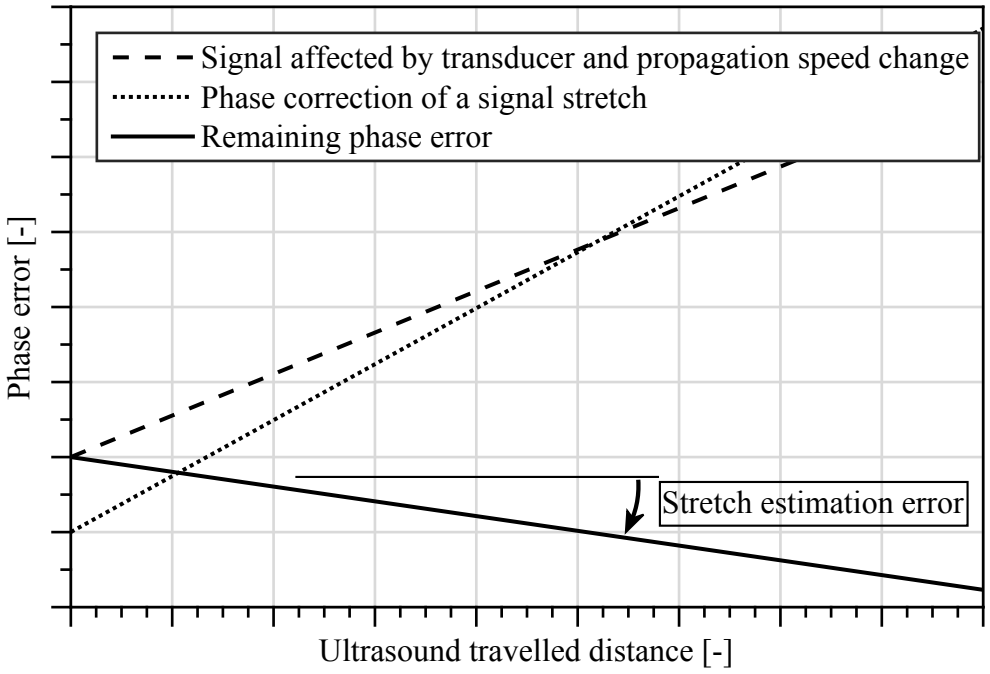

Figure 6.7: Problem with single-stretch compensation methods: The phase of the ultrasonic signal is altered according to the dashed line, whereas the signal stretch compensates for the phase error according the dotted line. The remaining phase estimation error is represented by the black line.

If the phase change of the excitation is not compensated for on the ultrasonic time traces (for example shown in Figure 6.6) the baseline and the (stretched only) reading signal will be different. Obviously this creates a problem at those locations of the time signal where the amplitude of the wave-packets are large (e.g. at echoes originating from features), as the residual signal will increase above the noise threshold. Rather, it is important to apply compensation to decrease the residual levels so that the damage detection chances are increased.

Three different cases were investigated (shown in Figure 6.8) in order to estimate the severity of the uncompensated temperature effects on the residual signal: (a) the echo envelope is matched up with the baseline's envelope, (b) the stretch factor is estimated and the stretch is applied on the uncompensated reading signal, and (c) the signal stretch is estimated on a reading signal which has been compensated for phase change.

For all cases, the residual levels are calculated for reflectors, which reflected 10% of the

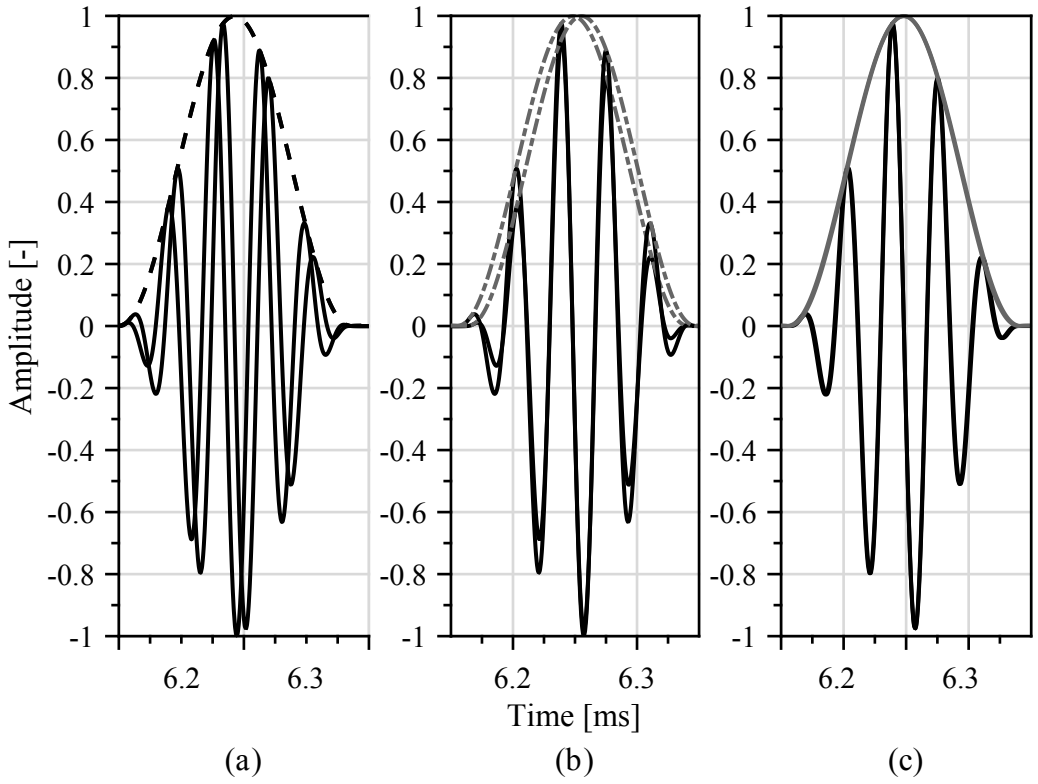

Figure 6.8: Different cases for compensation. Signal stretched using the envelope as the reference (a); stretch estimated using the acquired ultrasonic signal (b); both signal stretch and phase compensation is applied.(c).

incident wave, as this magnitude of reflection is typical for feature reflections on pipelines. Figure 6.9 shows the residual levels (compared to the incident wave's amplitude) for the three cases). It can be observed that the residual levels are the highest, when the signal stretch is estimated on the envelope of the signal (case (a)). Note that in case (a) despite the stretch being estimated from the envelope of the signal, the residual is calculated by subtracting the signal itself, not the envelope. If the signal stretch is estimated on the ultrasound signal itself, the residual levels are lower (case (b)). However, this way an imperfect stretch estimate is made as previously discussed. The lowest residual levels are reached (therefore the most favourable case is), when the phase change is recovered, and the propagation speed change is compensated by a signal stretch (case (c)). The remaining error in this case is the distortion in the signal shape due to the signal stretching [51]. Figure 6.9 shows, that the decrease in the residual when comparing case (b) and (c) is around 7.3 dB, but this depends on how severe the transducer phase change is as a result

of temperature change. In the simulation it was assumed, that the temperature change results both in a phase change of 1 degree and 0.66m/s reduction in propagation speed. Therefore by compensating the phase change caused by the transducer, the residual levels can be decreased by several dB.

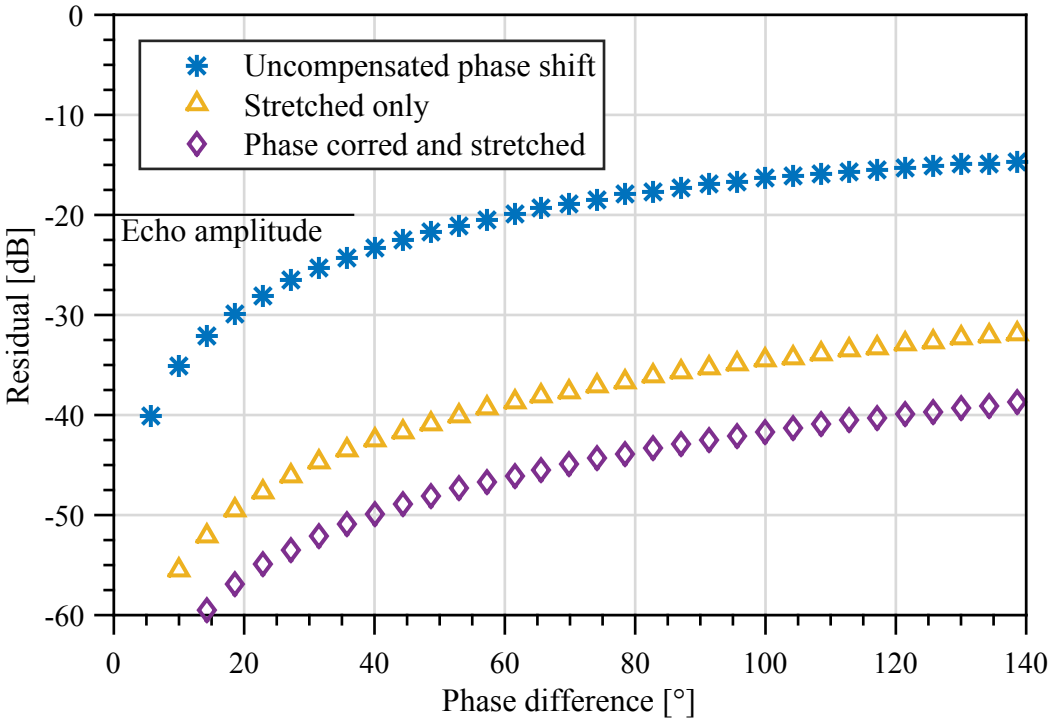

Figure 6.9: Residual error after baseline subtraction associated with different methods (shown in Figure 6.8) on a logarithmic scale. The error was calculated for a 10% reflector.

6.5 Proposed, iterative compensation technique

6.5.1 Compensation method

An iterative temperature compensation method was developed which compensates for the transducer phase response changes in addition to the commonly used propagation speed change compensation methods. For presentation purposes, the concept of the compensation technique and the results are shown on torsional guided wave signals acquired by the EMAT transducer. The operation of the EMAT transducer is presented in Chapter 3 and [177]. It was developed to offer an alternative to bonded on sensors with the aim of achieving better long-term signal stability. However, it is still affected by temperature variations which must be compensated for. The torsional guided wave signals were acquired on a 5-meter long 3-inch NPS mild steel pipe using electromagnetic acoustic transducers. As shown in Figure 6.10, two transmitter transducers are used for the measurements so that directional control can be achieved. The receiving transducer is placed 0.4 m from the transmitting transducers. The effect of the axial separation is that the incident (direct) wave is separated from the cross-talk signal (the cross-talk being the transmitted signal electromagnetically coupled to the receiver transducer). In conventional EMATs, the cross-talk is magnitudes higher than the ultrasound signal itself, and would prevent receiving the ultrasound signal for a significant time, a special cross-talk reduction hardware system was developed [144]. This makes possible to suppress the cross-talk to the minimal level and receive the incident wave of the ultrasound signal as shown in Figure 6.11.

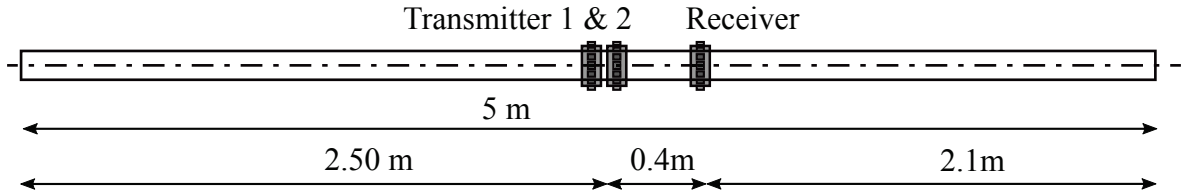

Figure 6.10: Measurement setup for acquiring signals on a 5 meter long 3-inch NPS pipe using two transmitting and one receiving transducer

As the wave-packets are affected by both transducer performance changes, and the arrival time change depending on the propagated distance, it is not possible to separate the two effects when only one wave-packet is present in the time signal. Rather, it is possible

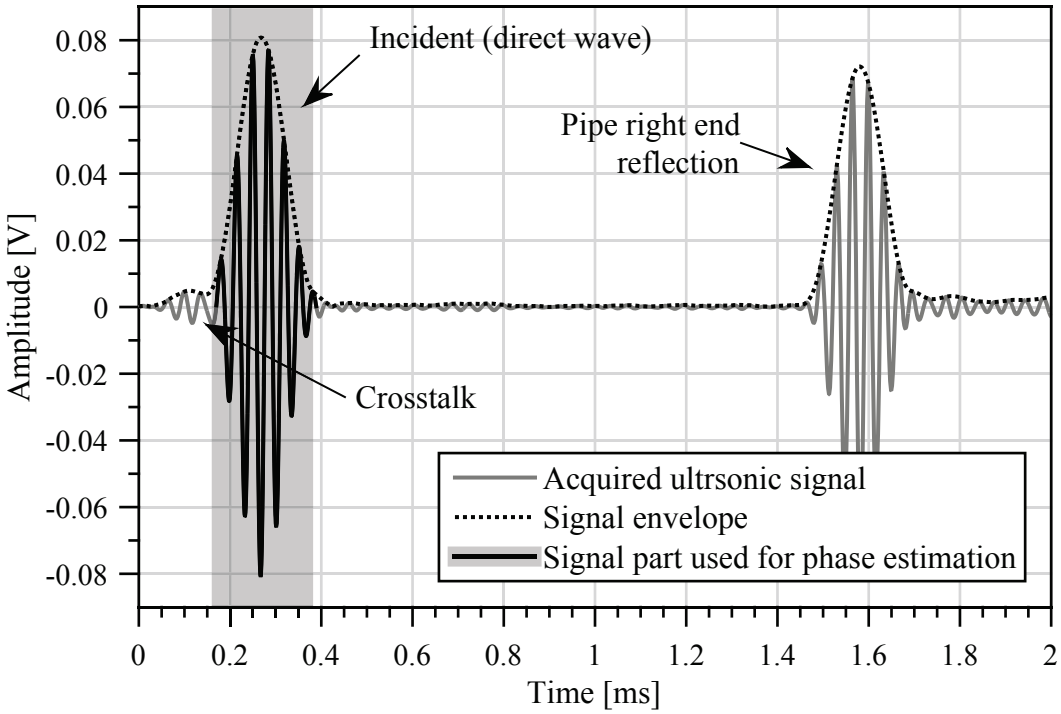

Figure 6.11: Acquired right travelling torsional guided wave travelling on the 3-inch test pipe. The incident wave-packet of the signal is used for phase change estimation and is highlighted in black on a grey background.

if the signal has multiple wave-packets. For the presented signals, one of the required wave-packets is the incident wave, which has high amplitude, and has propagated for a short distance only (shown in black in Figure 6.11). As this incident wave has travelled for a small distance only, it is mainly affected by the transducer performance changes. The other echoes, which are reflected from pipe features (end reflections for the presented case) will provide the required additional information for the compensation method. These later echoes are more dominantly affected by the arrival time change, as the propagation distance is significantly larger. It is challenging to develop a one-step compensation method, as all echoes are affected by the combination of the phase-change and the propagation speed change. In other words, no echo is available which isn't affected by the propagation speed change, therefore the transducer phase change cannot directly be estimated. Also, the later echoes are not only affected by the propagation speed change but the transducer performance as well. This leads to an iterative method, which performs signal stretch and phase compensations multiple times.

The idea behind the iterative method is that once a good propagation speed change estimate exists (and is corrected for), a more precise phase change can be estimated. In addition, once a good estimate of the phase correction is available, a more precise stretch estimate can be made. Therefore, in the first step, an initial propagation speed change is estimated, and the phase change is estimated after the propagation speed change is corrected for. In the next step, a more precise propagation speed change is estimated on the phase compensated signal. When the phase is estimated on an early arrival and the stretch on a later echo (as shown in Figure 6.11), the estimated values converge rapidly. For presentation purposes 5 iterations were performed, but it will be discussed, that for most signals less number of iterations will be satisfactory. The whole iterative phase compensation method is shown in a flowchart in Figure 6.12. As the phase corrections are always performed on the original reading signal, and the stretch is performed on a signal which was phase corrected only, the rounding errors in the iterative method do not add up. This means that the final signal will be phase corrected and stretched only once in the final step.

6.5.2 Frequency dependent phase compensation of the ultrasound signal

In the previous sections it was assumed that the transducer phase change caused by the temperature change is equal and uniform across all frequencies, and the shape of the signal envelope does not change. Unfortunately, this is not necessarily true. The phase change of the transducer might be frequency dependent, therefore not only the phase of the carrier wave, but the shape of the envelope can change as well. This means that the Fourier transform of the altered packet will be:

$$F'(\omega) = e^{-i \cdot p(\omega)} \cdot F(\omega) \tag{6.8}$$

where $F(\omega)$ is the spectrum of the excitation signal, $p(\omega)$ is the frequency dependent

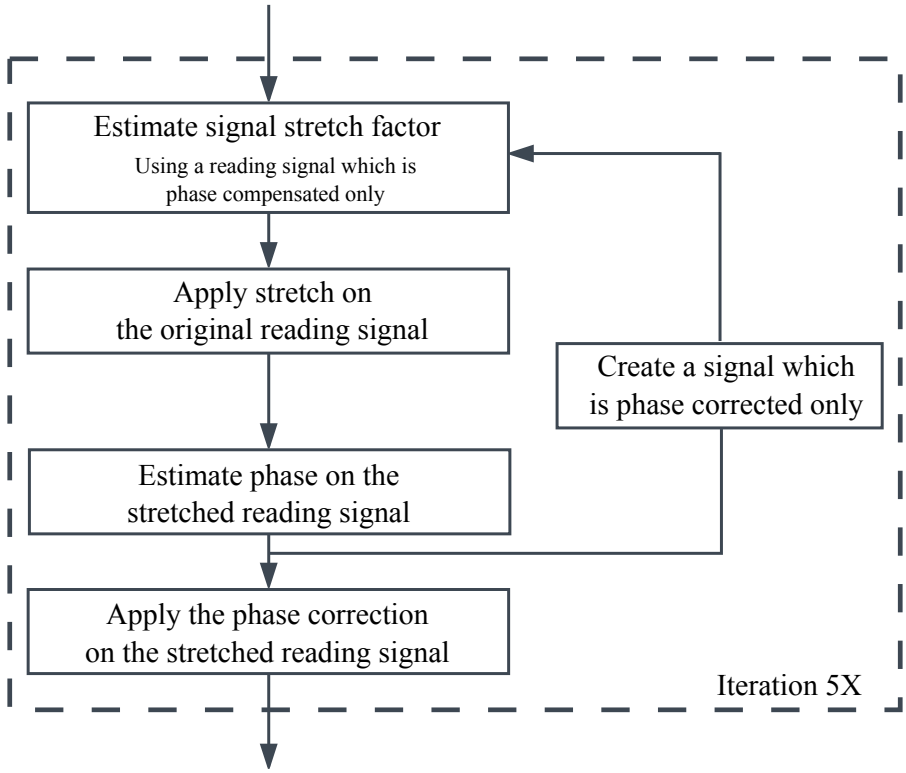

Figure 6.12: Flowchart of the iterative temperature compensation method: The signal stretch is estimated on a signal which is phase compensated only (in the first iteration the signal is simply the original reading signal). Then the stretch factor is applied on the original reading signal. Then the phase difference is estimated between the baseline and the reading signal, and is applied to the stretched signal. This iteration is repeated 5 times, as after this number of iterations the stretch and phase estimates only change negligibly.

phase change. $F'(\omega)$ is then the excitation signal at different temperature which contains the temperature induced phase changes.

In order to calculate the frequency dependent phase correction, the Fourier transform is calculated for both the baseline signal's incident wave and the reading signal's incident wave. A frequency filter is then applied on the signal spectra so that only the main lobe is used for further calculations. The ratio between the two calculated complex Fourier spectra is the frequency dependent amplitude and phase correction. The phase correction is then applied on the Fourier transform of the whole reading signal, and the inverse Fourier transformation is the phase compensated reading signal.

An example of the frequency dependent magnitude and phase correction is shown in Figure 6.13 when the baseline was acquired at room temperature, and the reading was acquired on a 64.5 °C pipe.

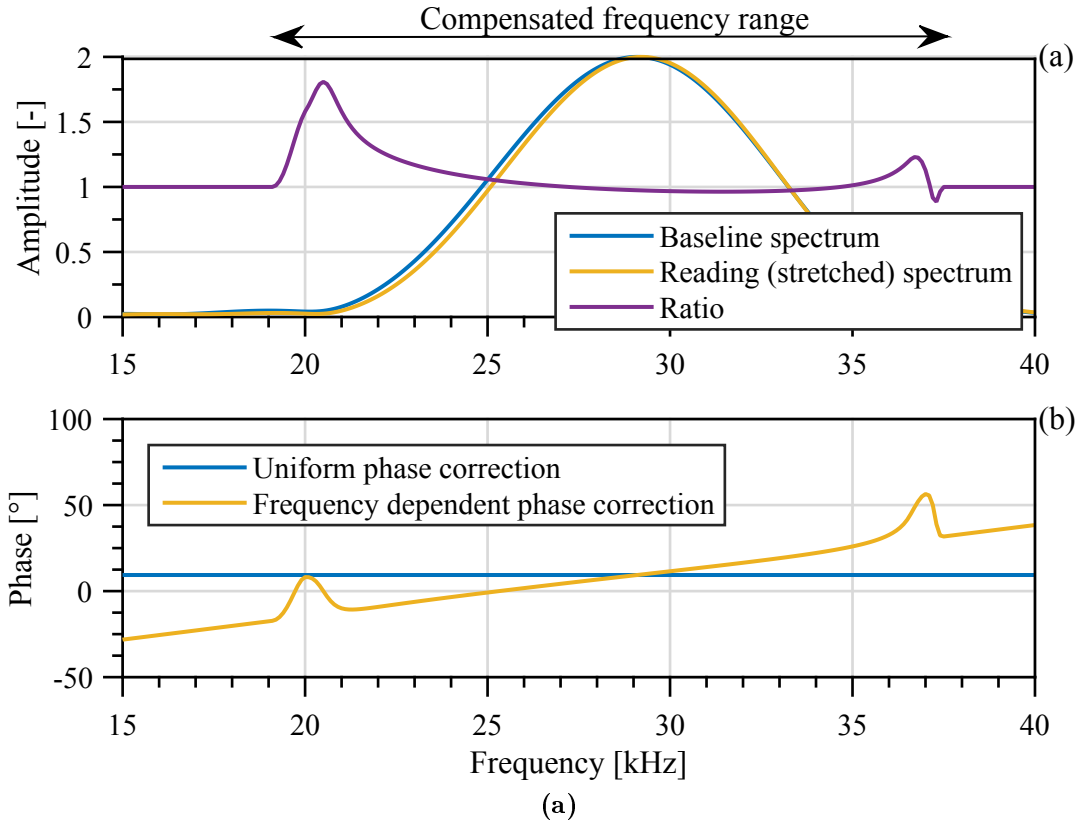

Figure 6.13: The Fourier magnitude spectrum of the baseline's and the stretched reading signal's incident wave-packet is slightly different due to the performed stretch (a). The frequency dependent correction corrects for its unwanted effect (frequency noise) by applying a magnitude (a) and phase (b) correction on the ultrasonic signal. The compensated frequency range is selected as the main bandwidth of the excitation signal spectra (19 kHz-37.5 kHz in this example). The estimated uniform phase is shown for reference.

It is important to note, that by performing the frequency dependent phase correction on the stretched signals, an additional benefit is implemented: The signal stretch performed on the ultrasonic signal alters the frequency content of the wave packets (see Figure 6.13a), and it will create the so-called frequency noise. In case the frequency dependent phase correction is applied, the shift in frequency is recovered, and the frequency noise is removed. Croxford et al. have presented the theoretical calculations for removing the frequency noise [178]. They correct the reading signal in the frequency domain by the ratio of the stretched and non-stretched wave-packets (also in the frequency domain). Another paper describes that in practice, this would "amplify noise at the extremes of the available bandwidth", and a frequency bandpass filter must be used the same way as in the proposed method [179].

The frequency dependent phase compensation corrects for the frequency noise in a similar manner, where the wave-packets are selected from the ultrasonic signal. Because the wave-packets are selected from the ultrasonic waveforms, both the frequency noise and the phase change is removed in one step.

6.6 Experimental results

6.6.1 Compensation of ultrasonic signals acquired with EMATs

The phase compensation method was tested on acquired torsional guided wave signals. The baseline signal is shown in Figure 6.11, where the incident wave is highlighted. The iterative compensation method was applied to experimentally acquired signals. The incident wave of example signals are shown in Figure 6.14 when the baseline was acquired on a room temperature pipe (23 °C), and the reading signal acquired on a pipe at 64.5 °C. The baseline signal is plotted in black, the stretched reading signal with blue dotted line, and the reading signal, which is stretched and phase corrected is plotted in yellow. It can be observed, that the signal, which is stretched and phase compensated and the baseline resemble each other much more closely than the baseline and the signal that is only stretched.

The iteration steps in the compensation method can be repeated until the desired precision is reached. It was observed, that in the presented measurement setup the estimated values are exponentially converging to the final value. For example, for an iterative compensation where the propagation speed difference of the signals was 26 m/s (50 °C temperature difference), the estimate converged to within 0.03m/s of the final result within 3 steps.

It is important to note that a stretch performed on the ultrasonic signal distorts the shape of the wave packet (squeezing or expanding the wave packets). After subtraction, this results in small residual signals. This is often called the "frequency noise", as the stretching of the wave-packet slightly alters the frequency content of the signal. It is possible to compensate for the wave packet's shape distortion with the ratio of the original and stretched wave packet's spectra [178, 179]. If the iterative temperature compensation method uses frequency dependent phase difference estimation between the baseline and the

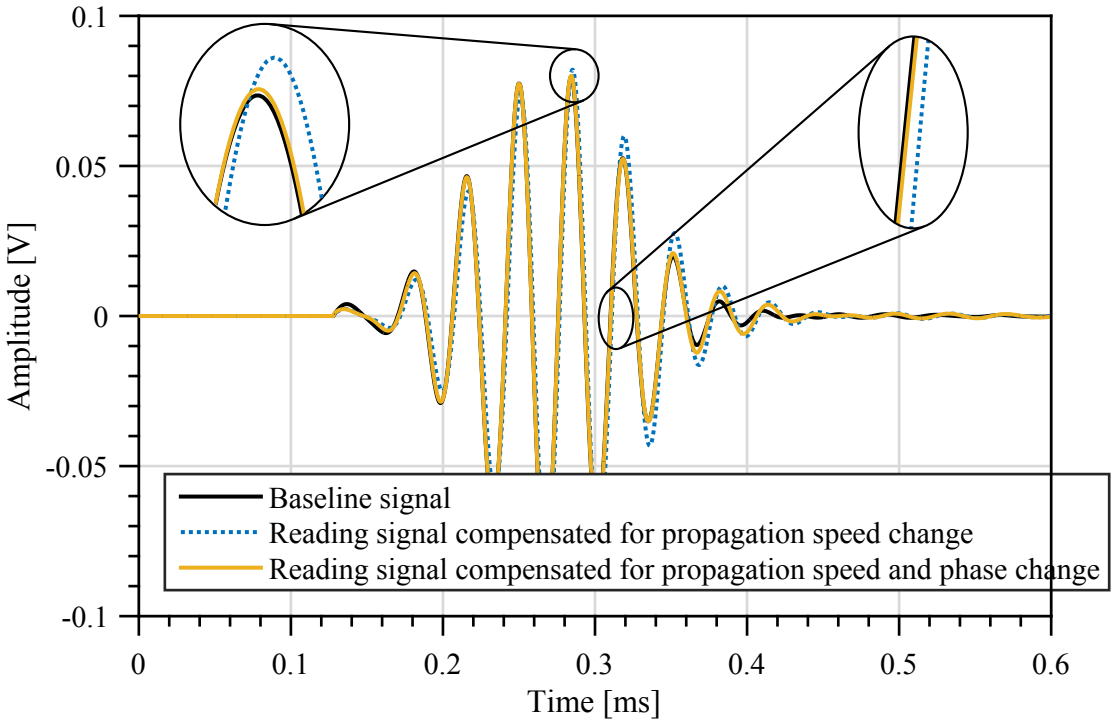

Figure 6.14: The incident wave of the ultrasonic signals: baseline signal (black), reading signal compensated for propagation speed (dashed), phase and propagation speed change compensated (grey). The temperature difference between the baseline and the reading was 41.5 °C.

(stretched) reading signal, the frequency dependent phase correction will automatically correct for the frequency noise as well.

6.6.2 Residual signals

The improvement of the proposed compensation method can be demonstrated on the residual signals. Figure 6.15 shows the calculated residual signals when only the propagation speed is compensated (shown in dashed blue), and when the phase response change is compensated as well (yellow). As expected, the residual is highly improved at the echo location, and the residual is not sacrificed at the coherent noise part of the signal.

20 dB improvement was achieved at the echo location (1.5-1.7 milliseconds) compared to the conventional signal processing techniques, when the temperature difference of the pipe during the acquisition was 41.5 °C. However, at regions where coherent noise is temperature dependent (such as tail of echo) only 7dB improvement was reached. One possible reason is that the tail of the echoes are temperature dependent (further to the

transducer induced changes). Other possible reason is that the direction control might not be perfect, as the echo coming from the other direction (arriving roughly at 1.8 ms) is not perfectly processed in the directional control algorithm. Further evaluation was not performed on the tail behaviour so that the measurement setup is not disturbed, as during the heating cycles a long-term stability evaluation took place as well.

The improved residual levels results in a much higher sensitivity (up-to 7 dB) for small defects at the feature reflections.

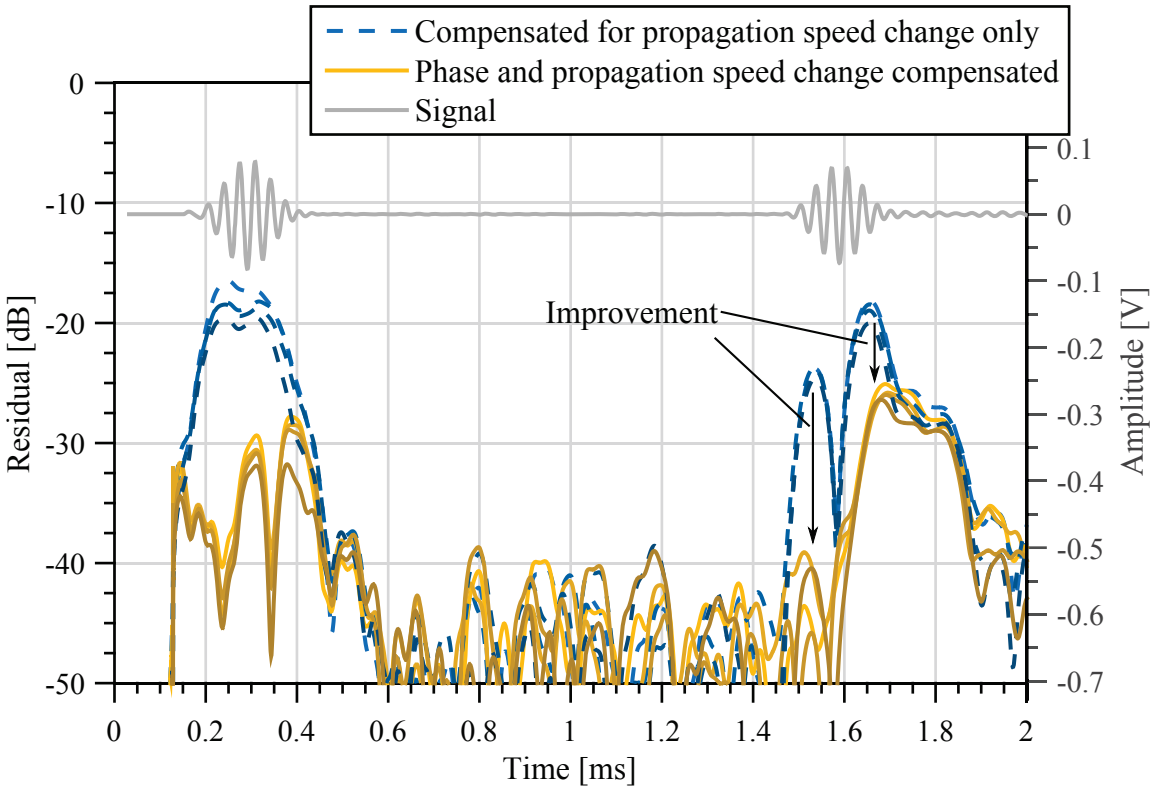

Figure 6.15: Calculated residual signals when the temperature difference between the baseline and the reading signals was 41.5 °C. The residual is calculated when the reading signals were compensated for the propagation speed only (dashed), and when it was also phase compensated (solid). For demonstration purposes for each compensation strategy four set of residual signals are shown with different darkness. The signals corresponding for each residual were acquired at a different time during the thermal cycling.

The compensation method was tested whilst several temperature cycles were performed on the system. The signals were collected during every cycle and on roughly every degree Celsius temperature change. Further results were selected from the large acquired data-set. Figure 6.16 shows the residual signals for the conventional algorithm (dashed) and the proposed phase compensation algorithm (solid) for 15°C (a) and 30 °C (b) temperature

difference.

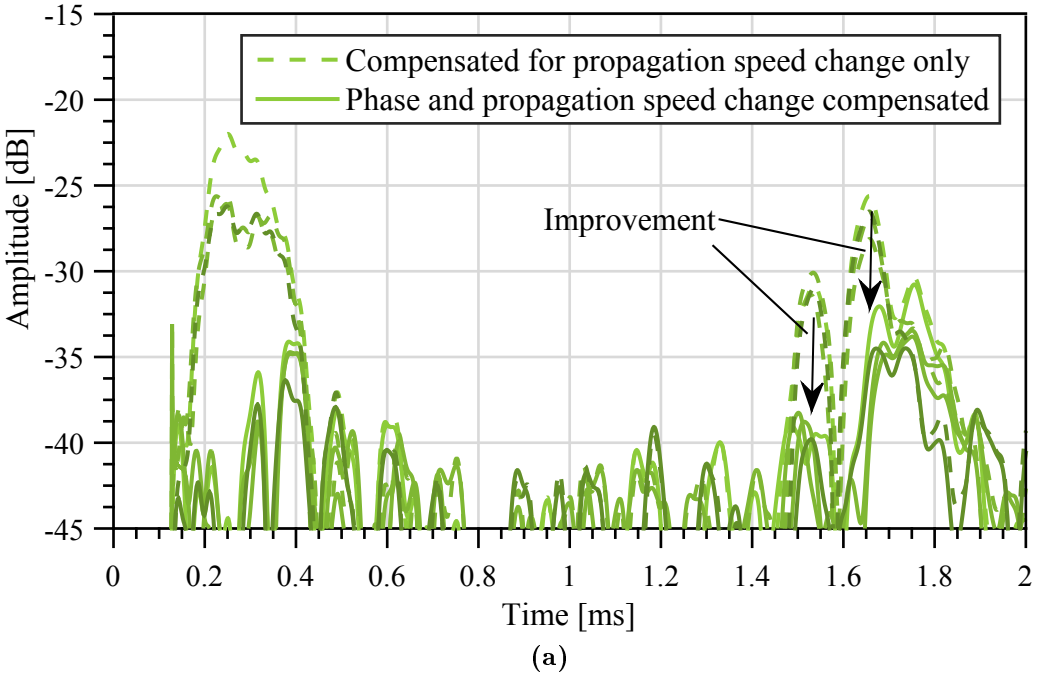

(a)

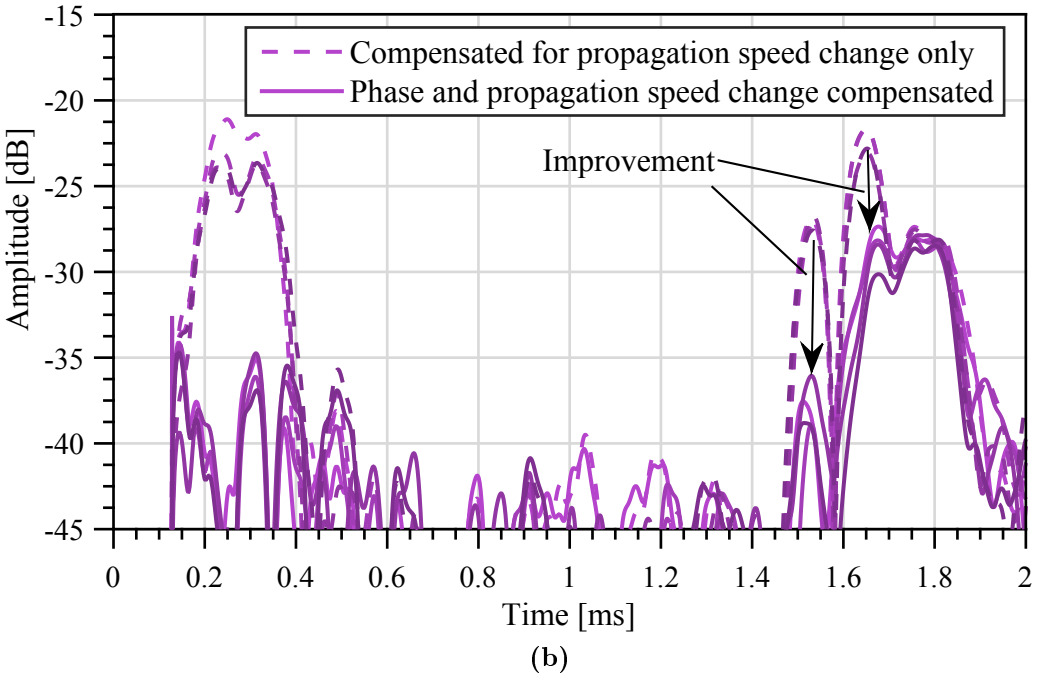

(b)

Figure 6.16: Residual signals plotted for conventional signal stretch (dashed), and when the hereby-presented temperature compensation algorithm was applied (solid). The residual signals and the improvement of the proposed compensation method is shown when the temperature between the baseline and the reading signals was 15°C (a) and 30°C (b). The residual signals are shown for four signals with a different darkness. The compensated signals were selected from different temperature cycles to demonstrate robustness of the technique on different signals.

Obviously, for lower temperature differences fewer temperature effects are to be removed, therefore the phase compensation has lower effect. This also implies that for large temperature differences (100°C+) the phase compensation method will have even larger effect, and could be essential for monitoring applications.

6.6.3 Improved stretch factor estimation

A large number of reading signals were acquired when the pipe temperature was varied from room temperature up to 80 °C (maximum temperature of the pipe outer surface being 73 °C). The propagation speed was estimated for each reading signal. Figure 6.17 shows the estimated propagation speed as a function of the pipe temperature for each iteration step. The estimated stretch factor is already close to the final estimate after the second iteration step. It is thought, that the number of iterations that is needed for a good estimate depends on the echo location. In the case when the source of the echo (reflector) that is used for propagation speed estimation is far enough (>2-3 meters) from the receiving transducer, the convergence is quick.

6.6.4 Results when defect reflection is present in the acquired reading signal

The iterative phase compensation method was tested when a small defect reflection is present in the acquired reading signal. A synthetic reading signal (artificial damage component superposed on acquired signals) was created, where a simulated defect reflection is superposed onto the experimentally acquired signal. The use of synthetic datasets is common for damage detection investigations [54, 180, 181]. The defect reflection is simulated to be 200 mm from the pipe end, therefore the defect reflection is expected to be around 1.45 milliseconds which overlaps with the pipe end reflection. The simulated amplitude for the defect reflection is 3% compared to the pipe end reflection.

Both the conventional stretch based and proposed iterative (stretched and phase compensated) temperature compensation methods were applied onto the reading signal and the residual signals are plotted in Figure 6.18. For reference purposes the residual is plotted with dashed lines when no defect is present in the reading signal. Also, the baseline signal

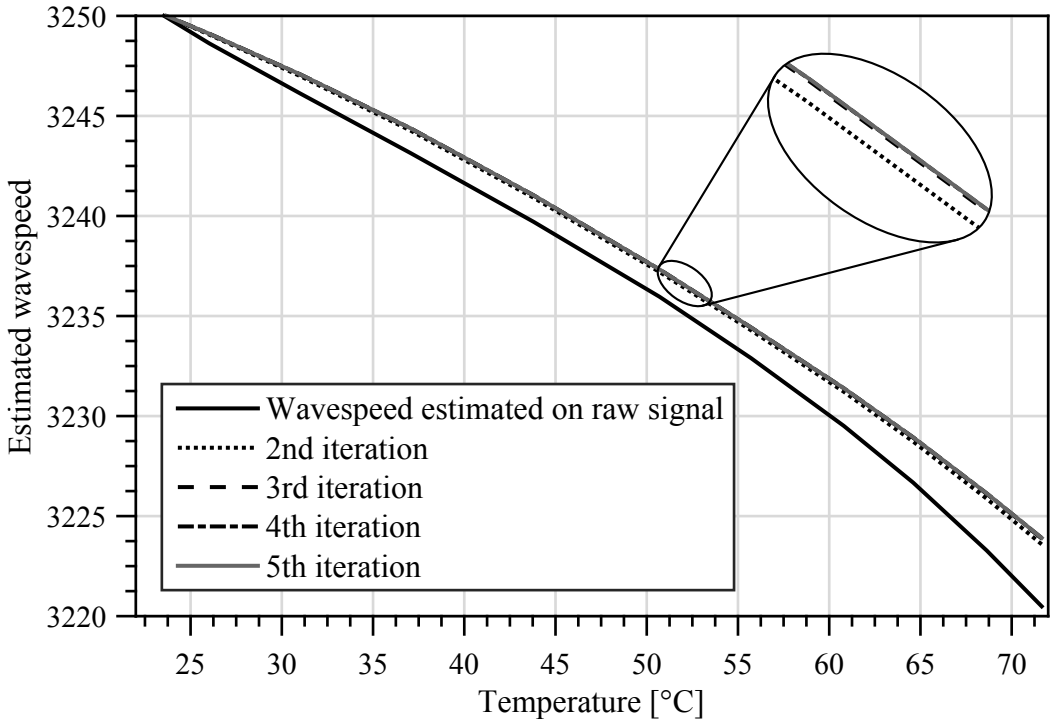

Figure 6.17: Estimated wavespeed as a function of the pipe temperature for each steps in the iterative compensation method. The estimated wavespeed quickly converges to the final value.

is shown in grey for clarity. The residuals for the conventional stretch based temperature compensation is plotted in Figure 6.18a, where the presence of the defect reflection does not increase the residual level significantly (at 1.45 ms). In contrast, Figure 6.18b shows the residual signals when the iterative temperature compensation method was applied. When the defect reflection is present in the reading signal, the residual (at 1.45 ms) is significantly larger compared to the defect-free option. This implies, that by compensating for the transducer phase response changes the residual levels are decreased, and the defect reflection is easier to identify from the residual signals.

In the residual signal from 1.65 ms to 1.85 ms the coherent noise is relatively large as the pipe end reflection is a 100 % reflector. It is expected that most features in pipelines (e.g. welds) will have a reflection coefficient ~10%, so that the noise in those residuals are expected to be lower as well.

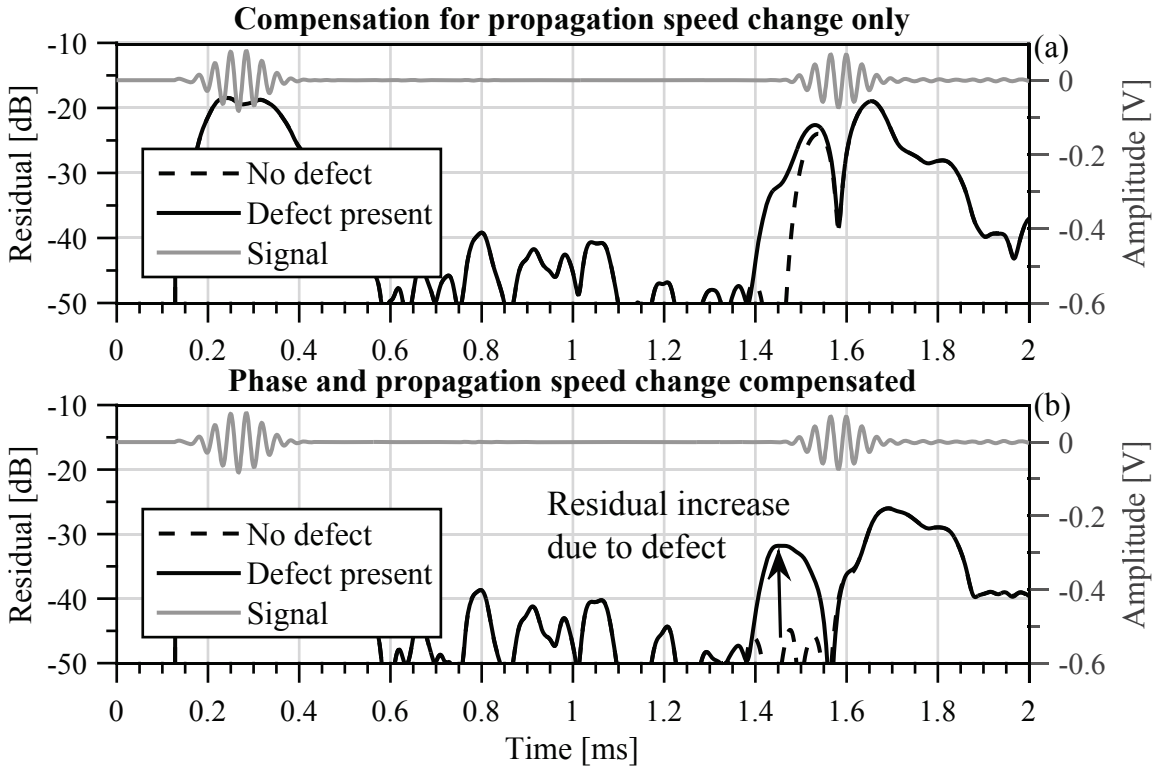

Figure 6.18: Residual signals using synthetic reading signal (a 3% defect reflection is simulated 200 mm away from the pipe end reflection and is added to the acquired measurement data). Adding a defect to the reading signal has only a small effect in the residual levels for convention stretch-based temperature compensation (a), however the presence of the defect significantly increase the residual levels when the proposed iterative compensation method is used (b). The temperature difference between the baseline and the reading signal was 41.5 °C.

6.7 Discussion

6.7.1 Uneven pipe temperature

As discussed in the previous section, the conventional temperature compensation methods will result in an imperfect stretch estimate as the excitation phase differences influence the stretch estimation algorithm. The newly proposed method has the advantage of estimating a more precise stretch factor. The benefit of the precise stretch factor estimation is legitimate only if the pipe temperature is fairly uniform along the whole pipe. In contrast, it is possible for large structures to have a temperature gradient along the axis, for example if insulation is missing, or part of the pipe is buried. In case the pipe segments are at different temperatures, it is suggested that multiple stretch factors are applied to different pipe segments [35]. Should multiple stretch factors be required for the compensation, the

importance of a precise stretch estimate is reduced. However, the improvement of the phase compensation will still be beneficial, as the defect monitoring capability will be improved at the feature locations by the reduced the residual levels.

6.7.2 Transducer ageing

It is possible, that the transducer performance changes over time. For example the degradation of bonded piezoelectric transducers was investigated by researchers [65, 66], and it was concluded that amplitude and phase changes might result when the adhesives are affected by cyclic thermal loading. In case the reading signal is collected on a degraded transducer (assuming the signal strength is still adequate), the phase compensation method would be able to detect and correct for the phase changes caused by the degradation. The severity of the degradation could then be monitored from the phase difference estimates.

A similar concept was developed by Mulligan et.al. for correcting the ultrasonic signals in imaging applications [63]. The phase difference caused by the degradation was estimated from electrical admittance curves, rather than a reference part of the signal.

6.7.3 Phase compensation for signal processing methods other, than baseline subtraction

The improvement of the proposed compensation method was demonstrated with the improvement in the residual signals. One might ask, what improvement is reached when other damage detection algorithms, like Independent Component Analysis [53, 54], Singular Value Decomposition [52] are used. It is thought that the phase compensation algorithm should improve the damage detection algorithm for those signal processing methods as well. The ICA method still searches for changes in signals (which is plotted in the weights functions), with the difference, that the changes are plotted individually, for different parts of the signal (components). Then, by reducing the severity of temperature effects with the phase compensation, the weight of the non-damage related components will decrease as well.

6.7.4 Masking the defect signal

Usually, processing the signals there is a concern, that the damage related signal component is suppressed by the EOC compensation method. The same question arises for the proposed phase compensation method. However, as the phase difference is estimated on the incident wave (early echo), a damage far from the transducer will not influence the estimated phase correction value. On the other hand, for the presented measurement setup, the incident wave is a 100% amplitude signal. Small defects (near the transducers) will be superposed to the incident wave, but will not change the estimated phase drastically. For example, a 5% defect near the incident wave will result in a 0.5% error on a 10% reflector. As an extra caution, it is still an option to perform the baseline subtraction with and without phase compensation and compare the results.

6.8 Summary

In this chapter, a novel approach is proposed which compensates for both the transducer phase response changes and the propagation speed changes on the ultrasonic signal. An iterative compensation method is suggested, which uses the incident wave for phase change estimation, and the rest of the ultrasonic signal (echoes) for propagation speed change estimation. The propagation speed, then the excitation phase difference is compensated in each step, where a more precise estimation can be performed in each step. The estimate values converge to their final value quickly, and the convergence region of 0.1% is reached within 3 steps.

It was also investigated when the transducer phase response change is frequency dependent. For this problem, a frequency depended phase correction was suggested. The proposed method has the advantage that it automatically compensates for the so-called "frequency noise" which is the result of signal stretch applied onto the signals. The improvement of the proposed compensation method compared to the single-stretch based methods is demonstrated on the residual signals. 20 dB improvement was achieved at the echo location compared to the conventional signal processing techniques when the temperature difference of the pipe during the acquisition was 41.5 °C. However, at regions

where coherent noise is temperature dependent (such as the tail of the echo) only 7dB improvement was reached. The decrease in the residual signal means that the effects of the temperature change are better compensated, therefore smaller defects can be identified near the reflectors.

Chapter 7

Long-term stability of the Guided Wave EMAT system

7.1 Introduction

Structural Health Monitoring (SHM) systems rely on stable transducers to guarantee the required sensitivity for damage detection. This chapter investigates the long-term stability of the torsional guided wave Electromagnetic Acoustic Transducer (EMAT) that was developed in this thesis. The stability is evaluated from ultrasonic signals, which were acquired during a 1.5-year long test. The transducer and the structure were exposed to temperature changes (up-to 80°C 100+ times). The observations of the long-term test results and the causes of the behaviour are discussed.

Parts of this chapter have been extracted from publication [P4], which has been accepted for publication in the journal "Structural Health Monitoring".

7.2 Motivation

During guided wave monitoring signals are compared to estimate structural changes. However, monitoring of structures can only be performed reliably when stable transducers are used for the signal acquisitions. Any instability of the transducer could change the signal, and that change might be mistaken for a defect in the structure. By deploying trans-

ducers which have high stability for long time periods even small defects can be identified as signal changes caused by small reflections from defects exceed the result of transducer changes. Transducer stability is therefore a key requirement for SHM applications. Only a few reports that investigate the long-term stability of the sensors are available. Measurements with piezoelectric transducers have shown great performance in the short-term, but their performance decreased for long-term applications [64]. Different research has reported that temperature swings alter the performance of bonded piezoelectric transducers [65,66]. Electromagnetic Acoustic Transducers (EMATs) however operate contactless, and do not need to be bonded to the structure. Because of their contactless operation mechanism, researchers suggested that they are also stable [67]. However, just because EMATs are not bonded it cannot be directly inferred that they are stable. Therefore, the long-term stability of EMATs is evaluated in this research work.

7.3 Possible effects of instabilities in a transducer array on the ultrasonic signal

A torsional guided wave transducer for applications on a 3-inch NPS pipe with 12 equally distributed excitation locations (patches) around the circumference was designed [182]. Pure torsional waves are generated when each patch is excited by the same force [183]. Ideally, these excitation forces remain the same throughout the monitoring period (long-term life of the installed transducer). However, transducer (force) output stability might be disturbed if the structure is exposed to large temperature variations. The repeated exposure to temperature swings might alter the performance of the excitation mechanism as for example encountered in piezoelectric transducer systems [65]. Both transduction and reception mechanisms are important, as the acquired signals are influenced by the reception mechanism as well.

The excitation waveform for the guided wave inspection is usually a narrow-band signal (Hanning windowed tone-burst for our measurement) [94, 95], therefore, the changes on each individual excitation patch can be described as a combination of a change in amplitude and a change in phase. These changes will then alter the acquired ultrasonic signals.

Two major categories of transducer changes are distinguished by the author depending on how the excitation patches change compared to one another. The first is, when all excitation patches in the EMAT array change by the same amount (same amplitude and phase), as shown in Figure 7.1a. The second (less favourable) case is, when the transducer degradation is not uniform on all excitation locations as shown in Figure 7.1b.

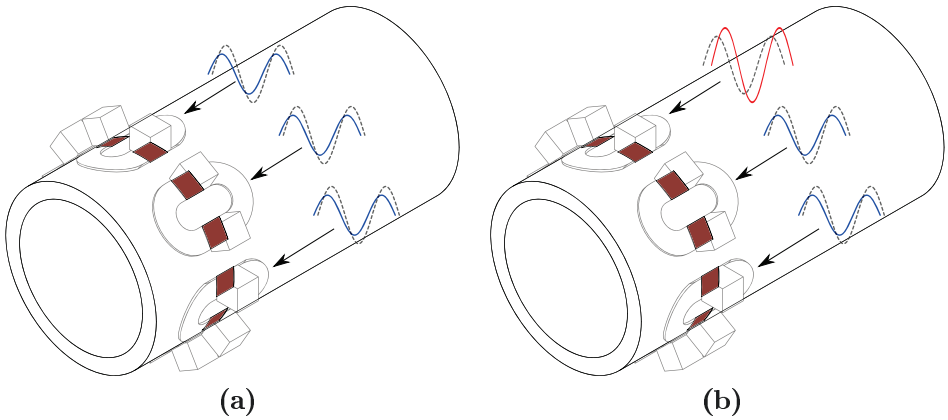

Figure 7.1: Different cases of transducer array degradation: all excitation patches generate tangential forces to excite torsional wave in the pipe. The excitation force might change in a uniform way (a), or some of the excitation patches are altered by a different amount (b). The original (reference) excitation is shown by dashed line, and the changed force signals are shown in blue and red.

7.3.1 Uniform changes on all excitation patches

The effect caused by transducer degradation is easier to predict for the first (uniform) case when all excitation patches change in the same way. The effect of uniform phase change is significant where wave reflections are present in the ultrasonic signals. The change in the echoes will result in an increased residual signal, and therefore limit the damage sensitivity near reflectors. The uniform change in excitation amplitude will result in an ultrasonic signal, which is a scaled version of the original signal. This can simply be compensated by scaling the signal in post-processing. Alternatively, if the phase of the excitation signal changes uniformly, the excited signal will suffer the same phase change. It will then result in a signal where the carrier sine wave is changed, but the envelope of the signal is unaffected. The compensation of this uniform phase change is a bit more challenging, but is possible when a reference wave packet is available in the signal. A

proposed compensation method is briefly referred to in Section 7.7.1.

7.3.2 Non-uniform changes on the excitation patches

A more complex situation arises when the excitation signal changes in a different way on each excitation patch. This will result in a non-uniform force distribution around the circumference (or a change in the default distribution) and can lead to the excitation of other unwanted modes (like flexural modes). These modes are usually dispersive and travel at different speed than the main torsional wave. This will then change the coherent noise of the whole signal and would reduce the damage sensitivity on the whole length of the monitored pipeline. Unless the actual excitation forces can be measured at each location, the uneven transducer degradation is difficult to compensate for.

7.4 Stability evaluation of the Guided wave EMAT array

7.4.1 Temperature cycling of the EMAT Guided wave transducer

The design of an Electromagnetic Acoustic Transducer (EMAT) was presented in Chapter 3. In Chapter 5 it has been detailed how the transducer can be modified for high-temperature applications so that its maximum operating temperature increases above 200°C. However, the long-term tests were started before developing the high-temperature resistant transducer, and the transducer that was tested for long-term stability was equipped with Neodymium-Iron-Boron magnets only. The Neodymium-Iron-Boron magnets (used for the prototype) are rated to the maximum operating temperature of 80 °C, therefore the temperature of the transducer and the structure was kept below this rating.

As also described in Chapter 3 transmitting and receiving transducers were placed onto a 5-meter long 3-inch NPS 3 SCH 40 carbon steel pipe as shown in Figure 7.2. The structure was exposed to repeated temperature swings to imitate the environmental changes and to accelerate any long-term transducer changes. A 5-meter long electrical heater (custom-made finned air heater, Clarian UK Ltd.) was placed inside the pipe along its axis. The

transmitter and receiver transducers are separated by 0.4 m so that the incident (direct) wave is partially separated from the cross-talk. The reception of the incident wave is made possible by a special cross-talk reduction design (see Chapter 3); so that the cross-talk signal does not mask the incident wave [144].

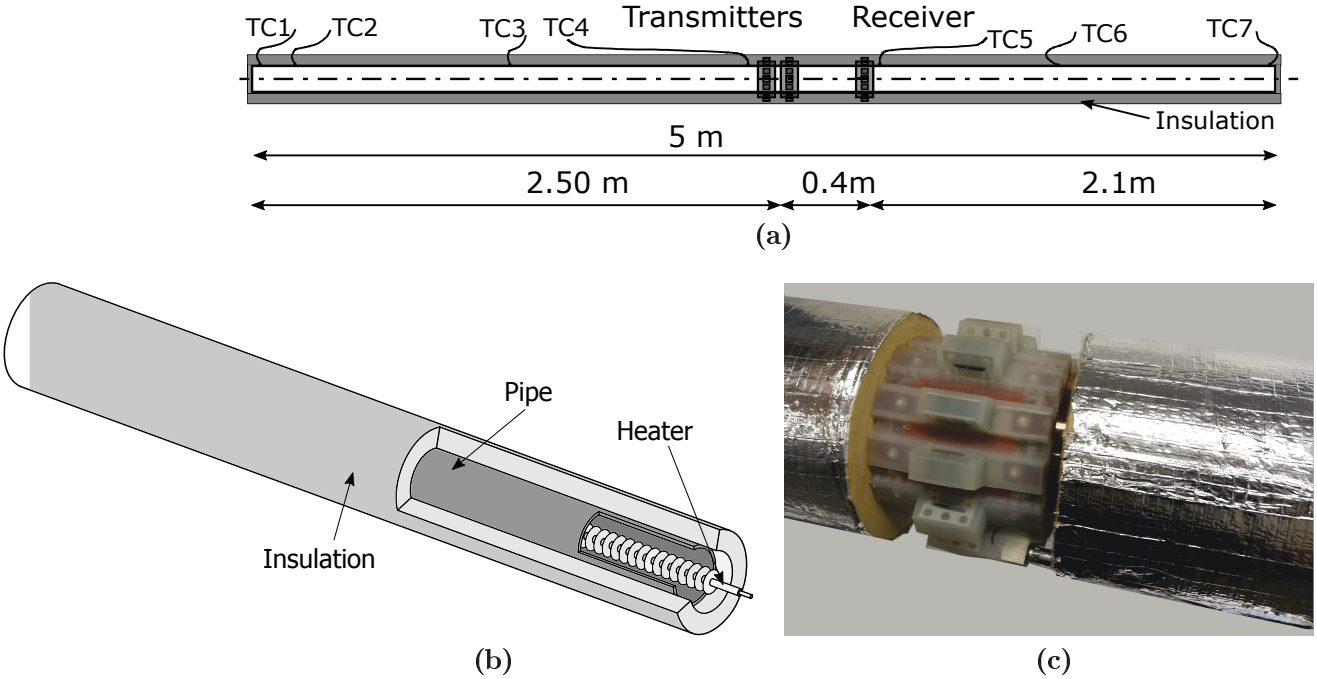

Figure 7.2: Measurement setup for evaluating the log-term stability of EMATs: Transmitter and receiver transducers are placed onto a 5-meter long 3-inch NPS 3 SCH 40 carbon steel pipe. The temperature of the pipe is monitored at 7 locations (a). An electric heater placed at the core of the pipe is used for heating (b). The outside of the pipe is insulated for more uniform temperature distribution (during the tests insulation was placed over the transducer as well) (c).

The EMAT array transducer was installed onto the pipe in December 2016, and regular measurements were recorded for a period of over 1.5 years. After initial measurements were acquired at room temperature for ~6 weeks the pipe was heated by the 5 m long electrical heater element, and the power was controlled by a feedback temperature controller (On/Off Temperature Controller, RS Components Ltd.). The heater was placed inside the pipe along its axis before starting the long-term measurements so that the ultrasonic signals are not affected upon installation. The pipe was then exposed to numerous (100+) heating cycles as shown in Figure 7.3. In each heating cycle, the pipe was heated to a selected temperature, this temperature was then maintained until a steady temperature was reached along the pipe, and signals were acquired during the cooling stage. The

temperature was recorded with 8 thermocouples distributed along the pipe (TC-08, Pico Technology) as shown in Figure 7.2. 7 thermocouples were placed onto the outside of the pipe, one was placed in the inside. In total 9440 directionally controlled [122, 184] signals were collected between the beginning of December 2016 and the beginning of September 2018. The temperature of the pipe at the receiver transducer location for each measurement is shown in Figure 7.3. The repetition rate of the measurements was set so that signals were recorded roughly at every degree Celsius during cooling off. Close to room temperature, the measurements were initiated every 2-3 hours. Note that the x-axis in figure 7.3 shows the measurement number and its scale is not representative of the actual elapsed time of the monitoring experiment. (I.e. far fewer measurements were taken between 2018 January and September)

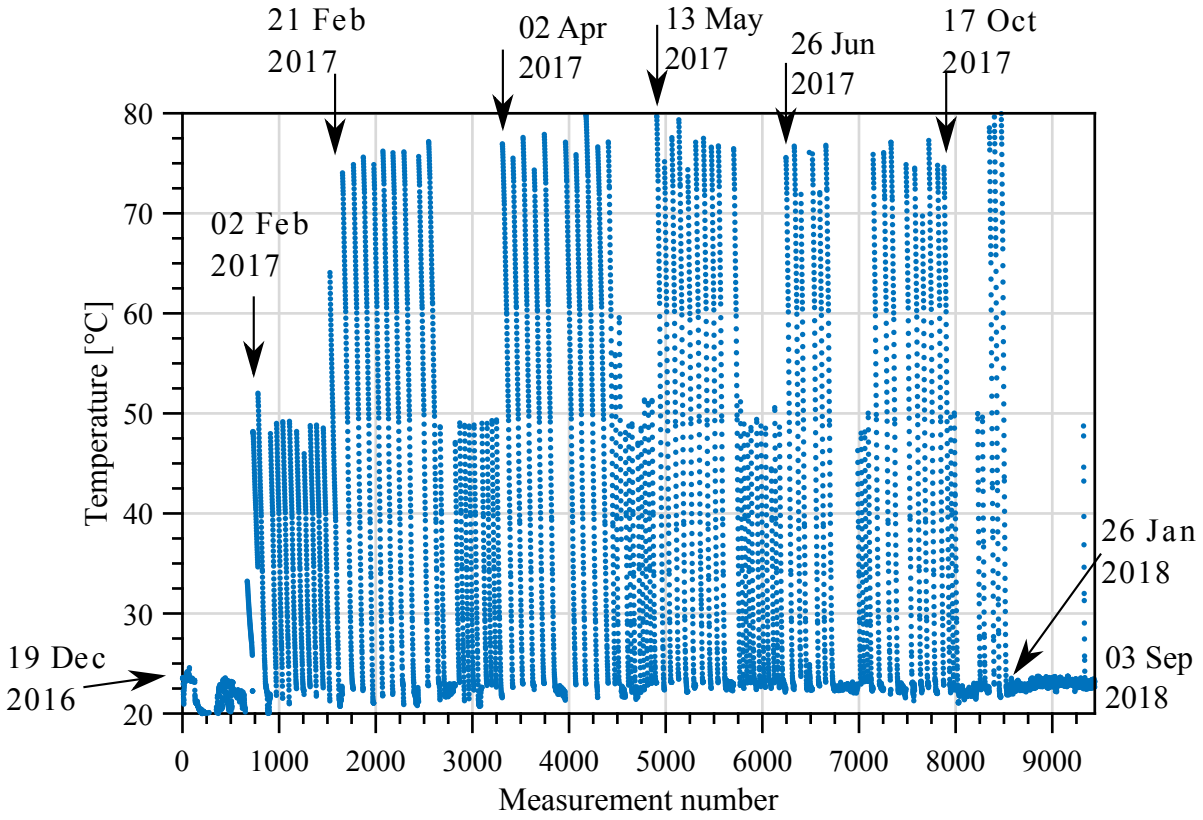

Figure 7.3: Temperature reading of thermocouple 5 (installed at the receiving transducer) for each measurement during the long-term temperature cycling of the EMAT transducer.

7.4.2 Long-term stability of the guided wave EMAT array

During the 21 months of long-term measurements, a large number of guided wave signals were collected on the 3-inch pipe. The acquired signals have been compensated for change in the torsional wave's propagation speed by the Baseline Signal Stretch [51, 176, 178] method. An optimal stretch factor is estimated on the pipe end reflection, and the whole signal is stretched accordingly. The temperature compensation is performed before the stability evaluation so that the investigated parameters are less affected by temperature. A few randomly selected room temperature signals (22.6-23°C) (travelling to the right direction of the pipe) are shown in Figure 7.4. The two large wave-packets in the time signal are the incident wave (0.2 - 0.35 milliseconds) and the pipe right end reflection (1.5 - 1.7 milliseconds). Between the two echoes, the coherent noise can be observed.

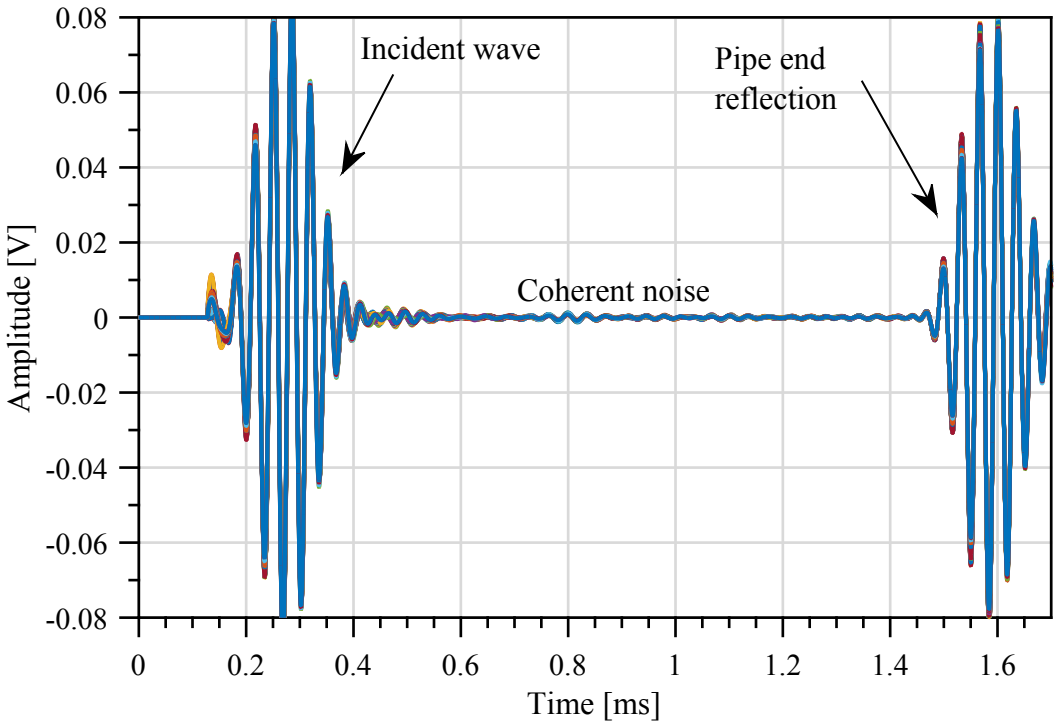

Figure 7.4: Experimentally acquired right traveling torsional guided wave signals. 57 randomly selected signals are shown which were acquired on a room temperature pipe (22.6-23°C) over the 14 months monitoring period. Signal stretch was applied onto the signals to reduce the effect of propagation speed changes.

As mentioned previously, the non-uniform changes in the excitation patches will generate (or change) the unwanted modes, which will change the coherent noise of the signal. The

signal part from 0.73 to 1.44 milliseconds was selected to evaluate the coherent noise over the long-term evaluation period. The maximum value of the residual signal (difference between the baseline and the reading signal) for the given time period was collected for each measurement. Figure 7.5 shows the evaluated maximum residual values for each room temperature measurement relative to the incident wave amplitude. On examination of the residuals, it was noticed that the residual level varied for some measurements, but no long-term trend can be observed during these random variations. When observing the corresponding signals it was noticed that variations in Figure 7.5 are the result of changes in the SNR of the measurements. By the end of the 21 months, the observed difference in the coherent noise level was 0.8%. This means that defects with small reflection coefficient (e.g. 1.5-2%) would be picked up with high confidence, and the damage detection capability is not affected. Damage was not introduced to the pipe, so that the long-term measurement is not affected. Furthermore, as the change in coherent noise level was evaluated as the maximum value of the residual signal over the whole range of the time period (0.73 to 1.44ms) this estimation is very conservative.

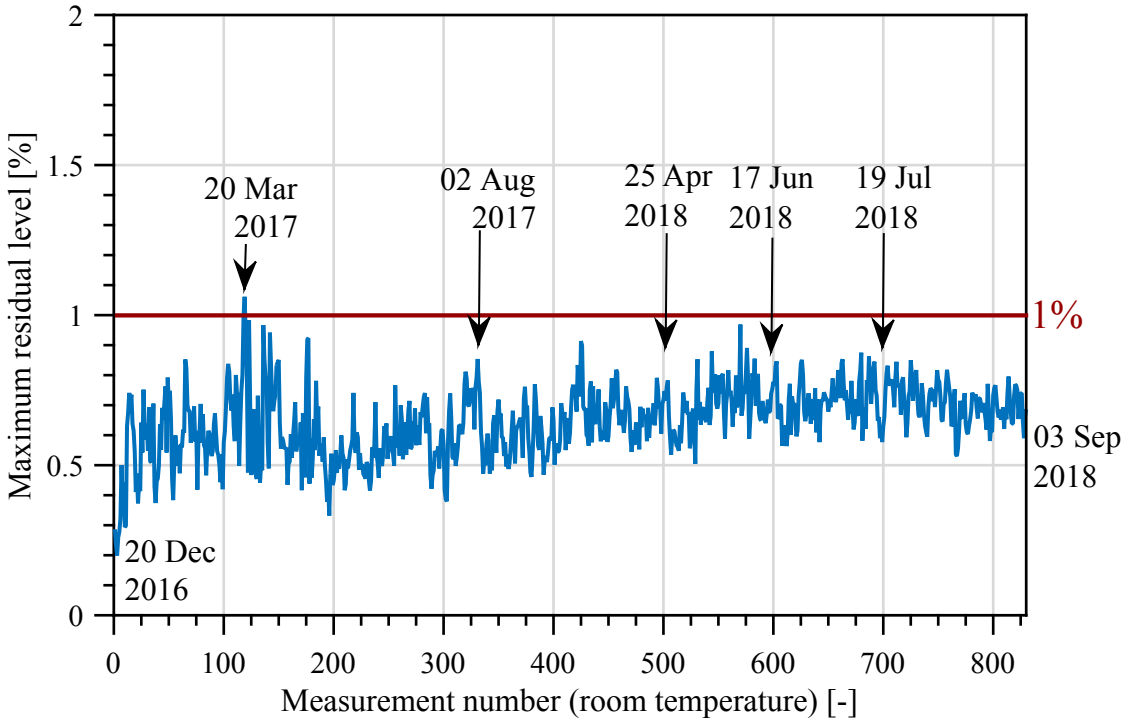

Figure 7.5: Maximum difference between each room temperature signal and the baseline at the coherent noise part of the signal.

The stability of the transducer is also evaluated on the incident wave (0.2-0.35 milliseconds) as this part of the signal has propagated only for a short time, and any change is quite likely to be originating from changes in the transducer. The Hilbert envelope [97] was calculated for the signals, and the peak signal amplitude is recorded for each measurement. Furthermore, the phase of the incident wave-packet is evaluated after applying a Tukey window. The frequency spectrum is calculated from the windowed time signals, and the phase value at the centre frequency (27 kHz) is recorded for each measurement. The recorded amplitude and phase values are shown in Figure 7.6 for each measurement.

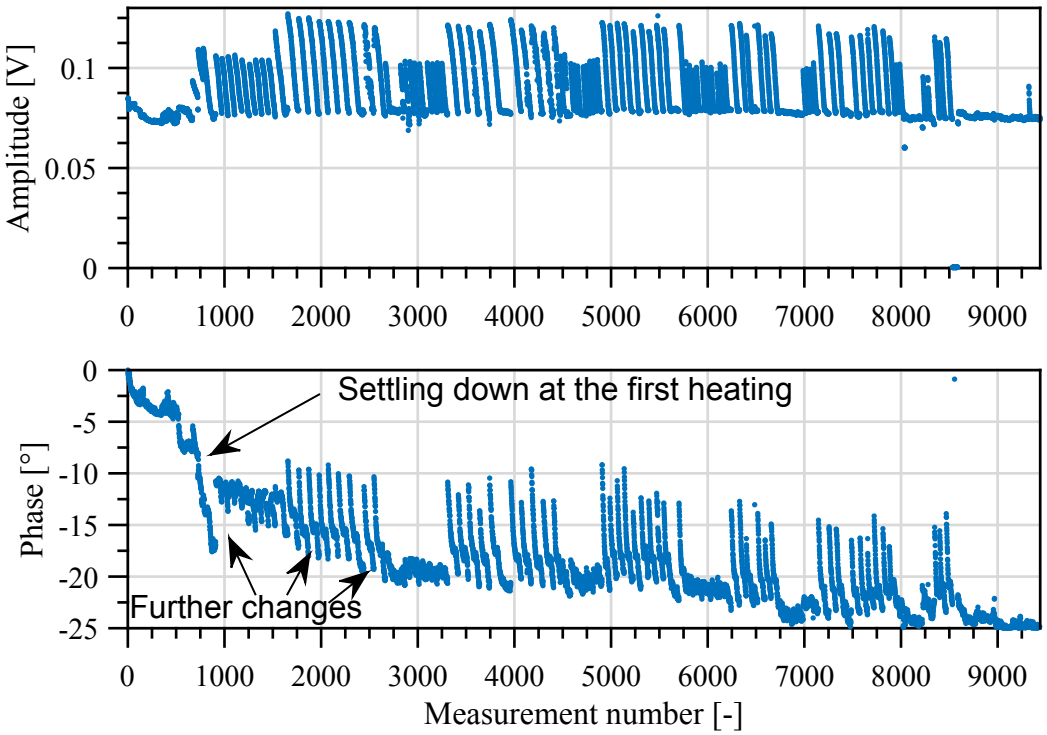

Figure 7.6: Evaluated amplitude (a) and phase (b) values of the incident wave-packet of the acquired ultrasonic signal. The values were evaluated for every measurement during the long-term temperature cycling of the EMAT measurement system. A temperature dependent behaviour can be seen for both the amplitude and the phase, but the long-term trend is obvious only for the phase values.

The regular spikes seen on both amplitude and phase chart is caused by the temperature dependent behaviour of the transducer. When observing the long-term effects, it can be concluded that the amplitude remained stable for the whole measurement, and no obvious irreversible trend is observed (last signal is within 3.7% of the original value). However, long-term changes can be observed on the phase of the wave-packet. The majority of the

phase change (17.24°) happened before the highest temperature exposure. An additional phase change is observed on the following 90 heating cycles, but this change is much smaller (additional 7.2°). The change in the phase values of the incident wave highlight the transducer changes which are the result of uniform change on all excitation patches.

7.5 Investigation of instability sources

The result of the long-term instability test is adequate for SHM applications; however, it is worth investigating what mechanism influences the stability, so that further improvement can be achieved. The torsional guided wave EMAT system is complex, and the cause of the small, but obvious, observed long-term change is unknown. Therefore, sub-systems in the EMAT system were tested to assess their stability individually. The following investigations were performed. The long-term monitoring (measurement setup described previously) was left undisturbed, and a new test setup was built in order to investigate the instability sources.

7.5.1 Signal acquisition electronics system

It was ruled out that the electrical transmit and receive instrumentation of the EMAT system could have given rise to the changes by regularly connecting the instrumentation to a signal attenuator (rather than the EMAT) and tracking the response across it. The results did not show any sign that the instrumentation could be the cause of any changes in the signal. Furthermore, as the instrumentation itself is placed outside the insulation of the pipe, no accelerated change is expected in its performance when the pipe is heated for the first time. Therefore, the observed long-term drifts are most likely to be associated with transducer related changes.

7.5.2 Transducer input current

Another long-term measurement was started where the input current of the transmitting transducer was measured in addition to the signal itself. The pipe was exposed to 35 heating cycles, with the temperature of the pipe reaching 80 °C. The measured current

waveforms show reversible changes as a function of the temperature (as presented in Chapter 6, [185]), but no long-term change or degradation was noticed. Figure 7.7 shows the input current waveforms when the pipe and the transducer was at room temperature. The legend displays the highest temperature the transducer was previously exposed to. The maximum change in the current waveform between the first and the last measurement was 0.39%, and 0.24°. This level of change is insignificant compared to the phase changes of Figure 7.6.

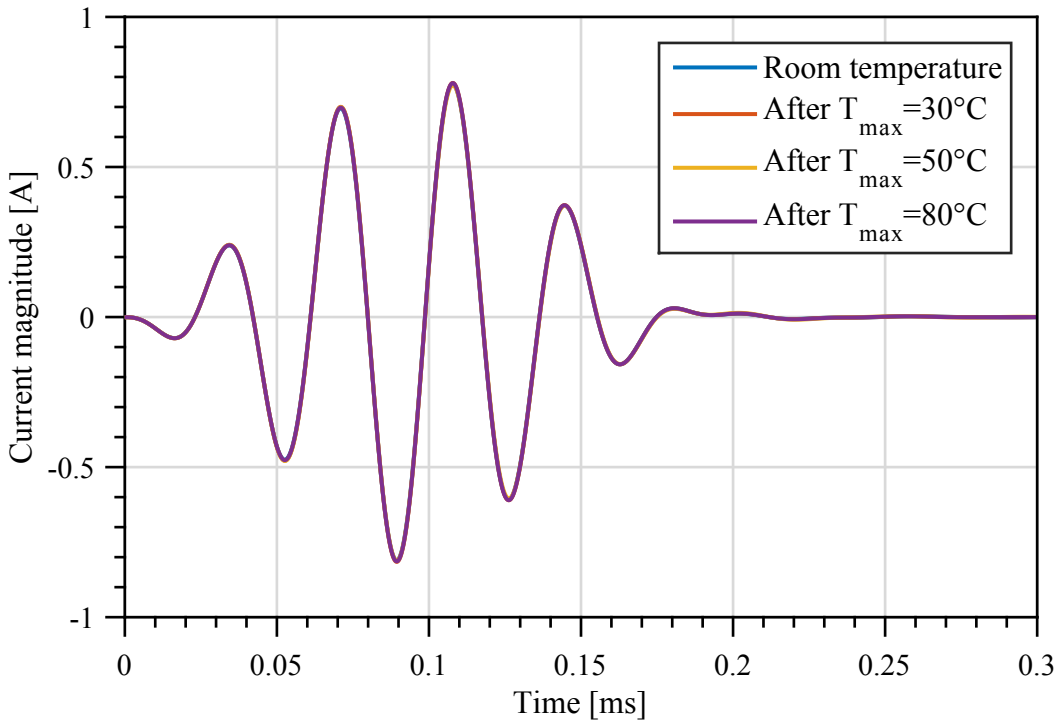

Figure 7.7: Measured excitation current waveforms of the EMAT at room temperatures. Legend shows the highest temperature the transducer and the structure have been exposed to.

7.5.3 Transducer impedance

Additionally, during the repeated measurements the impedance of the transmitter and receiver transducers was recorded as well when the pipe and the transducers reached room temperature. Figure 7.8 shows acquired impedance values (real and imaginary part) of the transmit transducer. The impedance was measured by a 16777k Impedance analyser (SinePhase). The change in the measured values varies by around 0.32% in amplitude and

0.09° in phase. Since both the coil input current and the impedance have been measured, and both are stable, it can be implied that the induced eddy current is repeatable as well. The change in the eddy current could be picked up either from the impedance change or from the input current change.

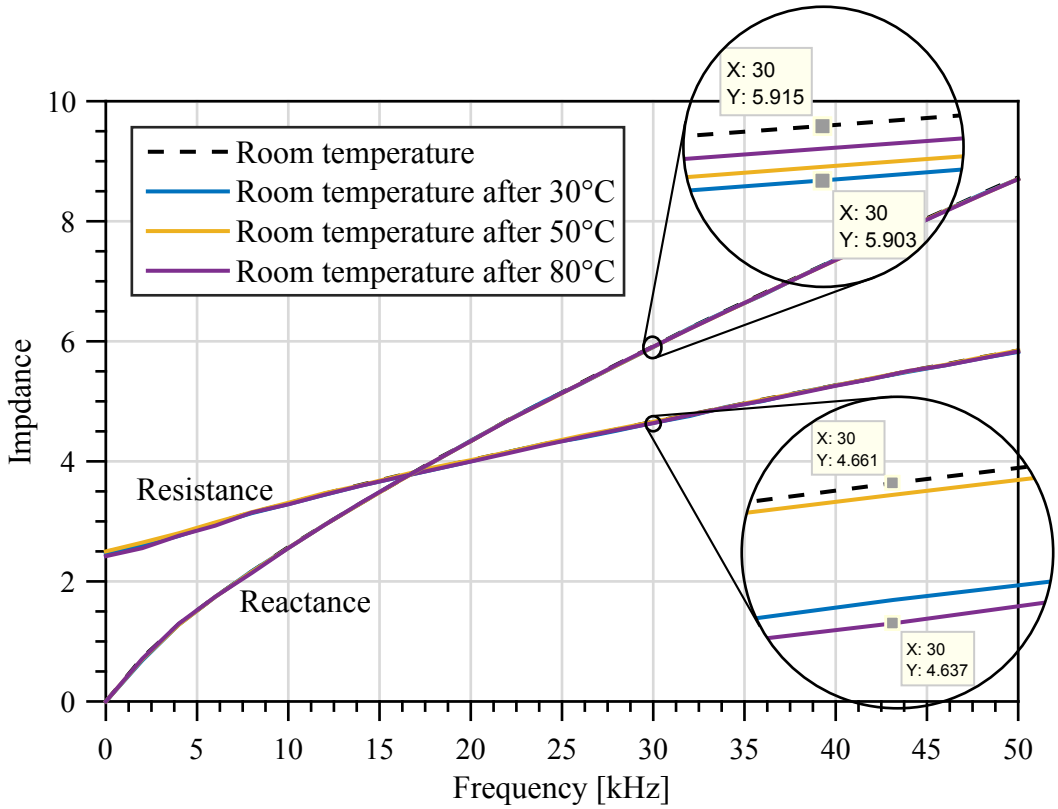

Figure 7.8: Measured impedance of the transmitting transducer for the frequency range of 0-50 kHz. All measurements performed at room temperature, the legend shows the highest temperature the transducer and the structure have been exposed to.

7.5.4 Mechanical position of the transducer

The EMAT array is designed so that the 6 coils (and 12 magnets) are evenly distributed along the circumference of the pipe. If for any reason the position of the coils or the magnets changes the excited ultrasound will change as well. The reported measurements were done on carbon steel pipes. Therefore, the magnets of the transducer will hold the transducer segments in place, preventing the displacement of the segments of the EMAT array. For measurements performed on non-ferromagnetic structures, the EMAT should be clamped to the surface so that the dislocation of the transducer parts is avoided.

7.5.5 Influence of interlayer material

The EMAT transducer operates contactless, does not require any adhesive in order to work. Nevertheless, the EMAT coils are pushed to the pipe surface by the permanent magnets. The Lorentz force of the EMAT is concentrated on the structure's surface, which is in contact with the transducer. Measurements show, that the generated ultrasound is then influenced by the materials contacting the surface. More importantly, if the contact behaviour changes, then the excited ultrasonic signal will change as well (both amplitude and phase). Several tests and measurements were performed, and it is supposed, that the contact material (interlayer between the transducer and the pipe surface) influences the performance and the stability of the low frequency guided wave EMATs. These measurement results will be detailed in the next Section.

7.6 Investigation of contact material influence

As described above, it was observed that the material between the coil wiring and the pipe surface influences the ultrasound that is excited by the EMAT transducers. Originally, a thin Kapton sheet was used to electrically insulate the coils from the conductive specimen. Afterwards, several different insulation materials were tested and it was concluded that the (otherwise repeatable) performance is dependent on the sheet material. Experiments were performed to support and verify the conjecture that the contact material influences the excited ultrasound:

7.6.1 Different contact types

To support the hypothesis of the contact material influence, 5 different contact type was tested:

- A central air gap was introduced over the excitation patch by means of a ceramic spacer that contains a hole (~0.5 mm lift-off)
- the PCB surface was directly in contact to the pipe surface
- Teflon sheet was introduced (Direct Plastics Ltd. PTFE 0.25mm)

- Insulating paper was used, RS Stock No. 775-7469 (0.25 mm)

- Kapton sheet was placed between the transducer and the pipe, RS Stock No. 536-3952 (0.05 mm lift-off)

To reduce uncertainties associated with a single set of measurements, 5 manufactured transducers were tested for each contact type. Additionally, as each of the 5 transmit transducers had two transmit channels, 10 measurements were performed for each type of contact setup. Figure 7.9 shows the relative recorded signal amplitudes. The recorded values were normalized to the default no interlayer material "PCB only" option to hide differences between transducers, and show only the differences caused by contact material influence.

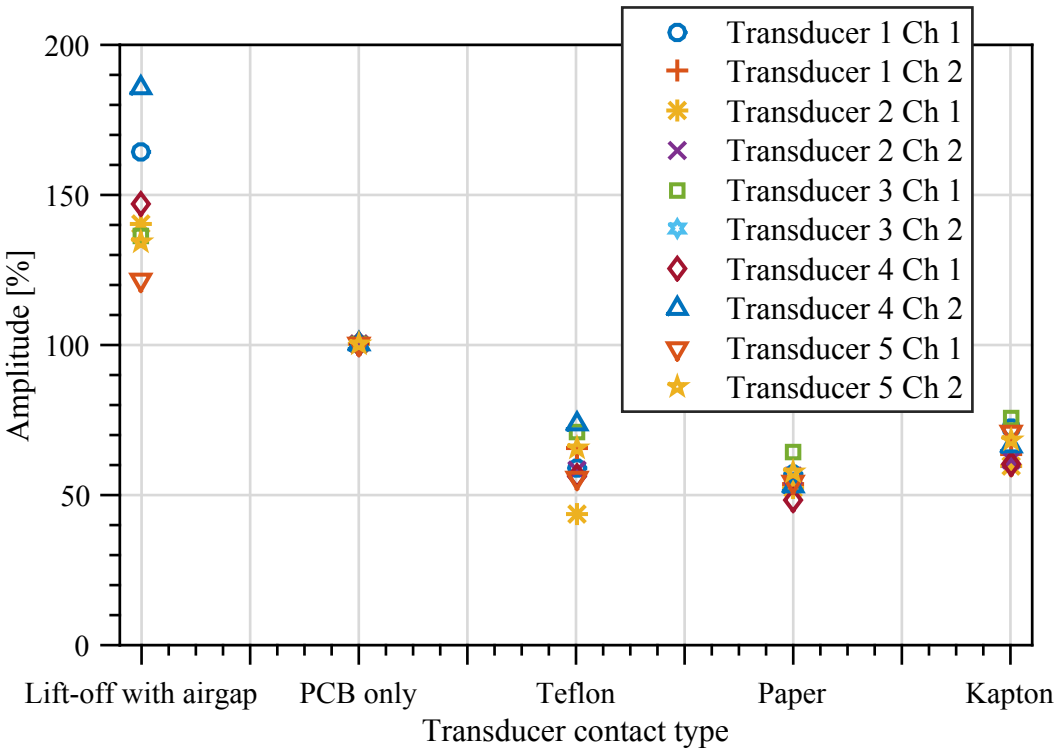

Figure 7.9: Amplitude of the acquired signals for each transducer prototype when different interlayer material was placed between the transducers and the pipe surface.

7.6.2 Amplitude vs lift-off

Ultrasonic signals were recorded with different transducer lift-off values. For these measurements, different numbers of plastic sheets (which do not affect the electric and magnetic fields) were placed in between the transducer and the pipe surface to measure signals with different lift-off values. Decreases in both the eddy current and the static magnetic field are expected for increased lift-off distances. Nonetheless, it was observed that the signal amplitude increases (by 28% at 1 mm lift-off) when spacers were inserted underneath the transducer as shown in Figure 7.10. It is believed that the increase in the signal amplitude is caused by a reduction in the mechanical shear coupling between the transducer and the pipe at the contact patch.

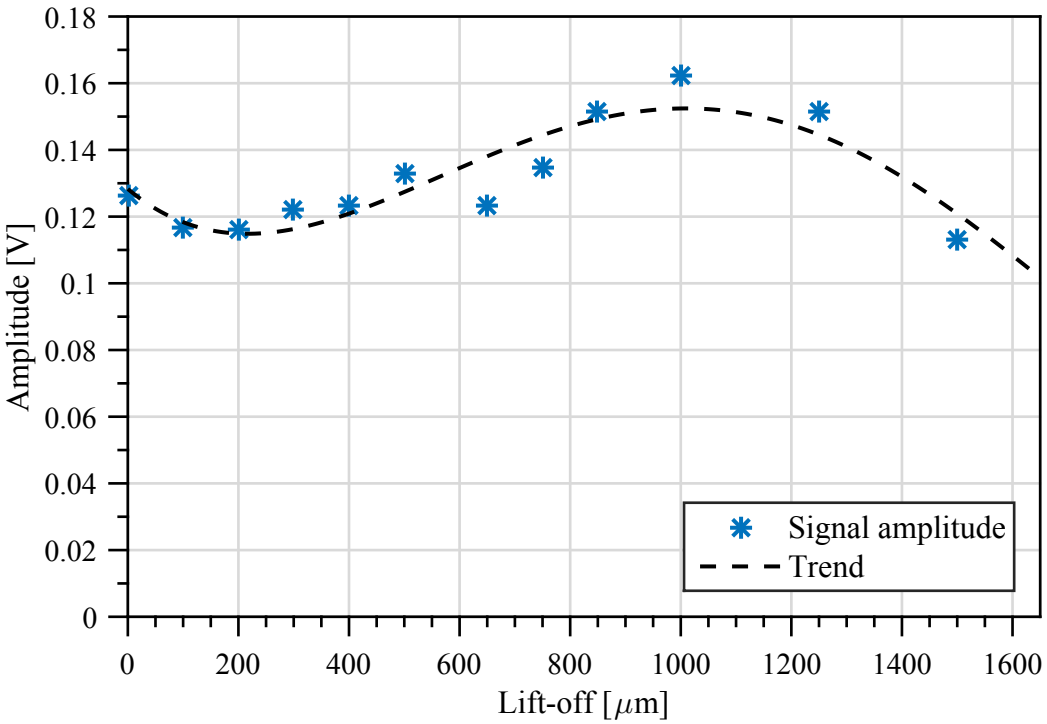

Figure 7.10: Measured signal amplitude when different number of plastic sheets were placed between the transducer and the pipe surface to generate artificial lift-off.

7.6.3 Different number of Kapton layers

Different numbers of thin Kapton insulating sheets (75µm each) have been inserted underneath the transducer and signals have been measured. The overall thickness of these

Kapton sheets are much less than at the previous lift-off measurement, hence limited change is expected in the signal due to the decrease in eddy current and magnetic field. However, it has been observed, that when multiple sheets have been inserted the shape of the envelope of the wave-packet changed significantly (Figure 7.11). Despite the 5-cycle Hanning windowed tone-burst excitation, significantly more cycles can be observed with a slowly decaying envelope. This slowly decaying envelope is likely to be caused by mechanical vibration of the transducer, which got worse as more Kapton sheets were inserted.

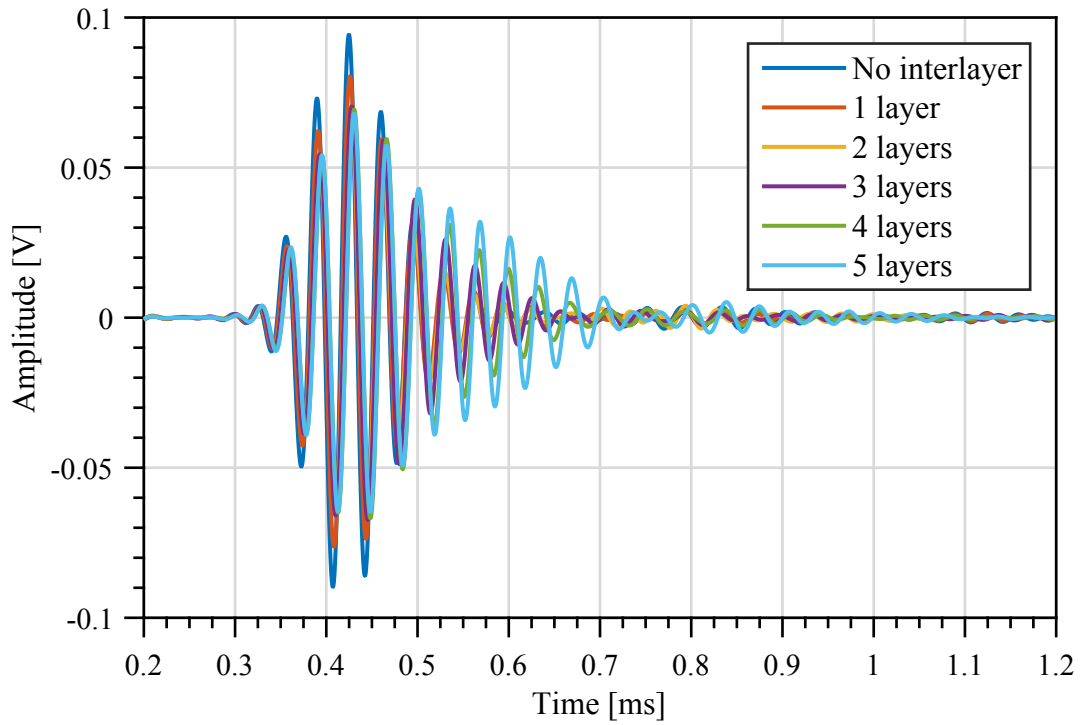

Figure 7.11: Acquired ultrasonic signals when different number of Kapton layers were placed between the EMAT transducer and the pipe surface.

7.6.4 Transfer function

Ultrasonic signals were recorded by the EMAT for multiple frequencies when different contact materials were placed between the transducer and the pipe surface, and signals were collected over a wide frequency range (20-70 kHz). It has been observed, that the signal amplitude is influenced by the contact material, as the peak gain of the transfer

function was measured to be at different frequencies (between 38 and 48 kHz). Figure 7.12 shows the normalized signal amplitudes for different contact materials. The shift in the peak amplitude (resonant frequency) is the result of different coupling material between the transducer and the pipe.

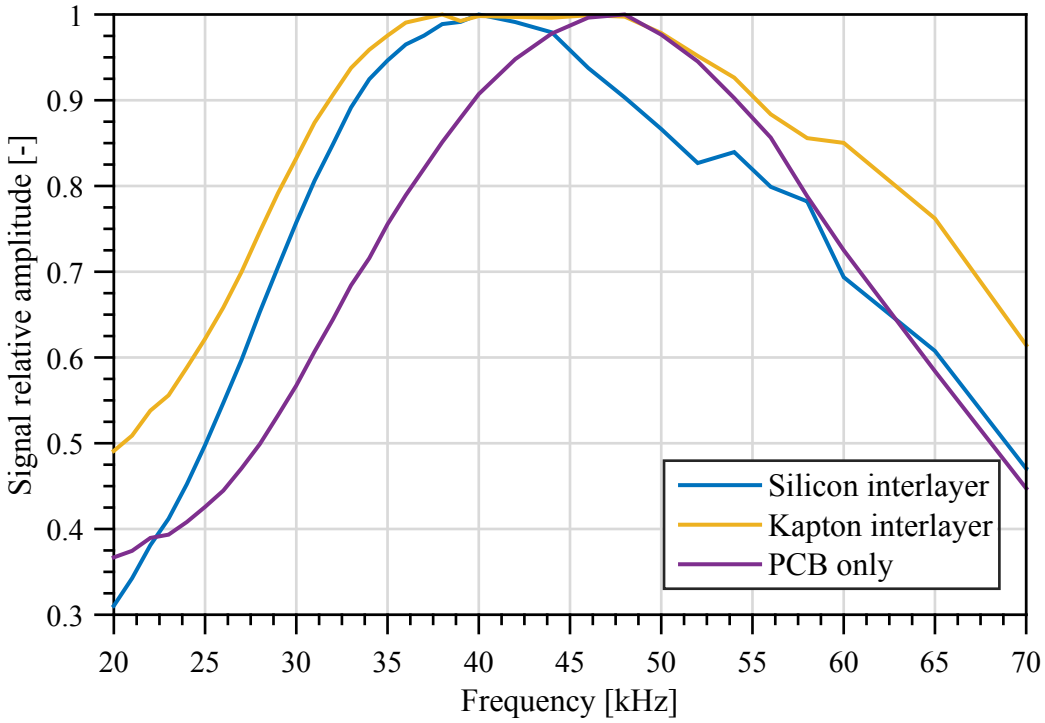

Figure 7.12: Normalized amplitude of the measured torsional guided wave signal at different frequencies for different contact materials. For all measurements, the excitation voltage was set to the same value.

7.6.5 Different number of magnets

Another credible test result is the test when a pair of signals was collected on two different EMAT transducer versions and the signals were compared. In the first measurement, the EMAT was equipped with a single cubic magnet, and in the second measurement, additional cubic magnets were placed on the top of each existing magnets, as shown in Figure 7.13.

While performing the measurement the PCB was fixed to the pipe and the original magnets were not moved. As the extra magnets are too far away from the PCB the eddy current is not influenced by them and the eddy current should be the same in the pipe

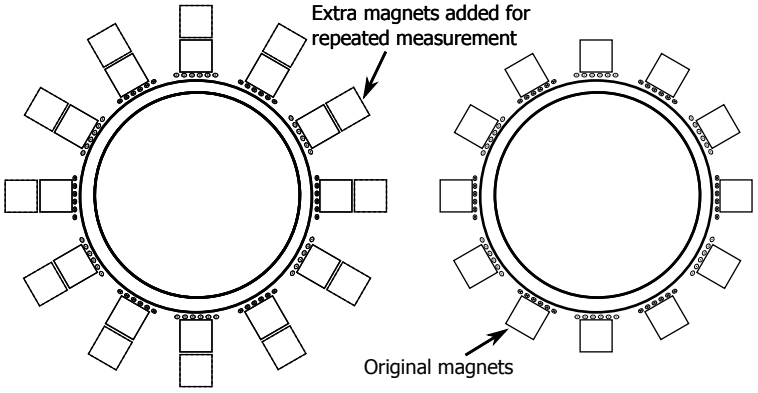

Figure 7.13: Transducer setup, which highlights the influence of the contact material on the ultrasound excitation. Measurements are performed when one cubic magnet is placed to all excitation patches, and when an extra set of magnets are placed onto the original ones.

(this was confirmed by checking the input impedance of the coil and FE modelling). This would mean that for conventional EMAT modelling (where the contact material is not included in the model) no change in the signal's phase is expected. On the other hand, as the second magnet is placed on the top of the original one it is expected that the static magnetic field increases by a few percent [186]. The experimental signals show, that the signal amplitude increases, as signals when 1 and 2 magnets have been placed on each excitation patch are shown in Figure 7.14.

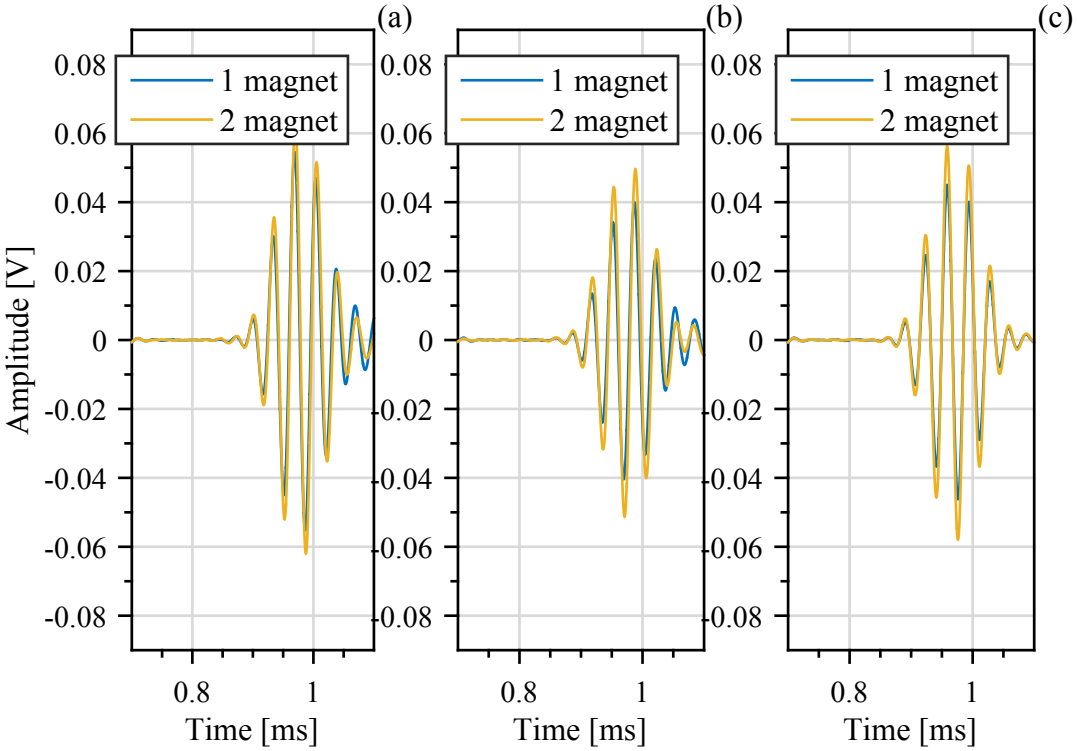

Figure 7.14: Recorded and normalized time signals when one (blue) and two (yellow) set of magnets have been used in the EMAT. The signals are shown for three cases when different materials (Printed-circuit-board only (a), Kapton sheet (b), Silicon layer(c)) have been placed between the EMAT and the structure.

However, unexpectedly the phase of the acquired signal changes as well. Figure 7.15 shows normalized signals, where the phase difference can be observed. Three different materials were tested: the PCB itself, Kapton sheet, a silicon sheet, and the silicon sheet performed the best as a contact material (showing the lowest phase variation). The phase shift of 12.07°, 14.08° and 1.01° have been observed for the three cases (PCB, Kapton and Silicon respectively). This implies that the contact material between the transducer and the pipe surface influences the ultrasonic signal, and materials have different effect.

7.6.6 Mechanism of the wave excitation (reasoning)

The EMAT presented in this document is designed so that it excites the ultrasonic wave via the Lorentz force mechanism. The excitation is often said to be contactless as the Lorentz force is generated on the eddy current inside the pipe, however, an opposite force is also generated on the transducer due to the coil current. Then, as the permanent magnets

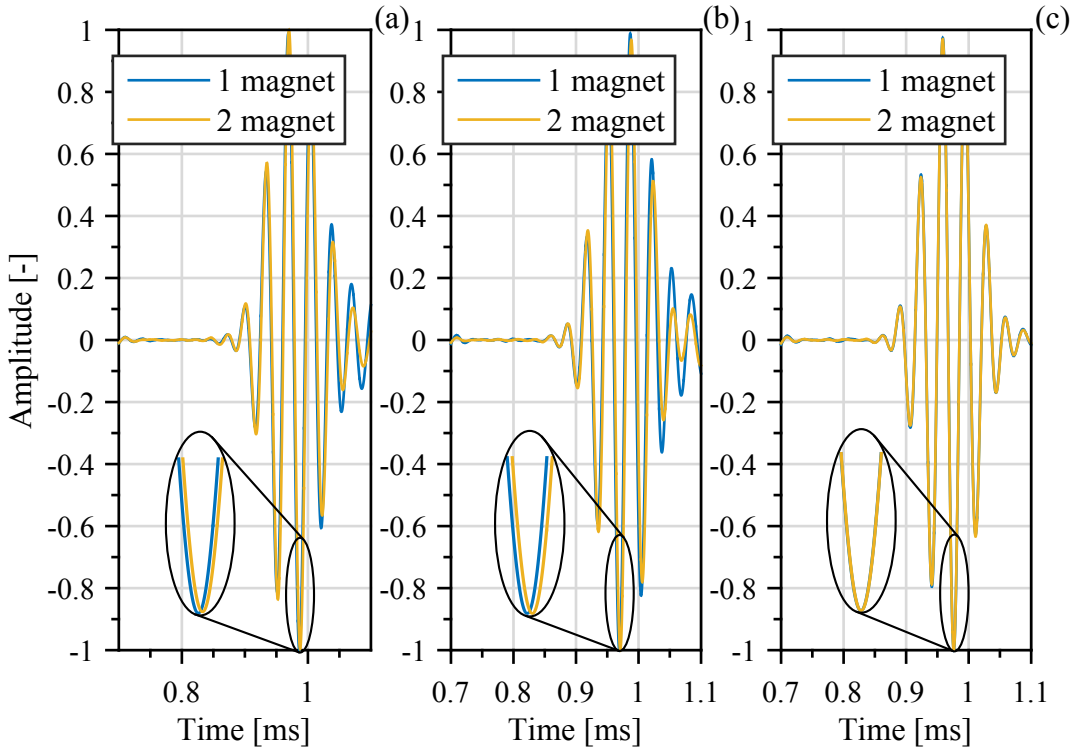

Figure 7.15: Recorded and normalized time signals when 1 (blue) and 2 (yellow) set of magnets have been used in the EMAT. The signals are shown for three cases when different materials (Printed-circuit-board only (a), Kapton sheet (b), Silicon layer(c)) have been placed between the EMAT and the structure.

push the EMAT coils onto the specimen surface the vibration of the coil influences the displacement of the pipe/specimen surface as shown in Figure 7.16. For different materials the coupling between the transducer and the pipe is different, hence the transfer function is different as well. It then means that the contactless operation of the EMAT is somewhat altered by the contact material performance.

As each material has different behaviour, the vibration of the EMAT coils can couple to the pipe surface, potentially affecting the wave generation. Ideally, a contact material should be chosen which could isolate the vibration of the coils.

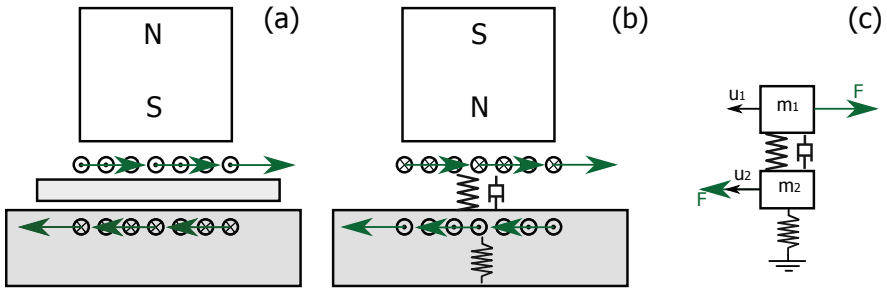

Figure 7.16: Excitation mechanism of the EMAT transducer: the Lorentz force acts on both the eddy current and the coil current, but with a different direction (a). The material that is in contact between the coil wiring and structure influences the excitation (b). A simplified model of the excitation is shown on the right (c).

7.7 Discussion - Compensation and transducer improvement

7.7.1 Compensation

As discussed above, non-uniform changes on the excitation patches are practically impossible to compensate for as uneven changes will result in different dispersive modes being generated and hence a change in coherent noise. However, the effects of uniform changes will change the amplitude of the signal, or the phase of the carrier sine wave. These changes (governing all excitation patches) can be compensated for. The long-term measurement setup is designed so that the transmitting and receiving transducers are separated (see Figure 7.2), and the incident wave can be received due to the special cross-talk reduction system [144]. The incident wave (0.15-0.4 millisecond on Figure 7.4) can then be used as a reference for compensation. An amplitude and phase compensation method was developed (as presented in Chapter 6), which uses the incident wave as a reference, and compensates the reading signals accordingly [185]. This compensation method cannot only compensate temperature-induced changes of the transducer, but is able to compensate for long-term changes of the transducer performance.

The residual levels are calculated at the pipe's right end reflection, and are shown in Figure 7.17. The residual levels are normalized to the end reflection amplitude. Two compensation methods were compared: In the first case (blue) the reading signals are compensated for propagation speed change (BSS method), and changes in echo amplitude

(Distance Amplitude Correction method). The second line (black) shows the residual levels when the reading signals have been compensated for the long-term phase changes in the excitation.

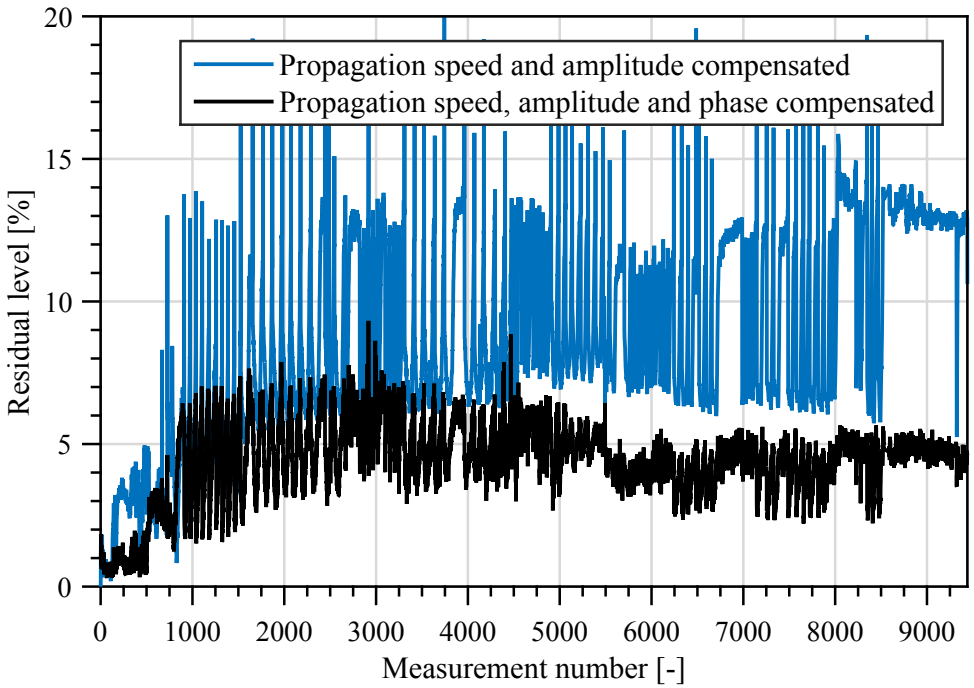

Figure 7.17: Residual levels of the ultrasonic signals at the pipe right end reflection for each measurement during the long-term stability test of the EMAT. The residual level is shown in blue when the propagation speed and the amplitude of the signal was corrected, and is shown in black when the excitation phase differences are also corrected.

By applying the additional correction to the signal, the residual levels clearly decreased. The residual level of ~3% to 5% can be observed when the phase compensation method was applied to the reading signals, which is quite a noticeable improvement at a location of a reflector with 100% Reflection Coefficient (RC).

7.7.2 Transducer improvement

The previous section has shown that compensation techniques can result in noticeable improvements. However, it is more favourable to design a transducer, which is stable for long time, and the highest sensitivity is guaranteed. The previous sections have shown that the material that is in contact with the transducer and the pipe surface influences the excitation. It was found that different materials affect the EMAT performance in different

ways. A silicone interlayer was installed between the transducer and the pipe that can decouple the transducer from the pipe surface better, and the EMAT is less sensitive to temperature swings.

To confirm this, new temperature cycled stability tests were started and different transducers were tested. Transducers were exposed (in separate measurements) to four temperature cycles with maximum temperature of 30, 50, 80 and 80 °C. Figure 7.18 shows the evaluated phase values of the incident wave (blue), and the temperature exposure of the pipe (grey).

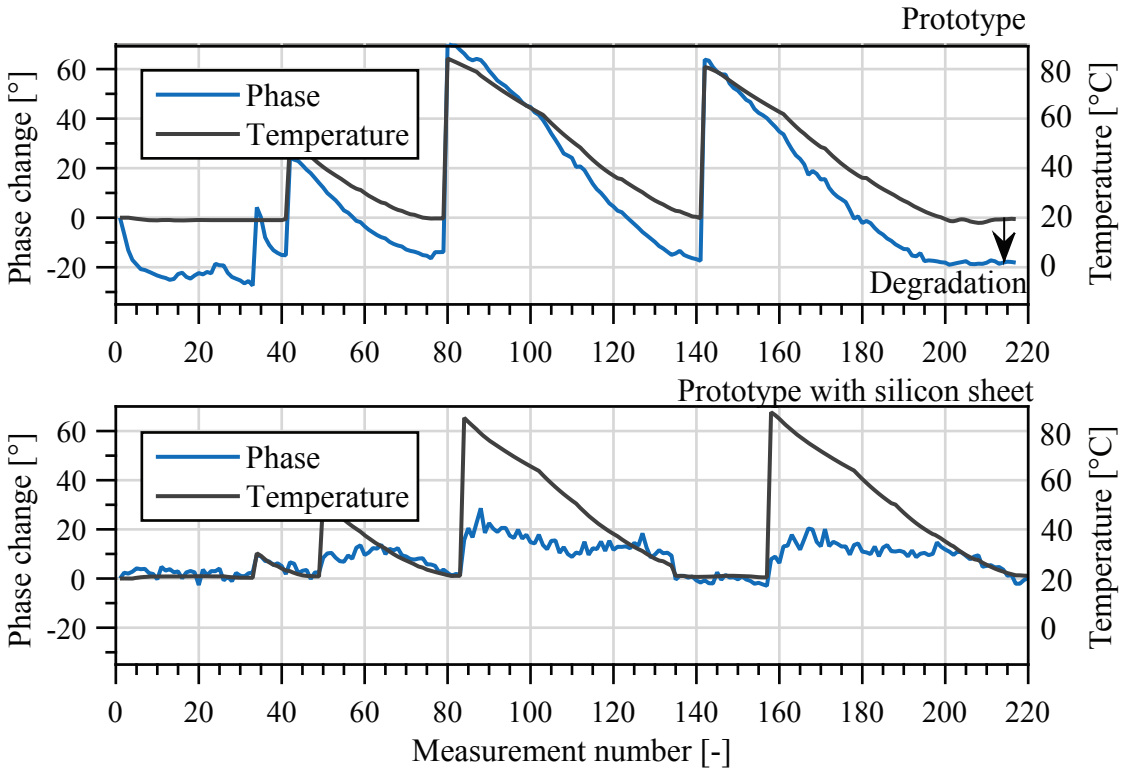

Figure 7.18: Evaluated phase change of the ultrasonic signals acquired when (a) previous EMAT design was used and (b) when silicon sheet was separating the EMAT coils from the pipe surface. The transducers were exposed to 30, 50, 80, 80 °C heating cycles.

The previous EMAT transducer prototype which is equipped with an air-gap was placed onto the pipe (Figure 7.18a); Figure 7.18b shows the results when a silicone layer was placed in between the transducer and the pipe surface. The results indicate that in the case when a silicone layer was used as a contact material the signals were less sensitive to temperature changes. In addition, the estimated phase values showed much larger stability, as no trend can be observed for the transducer with silicone contact material.

7.8 Summary

This chapter presents quantitative evaluation of the long-term stability of a torsional guided wave Lorentz force EMAT transducer. Long-term measurement results for 94 temperature cycles with the highest temperature reaching 80°C are presented. The signals were acquired between December of 2016 and the autumn of 2018. The evaluated data shows that the signals can be measured with high robustness, as the amplitude of the signal remained stable (within 3.7% of original value). However, the phase of the acquired signal (evaluated at the incident wave, which has directly travelled from the transmitting transducers to the receiver transducer) changed considerably (17.24°) during the early stage of the evaluation until the highest temperature exposure was reached. The change in the signal's phase is much less (additional 6.08°) in the following 83 temperature cycles. Changes at the coherent noise of the signal (0.73 to 1.44 milliseconds) were minimal, as the residual signal (difference between baseline and reading) is less than 1%, which is comparable with the random noise level.

Parts of the EMAT system were tested further individually to find explanations for the observed behaviour. In a repeated test, the input current of the transducer was monitored, which showed only 0.39% amplitude, and 0.24° phase change between room temperature measurements. The electrical impedance of the transducer was also measured at room temperatures, and it showed the maximum difference of 0.32% in amplitude and 0.09° in phase.

It was recognized, that the Lorentz force is not only generated on the eddy current, but also on the coil current, causing a vibration in the transducer. Then, as the permanent magnets push the transducer to the pipe surface, the transducer vibration can affect the wave generation depending on the contact material properties. The results show that the stability of excitation mechanism of the EMAT that is often said to be contactless does show to be very sensitive to the interlayer and therefore the contact between EMAT and pipe is more important than previously believed. Different contact materials have been tested and it was shown that a silicone interlayer can decrease phase variations (caused by temperature) significantly, and can further increase the stability.

Chapter 8

Conclusions

8.1 Thesis review

This thesis investigates the feasibility of using a Lorentz force based Electromagnetic Acoustic Transducer for pipeline health monitoring. The EMAT transducer was designed so that it can excite and receive low frequency (~30 kHz) ultrasonic guided waves on 3 inch NPS metallic pipes. The wave mode was chosen to be the fundamental torsional mode as it offers several advantages, such as non-dispersive propagation, equal sensitivity for defects at any cross-sectional location.

The excitation mechanism was investigated by performing separate 3D Finite Element simulations for the magnetic field and eddy current generation, and the results of these simulations were combined to estimate the excited force distribution. The mode purity of the generated wave was analysed in an additional FE simulation. The EMAT prototype was manufactured and equipped with a special crosstalk reduction design, so that the dead-zone of the measurement is minimized. A high-temperature resistant version of the transducer was also developed which utilized different material selection and high temperature Samarium-Cobalt (SmCo) magnets. Torsional guided wave signals were acquired when the pipe and the structure was heated up to 210°C.

The temperature dependence of the signals were investigated, and it was found that additional to the propagation speed changes the transducer response changes also affects the signals. The currently used compensation strategies focus on the compensation of

propagation speed differences only. It was shown that by adding the extra term, by compensating the transducer related changes the temperature effects could be reduced on the signals. The compensation methods were developed so that it uses only the acquired signals for compensation, therefore this method could be used in other applications as well.

As the transducer is designed for Structural Health Monitoring, it is required that it can operate for long time periods. Therefore, its stability was evaluated during a long-term test where more than hundred heating cycles were performed on the pipe and the structure. The phenomena affecting the long-term stability of the transducer are discussed.

8.2 Key findings

The main findings of the thesis are:

- It has been shown how a low power (<4W) torsional guided wave EMAT system can be designed that can transmit and receive signals with more than 40dB SNR with respect to random noise and mode purity of ~40dB with respect to coherent noise.
- The cross-talk signal (which is the transmitted waveform coupled to the receiver transducer via electro-magnetic mechanisms) can be almost completely eliminated from the ultrasonic signal by using a special coil wiring pattern and magnet arrangement.
- A novel compensation method for temperature induced signal changes that enables higher sensitivity detection of defects near reflectors has been presented. It was demonstrated that the temperature induced changes (ΔT=41°C) can be suppressed by 7 to 15 decibels.
- It has been observed, that the torsional guided wave EMATs can generate highly repeatable signals, however the excitation mechanism that was previously believed to be contactless has been shown to be sensitive to the mechanical coupling material between structure and the EMAT.

The transduction mechanism of the Lorentz force EMATs is usually poor, therefore an EMAT based measurement system is challenging to implement. Several ways to increase the SNR were investigated. The input power of the EMAT is usually limited due to safety limits, and the signal amplitude can be maximized by minimizing the losses in the transduction. Alternatively, the measurement noise should be decreased by applying a noise cancelling sheet at the receiver transducer and using special (twisted pair shielded) cables for connection. The receiver amplifier electronics also influences the SNR, therefore ultra-low noise receiver amplifier is used in the electronics. Further SNR increase can be achieved by traditional signal processing methods such as band-pass filtering and performing the required number of averages.

In EMATs the cross-talk signal, which is coupled directly from the transmitting transducer to the receiving one can be magnitudes larger than the ultrasonic signal itself. It could then saturate the receiving amplifiers and the electronics and prevent the reception for some time, resulting in a dead-zone in the measured area. To prevent this, the cross-talk is eliminated by a special transducer and electronics design. It was found that two main effects contribute to the cross-talk generation (electrostatic and electromagnetic coupling). The electrostatic coupling (capacitive through the metal structure) is eliminated by differential signals, so that the net charge on the EMAT transmit coils is zero. The electromagnetic coupling is removed by an alternative receiver coil wiring, where the polarity of every second coil is changed, resulting in a zero net magnetic flux. Magnets on the altered coils are flipped as well so that it is possible to receive the torsional wave.

Compensation of temperature changes in the ultrasonic signals is a widely discussed topic. Most methods investigate the signal changes induced by propagation speed changes. In this thesis it was found that by adding additional compensation for the temperature induced transducer response changes (amplitude and phase) the residual signals (difference between signals) are reduced. The improvement can be observed at echo location of the signal, which directly means improvement in sensitivity near pipe features (welds, supports, etc.).

The stability of the guided wave EMAT was evaluated during a long-term (1.5 years) test, where the pipe and the transducers were exposed to more than 100 heating cycles. It was found that despite the contactless operation mechanism changes were observed on

the acquired signals (mainly in the phase of the signal). The monitoring operation of the transducer was not reduced significantly, as highly repeatable signals were acquired and minimal changes were recorded at the coherent noise of the signal. It was shown that the EMAT is electrically stable (electronics, input current and impedance is stable), but the contact material influences the wave generation. It was found that the transducer vibrates as well due to the Lorentz force being generated on the coil current (with different polarity as the desired excitation), and this can alter the wave generation depending to the contact material. It was found that different materials behave differently, influencing the wave generation and the stability in a different manner.

8.3 Further work

The presented Guided Wave EMAT operates at low power excitation (<4W), but it might be desirable to excite even lower power levels to meet the requirements for stricter safety limits. In addition, it can be expected that the strength of the signals acquired on different pipe sizes and schedules are different. This would yield a lower SNR. Therefore, it could be beneficial to further increase the signal strength. Separate optimization of transmitter and receiver transducer and increasing of magnet sizes could both result in increased signal strength.

In chapter 4 it was detailed how the mode purity of the generated torsional wave is affected by imperfections such as uneven lift-off or slight corrosion on the pipe surface. In some cases, this could lead to unacceptable coherent noise levels, where the damage sensitivity is reduced. Although it increases the complexity of the system, the transducer can be modified for multi-segment array where the excitation at each segments are balanced so that the symmetric mode purity is guaranteed. Available commercial products usually support multi-segment arrays [72, 187], and it should be investigated how much improvement is reached with the increased complexity.

The high temperature version of the guided wave EMAT was exposed to the maximum temperature of 210°C, where it was possible to record signals. It would be beneficial to test the operating temperature limit of the transducer and evaluate the temperature, where the current design fails. Alternatively, it is advantageous to further increase this

operational temperature range to increase the number of potential applications.

It was observed that the wave generation of the EMAT transducer is influenced by the contact material. The vibration of the transducer is mechanically coupled to the structure through the contact material, but the exact mechanism is not perfectly understood. It would be beneficial to improve the understanding the effect of contact material on the excitation so that the highest possible stability is guaranteed.

This page intentionally left blank

References

[1] American Welding Society, "A History of Nondestructive Testing; Online, Retrieved from: https://trainingndt.com/ndt-news/entry/a-history-of-nondestructive-testing," 2015.

[2] Jason Butz, "The Evolution and History of Nondestructive Testing | Inspectioneering," *Inspectioneering Journal*, vol. 18, no. 3, 2012.

[3] British Standard Institution, "BS 9690-2:2011 - Non-destructive testing. Guided wave testing. Basic requirements for guided wave testing of pipes, pipelines and structural tubulars," 2011.

[4] British Standard Institution, "DD CEN/TS 15053:2005 - Non-destructive testing. Recommendations for discontinuities-types in test specimens for examination," 2005.

[5] I. O. for Standardization, "ISO 15549:2008(en), Non-destructive testing - Eddy current testing - General principles," 2008.

[6] B. Masschaele, M. Dierick, L. Van Hoorebeke, V. Cnudde, and P. Jacobs, "The use of neutrons and monochromatic X-rays for non-destructive testing in geological materials," in *Environmental Geology*, vol. 46, pp. 486–492, 2004.

[7] N. Uhlmann, M. Salamon, F. Sukowski, and V. Voland, "Characterization and comparison of direct and indirect converting X-ray detectors for non-destructive testing (NDT) in low-energy and high-resolution applications," *Nuclear Instruments and Methods in Physics Research, Section A: Accelerators, Spectrometers, Detectors and Associated Equipment*, vol. 591, pp. 46–49, jun 2008.

[8] R. Hanke, T. Fuchs, and N. Uhlmann, "X-ray based methods for non-destructive testing and material characterization," *Nuclear Instruments and Methods in Physics Research Section A: Accelerators, Spectrometers, Detectors and Associated Equipment*, vol. 591, pp. 14–18, jun 2008.

[9] H. A. Sabbagh, "Advances in Modeling Eddy-Current NDE of Ferromagnetic Bodies," *AIP Conference Proceedings*, vol. 657, pp. 383–389, apr 2003.

[10] H. Shaikh, N. Sivaibharasi, B. Sasi, T. Anita, R. Amirthalingam, B. P. C. Rao, T. Jayakumar, H. S. Khatak, and B. Raj, "Use of eddy current testing method in detection and evaluation of sensitisation and intergranular corrosion in austenitic stainless steels," *Corrosion Science*, vol. 48, pp. 1462–1482, jun 2006.

[11] J. García-Martín, J. Gómez-Gil, and E. Vázquez-Sánchez, "Non-Destructive Techniques Based on Eddy Current Testing," *Sensors*, vol. 11, pp. 2525–2565, feb 2011.

[12] M. Saka, I. Sato, and H. Abé, "NDE of a 3-D surface crack using magnetic field induced by DC current flow," *NDT & E International*, vol. 31, pp. 325–328, oct 1998.

[13] D. Lesselier and A. Razek, *Electromagnetic Nondestructive Evaluation (III)*. No. III, Amsterdam: IOS Press, 1999.

[14] H. G. Ramos and A. L. Ribeiro, "Present and future impact of magnetic sensors in NDE," in *Procedia Engineering*, vol. 86, pp. 406–419, 2014.

[15] R. Jarvis, P. Cawley, and P. B. Nagy, "Current deflection NDE for the inspection and monitoring of pipes," *NDT&E International*, vol. 81, pp. 46–59, 2016.

[16] B. Raj, T. Jayakumar, and M. Thavasimuthu, *Practical non-destructive testing*. Cambridge, UK: Woodhead Publishing Limited, 2007.

[17] J. L. Rose, *Ultrasonic Guided Waves in Solid Media*. Cambridge: Cambridge University Press, 2004.

[18] K. F. Graff, *Wave motion in elastic solids*. Oxford: Oxford University Press, 1991.

[19] A. Van Pamel, C. R. Brett, P. Huthwaite, and M. Lowe, "Finite element modelling of elastic wave scattering within a polycrystalline material in two and three dimensions," *The Journal of the Acoustical Society of America*, vol. 138, pp. 2326–2336, oct 2015.

[20] J. S. Egerton, M. J. S. Lowe, P. Huthwaite, and H. V. Halai, "Ultrasonic attenuation and phase velocity of high-density polyethylene pipe material," *The Journal of the Acoustical Society of America*, vol. 141, p. 1535, 2017.

[21] I. O. for Standardization, "ISO 18211:2016 - Non-destructive testing Long-range inspection of above-ground pipelines and plant piping using guided wave testing with axial propagation," 2016.

[22] A. Demma, P. Cawley, and M. Lowe, "The reflection of the fundamental torsional mode from cracks and notches in pipes," *Acoustical Society of America*, vol. 114, no. 2, pp. 611–626, 2003.

[23] D. N. Alleyne and P. Cawley, "The excitation of Lamb waves in pipes using dry-coupled piezoelectric transducers," *Journal of Nondestructive Evaluation*, vol. 15, pp. 11–20, mar 1996.

[24] D. N. Alleyne, M. Lowe, and P. Cawley, "The Reflection of Guided Waves From Circumferential Notches in Pipes," *Journal of Applied Mechanics*, vol. 65, pp. 635–641, sep 1998.

[25] M. Lowe, D. N. Alleyne, and P. Cawley, "The Mode Conversion of a Guided Wave by a Part-Circumferential Notch in a Pipe," *Journal of Applied Mechanics*, vol. 65, pp. 649–656, sep 1998.

[26] S. H. Cho, H. W. Kim, and Y. Kim, "Megahertz-range guided pure torsional wave transduction and experiments using a magnetostrictive transducer.," *IEEE transactions on ultrasonics, ferroelectrics, and frequency control*, vol. 57, pp. 1225–9, may 2010.

[27] Z. Liu, J. Fan, Y. Hu, C. He, and B. Wu, "Torsional mode magnetostrictive patch transducer array employing a modified planar solenoid array coil for pipe inspection," *NDT & E International*, vol. 69, pp. 9–15, jan 2015.

[28] A. Løvstad and P. Cawley, "The reflection of the fundamental torsional mode from pit clusters in pipes," *NDT and E International*, vol. 46, no. 1, pp. 83–93, 2012.

[29] M. Ratassepp, S. Fletcher, and M. Lowe, "Scattering of the fundamental torsional mode at an axial crack in a pipe.," *The Journal of the Acoustical Society of America*, vol. 127, pp. 730–40, feb 2010.

[30] Guided Ultrasonics Ltd, "Online, Retrieved from: http://www.guided-ultrasonics.com/," 2016.

[31] Plant Integrity Ltd, "Guided waves for offshore structures; Online, Retrieved from: http://www.plantintegrity.com/," 2016.

[32] MKC NDT, "NDT Equipments and systems; Online, Retrieved from: http://www.mkckorea.com/english.htm," 2016.

[33] R. Carandente, J. Ma, and P. Cawley, "The scattering of the fundamental torsional mode from axi-symmetric defects with varying depth profile in pipes," *The Journal of the Acoustical Society of America*, vol. 127, pp. 3440–3448, jun 2011.

[34] J. Davies, *Inspection of pipes using low frequency focused guided waves.* PhD thesis, Imperial College London, 2008.

[35] A. Galvagni, *Pipeline health monitoring.* PhD thesis, Imperial College London, 2013.

[36] A. Galvagni and P. Cawley, "The reflection of guided waves from simple support in pipes," *The Journal of the Acoustical Society of America*, vol. 129, pp. 1869–1880, apr 2011.

[37] P. Cawley, M. Lowe, D. N. Alleyne, B. Pavlakovic, and P. D. Wilcox, "Practical long range guided wave testing: Applications to pipes and rail," *Materials Evaluation*, vol. 61, no. 1, pp. 66–74, 2003.

[38] M. Lowe and P. Cawley, "Long Range Guided Wave Inspection Usage, Current Commercial Capabilities and Research Directions," 2006.

[39] E. Leinov, M. Lowe, and P. Cawley, "Investigation of guided wave propagation and attenuation in pipe buried in sand," *Journal of Sound and Vibration*, vol. 347, pp. 96–114, 2015.

[40] E. Leinov, M. Lowe, and P. Cawley, "Ultrasonic isolation of buried pipes," *Journal of Sound and Vibration*, vol. 363, pp. 225–239, 2016.

[41] M. Evans and T. Vogt, "Reliability of guided wave ultrasonic testing," in *10th European Conference on Non-Destructive Testing, Moscow ,*, 2010.

[42] P. Cawley, F. Cegla, and A. Galvagni, "Guided waves for NDT and permanently-installed monitoring," *Insight - Non-Destructive Testing and Condition Monitoring*, vol. 54, pp. 594–601, nov 2012.

[43] R. Charchuk, C. Werstiuk, M. Evans, and E. Sjerve, "High Temperature Guided Wave Pipe Inspection," in *4th International CANDU In-service Inspection Workshop and NDT in Canada*, (Toronto), 2012.

[44] A. J. Croxford, P. D. Wilcox, B. W. Drinkwater, and G. Konstantinidis, "Strategies for guided-wave structural health monitoring," *Proceedings of the Royal Society A: Mathematical, Physical and Engineering Sciences*, vol. 463, no. 2087, pp. 2961–2981, 2007.

[45] C. R. Farrar and K. Worden, "An introduction to structural health monitoring," *Philosophical Transactions of the Royal Society of London A: Mathematical, Physical and Engineering Sciences*, vol. 365, no. 1851, pp. 303–315, 2007.

[46] H. Sohn, "Effects of environmental and operational variability on structural health monitoring," *Philosophical Transactions of the Royal Society of London A: Mathematical, Physical and Engineering Sciences*, vol. 365, no. 1851, pp. 539–560, 2007.

[47] K. Worden and G. Manson, "The application of machine learning to structural health monitoring," *Philosophical Transactions of the Royal Society of London A: Mathematical, Physical and Engineering Sciences*, vol. 365, no. 1851, 2007.

[48] K. Worden, C. R. Farrar, G. Manson, and G. Park, "The fundamental axioms of structural health monitoring," *Philosophical Transactions of the Royal Society of London A: Mathematical, Physical and Engineering Sciences*, vol. 463, no. 2082, pp. 1639–1664, 2007.

[49] C. A. Dan, P. Kudela, and W. Ostachowicz, "Compensation of Temperature Effects on Guided Wave Based Structural Health Monitoring Systems," *Proceedings of 7th European Workshop on Structural Health Monitoring*, pp. 355–362, 2014.

[50] G. Konstantinidis, P. D. Wilcox, and B. W. Drinkwater, "An investigation into the temperature stability of a guided wave structural health monitoring system using permanently attached sensors," *IEEE Sensors J.*, vol. 7, no. 5, pp. 905–912, 2007.

[51] A. J. Croxford, J. Moll, P. D. Wilcox, and J. E. Michaels, "Efficient temperature compensation strategies for guided wave structural health monitoring.," *Ultrasonics*, vol. 50, no. 4-5, pp. 517–28, 2010.

[52] C. Liu, J. B. Harley, M. Bergés, D. W. Greve, and I. J. Oppenheim, "Robust ultrasonic damage detection under complex environmental conditions using singular value decomposition.," *Ultrasonics*, vol. 58, pp. 75–86, apr 2015.

[53] A. Hyvarinen and E. Oja, "Independent Component Analysis : A Tutorial," *Neural Networks*, vol. 1, pp. 1–30, 1999.

[54] J. Dobson and P. Cawley, "Independent Component Analysis for Improved Defect Detection in Guided Wave Monitoring," *Proceedings of the IEEE*, vol. 104, no. 8, pp. 1620–1631, 2015.

[55] Heinlein S, C. P, and et al Vogt TK, "Structural health monitoring of a pipe using permanently installed guided wave sensors," *Mater Eval*, vol. 76, pp. 1118–1127, 2018.

[56] H. Nishino, S. Takashina, F. Uchida, M. Takemoto, and K. Ono, "Modal Analysis of Hollow Cylindrical Guided Waves and Applications," *Japanese Journal of Applied Physics*, vol. 40, pp. 364–370, jan 2001.

[57] M. Hirao and H. Ogi, *EMATs for Science and Industry: Noncontacting Ultrasonic Measurements*. Osaka: Springer Science & Business Media, 2013, 2003.

[58] P. B. Ostergaard, "Magnetostrictive generation and detection of longitudinal, torsional, and flexural waves in a steel rod," *Acoustical Society of America*, vol. 96, no. August, pp. 1202–1204, 1994.

[59] Y. Y. Kim, C. I. Park, S. H. Cho, and S. W. Han, "Torsional wave experiments with a new magnetostrictive transducer configuration.," *The Journal of the Acoustical Society of America*, vol. 117, no. 6, pp. 3459–3468, 2005.

[60] K. H. Sun, S. H. Cho, and Y. Y. Kim, "Topology design optimization of a magnetostrictive patch for maximizing elastic wave transduction in waveguides," *IEEE Transactions on Magnetics*, vol. 44, no. 10, pp. 2373–2380, 2008.

[61] Y.-G. Kim, H.-S. Moon, K.-J. Park, and J.-K. Lee, "Generating and detecting torsional guided waves using magnetostrictive sensors of crossed coils," *NDT & E International*, vol. 44, pp. 145–151, 2011.

[62] R. B. Thompson, "Generation of horizontally polarized shear waves in ferromagnetic materials using magnetostrictively coupled meander-coil electromagnetic transducers," *Appl. Phys. Lett*, vol. 34, no. 175, 1979.

[63] K. R. Mulligan, N. Quaegebeur, P. Masson, L.-P. Brault, and C. Yang, "Compensation of piezoceramic bonding layer degradation for structural health monitoring," *Structural Health Monitoring*, vol. 13, no. 1, pp. 68–81, 2013.

[64] G. Konstantinidis, B. W. Drinkwater, and P. D. Wilcox, "The Long Term Stability of Guided Wave Structural Health Monitoring Systems," *AIP Conference Proceedings*, vol. 820, no. 10, pp. 1702–1680, 2006.

[65] V. A. Attarian, F. Cegla, and P. Cawley, "Long-term stability of guided wave structural health monitoring using distributed adhesively bonded piezoelectric transducers," *Structural Health Monitoring*, vol. 13, pp. 265–280, feb 2014.

[66] M. Sborikas, J. L. Ealo, and M. Wegener, "Effects of temperature on electromechanical properties and ultrasonic performance of piezoelectric cellular PP films," *Sensors and Actuators A: Physical*, vol. 245, pp. 1–9, 2016.

[67] H. Gao, S. Ali, B. Lopez, and P. Lopez, "New developments in EMAT techniques for surface inspection," *AIP Conference Proceedings*, vol. 1511, no. 902, 2013.

[68] P. S. Babiarz, "Intrinsic Safety Circuit Design Online, Retrieved from: https://www.omega.com/techref/pdf/z131-148.pdf," 2016.

[69] S. Fujimoto, T. Namihira, K. Iwata, and M. Kobayashi, "Curie temperature and high temperature behavior of Pb(Zr,Ti)O3/Pb(Zr,Ti)O3 sol-gel composites," *Japanese Journal of Applied Physics*, vol. 54, jul 2015.

[70] A. Mohimi, T.-H. Gan, and W. Balachandran, "Development of high temperature ultrasonic guided wave transducer for continuous in service monitoring of steam lines using non-stoichiometric lithium niobate piezoelectric ceramic," *Sensors and Actuators A: Physical*, vol. 216, pp. 432–442, 2014.

[71] R. Kazys, A. Voleisis, and B. Voleisiene, "High temperature ultrasonic transducers: review," *ULTRAGARSAS (ULTRASOUND)*, vol. 63, no. 2, 2008.

[72] Guided_Ultrasonics_Ltd, "gPIMS® Ring; Online, Retrieved from: http://www.guided-ultrasonics.com/gpims/," 2017.

[73] C. T. Searfass and B. R. Tittmann, "High temperature ultrasonic transducer up to 1000 C using lithium niobate single crystal," *Applied Physics Letters*, vol. 97, p. 232901, dec 2010.

[74] Plant Integrity Ltd., "Monitoring with high-temperature permamount; Online, Retrieved from: http://www.teletestndt.com," 2018.

[75] Magma Magnetic Technologies Ltd, "High temperatures neodymium magnets; Online, Retrieved from: http://www.magmamagnets.com/permanent-magnets/neodymium-rare-earth-magnets/high-temperatures-neodymium-magnets/," 2017.

[76] C.-T. G. &. Co., "Samarium Cobalt Magnets Online, Retrieved from: http://www.cy-magnetics.com," 2006.

[77] M. Lowe, "Matrix techniques for modeling ultrasonic waves in multilayered media," *IEEE Transactions on Ultrasonics, Ferroelectrics and Frequency Control*, vol. 42, pp. 525–542, jul 1995.

[78] B. Pavlakovic, M. Lowe, D. N. Alleyne, and P. Cawley, "Disperse: A General Purpose Program for Creating Dispersion Curve," *Annual Review of Progress in Quantitative Nondestructive Evaluation*, vol. vol 16, pp. p 185–192, 1997.

[79] Imperial College London, "Disperse; Online, Retrieved from: http://www.imperial.ac.uk/non-destructive-evaluation/products-and-services/disperse/," 2016.

[80] J. Hou, K. R. Leonard, and M. K. Hinders, "Automatic multi-mode Lamb wave arrival time extraction for improved tomographic reconstruction," *Inverse Problems*, vol. 20, no. 6, pp. 1873–1888, 2004.

[81] P. Huthwaite and F. Simonetti, "High-resolution guided wave tomography," *Wave Motion*, vol. 50, no. 5, pp. 979–993, 2013.

[82] R. Howard and F. Cegla, "On the probability of detecting wall thinning defects with dispersive circumferential guided waves," *NDT & E International*, vol. 86, pp. 73–82, 2017.

[83] M. Clough, M. Fleming, and S. Dixon, "Circumferential guided wave EMAT system for pipeline screening using shear horizontal ultrasound," *NDT & E International*, vol. 86, pp. 20–27, mar 2017.

[84] M. L. Nayyar, R. C. King, and S. Crocker, *Piping Handbook*. New York: McGraw Hill Professional, 7th ed., 1999.

[85] P. Cawley and D. Alleyne, "The use of Lamb waves for the long range inspection of large structures," *Ultrasonics*, vol. 34, no. 2-5, pp. 287–290, 1996.

[86] A. Demma, P. Cawley, M. Lowe, A. Roosenbrand, and B. Pavlakovic, "The reflection of guided waves from notches in pipes: a guide for interpreting corrosion measurements," *NDT & E International*, vol. 37, pp. 167–180, apr 2004.

[87] Nurmalia, N. Nakamura, H. Ogi, and M. Hirao, "EMAT pipe inspection technique using higher mode torsional guided wave T(0,2)," *NDT & E International*, vol. 87, pp. 78–84, 2017.

[88] A. Velichko and P. D. Wilcox, "Excitation and scattering of guided waves: Relationships between solutions for plates and pipes," *The Journal of the Acoustical Society of America*, vol. 125, pp. 3623–3631, jun 2009.

[89] A. Løvstad and P. Cawley, "The reflection of the fundamental torsional guided wave from multiple circular holes in pipes," *NDT&E International journal*, vol. 44, pp. 553–562, 2011.

[90] K. Simonyi, *A cultural history of physics*. Florida: CRC Press, 2012.

[91] H. M. G. Ramos, O. Postolache, F. C. Alegria, and A. Lopes Ribeiro, "Using the skin effect to estimate cracks depths in metallic structures," in *2009 IEEE Intrumentation and Measurement Technology Conference*, pp. 1361–1366, IEEE, may 2009.

[92] J. Isla, M. Seher, R. Challis, and F. Cegla, "Optimal impedance on transmission of Lorentz force EMATs," in *AIP Conference Proceedings*, vol. 1706, p. 090012, AIP Publishing, 2016.

[93] M. Seher, R. Challis, J. Isla, and F. Cegla, "The effect of metal load material and impedance matching on EMAT performance," *Insight: Non-Destructive Testing and Condition Monitoring*, vol. 58, pp. 536–543, oct 2016.

[94] J. Harris, "On then Use of Windows with the Discrete for Harmonic Analysis Fourier Transform," *Proceedings of the IEEE*, vol. 66, no. 1, pp. 51–83, 1978.

[95] Z. Maekawa and P. P. Lord, *Environmental and architectural acoustics*. London: E. & F.N. Spon, 1994.

[96] K. M. M. Prabhu, *Window functions and their applications in signal processing.* New York: CRC PRESS, 2014.

[97] P. Y. Ktonas and N. Papp, "Instantaneous envelope and phase extraction from real signals: Theory, implementation, and an application to EEG analysis," *Signal Processing*, vol. 2, pp. 373–385, 1980.

[98] Lewis Embree Franks, *Signal Theory.* Englewood Cliffs, N.J.: Prentice-Hall, 1981.

[99] A. Gajdacsi and F. Cegla, "High accuracy wall thickness loss monitoring," in *AIP Conference Proceedings, Volume 1581, Issue 1, p.1687-1694*, vol. 1581, pp. 1687–1694, 2014.

[100] T. Clarke, F. Simonetti, and P. Cawley, "Guided wave health monitoring of complex structures by sparse array systems: Influence of temperature changes on performance," *Journal of Sound and Vibration*, vol. 329, pp. 2306–2322, 2009.

[101] J. Isla and F. Cegla, "Coded Excitation for Pulse-Echo Systems," *IEEE Transactions on Ultrasonics, Ferroelectrics, and Frequency Control*, vol. 64, pp. 736–748, apr 2017.

[102] M. Golay, "Sieves for Low Autocorrelation Binary Sequences," *IEEE Transactions on Information Theory*, vol. 23, pp. 43–51, jan 1977.

[103] H. W. Kim, J. K. Lee, and Y. Y. Kim, "Circumferential phased array of shear-horizontal wave magnetostrictive patch transducers for pipe inspection.," *Ultrasonics*, vol. 53, pp. 423–31, feb 2013.

[104] Y. Y. Kim and Y. E. Kwon, "Review of magnetostrictive patch transducers and applications in ultrasonic nondestructive testing of waveguides.," *Ultrasonics*, vol. 62, pp. 3–19, sep 2015.

[105] Hoe Woong Kim, Young Eui Kwon, Joo Kyung Lee, and Yoon Young Kim, "Higher torsional mode suppression in a pipe for enhancing the first torsional mode by using magnetostrictive patch transducers," *IEEE Transactions on Ultrasonics, Ferroelectrics and Frequency Control*, vol. 60, pp. 562–572, mar 2013.

[106] H. Kuansheng, H. Songling, Z. Wei, W. Zheng, W. Shen, and H. Zijing, "A new frequency-tuned longitudinal wave transducer for nondestructive inspection of pipes based on magnetostrictive effect," in *2010 IEEE Sensors Applications Symposium (SAS)*, pp. 64–68, IEEE, feb 2010.

[107] Z. Liu, J. Zhao, B. Wu, Y. Zhang, and C. He, "Configuration optimization of magnetostrictive transducers for longitudinal guided wave inspection in seven-wire steel strands," *NDT & E International*, vol. 43, pp. 484–492, sep 2010.

[108] E. C. Ashigwuike, O. J. Ushie, R. Mackay, and W. Balachandran, "A study of the transduction mechanisms of electromagnetic acoustic transducers (EMATs) on pipe steel materials," *Sensors and Actuators A: Physical*, vol. 229, pp. 154–165, jun 2015.

[109] R. Ribichini, F. Cegla, P. B. Nagy, and P. Cawley, "Study and comparison of different EMAT configurations for SH wave inspection.," *IEEE transactions on ultrasonics, ferroelectrics, and frequency control*, vol. 58, no. 12, pp. 2571–81, 2011.

[110] M. J. Sablik, "Relationship between magnetostriction and the magnetostrictive coupling coefficient for magnetostrictive generation of elastic waves," in *AIP Conference Proceedings*, vol. 615, pp. 1613–1620, AIP, may 2002.

[111] M. Seher and P. B. Nagy, "On the separation of Lorentz and magnetization forces in the transduction mechanism of Electromagnetic Acoustic Transducers (EMATs)," *NDT & E International*, vol. 84, pp. 1–10, dec 2016.

[112] B. Clausse and A. Lhémery, "Transformation of body force generated by non-contact sources of ultrasound in an isotropic solid of complex shape into equivalent surface stresses," *Wave Motion*, vol. 60, pp. 135–148, 2016.

[113] Nurmalia, N. Nakamura, H. Ogi, and M. Hirao, "Mode conversion of torsional waves generated by electromagnetic acoustic transducer," vol. 1511, pp. 909–915, AIP Publishing, 2013.

[114] Y. Wang, X. Wu, P. Sun, J. Li, and J. L. Yugang Wang, Xinjun Wu, Pengfei Sun, "Enhancement of the excitation efficiency of a torsional wave PPM EMAT array for

pipe inspection by optimizing the element number of the array based on 3-D FEM," *Sensors*, vol. 15, pp. 3471–3490, jan 2015.

[115] S. Hill and S. H. K, "A New EMAT Design for Generating Torsional Guided Wave Modes for Pipe Inspections," *Review of Progress in Quantitative Nondestructive Evaluation*, vol. 1806, 2016.

[116] S. Hill, S. Dixon, H. Sri, K. Reddy, P. Rajagopal, K. Balasubramaniam, and S. H. Reddy, "A new electromagnetic acoustic transducer design for generating torsional guided wave modes for pipe inspections," *AIP Conference Proceedings*, vol. 1806, no. 050003, 2017.

[117] S. Huang, S. Wang, W. Li, and Q. Wang, "Analytical Method of EMAT Based on Lorentz Force Mechanism," in *Electromagnetic Ultrasonic Guided Waves*, pp. 43–102, Springer, Singapore, 2016.

[118] R. Ribichini, F. Cegla, P. B. Nagy, and P. Cawley, "Experimental and numerical evaluation of electromagnetic acoustic transducer performance on steel materials," *NDT & E International*, vol. 45, no. 1, pp. 32–38, 2012.

[119] A. Allaby and M. Allaby, *A dictionary of earth sciences.* Oxford University Press, 1999.

[120] Comsol ® INC, "COMSOL ® Multiphysics ®; Online, Retrieved from: https://www.comsol.com/," 2016.

[121] A. Demma, *The interaction of guided waves with discontinuities in structures.* PhD thesis, Imperial College of Science, Technology and Medicine, 2003.

[122] D. N. Alleyne, B. Pavlakovic, M. Lowe, and P. Cawley, "The Use of Guided Waves for Rapid Screening of Chemical Plant Pipework," *Journal of the Korean Society for Nondestructive Testing*, vol. 22, no. 6, pp. 589–598, 2002.

[123] S. S. Rao and S. S. Rao, "Chapter 21 - Finite Element Analysis Using ABAQUS," in *The Finite Element Method in Engineering*, pp. 671–701, Elsevier, 2018.

[124] M. B. Drozdz, *Efficient finite element modelling of ultrasound waves in elastic media*. PhD thesis, Imperial College of Science, Technology and Medicine, 2008.

[125] X. Jian, S. Dixon, R. S. Edwards, and J. Morrison, "Coupling mechanism of an EMAT," *Ultrasonics*, vol. 44, pp. 653–656, 2006.

[126] W. Luo and J. L. Rose, "Guided wave thickness measurement with EMATs," *Insight: Non-Destructive Testing and Condition Monitoring*, vol. 45, no. 11, pp. 735–739, 2003.

[127] M. Seher, P. Huthwaite, M. Lowe, P. B. Nagy, and P. Cawley, "Numerical design optimization of an EMAT for A0 Lamb wave generation in steel plates," *AIP Conference Proceedings*, vol. 1581 33, pp. 340–347, 2014.

[128] R. Ribichini, F. Cegla, P. B. Nagy, and P. Cawley, "Quantitative modeling of the transduction of electromagnetic acoustic transducers operating on ferromagnetic media," *IEEE Transactions on Ultrasonics, Ferroelectrics, and Frequency Control*, vol. 57, no. 12, pp. 2808–17, 2010.

[129] P. D. Wilcox, M. Lowe, and P. Cawley, "Omnidirectional guided wave inspection of large metallic plate structures using an EMAT array," *IEEE Transactions on Ultrasonics, Ferroelectrics, and Frequency Control*, vol. 52, no. 4, pp. 653–665, 2005.

[130] M. Hirao and H. Ogi, "An SH-wave EMAT technique for gas pipeline inspection," *NDT & E International*, vol. 32, pp. 127–132, apr 1999.

[131] Engineering TiePie, "Handyscope HS3 key specifications; Online, Retrieved from: https://www.tiepie.com/en/products/Oscilloscopes/Handyscope_HS3/Key_specifications," 2017.

[132] Maplin Electronics, "Kemo 40W Power Amplifier Module | maplin," 2017.

[133] K. S. Ho, T. H. Gan, D. R. Billson, and D. A. Hutchins, "Application of pulse compression signal processing techniques to electromagnetic acoustic transducers for noncontact thickness measurements and imaging," *Review of Scientific Instruments*, vol. 76, p. 054902, may 2005.

[134] D. Rueter, "Induction coil as a non-contacting ultrasound transmitter and detector: Modeling of magnetic fields for improving the performance," *Ultrasonics*, vol. 65, pp. 200–210, 2016.

[135] Analog Devices, "AD8331 Evaluation Board; Online, Retrieved from: http://www.analog.com/media/en/technical-documentation/evaluation-documentation/154207235AD8331EB_a.pdf," 2006.

[136] Analog Devices, "Ultralow Noise VGAs with Preamplifier and Programmable R IN; Online, Retrieved from: http://www.analog.com/media/en/technical-documentation/data-sheets/AD8331_8332_8334.pdf," 2016.

[137] AMS Technologies AG, "High Precision HF Current Transformers, Electronic Components; Online, Retrieved from: https://www.amstechnologies-webshop.com/electronic-components/high-precision-hf-current-transformers/?p=1," 2017.

[138] D. L. Robot Electronics, "USB RLY08 Technical Documentation; Online, Retrieved from: https://www.robot-electronics.co.uk/htm/usb_rly08tech.htm," 2018.

[139] X. Ding, X. Wu, and Y. Wang, "Bolt axial stress measurement based on a mode-converted ultrasound method using an electromagnetic acoustic transducer.," *Ultrasonics*, vol. 54, pp. 914–920, mar 2014.

[140] M. Cong, X. Wu, and C. Qian, "A Longitudinal Mode Electromagnetic Acoustic Transducer (EMAT) Based on a Permanent Magnet Chain for Pipe Inspection," *Sensors*, vol. 16, p. 740, jan 2016.

[141] A. Furusawa, F. Kojima, and A. Morikawa, "Mode control of guided wave in magnetic hollow cylinder using electromagnetic acoustic transducer array," *Nuclear Engineering and Technology*, vol. 47, no. 2, pp. 196–203, 2015.

[142] R. Inc., "RPR-4000 High Power Pulser Receiver; Online, Retrieved from: http://www.ritecinc.com/index.php/our-products/systems," 2017.

[143] A. Rich, "Understanding intererence-type Noise," *Analog Dialogue*, vol. 16, no. 3, pp. 16–19, 1982.

[144] F. Cegla and B. Herdovics, "Guided Wave testing- patent application GB1604440.6 publication number: WO2017/158318," 2016.

[145] B. Whitlock, *Understanding, finding, & eliminating ground loops*. Chatsworth, California: MIT, 2008.

[146] R. M. Bozorth and IEEE Magnetics Society., *Ferromagnetism*. IEEE Press, 1993.

[147] K.-H. Brensing and B. Sommer, *Steel Tube and Pipe Manufacturing Processes*. Dusseldorf: Salzgitter Mannesmann International GmbH.

[148] D. Atherton and W. Czura, "Finite element calculations on the effects of permeability variation on magnetic flux leakage signals," *NDT International*, vol. 20, pp. 239–241, aug 1987.

[149] D. L. Atherton and L. Clapham, "Magnetic Properties of Pipeline Steels are Variable," in *2004 International Pipeline Conference, Volumes 1, 2, and 3*, pp. 1033–1040, ASME, jan 2004.

[150] ASTM International, "A530/A530M-12 Specification for General Requirements for Specialized Carbon Steel and Alloy Steel Pipe," 2012.

[151] Q. Cheng, Y. Gan, P. Wang, W. Sun, Y. Xu, and Y. Liu, "The study on temperature field variation and phase transition law after shutdown of buried waxy crude oil pipeline," *Case Studies in Thermal Engineering*, vol. 10, pp. 443–454, sep 2017.

[152] H. Li and J. Zhang, "Viscosity prediction of non-Newtonian waxy crude heated at various temperatures," *Petroleum Science and Technology*, vol. 32, no. 5, pp. 521–526, 2014.

[153] J. Zhao, H. Dong, X. Wang, and X. Fu, "Research on heat transfer characteristic of crude oil during the tubular heating process in the floating roof tank," *Case Studies in Thermal Engineering*, vol. 10, pp. 142–153, sep 2017.

[154] X. Jiang, K. Kim, S. Zhang, J. Johnson, and G. Salazar, "High-Temperature Piezoelectric Sensing," *Sensors*, vol. 14, pp. 144–169, dec 2013.

[155] F. Cegla, P. Cawley, J. Allin, and J. Davies, "High-temperature (>500 C) wall thickness monitoring using dry-coupled ultrasonic waveguide transducers," *IEEE Transactions on Ultrasonics, Ferroelectrics, and Frequency Control*, vol. 58, no. 1, pp. 156–167, 2011.

[156] P. Mudge, "Use of Guided Wave Inspections to Monitor the Integrity of Nuclear Power Station Boilers," in *Sensors, Algorithms and Applications for Structural Health Monitoring*, pp. 37–46, Springer, Cham, 2018.

[157] N. Lunn, S. Dixon, and M. Potter, "High temperature EMAT design for scanning or fixed point operation on magnetite coated steel," *NDT & E International*, vol. 89, pp. 74–80, 2017.

[158] M. Kogia, T.-H. Gan, W. Balachandran, M. Livadas, V. Kappatos, I. Szabo, A. Mohimi, and A. Round, "High Temperature Shear Horizontal Electromagnetic Acoustic Transducer for Guided Wave Inspection," *Sensors*, vol. 16, p. 582, apr 2016.

[159] A. S. Kim and F. E. Camp, "High performance NdFeB magnets," *Journal of Applied Physics*, vol. 79, p. 5035, 1996.

[160] G. Bai, R. Gao, Y. Sun, G. Han, and B. Wang, "Study of high-coercivity sintered NdFeB magnets," *Journal of Magnetism and Magnetic Materials*, vol. 308, pp. 20–23, jan 2007.

[161] J. F. Liu, Y. Zhang, D. Dimitrov, and G. C. Hadjipanayis, "Microstructure and high temperature magnetic properties of Sm(Co, Cu, Fe, Zr)z (z=6.7-9.1) permanent magnets," *Journal of Applied Physics*, vol. 85, p. 2800, feb 1999.

[162] D. Givord, P. Tenaud, and T. Viadieu, "Coercivity mechanisms in ferrites and rare earth transition metal sintered magnets (SmCo/sub 5/, Nd-Fe-B)," *IEEE Transactions on Magnetics*, vol. 24, pp. 1921–1923, mar 1988.

[163] J. Liu and M. Walmer, "Thermal Stability and Performance Data for SmCo 2:17 High-Temperature Magnets on PPM Focusing Structures," *IEEE Transactions on Electron Devices*, vol. 52, pp. 899–902, may 2005.

[164] I. Smooth-On, "Dragon Skin® 30 Product Information ; Online, Retrieved from: https://www.smooth-on.com/products/dragon-skin-30/," 2018.

[165] T. Clarke, F. Simonetti, and P. Cawley, "Guided wave health monitoring of complex structures by sparse array systems: Influence of temperature changes on performance," *Journal of Sound and Vibration*, vol. 329, no. 12, pp. 2306–2322, 2010.

[166] C. A. Dan, P. Kudela, M. Radzieński, and W. Ostachowicz, "Temperature Effects Compensation Strategy for Guided Wave Based Structural Health Monitoring," *6th International Symposium on NDT in Aerospace, 12-14th November 2014*, 2014.

[167] G. Konstantinidis, B. W. Drinkwater, and P. D. Wilcox, "The temperature stability of guided wave structural health monitoring systems," *Smart Materials and Structures*, vol. 15, pp. 967–976, aug 2006.

[168] A. C. Cobb, H. Kwun, L. Caseres, and G. Janega, "Torsional guided wave attenuation in piping from coating, temperature, and large-area corrosion," *NDT & E International*, vol. 47, pp. 163–170, 2012.

[169] D. N. Alleyne, B. Pavlakovic, M. Lowe, and P. Cawley, "Rapid, long range inspection of chemical plant pipework using guided waves," *The Journal of the Acoustical Society of America*, vol. 557, no. 114, pp. 2622–611, 2001.

[170] J. Morrison, S. Dixon, M. Potter, and X. Jian, "Lift-off compensation for improved accuracy in ultrasonic lamb wave velocity measurements using electromagnetic acoustic transducers (EMATs)," *Ultrasonics*, vol. 44, pp. e1401–e1404, dec 2006.

[171] J.-Y. Kim, L. J. Jacobs, J. Qu, and J. W. Littles, "Experimental characterization of fatigue damage in a nickel-base superalloy using nonlinear ultrasonic waves," *The Journal of the Acoustical Society of America*, vol. 120, no. 3, pp. 1266–1273, 2006.

[172] S. Assous, J. Rees, M. Lovell, L. Linnett, and D. Gu, "Bandwidth Enhancement: Correcting Magnitude and Phase Distortion in Wideband Piezoelectric Transducer Systems," in *Advances in Piezoelectric Transducers*, InTech, nov 2011.

[173] A. M. Hurst, S. Carter, D. Firth, A. Szary, and J. VanDeWeert, "Real-Time, Advanced Electrical Filtering for Pressure Transducer Frequency Response Correction," in *Proceedings of ASME Turbo Expo 2015*, p. V006T05A015, ASME, jun 2015.

[174] Y. Labyed and Lianjie Huang, "Super-resolution ultrasound imaging using a phase-coherent MUSIC method with compensation for the phase response of transducer elements," *IEEE Transactions on Ultrasonics, Ferroelectrics, and Frequency Control*, vol. 60, pp. 1048–1060, jun 2013.

[175] S. Ha, K. Lonkar, A. Mittal, and F. K. Chang, "Adhesive Layer Effects on PZT-induced Lamb Waves at Elevated Temperatures," *Structural Health Monitoring*, vol. 9, pp. 247–256, may 2010.

[176] J. B. Harley and M. F. Moura, "Scale Transform Signal Processing for Optimal Ultrasonic Temperature Compensation," *IEEE Transactions on Ultrasonics Ferroelectrics and Frequency Control*, vol. 15213, pp. 1–16, 2012.

[177] B. Herdovics and F. Cegla, "Structural health monitoring using torsional guided wave electromagnetic acoustic transducers," *Structural Health Monitoring*, vol. 17, no. 1, pp. 24–38, 2018.

[178] A. J. Croxford, P. D. Wilcox, G. Konstantinidis, and B. W. Drinkwater, "Strategies for overcoming the effect of temperature on guided wave structural health monitoring," in *Health Monitoring of Structural and Biological Systems* (T. Kundu, ed.), p. 65321T, International Society for Optics and Photonics, apr 2007.

[179] P. D. Wilcox, A. J. Croxford, J. E. Michaels, Y. Lu, B. W. Drinkwater, D. O. Thompson, and D. E. Chimenti, "A comparison of temperature compensation methods for guided wave structural health monitoring," in *AIP Conference Proceedings*, vol. 975, pp. 1453–1460, AIP, 2008.

[180] C. Liu, J. Dobson, and P. Cawley, "Efficient generation of receiver operating characteristics for the evaluation of damage detection in practical structural health monit-

oring applications," *Proceedings of the Royal Society A: Mathematical, Physical and Engineering Science*, vol. 473, p. 20160736, mar 2017.

[181] C. Liu and P. Cawley, "Practical Guided Wave SHM of Pipes Processing Multiple Data Sets to Give Reliable Defect Detection," in *8th European Workshop on Structural Health Monitoring (EWSHM 2016)*, (Bilbao), 2016.

[182] J. Davies and P. Cawley, "The application of synthetic focusing for imaging crack-like defects in pipelines using guided waves," *IEEE Transactions on Ultrasonics, Ferroelectrics and Frequency Control*, vol. 56, pp. 759–771, apr 2009.

[183] D. N. Alleyne, B. Pavlakovic, M. Lowe, and P. Cawley, "Rapid, long range inspection of chemical plant pipework using guided waves," in *AIP Conference Proceedings*, vol. 557, pp. 180–187, AIP, jun 2001.

[184] P. D. Wilcox, "Guided-Wave Array Methods," in *Encyclopedia of Structural Health Monitoring*, Chichester, UK: John Wiley & Sons, Ltd, jan 2008.

[185] B. Herdovics and F. Cegla, "Compensation of phase response changes in ultrasonic transducers caused by temperature variations," *Structural Health Monitoring*, mar 2018.

[186] J. M. Camacho and V. Sosa, "Alternative method to calculate the magnetic field of permanent magnets with azimuthal symmetry," *Revista Mexicana de Física E*, vol. 59, pp. 8–17, 2013.

[187] Olympus, "UltraWave LRT Instrument; Online, Retrieved from: https://www.olympus-ims.com/en/ultrawave/#!," 2017.

List of Publications

Written publications

[P1] B. Herdovics and F. Cegla. "Structural health monitoring using torsional guided wave electromagnetic acoustic transducers", *Structural Health Monitoring*, vol. 17, no. 1, pp. 2438, 2018.

[P2] B. Herdovics and F. Cegla. "Guided Wave testing- patent, publication number: WO2017/158318", in *World Intellectual Property Organization*. 2017

[P3] B. Herdovics and F. Cegla, "Compensation of phase response changes in ultrasonic transducers caused by temperature variations", *Structural Health Monitoring*, vol. 0, Mar 2018.

[P4] B. Herdovics and F. Cegla. "Long-term stability of Guided-wave EMAT systems", *Structural Health Monitoring*, Sep 2018. Recommended for publication (revision suggested)

Separate posters & oral presentations

[P5] B. Herdovics and F. Cegla. "Torsional guided wave EMAT for SHM", at *16th Anglo-French Physical Acoustics Conference (AFPAC)*, Marseille, France. 2017.

[P6] B. Herdovics and F. Cegla. "Torsional guided wave EMAT for Structural Healt Monitoring applications", poster presentation at *Review of progress in quantitative nondestructive evaluation*, Provo, USA. 2017.

[P7] B. Herdovics and F. Cegla. "Compensation of transducer induced waveform changes during monitoring", at *Review of progress in quantitative nondestructive evaluation*, Provo, USA. 2017.

[P8] B. Herdovics and F. Cegla. "Evaluation of the long-term stability of guided wave EMAT transducers", at *European Workshop on Structural Health Monitoring*, Manchester, UK. 2018.

[P9] J. Isla, B. Herdovics and F. Cegla, "SHM with EMATs", *8th European Workshop On Structural Health Monitoring (EWSHM 2016), 5-8 July 2016, Spain, Bilbao*

[P10] F. Cegla, B. Herdovics. "Coded excitation, motion and signal-to-noise ratio", *2018 IEEE International Symposium on Circuits and Systems (ISCAS),* Florence, Italy. 2018.